

ISSN 1573-160X

Vol. 32, Iss. 2

March – April

2025



Physical Oceanography

<http://physical-oceanography.ru/>



EDITORIAL BOARD

- Sergey K. Kononov** – Editor-in-Chief, Director of FSBSI FRC MHI, corresponding member of RAS, Dr.Sci. (Geogr.), ORCID ID: 0000-0002-5200-8448, secretary@mhi-ras.ru (Sevastopol, Russia)
- Vladimir N. Belokopytov** – Deputy Editor-in-Chief, Head of Department of FSBSI FRC MHI, Dr.Sci. (Geogr.), ORCID ID: 0000-0003-4699-9588 (Sevastopol, Russia)
- Aleksandr I. Kubryakov** – Deputy Editor-in-Chief, Chief Scientist Researcher of FSBSI FRC MHI, Dr.Sci. (Phys.-Math.), ORCID ID: 0000-0003-1899-9230, ResearcherID: F-8959-2014 (Sevastopol, Russia)
- Anton A. Bukatov** – Executive Editor, Leading Research Associate of FSBSI FRC MHI, Ph.D. (Phys.-Math.), ORCID ID: 0000-0002-1165-8428, journal@mhi-ras.ru (Sevastopol, Russia)
- Yuri V. Artamonov** – Head Scientist Researcher of FSBSI FRC MHI, Dr.Sci. (Geogr.), ResearcherID: AAC-6651-2020 (Sevastopol, Russia)
- Sergey V. Berdnikov** – Director of FRC SSC of RAS, Dr.Sci. (Geogr.), ORCID ID: 0000-0002-3095-5532 (Rostov-on-Don, Russia)
- Valery G. Bondur** – Scientific Supervisor of ISR "AEROCOSMOS", academician of RAS, Dr.Sci. (Techn.), ORCID ID: 0000-0002-2049-6176 (Moscow, Russia)
- Demuri I. Demetrashvili** – Head of the sector of mathematical modeling of geophysical processes of sea and atmosphere, the Nodia Institute of Geophysics of the Javakhishvili Tbilisi State University, Dr.Sci. (Phys.-Math.), ORCID ID: 0000-0002-4789-4852 (Tbilisi, Georgia)
- Sergey A. Dobrolyubov** – Dean of Faculty of Geography of MSU, academician of RAS, Dr.Sci. (Geogr.), prof., ResearcherID: A-9688-2012 (Moscow, Russia)
- Grigory I. Dolgikh** – Head Scientific Researcher of POI FEB of RAS, Dr.Sci. (Phys.-Math.), academician of RAS, prof., ORCID ID: 0000-0002-2806-3834 (Vladivostok, Russia)
- Vladimir A. Dulov** – Head of Laboratory of FSBSI FRC MHI, Dr.Sci. (Phys.-Math.), prof., ORCID ID: 0000-0002-0038-7255 (Sevastopol, Russia)
- Vladimir V. Efimov** – Head of Department of FSBSI FRC MHI, Dr.Sci. (Phys.-Math.), prof., ResearcherID: P-2063-2017 (Sevastopol, Russia)
- Vladimir V. Fomin** – Head of Department of FSBSI FRC MHI, Dr.Sci. (Phys.-Math.), ORCID ID: 0000-0002-9070-4460 (Sevastopol, Russia)
- Isaac Gertman** – Head of the Physical Oceanography Department of Israel Oceanographic & Limnological Research, Head of IOLR data center ISRAMAR, Ph.D. (Geogr.), ORCID ID: 0000-0002-6953-6722 (Haifa, Israel)
- Dmitry G. Gryazn** – Head of Department, Chief Metrologist of SRC of the "Concern CSRI Elektropribor" JSC, Dr.Sci. (Techn.), prof. of Mechatronics of ITMO University, Scopus Author ID: 25638150600 (Saint Petersburg, Russia)
- Rashit A. Ibraev** – Chief Scientist Researcher of INM of RAS, corresponding member of RAS, Dr.Sci. (Phys.-Math.), ORCID ID: 0000-0002-9099-4541 (Moscow, Russia)
- Igor K. Ivashchenko** – Senior Scientist of FSBSI FRC MHI, Ph.D. (Econ.) (Sevastopol, Russia)
- Vasily V. Knysh** – Head Scientist Researcher of FSBSI FRC MHI, Dr.Sci. (Phys.-Math.), prof., ResearcherID: B-3603-2018 (Sevastopol, Russia)
- Gennady K. Korotaev** – Scientific Supervisor of FSBSI FRC MHI, corresponding member of RAS, Dr.Sci. (Phys.-Math.), prof., ResearcherID: K-3408-2017 (Sevastopol, Russia)
- Vladimir N. Kudryavtsev** – Executive Director of Satellite Oceanography Laboratory of RSHU, Dr.Sci. (Phys.-Math.), prof., ResearcherID: G-1502-2014 (Saint Petersburg)
- Michael E. G. Lee** – Head of Department of FSBSI FRC MHI, Dr.Sci. (Phys.-Math.), prof., ORCID ID: 0000-0002-2292-1877 (Sevastopol, Russia)
- Gennady G. Matishov** – Deputy President of RAS, Deputy academician-Secretary of the Department of Earth Sciences of Supervisor of RAS – Head of the Oceanology, Atmospheric Physics and Geography Section, Scientific Supervisor of SSC of RAS, Supervisor of MMBI KSC of RAS, academician of RAS, Dr.Sci. (Geogr.), prof., ORCID ID: 0000-0003-4430-5220 (Rostov-on-Don, Russia)
- Nickolay A. Rimski-Korsakov** – Deputy Director (Marine Engineering) of FSBSI P.P. Shirshov IO of RAS, Dr.Sci. (Techn.), ResearcherID: K-8378-2017 (Moscow, Russia)
- Angelo Rubino** – Professor of Ca' Foscari University, Ph.D. (Phys. Oceanogr.), ORCID ID: 0000-0003-3857-4811 (Venice, Italy)
- Anatoly S. Samodurov** – Head of Department of FSBSI FRC MHI, Dr.Sci. (Phys.-Math.), ResearcherID: V-8642-2017 (Sevastopol, Russia)
- Georgy I. Shapiro** – Head of Plymouth Ocean Forecasting Centre of the University of Plymouth, Dr.Sci. (Phys.-Math.), prof. in Phys. Oceanogr. (Plymouth, Great Britain)
- Naum B. Shapiro** – Head Scientist Researcher of FSBSI FRC MHI, Dr.Sci. (Phys.-Math.), ResearcherID: A-8585-2017 (Sevastopol, Russia)
- Mikhail V. Shokurov** – Head Scientist Researcher of FSBSI FRC MHI, Dr.Sci. (Phys.-Math.), ORCID ID: 0000-0003-1595-8281 (Sevastopol, Russia)
- Elena F. Vasechkina** – Deputy Director of FSBSI FRC MHI, Chief Research Associate of FSBSI FRC MHI, Dr.Sci. (Geogr.), ORCID ID: 0000-0001-7007-9496 (Sevastopol, Russia)
- Elizaveta V. Zabolotskikh** – Head Scientist Researcher of RSHU, Dr.Sci. (Phys.-Math.), Scopus Author ID: 6506482460 (Saint Petersburg, Russian)
- Vladimir B. Zalesny** – Head Scientific Researcher of INM of RAS, Dr.Sci. (Phys.-Math.), prof., ORCID ID: 0000-0003-3829-3374 (Moscow, Russia)
- Andrey G. Zatsepin** – Chief of Laboratory of FSBSI P.P. Shirshov IO of RAS, Chief Research Associate of FSBSI P.P. Shirshov IO of RAS, Dr.Sci. (Phys.-Math.), ORCID ID: 0000-0002-5527-5234 (Moscow, Russia)
- George Zodiatis** – Senior Researcher of Laboratory of Coastal and Marine Research of the Institute of Applied and Computational Mathematics. for Research and Technology Foundation – Hellas, Ph.D. (Oceanol.), ResearcherID: J-3032-2013 (Heraklion, Crete, Greece)

ISSN 1573-160X

Vol. 32, no. 2. 2025

March – April

Founded in January 1987

Publication frequency:

6 issues per year

Physical Oceanography

Scientific and theoretical journal

FOUNDER AND PUBLISHER:

Federal State Budget Scientific Institution

Federal Research Centre

“Marine Hydrophysical Institute of RAS”

Peer reviewed scientific journal.

The Journal publishes original research results, review articles (at the editorial board's request) and brief reports on the following sections of hydrophysics:

- thermohydrodynamics of the ocean and atmosphere;
- analysis of observational results and methods of calculation of ocean hydrophysical fields;
- experimental and expeditionary studies;
- satellite hydrophysics;
- mathematical modelling of marine systems;
- automation of scientific research of the seas and oceans.

Objectives

- familiarisation of the world and Russian scientific community with the results of theoretical, experimental and expeditionary studies of the World Ocean;
- exchange of scientific information, experience, research and observation data with specialists from different regions of the country and abroad;
- increase of publication activity of national authors, rating of scientific organisations of Russia and level of national publications in the world scientific community according to their citation data;
- theoretical and practical assistance to scientists in preparing articles for printing that meet modern requirements of publication and scientific ethics;
- strengthening the popularity and authority of the publication, increasing the number of regular subscribers

The Journal is indexed in:

Google Scholar
Web of Science (ESCI)
Scopus

journal@mhi-ras.ru

<http://physical-oceanography.ru/>

Founder, Publisher and Editorial Office address:

2, Kapitanskaya St., Sevastopol, 299011

Russia

Phone, fax: + 7 (8692) 54-02-23

CONTENTS

Vol. 32, no. 2. 2025

March – April, 2025

ANALYSIS OF OBSERVATIONS AND METHODS OF CALCULATING HYDROPHYSICAL FIELDS IN THE OCEAN

- Voinov G. N., Sukhachev V. N.** Seasonal variation of tides in the Barents and Kara seas 151
- Maksimovskaya T. M., Zimin A. V., Atadzhanova O. A., Konik A. A., Moiseev D. V.** Variability of water characteristics in the northeastern part of the Greenland Sea during the winter periods in 2019–2023 174
- Bukatov A. A., Pavlenko E. A., Solovei N. M.** Investigation of the upper mixed layer variability in the Barents and Kara seas 187
- Sokolov A. N., Chubarenko B. V.** Long-term dynamics of the annual average wave heights in the Baltic Sea 197

MATHEMATICAL MODELING OF MARINE SYSTEMS

- Tikhonova N. A., Zakharchuk E. A., Vinogradov M. V., Travkin V. S.** Modeling of the Major Baltic inflow using a joint model of the North and Baltic seas 211

EXPERIMENTAL AND FIELD RESEARCH

- Bagaev A. V., Gurov K. I., Nuriev S. A.** Granulometric characteristics of bottom sediments in the sublittoral region of the Southern coast of Crimea in the area of Limenskaya Bay 238
- Shevchenko G. V., Chastikov V. N., Ulchenko V. A.** Features of hydrological regime nearby the Pacific coast of the northern Kuril Islands based on ship oceanographic surveys 253
- Dolgikh G. I., Dolgikh S. G., Bolsunovskii M. A.** Relationship between the energy of gravity and infragravity sea waves 270



All the materials of the journal are available under Creative Commons Attribution-NonCommercial 4.0 International (CC BY-NC 4.0)

Original article

Seasonal Variation of Tides in the Barents and Kara Seas

G. N. Voinov^{1, 2, ✉}, V. N. Sukhachev^{1, 3}

¹ *N. N. Zubov State Oceanographic Institute, Moscow, Russian Federation*

² *Arctic and Antarctic Research Institute, Saint Petersburg, Russian Federation*

³ *Saint Petersburg State University, Saint Petersburg, Russian Federation*

✉ voinovgn@mail.ru

Abstract

Purpose. The paper aims at the studies of features of seasonal variation of the main semidiurnal and diurnal tides in the annual cycle in the Barents and Kara seas according to the long-term data of sea level observations at all points (stations). The structure of seasonal course of the tide is estimated on the example of the M_2 and K_1 tides and physical mechanisms of its formation.

Methods and Results. The work was carried out according to the data of long-term tide gauge hourly observations of the sea level and 6-hourly interval series of the sea level measurements mainly from the ESIMO database from 1977 to the end of observations. Marine hydrometeorological year-book data since 1951 were also used. On the basis of the harmonic analysis of tides with the least square method of hourly annual and monthly time series of sea level, the average monthly values of amplitudes and phases of the main semidiurnal and diurnal tides at 17 points in the Barents Sea and 19 points in the Kara Sea are estimated. In general, the range of seasonal course of the M_2 tide in the Barents Sea increases from north to south and is most significant in the southeast of the sea. According to our classification, classic type 1 of the seasonal course of the M_2 tide is not predominant and is 35%, and anomalous type 3 is the most observed one, reaching 41% of 17 points. In the Kara Sea, classic type 1 of seasonal course of the M_2 tide is mainly observed with an amplitude maximum and phase minimum in July–September, manifesting itself in 74% of all cases in 19 points.

Conclusions. At each point of the Barents and Kara seas, individual time-stable seasonal annual course of main semidiurnal, diurnal and shallow tides is observed. The seasonal course of harmonic constants differs significantly among the points in terms of the degree of severity, shape of curves, time of occurrence of extreme values and magnitude of oscillation range. Moreover, seasonal variations of the constants of semidiurnal and diurnal tides are different. In the Barents Sea, the influence of drifting ice cover on the seasonal variations of main semidiurnal tides is much weaker than in the Kara Sea. The seasonal variations of amplitudes and phases of the daily K_1 tide are dominated by the semiannual period. The maximum deviations of amplitudes from the mean annual value (norm) are mainly 10–20%, and those of phases – 6–16°.

Keywords: Arctic, Barents Sea, Kara Sea, harmonic analysis of tides, seasonal course of the M_2 tide, seasonal course of the K_1 tide, amplitude, tide phase

Acknowledgments: the work was carried out within the framework of the state assignment on the RTW 4.6.14 Rosgidromet theme.

For citation: Voinov, G.N. and Sukhachev, V.N., 2025. Seasonal Variation of Tides in the Barents and Kara Seas. *Physical Oceanography*, 32(2), pp. 151-173.

© 2025, G. N. Voinov, V. N. Sukhachev

© 2025, Physical Oceanography



Introduction

The first information on the intra-annual course of the tide were found in the work of A. M. Bukhteev ¹. The results of the analysis of 12-month hourly series of tides for 1906–1907 in the Ekaterininskaya Gavan (settlement of Polyarnoe, the Barents Sea) by the Darwin method were presented. However, due to the complete absence of pronounced course in the tide in the annual cycle and presence of seasonal variations (small in magnitude) only in the M_2 tide amplitude, A. M. Bukhteev did not interpret this phenomenon as seasonal course.

For the first time in the world practice of tidal analysis, data on their seasonal course and an analytical model of the annual course of the M_2 tide disturbance were given in the work of R. H. Corkan [1]. This study was innovative and, perhaps, for this reason, it remained unclaimed for a long time. The model of R. H. Corkan in tide prediction has been used only since the end of the 20th century. As a result of the implementation of the project for the Northern Sea Route (NSR) development and the study of the tides of the Arctic seas of Russia in the 1930–40s, short-term (monthly and half-monthly) series of sea level observations were obtained at a number of polar stations. The results of tide processing by the Darwin method in the Kara and Laptev seas were published in eight issues of materials ².

A review of the results of the first issues of these materials made it possible for W. J. Wiese [2] to conclude that seasonal course of the tides of the Arctic seas is a widespread phenomenon. Based on these data, it was established that the amplitude of the tide decreases in winter and high water occurs later than in summer. This work proposed to relate the harmonic constants of the tide, determined at some time at a specific point, to the season or even to a specific month of the year. Later, the author of [3] explained the intra-annual fluctuations of the tide constants by the influence of not only fluctuations in the ice cover of the Arctic seas, but also long-term changes in the wind regime.

¹ Bukhteev, A.M., 1910. [*Observations of Tides in Murmansk and their Processing*]. Saint Petersburg: Printing House of the Naval Ministry, in the Main Admiralty, 56 p. Available at: <https://elib.rgo.ru/safe-view/123456789/227016/1/0L7Qui4yOTFfQnVodGVldiBBLk0uIE5hYmx5dWRlbnl5YSBwcmlsaXZvdsKgbmEgTXVybwFuZSBpIG8ucGRm> [Accessed: 02 April 2025] (in Russian).

² Arctic Institute, 1935. *Materials for the Study of Tides of the Arctic Seas of the USSR*. Proceedings of the Arctic Institute, Vol. 36, Iss. 1. Leningrad, 51 p.; Arctic Institute, 1936. *Hydrology. Materials for the Study of Tides of the Arctic Seas of the USSR*. Proceedings of the Arctic Institute, Vol. 52, Iss. 2. Leningrad, 80 p.; Arctic Institute, 1937. *Materials for the Study of Tides of the Arctic Seas of the USSR*. Proceedings of the Arctic Institute, Vol. 81, Iss. 3. Leningrad, 95 p.; Arctic Institute, 1938. *Materials for the Study of Tides of the Arctic Seas of the USSR*. Proceedings of the Arctic Institute, Vol. 119, Iss. 4. Leningrad, 82 p.; Arctic Institute, 1940. *Materials for the Study of Tides of the Arctic Seas of the USSR*. Proceedings of the Arctic Institute, Vol. 153, Iss. 5-6). Moscow; Leningrad, 199 p.; Arctic Institute, 1952. *Materials for the Study of Tides of the Arctic Seas of the USSR*. Proceedings of the Arctic Institute, Vol. 42, Iss. 7. Leningrad, 536 p.; Arctic Institute, 1952. *Materials for the Study of Tides of the Arctic Seas of the USSR*. Proceedings of the Arctic Institute, Vol. 50, Iss. 8. Leningrad, 295 p. (in Russian).

These publications, as new observations were obtained, gave rise to numerous studies of the seasonal course of the tides of the Arctic seas of Russia ³ [4].

To estimate the ice cover influence on the tidal constants, it was proposed in [4] to use coefficients of tide attenuation per kilometer of its path and corresponding delay in fractions of an hour. Subsequently, it was shown in [5] that the formulas used to calculate these coefficients gave extremely large calculation errors (up to 100%). Therefore, the obtained connections are not significant and reliable.

Many works of the mid-20th century on the key issue of seasonal course of the tide from the standpoint of modern science turn out to be not entirely reliable and even erroneous ^{4, 5} [6, 7] because of the following reasons.

1. Shortcomings of the tidal analysis methodology of that time and errors in the tidal analysis methods used.

2. Insufficiency of continuous annual series of tidal observations to obtain stable monthly mean values of tide constants or their seasonal variation.

3. Underestimation of the progressive model of R. H. Corkan [1] and use of non-harmonic characteristics (tide applied hour and magnitude) to estimate the seasonal course of tides.

4. Technical reason (lack of powerful computing tools until the early 1970s).

Let us reveal the content of the first, main reason (except for the other quite understandable ones). Previously, the 15-day series results processed by the Darwin method and the Admiralty method (AM) of tidal analysis per day were widely used. In the 1960s, many works appeared on the shortcomings of the Darwin method for 30 and 15 days, especially ⁶ [8]. The tide constants obtained from the semi-monthly series analysis have a pronounced time periodicity depending on astronomical conditions. To an even greater extent, this concerns the results of the analysis of daily observation cycles by the AM. The combined use of the results of processing monthly, semi-monthly and especially daily series for studying seasonal variations in tides is unacceptable.

³ Kopteva, A.V., 1945. [*Ice Cover Effect on the Velocity of Tidal Wave Distribution*]. Reports of the Jubilee Session. Arctic Research Institute of Glavsevmorput under the Council of People's Commissars of the USSR. 25th Anniversary. 1920–1945. Moscow: Glavsevmorput Publishing, 7 p. (in Russian).

⁴ Dremluyug, V.V., 1950. [Tides of the Chukchi and the Beaufort Seas due to Hydrometeorological Conditions]. In: *Proceedings of the Higher Arctic Marine Institute*. Glavsevmorput Publishing, 60 p. (in Russian).

⁵ Kopteva, A.V., 1959. *Tidal Phenomena of the Arctic Seas (Kara, Laptev, East Siberian, and Chukchi)*. Leningrad. State Research Center of the Russian Federation AARI. Inv. No. R-5562. Book 1, Chapters 1, 2, 193 p.; Kopteva, A.V., 1959. *Tidal Phenomena of the Arctic Seas (Kara, Laptev, East Siberian, and Chukchi)*. State Research Center of the Russian Federation AARI. Inv. No. R-5563. Leningrad. Book 2, Chapters 3, 4, pp. 194-317; Kopteva, A.V., 1959. *Tidal Phenomena of the Arctic Seas (Kara, Laptev, East Siberian, and Chukchi)*. State Fund of the State Scientific Center of the Russian Federation AARI. Inv. No. R-5564. Leningrad. Book 3, Chapters 5, 6, 7, pp. 318-482 (in Russian).

⁶ Altshuler, V.M., 1966. *Practical Issues of Analysis and Calculation of Sea Tides*. Leningrad: Gidrometeoizdat, 311 p. (in Russian).

A serious methodological error in many domestic works was the use of arithmetic averaging of the processing results (amplitudes and phases of tides), rather than the vector average calculation. The differences in the averaging results with large values of the spread of the tide amplitudes and phases can be large. By the way, it was demonstrated in [9], although the vector averaging method was not used later.

Calculation errors of this or that method and the accuracy of the obtained tides were not assessed at all. The calculations were checked not by the residual series, but by the precalculated one. Therefore, the defects in the observations were not recognized.

When using heterogeneous (in terms of processing) data with the arithmetic averaging technique, it is possible to obtain a completely unreliable dependence like in [6] where erroneous values of seasonal variations in the M_2 tide amplitudes and phases are given for Dikson Island, Cape Chelyuskina, Kotelny Island and Tiksi Bay. Nevertheless, the main conclusions of this work still remain relevant.

In the work ⁴, when studying the Chukchi and the Beaufort Sea tides, the AM was used as the main method of harmonic analysis. To determine the seasonal course of the tides at such points as Cape Schmidt, Wrangel Island and Ratmanov Island, the results of analyses for several years were arithmetically averaged for individual months of the year. However, the AM accuracy is low and depends on the influence of the level non-periodic fluctuations ⁶. Therefore, the obtained results of the curves of the M_2 tide seasonal course differ significantly from modern estimates [10, 11].

In the monograph on the Arctic Ocean (AO) tides [7], the M_2 tide seasonal course was studied for the Barents, White and Arctic (Kara, Laptev, East Siberian and Chukchi) seas. In each of these seas, 1–2 points with continuous hourly annual series were considered. The results of half-monthly series processing were widely used to construct the seasonal variation of the M_2 tide amplitudes and phases. That is why, even taking into account the results of processing of three annual series (one was taken from the work ¹), the seasonal variation of the M_2 tide constants in the Ekaterininskaya Gavan remained uncertain. Questionable results were also given for Teriberka Bay.

Later, in [8], point Ekaterininskaya Gavan was also considered, but the results of monthly series processing were taken, which made it possible to obtain a reliable seasonal course in the tidal amplitude but it still remained uncertain in the phase.

In [7], an attempt to classify the seasonal course of the tide in the Arctic seas was made but non-harmonic constants were used as criteria – the applied hour and the average spring tide value. If the applied hour is associated with the phase of the M_2 tide, then the tide value is determined by the values of the amplitudes of all the main tides. That is, the use of such criteria does not make physical sense for estimating the M_2 tide seasonal course and even more so for its typification. In essence, this meant a refusal to use the results of harmonic analysis. Therefore, no progress was achieved in understanding the mechanisms of the seasonal course of tides.

Unfortunately, extensive work⁵ on tidal phenomena in the Arctic seas had the aforementioned shortcomings (see points 1–3 above). As in other works, the results of processing half-monthly series were used to estimate the seasonal variation. The arithmetic averaging method was used to estimate the average seasonal annual variation of the M_2 tide amplitudes and phases. As a result, a stable intra-annual seasonal variation of the M_2 tide amplitudes and phases was not obtained for any of eight points cited in the work. Only a trend in individual seasons of the year was essentially revealed.

A review of the works on explaining the phenomenon of the seasonal tide variation in the 20th century is contained in publications [10, 11]. Following this review, we note that in [12, 13], the analytical model of R. H. Corkan [1] was supplemented and it was established that the annual disturbances of the M_2 and S_2 tides were similar and were caused by disturbing tides that were generated by meteorological factors and formed an annual modulation in M_2 , and the secondary MSK_2 and MKS_2 tides, being a result of friction forces, cause a semi-annual modulation. For the S_2 tide, the annual course is created by non-gravitational components of the T_2 and R_2 tides associated with meteorological causes.

In theoretical terms, the question of the ice cover influence on tidal phenomena in the Arctic seas was studied in [14, 15] where analytical solutions for particular cases of the propagation of Sverdrup and Poincaré waves in an idealized channel on open water and under ice cover were obtained. In these works, the conclusion about the weak influence of drifting ice on the tide and tidal currents was made.

The ice cover influence on the M_2 tide in the Arctic basin was studied by numerical experiments in [16], concluding the weak influence of drifting ice on the tide propagation.

In [17], based on the results of tidal dynamics modeling in the Arctic Ocean covered by drifting ice, a conclusion was made about the strong influence of fast ice and the weak influence of drifting ice on the formation of tides.

At the beginning of the 21st century, works where seasonal variations of the M_2 tide were explained not by ice cover but by other factors appeared. In [18], using numerical experiments with the assimilation of both coastal observations and altimetry measurements of the Topex-Poseidon mission, the dependence of the seasonal course of the M_2 tide on meteorological forces (up to 60% of the seasonal course) was established in the North Sea.

A completely different but very indicative approach to explaining the seasonal course of the M_2 tide was presented in [19]. A 2D model showed that seasonal stratification of water masses in the Yellow and East China Seas was responsible for the seasonal course of the M_2 tide. An extensive study of the seasonal course of the M_2 tide in the World Ocean using numerical modeling with the altimetry data assimilation for 19 years and long-term level measurements at points was carried out in [20]. The Arctic region is covered partially due to limitations in the satellite trajectories. The influence of meteorological forces and river runoff on the tides was

not taken into account in recent studies. It is clear that a wide field for future research remains open.

The results of mass processing of long-term time series of sea level observations in the Arctic seas for studying the seasonal course of tides are presented in [10, 11, 21, 22].

Seasonal course features of the main tides in the White, Laptev and Chukchi seas (six points in total) are considered in [23] where significant differences in the type of seasonal variation curves are noted both between points in one sea and between regions. When predicting tides in the seas, it is recommended to take seasonal course into account.

It follows from the aforementioned works that the most significant seasonal course of tides in the annual cycle, which is not associated with astronomical reasons, is observed in the AO on the shelf of the Arctic seas.

Due to the new project for the NSR development and advancement in the 21st century, a request for detailed studies of the patterns of distribution of sea tides in the shelf zone of the Arctic seas arose.

The paper aims at studying seasonal variation features of the main semidiurnal and diurnal tides in the annual cycle in the Barents and Kara seas where long-term hourly or urgent (four times a day) sea level observations were carried out.

Data and methods

The database of hourly tide gauge observations and urgent (four times a day) tide gauge measurements of sea level from the portal of the Unified System of Information on the Situation in the World Ocean (ESIMO, available at: <https://esimo.ru>) (All-Russian Research Institute of Hydrometeorological Information – World Data Center) for the period from 1977 until the end of observations was used as a basis for processing and analysis. Observations before 1977 in the Barents and Kara seas were selected from the materials stored in the AARI funds (tables TGM-8 for hourly data and TGM-1 for urgent measurements), as well as from materials². The materials of long-term observations of the level at 17 points of the Barents Sea and 19 points of the Kara Sea for different periods, mainly from 1962 (1977) to 1993 (and later) were used to study the seasonal course of semidiurnal and diurnal tides (Fig. 1, Table).

The longest series of hourly sea level observations were over 50 years (Table). On the contrary, some points with short-term hourly data (Tikhaya Bay – four years, the mouth of the Indiga River – seven years) were also observed. In general, the length of the series exceeded the nodal cycle period (19 years).

In the late 1980s – early 1990s, personal computers replaced electronic data processing machines in the USSR, which made it possible to process long-term time series of observations and apply harmonic analysis of tides using the least squares method (LSM).

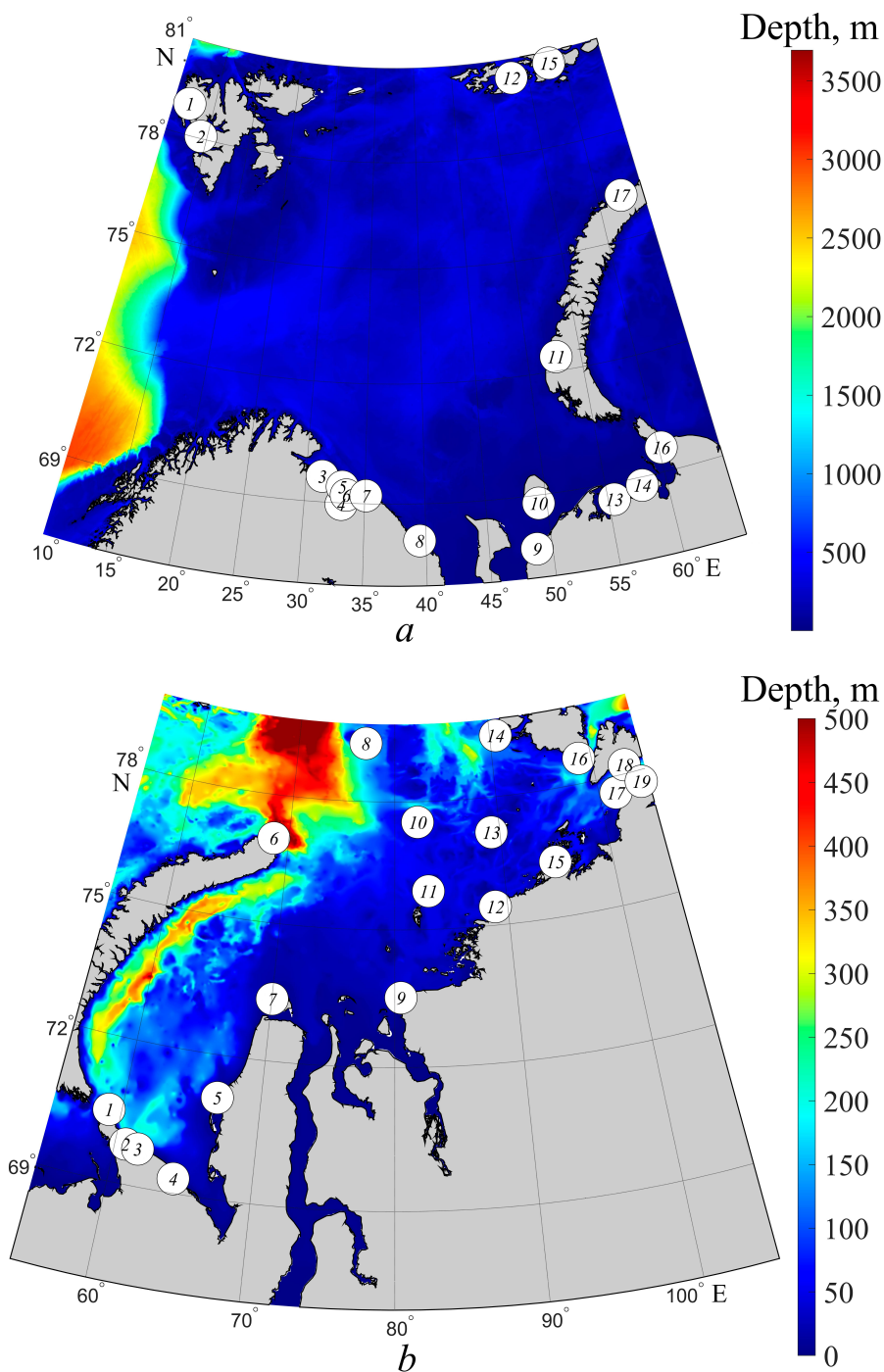


Fig. 1. Location of sea level observation points (stations) in the Barents (*a*) and Kara (*b*) seas (see Table for names of points)

Initial time series of sea level observations in the Barents and Kara seas

Point number	Point name	Latitude, ° N	Longitude, ° E	Analysis period	Number of years analyzed
1	2	3	4	5	6
<i>Barents Sea</i>					
1	New Alesund (West Svalbard)	78.93	11.95	1977–2018	42
2	Port of Barentsburg	78.07	14.25	1977–2012	36
3	Liinahamari (mouth of the Pechenga River)	69.63	31.37	1977–2004*	26
4	Port of Murmansk	68.97	33.07	1977–2012	35
5	Kislogubskaya PES Bay	69.40	33.10	1977–1992	16
6	Polyarnoe (Ekaterininskaya Gavan)	69.20	33.47	1958–2015	58
7	Teriberka Bay	69.20	35.10	1951–2015	65
8	Yokanga Bay	68.10	39.50	1977–1993	17
9	Mouth of the Indiga River	67.70	48.77	1977–1989*	7
10	Bugrino (Kolguev Island)	68.80	49.33	1977–1996**	20
11	Malye Karmakuly (polar station)	72.37	52.68	1977–2012**	36
12	Tikhaya Bay	80.35	52.80	1954–1957	4
13	Cape Konstantinovskiy	68.60	55.50	1977–1990*	11
14	Varandey Island	68.80	57.97	1978–1994*	11
15	Heiss Island (E. T. Krenkel observatory)	80.60	58.00	1972–1991	20
16	Cape Belyy Nos	69.60	60.22	1962–1992**	31
17	Russkaya Gavan Bay	76.20	62.58	1966–1991	26
<i>Kara Sea</i>					
1	(Cape Bolvanskiy Nos (named after E. K. Fedorov))	70.45	59.08	1962–1993	32
2	Yugorskiy Shar (polar station)	69.82	60.77	1962–1989	28
3	Port of Amderma	69.77	61.68	1962–1991	30
4	Mouth of Ust-Kara River	69.30	64.50	1962–1999*	38
5	Cape Kharasavey	71.10	66.75	1962–1979*	18
6	Cape Zhelaniya	76.95	68.57	1962–1983	22
7	Belyy Island (named after M. E. Popov)	73.33	70.03	1945–1982*	10
8	Wiese Island	79.48	76.98	1963–1980*	18
9	Dikson Island	73.50	80.50	1962–1992	31
10	Uyedineniya Island	77.50	82.20	1967–1990*	24
11	Izvestiya TSIK Islands	75.87	83.03	1962–2015	54
12	Cape Sterlegova	75.42	88.90	1963–1990*	28
13	Isachenko Island	77.15	89.20	1962–1990*	29
14	Golomyannyy Island	79.55	90.62	1963–2006	44
15	Pravdy Island	76.27	94.77	1962–1992	31
16	Krasnoflotskie Islands	78.63	98.73	1968–1987	20
17	Heiberg Islands	77.60	101.63	1967–1994	28
18	Solnechnaya Bay	78.22	103.07	1962–1991	30
19	Cape Chelyuskina (E. K. Fedorov observatory)	77.72	104.28	1962–1996	35

* The hourly series of observations contain some gaps.

** The 6-hourly interval series of sea level measurements are considered as well as all short-term hourly observations.

In the 1990s, a new methodological approach to the processing and analysis of sea tides was developed at AARI. Extended harmonic analysis of sea tides by the LSM is carried out according to a new technique with the inclusion of tides describing the seasonal course of the main semidiurnal, diurnal and shallow-water tides [10, 11, 21]. The method versions have been developed for the analysis of irregular observations, anomalous shallow-water tides and urgent observations [10, 11, 24–28]. The fundamental difference between the new version of extended harmonic analysis of sea tides by the LSM and other versions of this method is that it provides an adequate description of the seasonal course of tidal fluctuations in sea level for areas with a strongly expressed or anomalous course of tide constants in the annual cycle.

In [21], for the first time in the world practice of tidal analysis, seasonal course of main shallow tides was discovered. Complex combination tides responsible for the seasonal course of the M_4 , MS_4 , MN_4 , M_6 , $2MS_6$ and $2SM_6$ main shallow tides were identified and described. Taking these tides into account, the extended harmonic tidal analysis according to the AARI version makes it possible to identify 225 tides from the hourly annual series.

The classification of the types of seasonal course of tides of the main semidiurnal (M_2 , S_2 and N_2) and diurnal (K_1 and O_1) tides is given in [11] first in the world practice based on the results of the monthly series analysis over a long period at 19 points in the Arctic seas.

Here, no possibility of individual description of the features of harmonic analysis of tides at each point is given. Depending on the series length, their discreteness and quality of observations, various LSM versions were used in several approximations. All points were analysed with the LSM both for the entire observation period both for annual and monthly series but in the final form, a tidal model with tides describing the seasonal course of the tide was created for each point. An adequate tidal model was also created in parallel in the form of 12 files with harmonic constants of tides extracted from monthly series (32 tides in each month). In this case, for monthly series, the results for the K_1 , S_2 and N_2 tides in the second approximation were corrected to avoid the influence of the secondary π_1 , ψ_1 , φ_1 , P_1 , K_2 , T_2 , R_2 , ν_2 tides according to theoretical relationships. When studying the intra-annual course of the tide for the M_2 , S_2 , N_2 , K_1 and O_1 , M_4 , MS_4 , M_6 tides, the average vector values of the amplitudes and angles of the positions (phases) of the harmonics were calculated for each month of the year.

The seasonal variation of the amplitude is presented as relative change (dH) in its average value (H) as $dH = (H_m - H_g)/H_g$ (in percent), where H_m is average vector value of all series for a given month; H_g is average vector value for the entire period. Seasonal variation of the phase (dg) is given as a deviation of the average value of all series for a given month from the average for the entire period: $dg = (g_m - g_g)$. The standard deviation (SD, or σ) for the amplitude and phase was calculated using formulas for the vector average errors. For this purpose, the average and individual monthly values of the amplitude and phase were transformed into the $H\cos g$ and $H\sin g$ components. Based on them, the standard error was calculated for the σ_H amplitude and then for the σ_g phase [9].

To accomplish the task, long-term homogeneous hourly series reduced to one time zone and a single zero post are needed.

As a rule, scientific publications almost never disclose the reasons for gaps in observations of the level in the Arctic seas and poor data quality. This is considered a topic beyond the scope of a scientific paper. We will cover this issue in more detail here.

As is known, sea level observations in the Far North are carried out in very severe climatic conditions with risk to life. Of 19 points in the Kara Sea, only five had permanent tide gauge installations: the port of Amderma, Dikson Island, Cape Zhelaniya, Heiss Island and the Izvestiy TSIK Islands. At the remaining points, observations were carried out in the summer using temporary installations, and in the winter – in gullies on coastal fast ice, which is sometimes subject to destruction. Therefore, gaps in observations were caused by the impossibility of creating temporary installations during periods of fast ice destruction in spring or their destruction in summer under the influence of storms and drifting ice and in the transitional winter period before stable fast ice formation.

Gaps create inconveniences in calculations due to breaks in time series but they are not an obstacle to conducting harmonic analysis of tides by the LSM [24]. In fact, the quality of level observations depends not so much on gaps as on situations related to violations of the requirements of the Manual for Meteorological Stations and Posts, poor performance of instruments and dishonesty of observers [25–28].

According to [25–28], high-quality observations were carried out in the late 1950s – early 1980s. As the instrument base aged and the working conditions of observers worsened as well as due to a decrease in their qualifications and lack of regular inspection control, the quality of sea level observations also decreased.

In the 1990s, due to the Soviet Union collapse and the closure of a number of stations on the NSR due to lack of funding, a sharp deterioration in the quality of observations took place as an objective reason for the poor quality of observations. A subjective one was represented by the formation of the database that we received at ESIMO. It consisted of incorrect processing of mareograms untied by urgent sea level measurements. According to the rules of the instructions and requirements of the methodological departments of the research institutes, these urgent level measurements should be made strictly at whole hours. In practice, due to an insufficient number of observers, this rule cannot be observed, since the same observer is not able to be at the meteorological site and at the level post at the same time. Therefore, observers recorded not the true time of measurements but the required one (i.e. equal to a whole hour). Accordingly, mareograms were not processed according to the true time, errors were introduced into them (within ± 30 minutes or more). As a result, the time series lost their homogeneity [25–28].

To bring the sea level time series to a homogeneous state, a new methodology presented in general terms as a tide calibration method was developed [28]. It allows identifying questionable observations and defects of various origins in the level time series and, therefore, obtaining an objective estimate of the observation data quality.

In general, the state of the polar station network and, in particular, production of sea level observations has remained virtually unchanged compared to the level of the early 1990s described in detail in [29].

The best quality of sea level observations was achieved in the middle of the 20th century and steadily declined at the end of it. However, it was in the very middle of this period that sea level measurements were carried out in different time systems and with different altitude references. Until April 1961, local solar time was used, then – time alternately according to the second or third time zone until 1969, then – mainly according to the third time zone (Moscow decree) until 1990 and the time of the zero zone (Greenwich Universal Time) since 1991. The Baltic altitude system was introduced in 1991.

We converted measurement data into whole hours during observations in local time with direct and inverse Fourier transform [25].

Results and their analysis

It is known that the seasonal course of main tides has a stable quasi-periodic form at each point in the Arctic seas and in the seas of the World Ocean and the form of amplitude and phase curves of the main tides (conditionally the genotype) does not practically change over time [1, 10, 11]. The results of seasonal course study obtained at points with the longest time series confirm this conclusion. Therefore, this work presents estimates of the average monthly values of amplitudes and phases of the M_2 and K_1 tides in the Barents and Kara seas for a period of 19–38 years from the beginning of observations at each point.

For a compact presentation, the estimate results of the seasonal course of tides were grouped by several geographical areas in each sea. Fig. 2 shows seasonal course of the M_2 tide amplitude and phase in three areas of the Barents Sea. It is evident that in all six points of the Murmansk Coastal Region (from Liinahamari to Yokanga) (Fig. 2, *a*), the amplitude seasonal course has an identical shape of curves. An annual periodicity with a maximum amplitude in August (with an increase in the average annual norm by 3–4%) and a minimum phase in March (with a decrease of only 1–2° from the specified norm) is observed. According to the classification from [11], anomalous type 3 seasonal course is observed in this region.

The range of the seasonal variation is weakly expressed in the north of the Barents Sea (Fig. 2, *b*) on Spitsbergen Island (New Alesund and Barentsburg points). In the annual cycle, the amplitude increase in June is only 0.8–0.9% of the norm and phase decrease in September is about 1°. Seasonal variation proceeds here according to anomalous type 2. An anomalous seasonal tide variation of type 2 is distinguished at the Russkaya Gavan point (north of Novaya Zemlya) where the maximum amplitude is observed in April and reaches 3% and the minimum phase is observed in September and is about 7° below the norm. In Tikhaya Bay and on Heiss Island (Fig. 2, *b*), the seasonal variation is close to classical type 1, i.e. the amplitude increases in August–September and the phase also reaches its minimum in the summer.

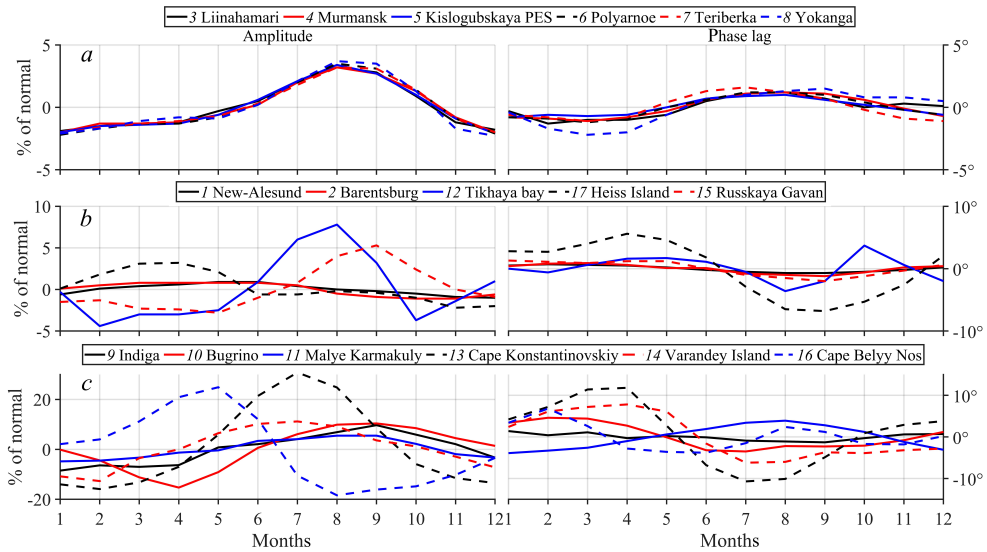


Fig. 2. Seasonal variation of the M_2 tide in the Barents Sea

The greatest differences in the type of seasonal variation curves and the most extreme values of amplitudes and phases are observed in the southeastern Barents Sea (Fig. 2, c). Indiga, Konstantinovskiy and Varandey points are located in the Kanino-Pechora Region (Fig. 1). The most pronounced seasonal variation of the M_2 tide is noted at Konstantinovskiy point (Pechora Bay) where the maximum amplitude of up to 31% of the norm and the minimum phase of up to 11° below the norm are observed in July.

In Pechora Bay, at Varandey and Konstantinovskiy points, the type of seasonal variation curves of amplitudes and phases is identical but the range of oscillations is smaller in the former. Classical type 1 of the seasonal variation is observed at both points which is also noted at Bugrino (Kolguev Island) where the increase in the M_2 tide amplitude in September reaches 10% of the norm and the decrease in the phase in the summer period is no more than 4° .

On Novaya Zemlya, at Malye Karmakuly, the seasonal course of the M_2 tide amplitude in the annual cycle reaches its maximum in August and is almost 6% of the norm. The phase course curve has an anomalous shape and a maximum in July which is about 5° from the norm. As a result, this seasonal variation can be attributed to anomalous type 3.

Finally, at Belyy Nos (south of the Yugorskiy Shar Strait), the maximum amplitude in the seasonal course occurs in May (about 25% above the norm) and in the phase seasonal course, a semi-annual periodicity with a minimum in June at 4° below the norm takes place. Therefore, type 4 of seasonal course is manifested here.

In general, the range of seasonal tide course in the Barents Sea increases from north to south and is most pronounced in the southeast of the sea.

Note that the average seasonal course of the semidiurnal M_2 , S_2 and N_2 tides has similar features but we can trace differences in the type of curves which are associated with differences in the spatial distribution of these tides. As a rule, annual periodicity prevails in the course of amplitudes and phases.

Classical type 1 of the seasonal M_2 tide course is not predominant and makes up 35% and anomalous type 3 is the most observed one, reaching 41% of 17 points. This fact can serve as indirect evidence that the impact of drifting ice cover is not the main factor in the formation of tide seasonal course in the Barents Sea. The points located in Pechora Bay where fast ice is formed in winter can be considered an exception.

Fig. 3 demonstrates the seasonal course curves of the M_2 tide amplitudes and phases in the Kara Sea grouped into four regions. We had the results of tide seasonal course in the Gulf of Ob and the Yenisei Gulf at our disposal but did not use them in this work since they are of independent interest. We will consider one more cause below.

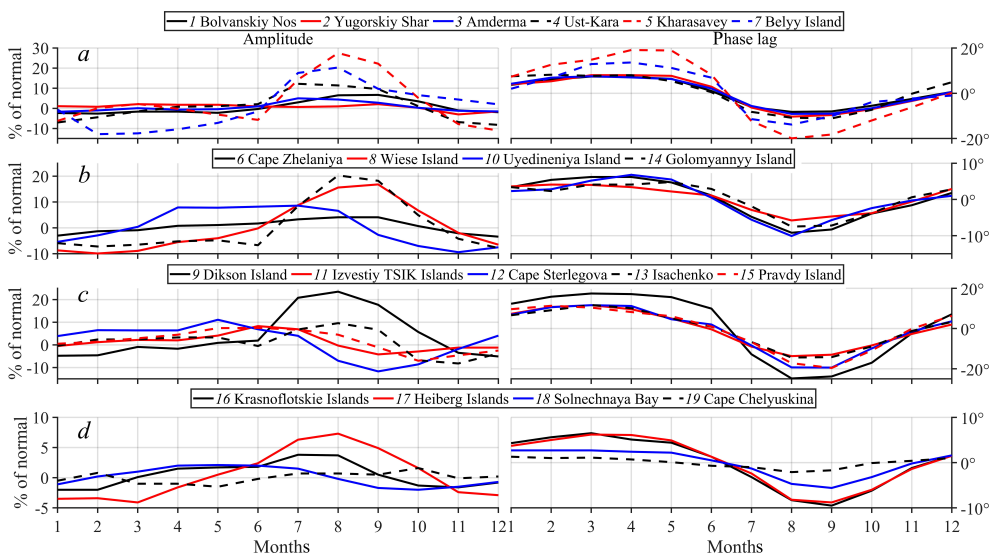


Fig. 3. Seasonal variation of the M_2 tide in the Kara Sea

A priori, one should expect similar changes in the seasonal course curves of the M_2 tide at points in the southwestern Kara Sea located in the same region homogeneous in hydrometeorological conditions. Indeed, the phase seasonal course at all points shows good agreement in the annual cycle (Fig. 3, *a*). However, significant differences are observed in the seasonal course of the M_2 tide amplitudes between points. In the variation of the M_2 tide curves, the annual course is expressed very weakly at Yugorskiy Shar and most clearly at Kharasavey with a maximum in August exceeding the norm by 28%.

In the northern part of the sea (Cape Zhelaniya, Wiese, Uyedineniya and Golomyanny islands), seasonal course of amplitude and phase curves has classical type 1 (Fig. 3, *b*). The variation is most pronounced at Golomyanny with a maximum amplitude of up to 17% in September and a minimum phase of 10° below the norm in August.

In the central part of the sea (Dikson, Izvestiy TSIK, Isachenko, Pravdy islands, Cape Sterlegova), an increase in the annual range of the M_2 tide seasonal course both in amplitude and in phase is observed. The most pronounced seasonal course occurs at Dikson where the tide amplitude increases by 24% and the phase decreases by 25° from the norm in August (Fig. 3, *c*). We note the anomalous annual course of the amplitude at Sterlegova point where it reaches a maximum in May with a deviation from the norm of 11%. However, at the same time the phase seasonal course has a classical form and its decrease (by 19° below the norm) occurs in September. At the Izvestiy TSIK and Pravdy points the amplitude seasonal course also follows anomalous type 2.

Finally, a decrease in the range of seasonal fluctuations in the M_2 tide amplitudes and phases is mainly observed in the southeastern part of the sea and in the Vilkitsky Strait (Fig. 3, *d*). The amplitude increase at Heiberg point does not exceed 7% of the average annual norm and in the Vilkitsky Strait at Chelyuskin, the seasonal course is generally of an uncertain nature (the values are not higher than the SD limits). However, the course of the M_2 tide phase curves demonstrates a classical form in all points: a decrease in the phase values is generally observed in September, it is weakly noticeable in summer at Solnechnaya point and is practically absent at Chelyuskina (the value does not exceed SD).

In general, an increase in the amplitudes of the M_2 semidiurnal tide in the Kara Sea in summer period (July–September) is mainly 7–12% of the norm and their decrease in winter period (March–April) reaches 8–11% relative to the norm.

In the seasonal variation of phases of the semidiurnal M_2 , S_2 , N_2 tides, common features are observed: annual periodicity exists everywhere while in the variation of phase curves, the maxima (March–April) and minima (August–September) practically coincide.

In general, according to the classification proposed in [11], classical type 1 of the M_2 tide seasonal course with the maximum amplitude and minimum phase in July–September is mainly observed in the Kara Sea area (74% of all cases). Anomalous type 2 accounts for 21% of cases, in one of which (Cape Chelyuskina) no statistically significant seasonal variation of the M_2 tide is found.

Does this result indicate confirmation of the widespread hypothesis about the predominant effect of ice cover on the phenomenon of tide seasonal course in the Arctic seas? Not quite so. Drifting and fast ice affects the tide propagation in different ways [10, 30, 31]. Especially strong fast ice effect on the tide occurs in shallow water while at critical depths of 12–15 m and less, the damping and delay are dramatically increased in the winter period [30]. This factor is associated with an increase in the seasonal cycle range at Cape Kharasavey and in the central part of the sea.

Semi-annual periodicity prevails in the seasonal course of the diurnal K_1 tide (Fig. 4), however, a combination of annual course in amplitude and semi-annual or annual course in phase can be observed. A period of 3–4 months is observed in a number of points. The moments of occurrence of extreme values of amplitudes and phases do not coincide in time in all cases.

The most consistent type of course between the points is observed at those of the Murmansk Coastal Region (Fig. 4, *a*). A half-year period in the course of amplitudes and phases exists there; however, a time shift between their maxima is observed. The K_1 tide amplitude reaches 13–19 cm, its seasonal course is clearly expressed with the first maximum in March and the second, main maximum up to 12–16% of the norm, in September. The minimum values during the phase are observed in February and a sharply expressed second minimum ($6\text{--}7^\circ$ from the norm) – in August.

Different types of the K_1 tide amplitude and phase curves are observed in other areas of the Barents Sea. Maximum amplitude deviations from the norm are mainly 10–20%, with phase deviations of $6\text{--}16^\circ$.

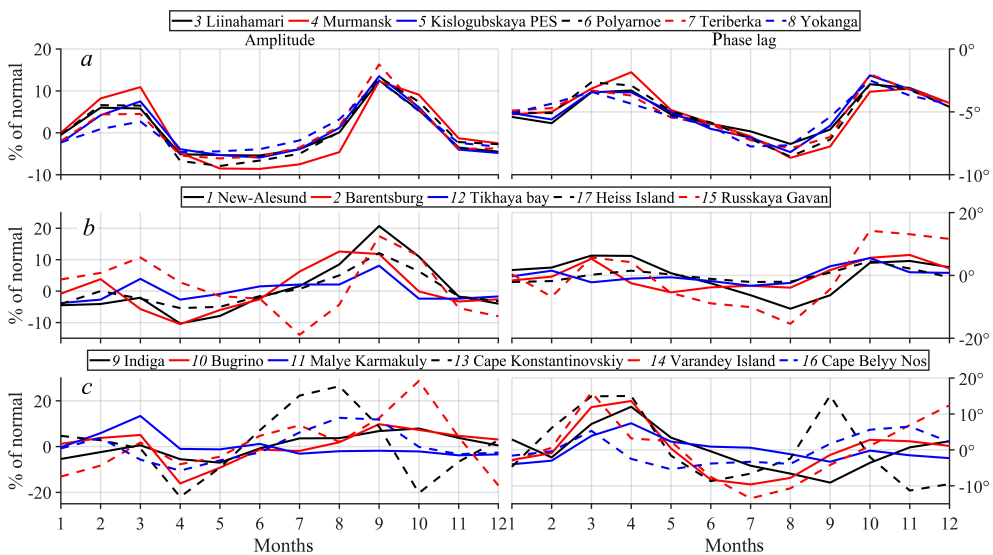


Fig. 4. Seasonal variation of the K_1 tide in the Barents Sea

In general, the annual course is poorly expressed in the curves of the seasonal variation of amplitudes and phases of the diurnal K_1 tide or the shape of the curves becomes uncertain due to the presence of shorter periods. According to the classification from [11], type 1 of the seasonal variation of the K_1 tide dominates in the Barents Sea and accounts for 76%. It should also be noted that the same seasonal course type of the constants of the K_1 and O_1 tides is observed only at three points.

As follows from the assessment of the M_2 tide seasonal course in the Barents Sea, no correspondence between type and nature of the curves course of the diurnal K_1 tide and the semidiurnal tide takes place. Preliminary analysis of the data does not reveal any dependence of the seasonal course of diurnal tides on the ice cover impact [10].

The appearance of curves in Fig. 5 indicates the seasonal course of the amplitudes and phases of the K_1 tide in the annual cycle in the Kara Sea, demonstrating a large variety. It is appropriate to recall here that not all extremes have significant estimates (above the confidence intervals based on SD). In general, the semi-annual periodicity in the course of the amplitude and phase curves, which is 68%, predominates. At the same time, the time of the onset of extremes in the amplitude and phase at individual points does not coincide.

The K_1 tide seasonal variation in amplitude and phase is most pronounced in the southwestern part of the sea and its southern central part. Moreover, the first amplitude maximum in the southwestern part is somewhat blurred in time, it is observed in January – March and accounts for 7–10% of the norm; the second one, main maximum, is traced in September and reaches 30–33% of the norm. However, the minima are not manifested in the phase so clearly and sometimes a period of 3–4 months occurs. In the southern central part, the first amplitude maximum is observed in February – March with 10–13% of the norm, and the second one, main maximum, is unstable in time, occurs in June–October and reaches 15–20% of the norm.

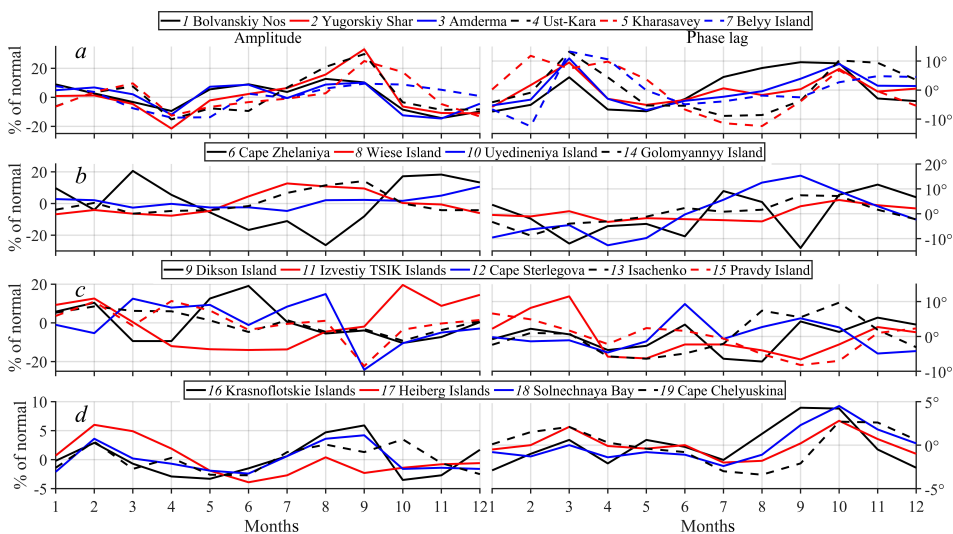


Fig. 5. Seasonal variation of the K_1 tide in the Kara Sea

Large amplitudes, on average up to 10–15% of the norm, are observed in the southwestern and northern Kara Sea as well as the phases of up to 5–10°.

In the southeastern part of the sea, extrema in the amplitude seasonal course do not exceed, on average, 5–10% of the norm and the phases are about 3–6°. Minimum values are noted in the Vilkitsky Strait.

The main conclusion from the assessment of the results of the K_1 diurnal tide seasonal course coincides with that concerning the Barents Sea made above. Seasonal variations of the semidiurnal M_2 tide and the diurnal K_1 tide are different. The obtained results make it possible to speak confidently about different physical nature of seasonal course formation of semidiurnal and diurnal tides [10].

No correspondence between the seasonal course curves of the amplitudes and phases of the diurnal K_1 and O_1 tides as well as between the curves of the semidiurnal tides was observed.

In [10], a simple analytical model explaining the seasonal course causes of the diurnal K_1 and O_1 tides was considered. As demonstrated in this work, in the harmonic analysis of monthly series, when isolating the K_1 tide in the second approximation, a standard separation by theoretical relations is used. In this case, the influence of the S_1 tide, which is close in angular velocity to the P_1 tide, is not taken into account. The contribution of the secondary S_1 tide can reach 6–8% of the main K_1 tide amplitude. If we separate the K_1 and P_1 tides from the annual series by real relations, i.e. if we perform demodulation, then the seasonal course may acquire an implicit form. Here, it should be borne in mind that a similar technique was applied in [10] to reduce the harmonic constants of the K_1 tide, obtained from the monthly series, to the average annual values.

A natural question about the difference degree between the “true” data and the data presented in our work on the K_1 tide seasonal course may arise. We have performed the following assessment. The K_1 tide amplitude in the Barents Sea is significantly greater than in the Kara Sea. Based on the results of our analyses of long-term observation series in the Barents and Kara seas, we can say the following: the average amplitude of the K_1 tide for 17 points in the Barents Sea is about 12 cm, for 19 points in the Kara Sea – about 3.5 cm; the average ratio of the amplitudes of the P_1 and K_1 tides in the Barents and Kara seas is 0.296 and 0.334, respectively (the theoretical ratio is 0.331); the phase difference of these tides from observations is on average –4.2 and –5.1°, respectively (it is zero in theory).

On the impact of the S_1 radiation tide. Its average amplitude for 17 points in the Barents Sea and 19 points in the Kara Sea according to observations is 0.66 and 0.16 cm, respectively. This tide is not involved in the standard division. Its impact on the seasonal course does not affect its structure (the tide can only affect the annual periodicity) but it can slightly weaken or increase the annual period amplitude [10].

It is clear that the standard division results in most points will differ insignificantly from the special division according to the ratios from observations. Therefore, a non-standard division has no practical sense. In general, the results of

the K_1 tide seasonal course presented in our work satisfactorily describe its structure and type of curves.

Seasonal variation of the O_1 tide in the Barents and Kara Seas has mainly a semi-annual periodicity in amplitude and phase, which is 58% of the norm for points in both seas. The difference in the form of the seasonal course curves of the diurnal K_1 and O_1 tides can be explained by the effect of some minor tides on the results of the O_1 tide monthly analyses. The O_1 tide group also contains such minor complex tides with significant amplitude as MP_1 and MS_1 , which are not separated in standard analyses of monthly series but can cause semi-annual periodicities in the usual analysis results. In the Barents and Kara seas, according to our results, the average amplitude of the O_1 tide is 2.4 and 2.9 cm, respectively. Therefore, consideration of the O_1 tide seasonal course is inappropriate for practical purposes.

However, everything is not so clear. In areas where fast ice is formed under shallow water conditions in winter, such as Pechora Bay, the Gulf of Ob and the Yenisei Gulf [10], the seasonal course of diurnal tides manifests itself as an anomalous natural phenomenon.

Despite the fact that the phenomenon of tide seasonal course in the World Ocean was revealed in 1934 [1] and has been known in the Arctic seas since 1936 [2], the tide in domestic and foreign tide tables is precalculated using the old classical method without taking into account the seasonal variation of semidiurnal and diurnal tides in the annual cycle. A qualitative turn in numerical modeling has occurred in the past decade and some tide models in the 21st century take into account the seasonal course of semidiurnal tides in the Arctic Ocean [32].

Conclusion

Based on the analysis results at 36 points in the Barents and Kara seas, in this work we have considered the seasonal course features of semidiurnal tides using the example of the M_2 tide and diurnal tides using the example of the K_1 tide. In general, the seasonal course range of tides in the Barents Sea increases from north to south and it is most significant in the southeast of the sea.

In all six points of the Murmansk Coastal Region (from Liinahamari to Yokanga), the seasonal variation of the M_2 tide amplitude has an identical shape of curves. An annual periodicity with a maximum amplitude in August with an increase of 3–4% from the average annual norm and a minimum phase in March with a decrease of only 1–2° from the norm is observed. According to the new classification of the seasonal variation of semidiurnal and diurnal tides, anomalous type 3 seasonal variation is observed in this region.

Seasonal variation range is weakly expressed in the northern Barents Sea on Spitsbergen Island (New Alesund and Barentsburg points). In the annual cycle, the amplitude increase in June is only 0.8–0.9% of the norm and the decrease in

phase in September is about 1° . The seasonal variation proceeds here according to anomalous type 2.

The greatest differences in the type of curves of the M_2 tide seasonal course and the most extreme values of amplitudes and phases are observed in the southeastern part of the Barents Sea in the Kanino-Pechora Region. The most pronounced anomalous seasonal course of the M_2 tide is noted in Pechora Bay. The maximum amplitude of up to 31% of the norm and the minimum phase of up to 11° below the norm are recorded at point Konstantinovskiy in July.

Classical type 1 of the M_2 tide seasonal course is not predominant and is 35% of the norm; anomalous type 3, reaching 41% of the norm at 17 points, is observed most frequently. This fact can serve as indirect evidence that the ice cover impact is not the predominant factor in the formation of seasonal tide course in the Barents Sea. The exceptions are points located in Pechora Bay where fast ice is formed in winter.

In the Kara Sea, the increase in the amplitudes of the semidiurnal M_2 tide in summer (July – September) is mainly 7–12% of the norm and their decrease in winter (March – April) reaches 8–11%.

In the central part of the sea, from Dikson to Pravdy islands where fast ice is formed in winter, an increase in the annual range of the M_2 tide seasonal course occurs both in amplitude and phase. The most pronounced seasonal course is observed on Dikson island in August where its amplitude increases by 24% of the norm and the phase decreases by 25° . However, at the points of Izvestiy TSIK, Sterlegova and Pravdy, the seasonal course of the tide amplitude follows anomalous type 2.

According to the proposed classification, classical type 1 of the M_2 tide seasonal course is mainly observed in the Kara Sea area with the maximum amplitude and minimum phase in July – September, which is 74% of the norm in 19 points. Anomalous type 2 accounts for 21% of cases, in one of which, at point Chelyuskina, no statistically reliable seasonal course of the M_2 tide is recorded.

Common features are observed in the seasonal variation of phases of the semidiurnal M_2 , S_2 , N_2 tides: annual periodicity is present everywhere while the maxima (March – April) and minima (August–September) coincide practically in the course of the phase curves.

The previously proposed hypothesis about different behavior of semidiurnal and diurnal tides in the annual cycle was confirmed. The exceptions are water areas (the Gulf of Ob, the Yenisei Gulf, etc.) where fast ice is formed under shallow water conditions in winter.

In general, the seasonal course of the K_1 tide in the Barents and Kara seas is dominated by the semiannual period which is observed in 76% of cases at points in the Barents Sea and in 68% of cases in the Kara Sea. At the Murmansk coast, where the K_1 tide amplitude reaches 13–19 cm, its seasonal course has a clearly defined form with the first maximum in March and the second, main maximum (up to 12–16% of the norm), in September. The minimum values during the phase are observed in

February and the ones with a sharply defined second minimum – in August (6–7° of the norm).

Seasonal variation of the K_1 tide in amplitude and phase is most pronounced in the Kara Sea in its southwestern and southern central parts. Moreover, the first amplitude maximum in the southwestern part, somewhat blurred in time, is observed in January – March and is 7–10% of the norm, and the second, main maximum, is traced in September and reaches 30–33% of the norm. However, the phase minima are not manifested so clearly, sometimes with a period of 3–4 months. In the southern central part, the first amplitude maximum is observed in February – March (10–13% of the norm) and the second, main maximum unstable in time, appears in June – October (15–20% of the norm).

In general, the phenomenon of semi-annual periodicity in the seasonal variation of the K_1 tide does not confirm its correlation with the effect of both drifting ice and water stratification. It is possible that the main factor here is stipulated by the peculiarities of the wind (breeze winds) and radiation regimes in the annual cycle.

It was determined in the works of domestic and foreign researchers that drifting ice cover had no significant effect on the propagation of tides. This conclusion was based on all available observational materials of currents from oceanographic moorings in the Arctic seas up to 1979 and on materials of century-long observations of tides at polar stations in the Barents and Kara seas up to the 1990s.

Based on numerical modeling results, the authors believe that the main cause for the seasonal course of semidiurnal tides is the effect of seasonal variation in stratification at the continental shelf and the next cause is the seasonal variation in the drifting ice cover in the Arctic Ocean.

The new results of seasonal course of semidiurnal and diurnal tides in the Barents and Kara Seas presented in this study, which were obtained by a new methodology in the processing and harmonic analysis of long-term series of sea level observations, make it possible to increase significantly the level of navigation safety and solve a number of economic problems on the Northern Sea Route.

REFERENCES

1. Corkan, R.H., 1934. An Annual Perturbation in the Range of Tide. *Proceedings of the Royal Society of London. Series A, Containing Papers of a Mathematical and Physical Character*, 144(853), pp. 537-559. <https://doi.org/10.1098/rspa.1934.0067>
2. Wiese, W.J., 1936. Preface. In: I.V. Maximov, 1936. *Hydrology. Materials for the Study of the Tides of the Arctic Seas of the USSR*. Transactions of the Arctic Institute, vol. 52(2). Leningrad: Glavsevmorput, pp. 5-7 (in Russian).
3. Wiese, W.J., 1939. [Arctic Warming and Tidal Surges]. *Arctic and Antarctic Research*, (5), pp. 37-42 (in Russian).
4. Maximov, I.V., 1953. [On the Dependence of Tidal Elements on the Sea Ice Cover]. *Scientific Notes of the Admiral Makarov Higher Arctic Maritime School*, (4), pp. 115-129 (in Russian).

5. Dvorkin, E.N. and Mandel, S.Z., 1989. [On the Influence of Ice Cover on the Variability of Tidal Constants]. *Proceedings of the AARI*, 414, pp. 76-85 (in Russian).
6. Maximov, I.V., 1949. [Seasonal Fluctuations of the Main Tidal Elements in the Seas of the Soviet Arctic]. *Transactions of the Arctic Institute*, 13, pp. 5-19 (in Russian).
7. Diesperova, R.A., 1954. [Tides of the Arctic Ocean]. In: SOI, 1954. *Proceedings of SOI*. Moscow: Gidrometeoizdat, 19, pp. 3-75 (in Russian).
8. Kagansky, A.S., 1965. [Some Features of Variability of Harmonic Constants of Tidal Level Fluctuations]. *Proceedings of SOI*. Moscow: Gidrometeoizdat, 85, pp. 84-90 (in Russian).
9. Maximov, I.V., 1941. *Principal Methods of Working up Observations of Sea-Currents*. Moscow; Leningrad: Glavsevmorput, 332 c. Transactions of the Arctic Institute. Vol. 155, 332 p. (in Russian).
10. Voinov, G.N., 1999. *The Tidal Phenomena in the Kara Sea*. Saint Petersburg: RGS, 117 p. (in Russian).
11. Voinov, G.N., 2003. New Interpretation of Seasonal Variability of Tides of the Russian Arctic Seas. *Russian Meteorology and Hydrology*, (9), pp. 59-70.
12. Amin, M., 1983. On Perturbations of Harmonic Constants in the Thames Estuary. *Geophysical Journal of the Royal Astronomical Society*, 73(3), pp. 587-603. <https://doi.org/10.1111/j.1365-246x.1983.tb03334.x>
13. Amin, M., 1985. Temporal Variations of Tides on the West Coast of Great Britain. *Geophysical Journal of the Royal Astronomical Society*, 82(2), pp. 279-299. <https://doi.org/10.1111/j.1365-246x.1985.tb05138.x>
14. Kulakov, M.Yu. and Legenkov, A.P., 1985. [Poincare Waves under the Ice Cover and on Clear Water]. *Proceedings of the AARI*, 389, pp. 59-70 (in Russian).
15. Legenkov, A.P., 1965. Reflection of Sverdrup Waves from the Ice Edge. *Izvestia Akademii Nauk SSSR. Fizika Atmosfery i Okeana*, 1(3), pp. 327-334 (in Russian).
16. Kowalik, Z., 1981. A Study of the M₂ Tide in the Ice-Covered Arctic Ocean. *Modeling, Identification and Control*, 2(4), pp. 201-223.
17. Kagan, B.A. and Sofina, E.V., 2009. Seasonal Variability of the M₂ Tide in the Arctic Ocean. *Fundamental and Applied Hydrophysics*, 2(4), pp. 31-37 (in Russian).
18. Huess, V. and Andersen, O.B., 2001. Seasonal Variation in the Main Tidal Constituent from Altimetry. *Geophysical Research Letters*, 28(4), pp. 567-570. <https://doi.org/10.1029/2000gl011921>
19. Kang, S.K., Foreman, M.G.G., Lie, H.-J., Lee, J.-H., Cherniawsky, J. and Yum, K.-D., 2002. Two-Layer Tidal Modelling of the Yellow and East China Seas with Application to Seasonal Variability of the M₂ Tide. *Journal of Geophysical Research: Oceans*, 107(C3), pp. 6-1-6-18. <https://doi.org/10.1029/2001JC000838>
20. Müller, M., Cherniawsky, J.Y., Foreman, M.G.G. and von Storch, J.-S., 2014. Seasonal Variation of the M₂ Tide. *Ocean Dynamics*, 64, pp. 159-177. <https://doi.org/10.1007/s10236-013-0679-0>

21. Voinov, G.N., 2007. Seasonal Variability of the Harmonic Constants of the Quarter-Diurnal and Sixth-Diurnal Constituents in the Barents Sea and White Sea. *Russian Meteorology and Hydrology*, 32(4), pp. 252-261. <https://doi.org/10.3103/S106837390704005X>
22. May, R.I., 2008. Linear and Nonlinear Tidal Phenomena in the Euro-Arctic Seas. *Arctic and Antarctic Research*, 3(80), pp. 115-125 (in Russian).
23. Kulikov, M.E., Medvedev, I.P. and Kondrin, A.T., 2020. Features of Seasonal Variability of Tidal Sea-Level Oscillations in the Russian Arctic Seas. *Russian Meteorology and Hydrology*, 45(6), pp. 411-421. <https://doi.org/10.3103/S1068373920060047>
24. Voinov, G.N., 2004. Harmonic Analysis of Tides from Irregular Multilayer Sea Level and Current Observations. *Oceanology*, 44(2), pp. 156-162.
25. Voinov, G.N., 2009. Harmonic Analysis of Tides from Standard Observations of the Sea Level. *Russian Meteorology and Hydrology*, 34(7), pp. 464-472. <https://doi.org/10.3103/S1068373909070061>
26. Voinov, G.N., 2011. Methods for Quality Control and Revision the Multiyear Time Series of Sea Level Observations. *Arctic and Antarctic Research*, (4), pp. 51-61 (in Russian).
27. Voinov, G.N., 2013. The Quality of the Multiyear Sea Level Data on the Stations System in the Coastal Zone in North-West Seas and in Arctic Seas. *Proceedings of the State Oceanographic Institute*, 214, pp. 223-236 (in Russian).
28. Voinov, G.N., 2015. A Method for Transforming Hourly Observations of Sea Water Level to Homogeneous Series by Tide Calibration. *Arctic and Antarctic Research*, (2), pp. 68-80 (in Russian).
29. Komchatov, V.F. and Luchkov, V.P., 2011. Main Coastal Marine Hydrometeorological Stations System as a Basis for Investigations of Russian Federation Shelf Seas Regime and for Securing of Marine Activities Safety. *Proceedings of the State Oceanographic Institute*, 213, pp. 5-14 (in Russian).
30. Voinov, G.N., 1988. [Tidal Currents of the Arctic Seas]. *Proceedings of the Arctic and Antarctic Research Institute*, 128, 238 p.
31. Voinov, G.N. and Naumov, A.K., 2017. The Tides in the South-Western Kara Sea. Tides Calibration Method Effects. *Arctic and Antarctic Research*, (4), pp. 98-115 (in Russian).
32. Lyard, F.H., Allain, D.J., Cancet, M., Carrère, L. and Picot, N., 2021. FES2014 Global Ocean Tides Atlas: Design and Performance. *Ocean Science*, 17(3), pp. 615-649. <https://doi.org/10.5194/os-17-615-2021>

Submitted 26.03.2024; approved after review 25.06.2024;
accepted for publication 29.01.2025.

About the authors:

Gennady N. Voinov, Head of Laboratory, Saint Petersburg Branch of N. N. Zubov State Oceanographic Institute (38 Beringa Str., Saint Petersburg, 199397, Russian Federation); Chief Research Associate, Arctic and Antarctic Research Institute (38 Beringa Str., Saint Petersburg, 199397, Russian Federation), DSc. (Geogr.), **ORCID ID: 0000-0003-1657-049x**, **Scopus Author ID: 6602249564**, **ResearcherID: E-6141-2016**, voinovgn@mail.ru

Vladimir N. Sukhachev, Research Associate, Saint Petersburg Branch of N. N. Zubov State Oceanographic Institute (38 Beringa Str., Saint Petersburg, 199397, Russian Federation); Research Associate, Institute of Earth Sciences, Saint Petersburg State University (33-35, 10th Line of Vasilyevsky Island, Saint Petersburg, 199178, Russian Federation), CSc. (Geogr.), **ORCID ID: 0000-0003-4821-4342**, **Scopus Author ID: 55969236600**, **ResearcherID: N-7470-2015**, **SPIN-code: 4963-7802**, syhachev@mail.ru

Contribution of the co-authors:

Gennady N. Voinov – methodology, concept, data analyses and article text writing

Vladimir N. Sukhachev – provision of data on sea level, data analyses and editing

The authors have read and approved the final manuscript.

The authors declare that they have no conflict of interest.

Variability of Water Characteristics in the Northeastern Part of the Greenland Sea during the Winter Periods in 2019–2023

T. M. Maksimovskaya^{1, 2, ✉}, A. V. Zimin¹, O. A. Atadzhanova¹,
A. A. Konik¹, D. V. Moiseev²

¹ Shirshov Institute of Oceanology of RAS, Moscow, Russian Federation

² Murmansk Marine Biological Institute of RAS, Murmansk, Russian Federation

✉ maximovskaja.t@yandex.ru

Abstract

Purpose. The paper aims to present the results of *in situ* measurements, analyze the features of variability of water characteristics in the northeastern part of the Greenland Sea with an emphasis on the Marginal Frontal Zone in winter based on the onboard measurement results, as well as to assess the agreement between the reanalysis data and the *in situ* observations.

Methods and Results. The results of temperature and salinity measurements performed during the expeditionary research in the northeastern part of the Greenland Sea in winter periods of 2019–2023 are used in the paper. The temperature and salinity anomalies of the Atlantic waters are assessed by comparing the *in situ* data with the WOA-2023 climatic data. To evaluate the reanalysis quality, the data from the MERCATOR PSY4QV3R1, CMEMS GLORYS12v1 and TOPAZ5 products for the 0–40 m depths are involved. The comparison is carried out using the standard statistical methods: descriptive statistics, spatial correlation analysis and discrepancy function method. It is found that the studied frontal section between the Arctic and Atlantic waters could be traced up to 80 km from the ice edge. The maximum gradients of thermohaline characteristics in the Marginal Frontal Zone were recorded in 2023 under conditions of the significant positive temperature anomalies of surface waters of the Atlantic origin. It is shown that the reanalysis data describe accurately temperature and salinity only within the Atlantic water region.

Conclusions. The results of *in situ* measurements confirm the existence of stable positive water temperature anomalies relative to the climatic values in the surface layer of the Greenland Sea northeastern part in winter, which influence the characteristics of hydrological field gradients in the Marginal Frontal Zone. Being compared, the temperature and salinity fields resulted from the observation and reanalysis data have shown that the latter lack the datasets which describe reliably the thermohaline characteristics of waters near the ice edge.

Keywords: water temperature, water salinity, frontal zone, Marginal Frontal Zone, MERCATOR, GLORYS12v1, TOPAZ5, onboard observations, Greenland Sea

Acknowledgements: The study was carried out within the framework of state assignment themes FMWE-2024-0028 and FMEE-2024-0016.

For citation: Maksimovskaya, T.M., Zimin, A.V., Atadzhanova, O.A., Konik, A.A. and Moiseev, D.V., 2025. Variability of Water Characteristics in the Northeastern Part of the Greenland Sea during the Winter Periods in 2019–2023. *Physical Oceanography*, 32(2), pp. 174-186.

© 2025, T. M. Maksimovskaya, A. V. Zimin, O. A. Atadzhanova, A. A. Konik, D. V. Moiseev

© 2025, Physical Oceanography

Introduction

The northeastern part of the Greenland Sea (the Fram Strait) adjacent to the Svalbard archipelago (Fig. 1) is characterized by the interaction of waters of the Atlantic and Arctic origin and is also affected by melt waters coming from the shores of West Spitsbergen Island. A significant part of the water and heat



exchange between the Arctic basin and the World Ocean is carried out through the Fram Strait [1]. The Norwegian Current, which continues the North Atlantic Current and passes along the Norwegian slope, carries warm and salty Atlantic waters northwards into the Arctic Ocean. As it moves, the Norwegian Current is divided into two branches. One of them turns east into the Barents Sea and continues as the North Cape Current, the second branch moves along the Barents Sea western edge and the slope of Svalbard, becoming the core of the West Spitsbergen Current (WSC) divided into three branches. The western branch circulates mainly in the western and southwestern directions. The central WSC branch moves north over the shallow Yermak Plateau. The easternmost branch (the Spitsbergen branch) continues moving over the Svalbard northern slope and circulates cyclonically, submerging under freshened and cold Arctic waters [2, 3].

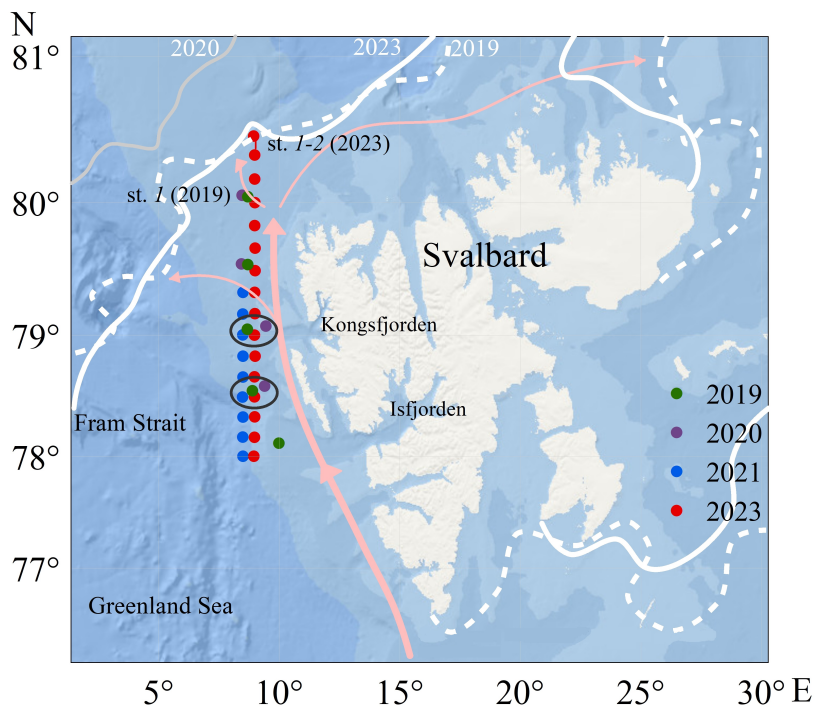


Fig. 1. Map of study area. Position of CTD sensing stations are shown by colored dots, areas of monitoring points – by black ellipses, position of currents – by pink arrows, position of ice edge in 2019 and 2023 – by solid and dashed white lines, position of ice edge in 2020 – by solid gray line

The Marginal Ice Zone (MIZ) is defined as a transition zone between ice-free sea and dense drift ice and extends from the imaginary line where 15% of the sea surface is covered by ice to the position of 80% ice cover concentration isoline [4]. Inside or outside the MIZ, a Marginal Frontal Zone (MFZ) is usually observed, the existence of

which is due to the interaction of relatively freshened cold Arctic waters formed as a result of ice melting and transformed Atlantic waters in an area located at a distance of several tens of kilometers from the ice edge [5]. Studies carried out in the Barents Sea MIZ in the spring of 2023 showed that the MFZ could be located units to hundreds of kilometers from the ice edge [6].

Complex and multi-scale processes of interaction in the ocean – sea ice – atmosphere system occur in the MFZ area. It is believed that atmospheric processes can significantly affect thermohaline structure variability in the area westwards and northwestwards of Svalbard [7]. In [8], the authors consider the MIZ position variability under effect of ocean dynamics associated with eddy structures recorded in the Fram Strait according to satellite radar observations. It is shown that ice edge displacement and eddy formation intensity are determined by the impact of wind conditions. In [9], it is found that tidal currents affect the variability of ice edge position and, accordingly, the MIZ characteristics. In this case, bottom relief gradients cause anomalies in the velocity of tidal currents, which is reflected in the marginal zone characteristics regardless of wind effect intensity. All the mentioned processes impact the parameters of turbulent flows; their consideration is important for qualitative description and forecasting of hydrometeorological conditions in the Arctic [10].

Global ocean models supplemented by ocean data reanalysis systems are constantly evolving and their results are shared openly in the form of quickly updated databases [11, 12]. In [13], it is noted that the main cause for the errors of ocean models in the Arctic region simulation is the use of subgrid process parameterization developed for mid-latitudes. Created sets of spatio-temporal values of water characteristics from these databases are often used (considering them verified) when solving applied problems, including those related to the detection of frontal zones [14] or recording changes in the available potential and kinetic energy of mesoscale eddies [15]. At the same time, a comparison of shipboard and model data for the region under study is not carried out, which does not always seem correct [16]. In [17], the results of oceanographic observations in the Arctic Ocean northwards of Svalbard are examined. In particular, a comparison with climate data from the Monthly Isopycnal/Mixed-layer Ocean Climatology (MIMOC) with 0.5° spatial resolution is performed. It was found that the upper layer of waters of the Atlantic origin was warmer and saltier according to observations than it was shown by the MIMOC climate data. Quality assessment of reconstruction of surface water characteristics by ocean databases according to repeated shipboard observations in the northeastern Greenland Sea in winter has not been previously carried out.

Thus, the work is purposed at analyzing the results of unique shipboard measurements for the winter period of 2019, 2020, 2021 and 2023, identifying the variability features of water characteristics in the northeastern Greenland Sea with an emphasis on the MFZ area as well as assessing the compliance of quickly updated ocean databases with the observation results.

Data and methods

The work is based on the data from ice edge visual observations and CTD sensing obtained during the expeditions of Murmansk Marine Biological Institute of RAS on R/V *Dalnie Zelentsy* in winter of 2019, 2020, 2021 and 2023. Measurements

of main hydrological parameters of marine environment were carried out by the CTD profiling method using the SEACAT SBE 19 plus V2 CTD probe. The studies were carried out on sections located in the waters northwestwards of Svalbard (Fig. 1) in the following periods: 20–21 November 2019, 6–7 November 2020, 23–25 November 2021 and 4–5 December 2023. To verify the results of ice edge visual observations carried out from the vessel, we used ice cover position data with a spatial resolution of $1/4^\circ$ prepared by the University of Bremen [18]. The isoline corresponding to 80% ice concentration was taken as the boundary of the ice edge position. It should be noted that the sections were made in relative proximity to the ice edge only in 2019 and 2023. In particular, in 2023, R/V *Dalniye Zelentsy* managed to come close to a field of large-sized ice with a concentration of 7–8 points. At the same time, CTD sensing was carried out directly in an area where the concentration did not exceed 1–2 points (visual observations from the vessel) with almost no risk of losing the sensing equipment. Those were the data that were used to describe the characteristics of the MFZ area waters. In 2020 and 2021, the northern points of the sections were located 144 and 141 km to the south of the ice edge, respectively; these data were used to assess the interannual variability of hydrological characteristics in this area.

To describe the variability of hydrological conditions, we used the data from two monitoring groups of stations (with their positions coinciding practically (Fig. 1)) carried out during the expeditions of 2019, 2020, 2021 and 2023. At these stations, for the upper layer (0–40 m), we estimated the deviation of *in situ* results from the climatic values of temperature and salinity given on the website <https://www.ncei.noaa.gov/access/world-ocean-atlas-2023/bin/woa23.pl> from the World Ocean Atlas 2023 over the thirty-year period from 1991 to 2020 with $1/4^\circ$ spatial resolution.

The following reanalysis products were applied to compare the CTD sensing results with the data of operational ocean models:

- CMEMS GLORYS12v1 (GLOBAL_MULTIYEAR_PHY_001_030 / E.U. Copernicus Marine Service Information (CMEMS). Marine Data Store (MDS). <https://doi.org/10.48670/moi-00021> (date of access: 05.02.2024));

- MERCATOR PSY4QV3R1 (GLOBAL_ANALYSISFORECAST_PHY_001_024 / Global Ocean Physics Analysis and Forecast. Marine Data Store (MDS). <https://doi.org/10.48670/moi-00016> (date of access: 05.02.2024));

- TOPAZ5 (ARCTIC_ANALYSISFORECAST_PHY_002_001 / Arctic Ocean Physics Analysis and Forecast. Marine Data Store (MDS). <https://doi.org/10.48670/moi-00001> (date of access: 05.02.2024)).

Selection of GLORYS12v1, PSY4QV3R1 and TOPAZ5 was determined by the availability of high spatial and temporal data resolution for the study area. GLORYS12v1 provided by Copernicus Marine Environment Monitoring Service is a global ocean reanalysis with daily discreteness and a spatial resolution of $1/12^\circ$. PSY4QV3R1, the European Group operational system for analysis and forecasting of the World Ocean, is characterized by a similar resolution. TOPAZ5 daily dataset, which uses the HYCOM model, contains information for the Arctic region with 6.25 km spatial resolution of output data. Quantitative comparison was performed

using the methodology described in detail in [16], according to which uniform arrays with the reduction of reanalysis and measurements data to uniform coordinates, horizons and dates of execution of each of the selected stations were formed. For comparison, two arrays were formed: the first one for the area of monitoring points of the region influenced by the Atlantic waters and the second one for the MFZ region where the interaction of the Arctic and Atlantic waters occurs. Then, a comparison of arrays was carried out by the average weighted values of temperature and salinity, divergence function, anomaly and correlation coefficient. To interpret divergence function (F), the classification proposed in [19] was applied: $0 \leq F < 1$ (good), $1 \leq F < 2$ (satisfactory) and $2 \leq F$ (poor).

Results and discussion

To analyze the interannual dynamics of temperature and salinity over a short interval (2019–2023), two monitoring areas (Fig. 1) were selected – northern and southern – within which hydrological stations were located at the closest possible distance from each other. The stations of the monitoring areas had a depth range from 45 to 1000 m (Fig. 2) since they were located at some distance from each other in the continental slope area. In general, at all the stations under consideration, the temperature varied within the range of 0.5–5.8 °C and the salinity varied within 33.4–35 PSU. The impact of cold and desalinated waters carried out from Kongsfjorden and Isfjorden of West Spitsbergen Island was observed in the upper 20 m layer at the stations that were closer to Svalbard. The easternmost position, correspondingly closer to Svalbard, was occupied by the stations completed in 2020. Here, at the 0 m horizon, the lowest temperature values of 1.45 °C and salinity of 33.45 PSU were observed. The southern group of stations was characterized by average temperature and salinity values of 4.2 °C and 34.8 PSU in the upper 40 m layer. Within the northern group of stations, similar average values were lower by 1.4 °C and 0.4 PSU. At the station from the northern group completed in 2023, a pycnocline was observed at a depth of 120 m; its existence was also due to the mixing of the WSC waters with the coastal Svalbard waters in shallow area.

To identify the relationship between the variability of thermohaline characteristics at the oceanographic stations under consideration and larger-scale processes over a given time interval, surface air temperature at meteorological stations on Svalbard and anomalies of water temperature and salinity in the monitoring areas were used. These anomalies were calculated relative to the climatic values from the World Ocean Atlas averaged over a 30-year period. The climatic values of temperature and salinity were calculated as average values over a 30-year period in the measurement months (November, December) averaged for each of the monitoring areas. Analysis of surface air temperature anomalies at meteorological stations in populated areas of Svalbard revealed significant warming in the winter period (after the “normal” period of 1960–2000) of 2000–2021 [20, 21]. Surface air temperature anomalies reached 3–6 °C. The WSC waters in the monitoring areas were characterized by positive temperature anomaly in the winter period from 2019 to 2023 (Fig. 3). Salinity anomaly value was close to the climatic norm in 2021 and 2023 and negative in 2019 and 2020 (–0.1 and –0.9, respectively). In 2020, significant negative salinity anomaly and low temperature

anomaly were observed. The coastal waters of Svalbard had an impact during this period; their temperature and salinity values were lower due to the influence of river runoff mainly of glacial and snow feeding and seasonal melting.

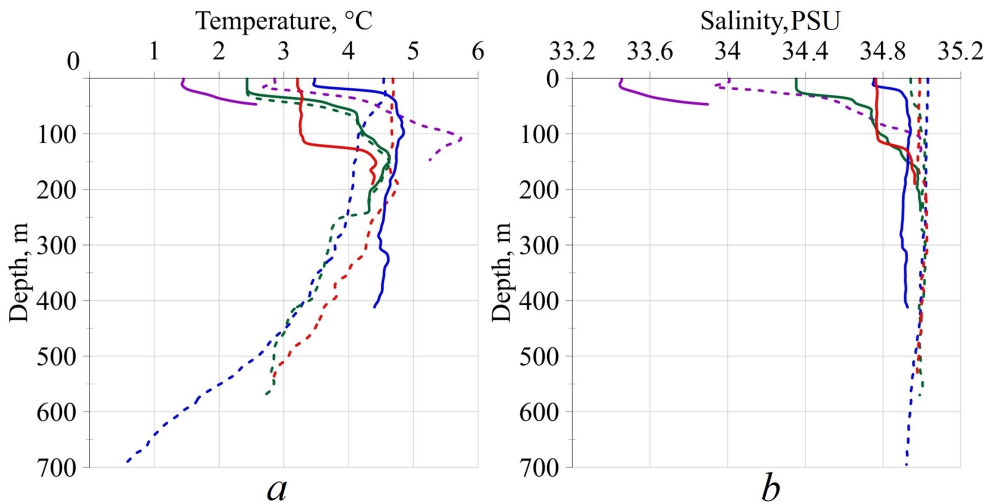


Fig. 2. Vertical profiles of water temperature and salinity at monitoring stations (stations of the northern group of points are marked with solid line, those of the southern group – by dotted line; stations completed in 2019 – by green line, in 2020 – by purple line, in 2021 – by blue line, in 2023 – by red line)

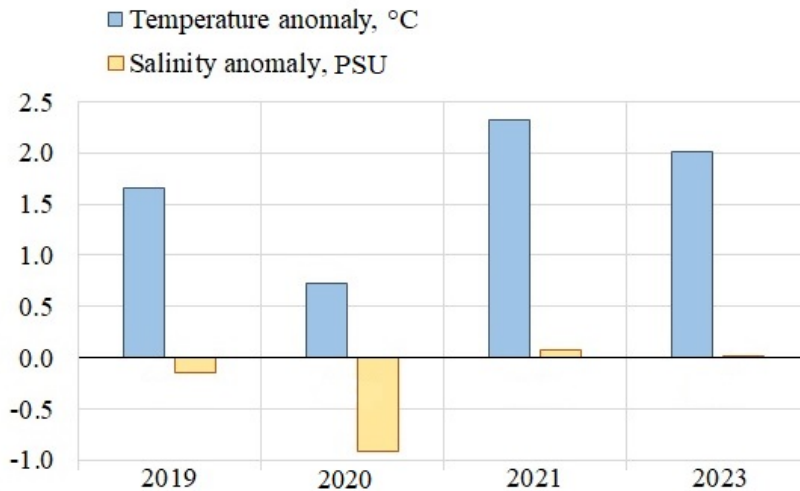


Fig. 3. Distribution of temperature and salinity anomalies in the monitoring areas during the winter periods in 2019–2023

Comparison of *in situ* and reanalysis data in monitoring areas located mainly in the Atlantic Ocean waters showed that PSY4QV3R1 and TOPAZ5 describe

the temperature and salinity of the WSC waters in the best possible manner. The discrepancy function with *in situ* data for all products as a whole had values close to zero, which corresponded to a “good” comparison result, and high significant correlation coefficients were also noted (Table 1). Statistical significance of relationship between the measured and model data series was determined at a significance level of 0.05. Since the calculated Student t-test varied within 2–5 and was less than the critical value (1.97–1.98), the discrepancies in the mean were significant. On average, the dispersion of the temperature series of measured data was 1°C^2 and for the reanalysis data – 0.8°C^2 . The salinity dispersion of *in situ* observations was 0.5 PSU^2 while it was two times smaller for the reanalysis – 0.25 PSU^2 . The reanalysis data indicated smoother temperature and salinity profiles in the coordinates under consideration, underestimating the values of real dispersion of the series. GLORIS12v1 reconstructed temperature and salinity of waters somewhat worse: average temperature for the series was overestimated by 0.7°C , salinity – by 0.3 PSU ; however, the correlation coefficient was quite high, the divergence function fell into the range of “good” values. In general, all three reanalysis datasets demonstrated a good result of reconstructing the thermohaline characteristics in the waters of the Atlantic origin.

Table 1

Statistical characteristics for comparing the data obtained at the monitoring stations located in the West Svalbard Current waters

Reanalysis	Average value (<i>in situ</i>)	Average value (reanalysis)	Anomaly	Cost function	Correlation coefficient
<i>Temperature, °C</i>					
PSY4QV3R1	3.54	3.49	0.05	0.05	0.80
GLORIS12v1	3.47	4.17	-0.70	0.69	0.79
TOPAZ5	3.53	3.44	0.09	0.09	0.90
<i>Salinity, PSU</i>					
PSY4QV3R1	34.54	34.68	-0.14	0.24	0.95
GLORIS12v1	34.55	34.83	-0.28	0.58	0.91
TOPAZ5	34.58	34.75	-0.17	0.33	0.96

The differences between the MIZ and surrounding waters consist in the presence of a thin freshened layer on the surface formed as a result of sea ice melting as well as the presence of convection and attenuation of wind waves and swell [22]. Within this area, in the northeastern Greenland Sea in the winters of 2019 and 2023, the MFZ was recorded by contact sensing data from a vessel. Fig. 4 represents the vertical distribution of temperature and salinity on the hydrological sections. Measurements in 2019 and 2023 were carried out with different spatial steps. The first station of the section performed in 2019 is located opposite Isfjorden

Bay at 10°E, the other four stations of the section passed along 8.9°E to 80°N. In 2023, CTD sensing stations were performed along the meridian (9°E) with a resolution of 10 nautical miles from 78°N towards the ice edge (at 80°30'N). The sections are directed along the West Spitsbergen Current, in the northern part they cross the MFZ and the Arctic waters. The stations are numbered from the northern station of the section. Water temperature on the section in 2019 varied within the range of $-0.5...4.7$ °C, salinity – 34–35 PSU. In 2023, the range of variability of thermohaline characteristics was $-1.3...4.8$ °C and 33.5–35 PSU. The layer of desalinated waters with negative temperature formed in the MIZ was separated by a pycnocline from the underlying transformed Atlantic waters at a depth of 10–30 m (Fig. 4). The frontal section, reflecting the position of the maximum temperature and salinity gradients, repeated the pycnocline outlines. Fig. 4 shows that the frontal section conventional line is drawn along the nearest isolines of hydrological characteristics.

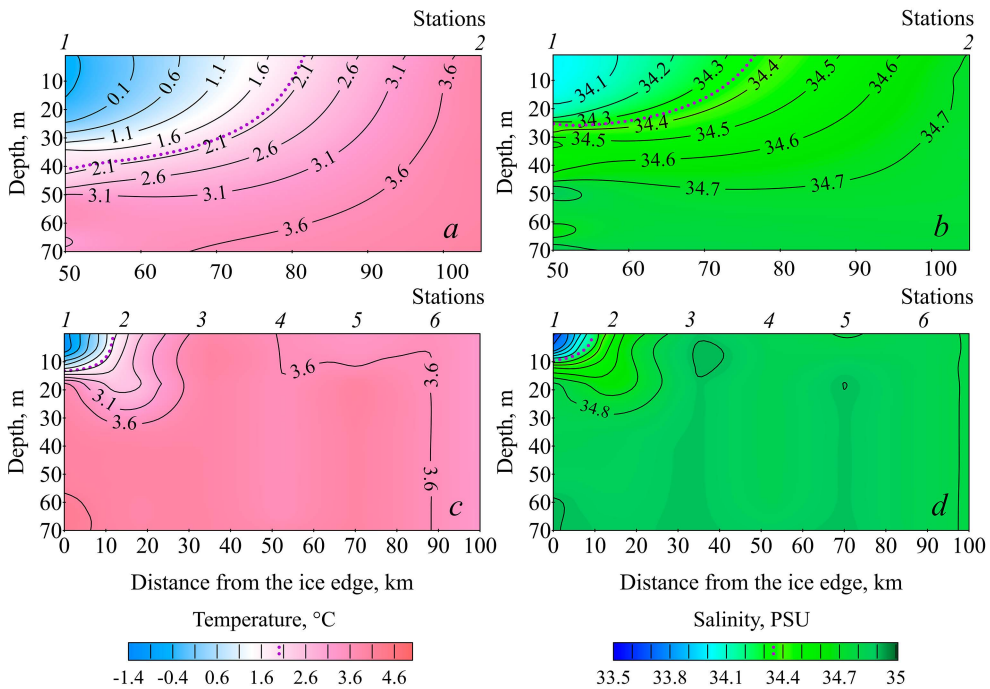


Fig. 4. Vertical distribution of temperature (left) and salinity (right) in the Marginal Frontal Zone on the sections in 2019 (*a, b*) and 2023 (*c, d*). Purple dotted line denotes the isotherm and isohaline along which the frontal sections of temperature and salinity run

On the section performed in 2019, the cold freshened Arctic waters (temperature < 0 °C, salinity < 34 PSU) were observed at the northern station in the upper 30 m layer, underlain by warmer and saltier waters of the West Spitsbergen Current (temperature > 3 °C, salinity > 34.5 PSU). During the study period, the horizontal temperature gradient between stations 1 and 2 reached 0.08 °C/km in the upper 20 m layer and decreased to zero values by the 90 m horizon, below which the temperature leveled off in the underlying warm layer of the Atlantic waters. The horizontal salinity gradient in the upper 20 m layer was

0.01 PSU/km, decreasing to zero at the 46 m horizon. The frontal boundary here was located between the stations at a distance of 30 km from the northernmost station and 80 km from the supposed ice edge according to the University of Bremen. The frontal zone depth did not exceed 70–80 m.

In 2023, the Arctic waters were traced in the upper 10 m layer. The horizontal temperature gradient between stations 1 and 3 reached 0.15 °C/km at the sea surface and decreased to zero at a depth of 30 m. The salinity gradient decreased from 0.04 PSU/km at the surface to zero at a depth of 20 m. The maximum temperature and salinity gradients were observed between stations 1 and 3 and amounted to 0.24 °C/km and 0.07 PSU/km. If the frontal division is drawn along this line, it will be located 7 km from the field of large-sized ice with a concentration of 8 points. The frontal zone depth did not exceed 30 m.

The results of contact measurements were compared with the reanalysis data for the stations in the distribution area of the Arctic waters and the MFZ. In 2019, only the northern station of the section (station 1) was in the frontal zone; in 2023, the northern station was in the zone of the surface Arctic waters and station 2 was in the frontal zone (Fig. 1). The models here overestimated temperature and salinity by an average of 1–3 °C and 0.2–0.6 PSU. The correlation coefficient had small values but it was statistically significant for all compared pairs of series, except for the case of comparing the measured salinity with the TOPAZ5 data. The discrepancy function had “satisfactory” values when using PSY4QV3R1 and GLORIS12v1. TOPAZ5 regional reanalysis demonstrated a “good” divergence function with low correlation coefficients, indicating low ability of the models to reconstruct the vertical variability trend of water temperature and salinity (Table 2).

Table 2

Statistical characteristics for comparing the data obtained in the Arctic waters zone and the Marginal Frontal Zone

Reanalysis	Average value (<i>in situ</i>)	Average value (reanalysis)	Anomaly	Cost function	Correlation coefficient
<i>Temperature, °C</i>					
PSY4QV3R1	1.75	–0.81	3.12	1.39	0.54
GLORIS12v1	1.10	2.91	–1.20	1.01	0.62
TOPAZ5	0.63	2.07	–0.69	0.95	0.27
<i>Salinity, PSU</i>					
PSY4QV3R1	34.44	33.66	0.78	1.79	0.54
GLORIS12v1	34.33	34.73	–0.40	1.00	0.65
TOPAZ5	34.25	34.17	0.08	0.22	0.38

Fig. 5 represents the water temperature and salinity profiles at station 2 located within the MFZ on the section in 2023. The reanalysis data of PSY4QV3R1 and TOPAZ5 revealed a significant underestimation of values (> 2 °C and > 1 PSU)

in the upper 7–15 m layer. That is, according to them, the distribution of the Arctic waters is observed at a greater distance than it was recorded by sensing data. On the contrary, GLORIS12v1 reanalysis showed a profile with values more typical of the Atlantic waters (temperature > 4 °C, salinity ≈ 35 PSU) and their distribution by depth.

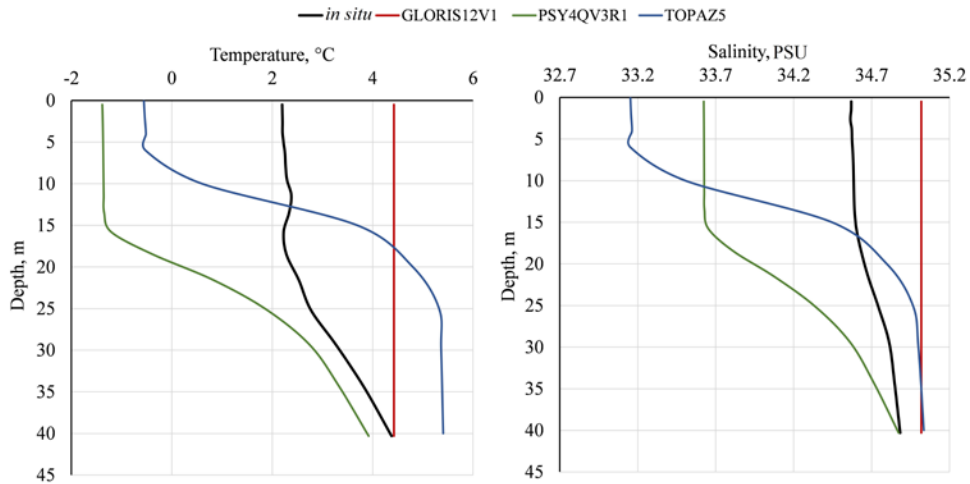


Fig. 5. Vertical distribution of temperature (left) and salinity (right) based on the *in situ* measurement and PSY4QV3R1, GLORIS12v1 and TOPAZ5 reanalysis data at station 2 on section in 2023

Average dispersion value ($1.7\text{ }^{\circ}\text{C}^2$) of temperature series according to measurement and reanalysis data differed by hundredths of a degree. Salinity dispersion was 0.4 PSU^2 according to *in situ* data and 0.5 PSU^2 according to the reanalysis data. The MFZ area was characterized by high variability of temperature and salinity, which was reflected in the reanalysis data, but they did not reconstruct width, depth, frontal section position and values of temperature and salinity gradients of frontal zone waters with sufficient accuracy. The temperature divergence function calculated for the MFZ by the reanalysis data was four times smaller than in the monitoring areas and that of salinity was 2.6 times smaller. The maximum model temperature deviation from that measured in the MFZ was 35 times greater than that in the WSC waters and that of salinity was three times greater. This also reflects the presence of significant errors in reconstructing the hydrological parameters near the ice edge by the models.

Comparison of *in situ* measurement data with the data from MERCATOR PSY4QV3R1, CMEMS GLORYS12v1 and TOPAZ5 revealed that the latter have good agreement of temperature and salinity values in the West Spitsbergen Current waters while the freshened cooled Arctic waters and the frontal zone between them (Arctic and Atlantic) are poorly reconstructed.

Conclusion

The considered winter periods of 2019–2023 were generally characterized as “warm” ones, with positive water temperature anomalies ranging from $0.7\text{ }^{\circ}\text{C}$ in 2020 to $2.3\text{ }^{\circ}\text{C}$ in 2021. The water temperature anomaly recorded in 2023 exceeded the similar one in 2019 by $0.6\text{ }^{\circ}\text{C}$.

In 2019, the frontal section was located 80 km from the ice edge and the MFZ was observed in the upper 30 m water layer. In 2023, the frontal section was recorded 10 km from the ice edge and the MFZ occupied the upper 10 m layer. Higher temperature gradients (0.08–0.24 °C/km) on the section in 2023 were also due to the increased temperature anomaly of the West Spitsbergen Current relative to 2019.

It was shown that the thermohaline characteristics of waters in the Marginal Frontal Zone area in the Greenland Sea northeastern part in winter had a complex structure and their description could not currently be based only on the data of global oceanographic models. The use of reanalysis data requires their careful verification and balanced approach. Only a comprehensive method with regard to all forms of available hydrological data will provide reliable information for assessing the variability of hydrological conditions in the Marginal Frontal Zone.

REFERENCES

1. Walczowski, W. and Piechura, J., 2011. Influence of the West Spitsbergen Current on the Local Climate. *International Journal of Climatology*, 31(7), pp. 1088-1093. <https://doi.org/10.1002/joc.2338>
2. Rudels, B., Korhonen, M., Budéus, G., Beszczynska-Möller, A., Schauer, U., Nummelin, A., Quadfasel, D., and Valdimarsson, H., 2012. The East Greenland Current and Its Impacts on the Nordic Seas: Observed Trends in the Past Decade. *ICES Journal of Marine Science*, 69(5), pp. 841-851. <https://doi.org/10.1093/icesjms/fss079>
3. Koenig, Z., Kolås, E.H. and Fer, I., 2021. Structure and Drivers of Ocean Mixing North of Svalbard in Summer and Fall 2018. *Ocean Science*, 17(1), pp. 365-381. <https://doi.org/10.5194/os-17-365-2021>
4. Strong, C., Foster, D., Cherkaev, E., Eisenman, I. and Golden, K.M., 2017. On the Definition of Marginal Ice Zone Width. *Journal of Atmospheric and Oceanic Technology*, 37(7), pp. 1565-1584. <https://doi.org/10.1175/JTECH-D-16-0171.1>
5. Rodionov, V.B. and Kostyanoi, A.G., 1998. *Oceanic Fronts of the Seas of the North European Basin*. Moscow: GEOS, 290 p. (in Russian).
6. Maksimovskaya, T.M., Zimin, A.V. and Moiseev, D.V., 2023. Results of Oceanographic Studies in the Marginal Ice Zone of the Barents Sea in the Spring of 2023. *Fundamental and Applied Hydrophysics*, 16(4), pp. 87-93. [https://doi.org/10.59887/2073-6673.2023.16\(4\)-7](https://doi.org/10.59887/2073-6673.2023.16(4)-7) (in Russian).
7. Selyuzhenok, V., Bashmachnikov, I., Ricker, R., Vesman, A. and Bobylev, L., 2020. Sea Ice Volume Variability and Water Temperature in the Greenland Sea. *The Cryosphere*, 14(2), pp. 477-495. <https://doi.org/10.5194/tc-14-477-2020>
8. Petrenko, L.A. and Kozlov, I.E., 2023. Variability of the Marginal Ice Zone and Eddy Generation in Fram Strait and near Svalbard in Summer Based on Satellite Radar Observations. *Physical Oceanography*, 30(5), pp. 594-611.
9. Watkins, D.M., Bliss, A.C., Hutchings, J.K. and Wilhelmus, M.M., 2023. Evidence of Abrupt Transitions between Sea Ice Dynamical Regimes in the East Greenland Marginal Ice Zone. *Geophysical Research Letters*, 50(15), e2023GL103558. <https://doi.org/10.1029/2023GL103558>
10. Semenov, V.A., 2021. Modern Arctic Climate Research: Progress, Change of Concepts, and Urgent Problems. *Izvestiya, Atmospheric and Oceanic Physics*, 57(1), pp. 18-28. <https://doi.org/10.1134/S0001433821010114>
11. Donlon, C., Martin, M., Stark, J., Roberts-Jones, J., Fiedler, E. and Wimmer, W., 2012. The Operational Sea Surface Temperature and Sea Ice Analysis (OSTIA) System. *Remote Sensing of Environment*, 116, pp. 140-158. <https://doi.org/10.1016/j.rse.2010.10.017>
12. Carton, J.A., Chepurin, G.A. and Chen, L., 2018. SODA3: A New Ocean Climate Reanalysis. *Journal of Climate*, 31(17), pp. 6967-6983. <https://doi.org/10.1175/JCLI-D-18-0149.1>

13. Repina, I.A., Artamonov, A.Yu., Varentsov, M.I. and Khavina, E.M., 2019. Air-Sea Interaction in the Arctic Ocean from Measurements in the Summer-Autumn Period. *Russian Arctic*, (7), pp. 49-61. <https://doi.org/10.24411/2658-4255-2019-10075> (in Russian).
14. Akhtyamova, A.F. and Travkin, V.S., 2023. Investigation of Frontal Zones in the Norwegian Sea. *Physical Oceanography*, 30(1), pp. 62-77.
15. Malysheva, A.A. and Belonenko, T.V., 2023. Variability of Potential and Kinetic Energy of Mesoscale Eddies in the Cape Basin. *Journal of Hydrometeorology and Ecology*, (73), pp. 684-698. <https://doi.org/10.33933/2713-3001-2023-73-684-698> (in Russian).
16. Zimin, A.V., Atajanova, O.A., Konik, A.A. and Gordeeva, S.M., 2020. Comparison of Hydrography Observations with Data of Global Products in the Barents Sea. *Fundamental and Applied Hydrophysics*, 13(4), pp. 66-77. <https://doi.org/10.7868/S2073667320040061> (in Russian).
17. Meyer, A., Sundfjord, A., Fer, I., Provost, C., Robineau, N.V., Koenig, Z., Onarheim, I.H., Smedsrud, L.H., Duarte, P. [et al.], 2017. Winter to Summer Oceanographic Observations in the Arctic Ocean North of Svalbard. *Journal of Geophysical Research: Oceans*, 122(8), pp. 6218-6237. <https://doi.org/10.1002/2016JC012391>
18. Spreen, G., Kaleschke, L. and Heygster, G., 2008. Sea Ice Remote Sensing Using AMSR-E 89 GHz Channels. *Journal of Geophysical Research: Oceans*, 113(C2), C02S03. <https://doi.org/10.1029/2005JC003384>
19. Eilola, K., Markus Meier, H.E. and Almroth, E., 2009. On the Dynamics of Oxygen, Phosphorus and Cyanobacteria in the Baltic Sea; A Model Study. *Journal of Marine Systems*, 75(1-2), pp. 163-184. <https://doi.org/10.1016/j.jmarsys.2008.08.009>
20. Karandasheva, T.K., Demin, V.I., Ivanov, B.V. and Revina, A.D., 2021. Air Temperature Changes in Barentsburg (Svalbard) in XX–XXI Centuries. Justification for Introducing a New Climate Standard. *Russian Arctic*, 2(13), pp. 26-39. <https://doi.org/10.24412/2658-4255-2021-2-26-39> (in Russian).
21. Ilyushenkova, I.A., Korzhikov, A.Ya. and Ivanov, B.V., 2023. Some Patterns of Formation of Extreme Surface Air Temperature in the Area of the Spitzbergen (Svalbard) Archipelago during the Cold Period. *Arctic and Antarctic Research*, 69(2), pp. 141-156. <https://doi.org/10.30758/0555-2648-2023-69-2-141-156> (in Russian).
22. Ilyin, G.V., Usyagina, I.S., Kasatkina, N.E., Valuiskaya, D.A. and Deryabin, A.A., 2017. Distribution of Radionuclides in the Marginal Ice Zone of the Barents Sea (Results of a Cruise in 2016). *Transactions of the Kola Science Center of the Russian Academy of Sciences: Oceanology*, 2(4), pp. 101-111 (in Russian).

Submitted 19.07.2024; approved after review 23.08.2024;
accepted for publication 29.01.2025.

About the authors:

Tatyana M. Maksimovskaya, Junior Research Associate, Shirshov Institute of Oceanology of RAS (30, 1st Line of Vasilievsky Island, Saint Petersburg, 119053, Russian Federation); Junior Research Associate, Murmansk Marine Biological Institute of RAS (17 Vladimirskaya Str., Murmansk, 183038, Russian Federation), **ORCID ID: 0000-0001-9136-6670**, **Scopus Author ID: 57735699200**, **ResearcherID: AAZ-6535-2020**, maximovskaja.t@yandex.ru

Alexey V. Zimin, Leading Research Associate, Shirshov Institute of Oceanology of RAS (30, 1st Line of Vasilievsky Island, Saint Petersburg, 119053, Russian Federation), DSc (Geogr.), **ORCID ID: 0000-0003-1662-6385**, **Scopus Author ID: 55032301400**, **ResearcherID: C-5885-2014**, zimin2@mail.ru

Oksana A. Atadzhanova, Senior Research Associate, Shirshov Institute of Oceanology of RAS (30, 1st Line of Vasilievsky Island, Saint Petersburg, 119053, Russian Federation), CSc (Geogr.), **ORCID ID: 0000-0001-6820-0533**, **Scopus Author ID: 57188718743**, **ResearcherID: R-7835-2018**, oksanam07@list.ru

Alexander A. Konik, Research Associate, Shirshov Institute of Oceanology of RAS (30, 1st Line of Vasilevsky Island, Saint Petersburg, 119053, Russian Federation), CSc (Geogr.), **ORCID ID: 0000-0002-2089-158X**, **Scopus Author ID: 57203864647**, **ResearcherID: AAB-7195-2020**, konikrshu@gmail.com

Denis V. Moiseev, Deputy Director for Science, Murmansk Marine Biological Institute of RAS (17 Vladimirskaia Str., Murmansk, 183038, Russian Federation), CSc (Geogr.), **ORCID ID: 0000-0003-0141-374X**, **Scopus Author ID: 35069960500**, **ResearcherID: C-1651-2015**, denis_moiseev@mmbi.info

Contribution of the co-authors:

Tatyana M. Maksimovskaya – formulation of research goals and objectives, selection of research methods, data collection and systematization, selection and analysis of literature, preparation of paper text, figure creation

Alexey V. Zimin – formulation of research goals and objectives, selection of research methods, text analysis

Oksana A. Atadzhanova – selection of research methods, text analysis

Alexandr A. Konik – selection of research methods, text analysis

Denis V. Moiseev – text analysis

The authors have read and approved the final manuscript.

The authors declare that they have no conflict of interest.

Investigation of the Upper Mixed Layer Variability in the Barents and Kara Seas

A. A. Bukatov, E. A. Pavlenko , N. M. Solovei

Marine Hydrophysical Institute of RAS, Sevastopol, Russian Federation

 *ekk.pavlenko@yandex.ru*

Abstract

Purpose. The study is purposed at analyzing spatial and temporal climatic variability of the upper mixed layer in the Barents and Kara seas on a climatic scale.

Methods and Results. Potential water density is calculated based on the ORAS5 reanalysis data on the average monthly values of potential temperature and salinity at the nodes of a grid of about 10 km with an irregular step over vertical up to a depth of about 400 m for the 1958–2022 period. The formed density array makes it possible to determine the upper mixed layer thickness in the Barents and Kara seas. Threshold criterion $\Delta\sigma = 0.03 \text{ kg/m}^3$ is used for its estimation. The obtained results permit to identify the areas notable for significant variability of the upper mixed layer thickness.

Conclusions. The analysis shows that the upper mixed layer maximum development falls on February and March, whereas the minimum one – on June and July. Thus, the highest values of the upper mixed layer thickness are observed in the seas under consideration during increased autumn-winter convection. In the cold half of a year (November – April), the upper mixed layer thickness averages 105 m in the Barents Sea and 23 m in the Kara Sea. The analysis of interannual variability of the average annual thickness values of these layers shows the presence of a positive climatic trend, i. e. a thickness increase in the upper mixed layers in the Barents and Kara seas in 1958–2022. The upward trend is observed both in the cold and warm halves of a year. The values of average annual thickness trends of the upper mixed layers in the Barents and Kara seas average 1.3 m/10 years and 1.2 m/10 years, respectively.

Keywords: Barents Sea, Kara Sea, upper mixed layer thickness, vertical mixing, linear trend, interannual variability

Acknowledgements: The study was carried out within the framework of theme of state assignment of FSBSI FRS MHI FNNN-2024-0001.

For citation: Bukatov, A.A., Pavlenko, E.A. and Solovei, N.M., 2025. Investigation of the Upper Mixed Layer Variability in the Barents and Kara Seas. *Physical Oceanography*, 32(2), pp. 187-196.

© 2025, A. A. Bukatov, E. A. Pavlenko, N. M. Solovei

© 2025, Physical Oceanography

Introduction

The upper mixed layer (UML) is formed due to thermal and dynamic interaction at the ocean-atmosphere boundary: surface heating, cooling, wind-wave mixing, intra-water exchange, etc. [1]. Its state affects the heat flux from the ocean into the atmosphere through the ice cover and largely determines the thermal balance of the Arctic Ocean surface. The ice cover formation and stability are associated with the UML thickness, thermohaline parameters and characteristics of the underlying halocline [2–5].



A significant reduction of the ice cover area at the beginning of the current century [5–10] resulted in the surface layer becoming more accessible to the direct effect of wind and solar radiation. Such a change in environmental conditions could not but affect thermohaline structure of the surface layer, which has indeed undergone significant changes in recent years. The origin of the Arctic surface layer waters and the variability of its characteristics were considered in a number of works [5, 11–15]. According to modern concepts, the surface layer is formed from river runoff waters, atmospheric precipitation and waters of the Atlantic and Pacific origin [5, 7, 8, 16]. In [13], presence of a decrease in the UML thickness over a 30-year period in six regions of the Arctic was determined based on the analysis of spatial and temporal variability of its characteristics for 1979–2012. In [5], the thickness and salinity of the Arctic Basin UML were calculated for the winter period of 1950–2013 according to an array of oceanographic data. Estimates of the UML thickness spatial distribution in the Kara Sea in August – November 2007 and 2008 obtained from expeditionary data are presented in [14].

The work is purposed at studying the UML thickness spatial and temporal variability in the Barents and Kara seas using the most complete modern climatic oceanographic data array.

Materials and methods

ORAS5 reanalysis arrays of average monthly potential temperature and salinity values at nodes of a grid of about 10 km with a non-uniform depth step of up to about 400 m for 1958–2022 represent the initial hydrological data. Potential density arrays for the Barents and Kara seas were formed on their basis to calculate the UML thickness. The study area is limited by coordinates 65–80°N, 16–102°E.

Three main groups of methods for calculating the UML thickness are as follows: threshold criterion methods, gradient methods and profile curvature analysis methods [13, 17]. In this work, in order to estimate the UML after several test calculations, we adopted a threshold criterion which determines the depth where potential water density is greater than its surface potential density by value $\Delta\sigma = 0.03 \text{ kg/m}^3$, with

$$\Delta\sigma = \sigma(z) - \sigma(z_{\min}), \quad (1)$$

$\sigma(z)$ is potential density at given depth z , $\sigma(z_{\min})$ is potential density at the surface [18, 19].

To analyze the interannual variability of the mixed layer, the average values of the UML thickness in the Barents and Kara seas were calculated for the cold (November – April) and warm (May – October) halves of a year. The thickness values of this layer were found for the western (65–80°N; 16–36°E) and eastern (65–80°N; 36–56°E) regions of the Barents Sea as well as for the western (65–80°N; 56–80°E) and eastern (65–80°N; 80–103°E) regions of the Kara Sea.

Analysis of results

The upper mixed layer of the Barents and Kara seas is formed due to mixing of waters coming from the adjacent basins of the Atlantic and Arctic oceans as well as

continental runoff waters. The UML thickness spatial distribution depends on the processes of ice formation and melting, development of autumn-winter convection and is also largely determined by the bottom relief¹.

Fig. 1 shows the UML thickness climatic intra-annual variation averaged over the water areas of the Barents and Kara seas. According to the analysis, this layer reaches its maximum development in February and March and its minimum in June and July. The UML thickness increases from east to west. Thus, its greatest values in the seas under consideration are observed during the period of autumn-winter convection development which occurs as a result of density increase in the surface layer with a decrease in water temperature and salinization due to ice formation in the upper sea layers.

In this period, the UML is considered as a layer of water involved in the processes of intensive autumn-winter convection which averages 105 m in the Barents Sea (from 65 m in November to 125 m in February) (Fig. 1, *a*). The estimates obtained for the Barents Sea are less than those given in [13], according to which the UML thickness in this sea in the winter period is 170 m.

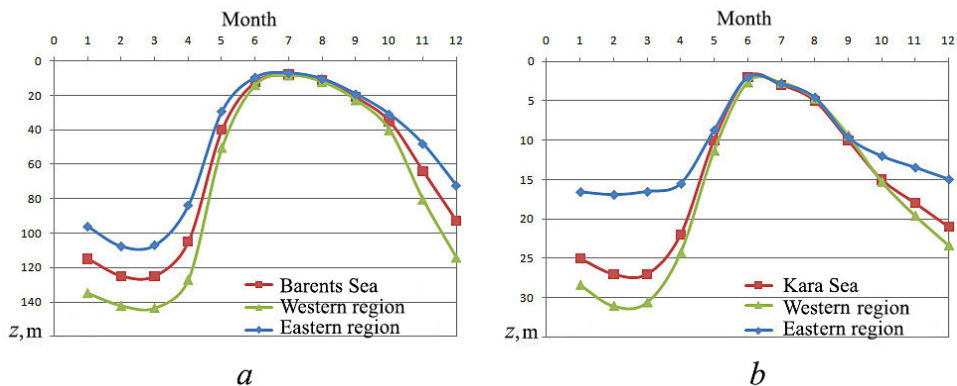


Fig. 1. Climatic intra-annual variation of UML thickness in the Barents (*a*) and Kara (*b*) seas

In the cold half of a year (November – April), the greatest UML thickness (360–390 m) is observed in the deepest areas of the Barents Sea (Western Trough, Central Basin), with its maximum in February and March (Fig. 2). This area is characterized by the distribution of non-freezing Atlantic waters where wind and air temperature are the most important factors determining stratification intensity. In winter, strong winds and low temperatures can cause mixing to depths of more than 200 m [20].

In the Barents Sea shallow areas (Central Bank, Gusinaya Bank, North Kanin Bank, Murmansk Rise), convection reaches the bottom earlier (November) than in the adjacent deep-water areas. In the northern part of the sea, convective mixing caused mainly by salinization during ice formation penetrates in the relative shallows, with the 50–100 m UML thickness (Fig. 2).

¹ Dobrovolsky, A.D. and Zalogin, B.S., 1982. *Seas of the USSR*. Moscow: MSU Publishing, 192 p. (in Russian).

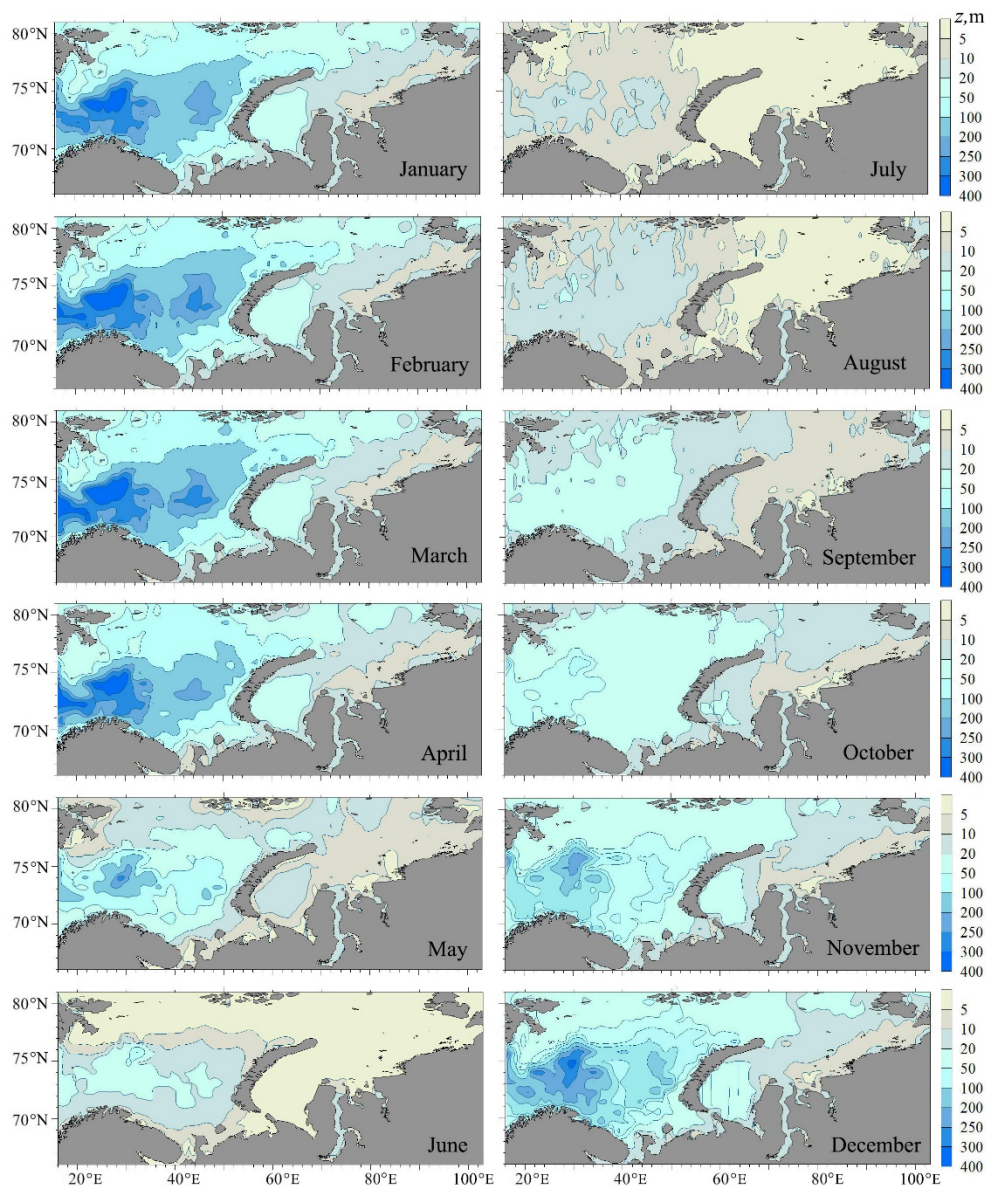


Fig. 2. UML thickness (m) in the Barents and Kara seas

In the Kara Sea, the average UML thickness during the cold season is 23 m (from 18 m in November to 27 m in February and March) (Fig. 1, *b*). Its maximum reaches about 130 m in March near the eastern shore of the Novaya Zemlya Archipelago (Fig. 2), where warmer homogeneous waters of the Barents Sea penetrate, equalizing the density vertically. The smallest UML thickness (up to 10 m) is observed in the Ob-Yenisei shallow waters in the area of the river plume distribution (Fig. 2).

In the warm period of a year (May – October), the upper layer density is significantly reduced during the maximum distribution of river waters, ice melting

and surface heating. Steady stratification is observed and the layer with the maximum buoyancy frequency values rises to the surface [21]. The UML thickness averaged over the entire water area is 8 m (from 2 m in June to 15 m in October) for the Kara Sea (Fig. 1, *b*), 21 m (from 8 m in July to 40 m in October) for the Barents Sea (Fig. 1, *a*). The obtained estimates for the Barents Sea are higher than those given in [13], according to which the UML thickness in this sea is 18 m in the summer period.

In the warm and cold periods of a year, the greatest UML thickness is noted in the Barents Sea in its deep-water areas. During the cold half of a year (February – March), it reaches 270 m and in the warm half of a year, it does not exceed 23 m throughout the sea by July (Fig. 2).

The Kara Sea UML thickness in spring is 20 m, with its maximum noted in the southwest, near the eastern coast of the Novaya Zemlya Archipelago. By June, the UML thickness in almost all areas of the Kara Sea does not exceed 5 m. An exception is the Gulf of Ob, for which density is typically equalized vertically up to 20 m throughout the summer period due to increased runoff. This is especially noticeable in the Barents Sea southwestern part where the North Cape Current waters of high salinity and temperature pass. As they move east, these waters are cooled relatively quickly and then descend, smoothing out the difference in layer density [21–23].

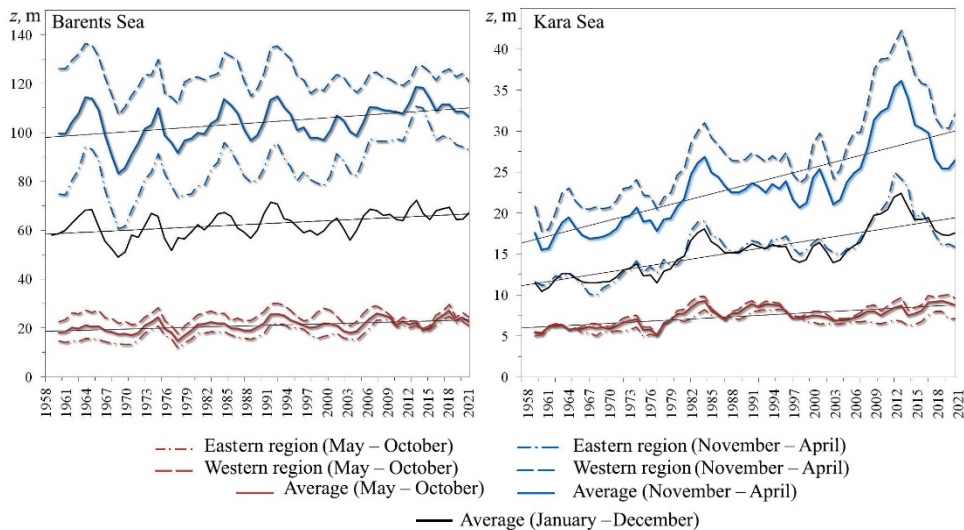


Fig. 3. Interannual variability of UML thickness, three-year moving average and linear trend for the Barents and Kara seas for 1958–2022

Fig. 3 demonstrates interannual variability of the UML thickness in the Barents and Kara seas in the cold and warm halves of a year. In these seas, the thickness of this layer changes synchronously and the correlation coefficient between the average annual thickness values is 0.62. Trend of the average annual UML thickness for the Barents Sea was 1.3 m/10 years, for the Kara Sea 1.2 m/10 years. Trend of the UML thickness for the Barents and Kara seas in the cold half of a year was

1.9 m/10 years and 2.1 m/10 years, in the warm half of a year 0.7 m/10 years and 0.4 m/10 years, respectively.

Analysis of the results revealed that an increase in the UML thickness was observed up to 72 m in the Barents Sea and up to 14 m in the Kara Sea in the mid-1960s (Fig. 3). It is known that large positive air temperature anomalies were noted in the Arctic in the 1950s – early 1960s. They were accompanied by increased melting of snow and ice and an increase in continental runoff [24]. This contributed to fresh water accumulation and an increase in the UML thickness during this period.

The smallest thickness of the surface layer over the entire study period was noted in the late 1960s – early 1970s amounting to 45 and 10 m in the Barents and Kara seas, respectively. This period coincides with the Great Salinity Anomaly in the North Atlantic which is mainly the result of the removal of sea ice and fresh water from the Arctic Basin through the Fram Strait [24].

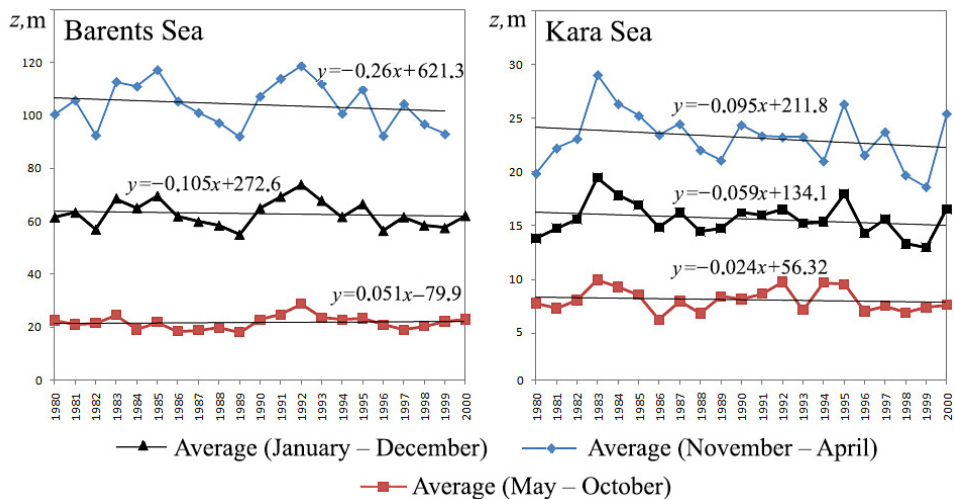


Fig. 4. Interannual variability of UML thickness and linear trend for the Barents and Kara seas for 1980–2000

The period from the late 1970s to the early 2000s is characterized by negative trends in the UML thickness (Fig. 4), which is consistent with the conclusions obtained in [13]. Since the early 2000s, an increase in the mixed layer thickness in the Arctic Basin has been observed due to the weakening of the Atlantic thermohaline circulation and intense summer warming in the Arctic in the 1990s – 2000s [5, 24].

Seasonal variations of the UML thickness trends in the Barents and Kara seas have regional features (Fig. 5). In the most dynamically active western region of the Barents Sea where a steady inflow of Atlantic waters takes place, the largest negative trends in the UML thickness are observed; it decreases in all months of a year. In January, the linear trend estimates reach 32 m/10 years.

The largest positive trends (42 m/10 years, February) were noted in the central and north-eastern regions of the Barents Sea in the cold half of a year. In the Kara Sea, negative trend values were noted against the background of a general steady tendency towards the UML thickness increase in the shelf zone.

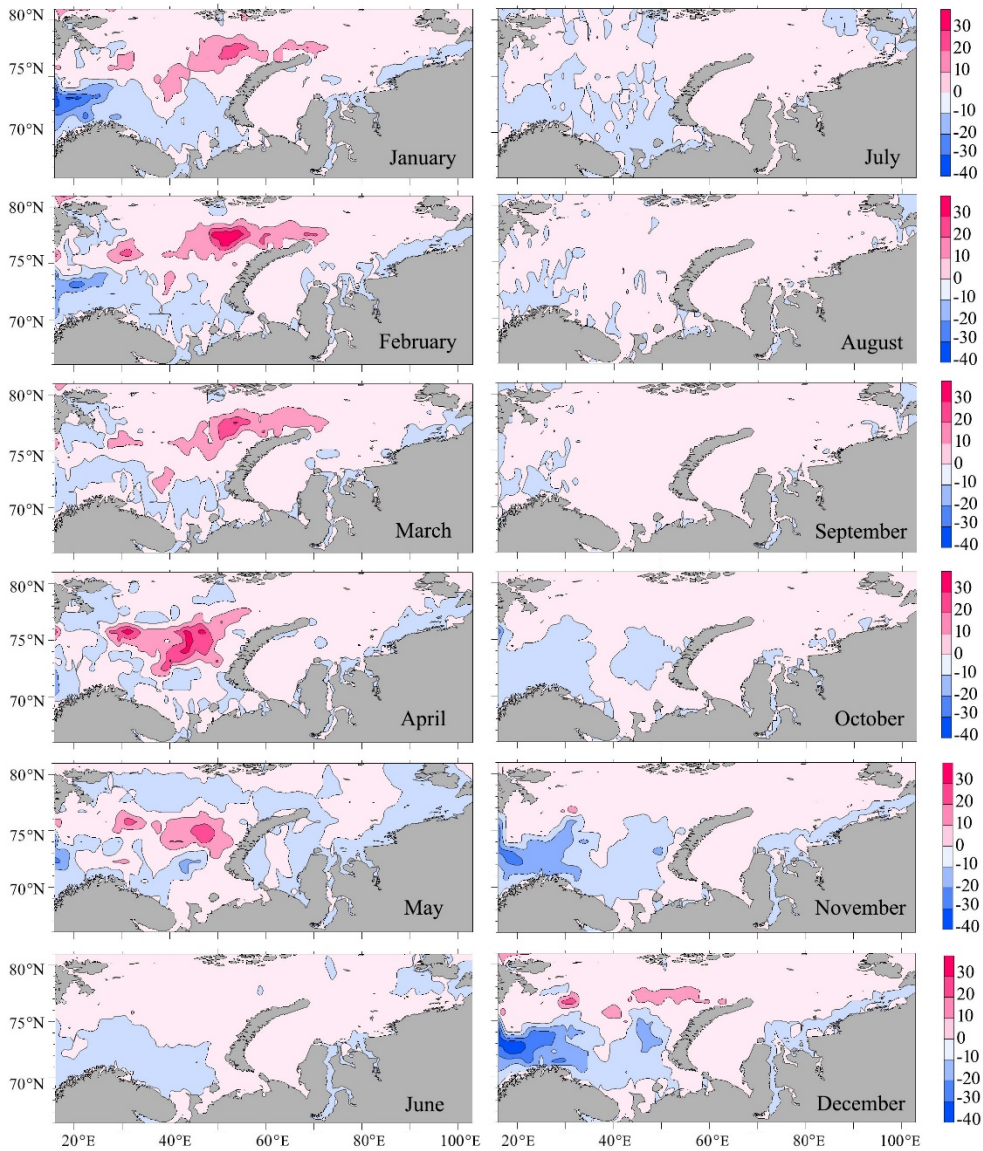


Fig. 5. Distribution of the linear trend coefficients (m/10 years) of UML thickness for 1958–2022

Conclusion

Based on the modern ORAS5 oceanographic data array for the long 1958–2022 period, the UML thickness climatic variability in the Barents and Kara seas was studied.

The analysis of the constructed average long-term fields of the UML thickness for the water areas of the seas under consideration made it possible to determine that the UML reaches its maximum vertical development in February and March and its minimum in June and July. Thus, the highest values of the UML thickness in the seas under consideration are observed during autumn-winter convection development.

In the cold half of a year (November – April), the basin-averaged UML thickness is 105 m in the Barents Sea and 23 m in the Kara Sea.

In the warm period of a year (May – October), during the maximum distribution of river waters, ice melting and surface heating, the water column is stratified well by depth and the layer of maximum buoyancy frequency values rises to the surface. The average UML thickness over all water areas is 21 m for the Barents Sea and 8 m for the Kara Sea.

The difference of UML thickness values and their geographical distribution in the seas under consideration can be explained by the difference in such main influencing hydrological and atmospheric factors that form the UML spatial-temporal structure as water exchange with neighboring oceans, ice processes, fluctuations in river runoff, atmospheric processes, surface heating and cooling, wind-wave mixing.

Tendencies towards the UML thickness increase in the Eurasian part of the Arctic Basin have been noted since the early 1970s. In the 1950–1970 period, when minimum values of the surface layer thickness were noted, extremely low values of the Arctic and North Atlantic oscillations and negative anomalies of river runoff into the seas of the Russian Arctic were observed. At the same time, starting from the 1990s, an increase in positive values of the Arctic Oscillation Index with a simultaneous increase in positive anomalies of river runoff as well as significant negative anomalies of the Arctic ice cover area have been observed.

The analysis of interannual variability of the average annual values of the UML thickness in the Barents and Kara seas also revealed the presence of a positive climatic trend in 1958–2022, i.e. an increase in the UML thickness. The trend towards an increase in the UML thickness is observed both in the cold and warm halves of a year. The magnitude of the trend in the average annual UML thickness was 1.3 m/10 years for the Barents Sea and 1.2 m/10 years for the Kara Sea. The growth rate of the UML thickness for the Barents and Kara seas was 1.9 m/10 years and 2.1 m/10 years in the cold half of a year and 0.7 m/10 years and 0.4 m/10 years in the warm half of a year.

REFERENCES

1. Luchin, V.A., 2018. Intra-Annual Variability of the Mixed Layer Parameters in the Okhotsk Sea. *Izvestiya TINRO*, 195(4), pp. 170-183. <https://doi.org/10.26428/1606-9919-2018-195-170-183>
2. Aagaard, K. and Coachman, L.K., 1975. Toward an Ice-Free Arctic Ocean. *Eos, Transactions American Geophysical Union*, 56(7), pp. 484-486. <https://doi.org/10.1029/EO056i007p00484>
3. Rudels, B., Anderson, L.G. and Jones, E.P., 1996. Formation and Evolution of the Surface Mixed Layer and Halocline of the Arctic Ocean. *Journal of Geophysical Research: Oceans*, 101(C4), pp. 8807-8821. <https://doi.org/10.1029/96JC00143>
4. Zakharov, V.F., 1996. *Sea Ice in the Climate System*. Saint Petersburg: Gidrometeoizdat, 213 p. (in Russian).
5. Cherniavskaia, E.A., Timokhov, L.A., Karpuy, V.Y. and Malinovskiy, S.Y., 2020. Interannual Variability of Parameters of the Arctic Ocean Surface Layer and Halocline. *Arctic and Antarctic Research*, 66(4), pp. 404-426. <https://doi.org/10.30758/0555-2648-2020-66-4-404-426>
6. Frolov, I.E., Gudkovich, Z.M., Karklin, V.P., Kovalev, E.G. and Smolyanitsky, V.M., 2007. *Scientific Research in the Arctic. Vol. 2. Climatic Changes in the Ice Cover of the Eurasian Shelf Seas*. Saint Petersburg: Nauka, 135 p. (in Russian).

7. Stroeve, J., Holland, M.M., Meier, W., Scambos, T. and Serreze, M., 2007. Arctic Sea Ice Decline: Faster than Forecast. *Geophysical Research Letters*, 34(9), L09501. <https://doi.org/10.1029/2007GL029703>
8. Kwok, R. and Rothrock, D.A., 2009. Decline in Arctic Sea Ice Thickness from Submarine and ICESat Records: 1958–2008. *Geophysical Research Letters*, 36(15), L15501. <https://doi.org/10.1029/2009gl039035>
9. Rostov, I.D., Dmitrieva, E.V., Rudykh, N.I. and Vorontsov, A.A., 2019. Climatic Changes of Thermal Condition in the Kara Sea at Last 40 Years. *Arctic and Antarctic Research*, 65(2), pp. 125-147. <https://doi.org/10.30758/0555-2648-2019-65-2-125-147> (in Russian).
10. Ashik, I.M., ed., 2021. *The Seas of the Russian Arctic in Modern Climatic Conditions*. Saint Petersburg: AARI, 360 p. (in Russian).
11. Macdonald, R.W., Harner, T. and Fyfe, J., 2005. Recent Climate Change in the Arctic and Its Impact on Contaminant Pathways and Interpretation of Temporal Trend Data. *Science of the Total Environment*, 342(1-3), pp. 5-86. <https://doi.org/10.1016/j.scitotenv.2004.12.059>
12. Frolov, I.E., Ashik, I.M., Kassens, H., Polyakov, I.V., Proshutinsky, A.Yu., Sokolov, V.T. and Timokhov, L.A., 2009. Anomalous Variations in the Thermohaline Structure of the Arctic Ocean. *Doklady Earth Sciences*, 429(2), pp. 1567-1569. <https://doi.org/10.1134/S1028334X09090323>
13. Peralta-Ferriz, C. and Woodgate, R.A., 2015. Seasonal and Interannual Variability of Pan-Arctic Surface Mixed Layer Properties from 1979 to 2012 from Hydrographic Data, and the Dominance of Stratification for Multiyear Mixed Layer Depth Shoaling. *Progress in Oceanography*, 134, pp. 19-53. <https://doi.org/10.1016/j.pocan.2014.12.005>
14. Vlasenkov, R.E., Smirnov, A.V. and Makshtas, A.P., 2010. Estimation of Potential Heating of the Surface Layer of the Kara and Laptev Seas in 2007 and 2008. *Arctic and Antarctic Research*, (2), pp. 35-39 (in Russian).
15. Sirevaag, A., De La Rosa, S., Fer, I., Nicolaus, M., Tjernström, M. and McPhee, M.G., 2011. Mixing, Heat Fluxes and Heat Content Evolution of the Arctic Ocean Mixed Layer. *Ocean Science*, 7(3), pp. 335-349. <https://doi.org/10.5194/os-7-335-2011>
16. Bukatov, A.A., Pavlenko, E.A. and Solovei, N.M., 2023. River Runoff Influence on the Density Stratification of the Russian Arctic Seas. In: T. Chaplina, ed., 2023. *Processes in GeoMedia – Volume VI*. Springer Geology Series. Cham: Springer, pp. 523-536. https://doi.org/10.1007/978-3-031-16575-7_47
17. Smirnov, A.V. and Korablev, A.A., 2010. Interrelationship between Mixed Layer Characteristics and Atmospheric Heat Fluxes in the Nordic Seas. *Arctic and Antarctic Research*, (3), pp. 79-88 (in Russian).
18. Toole, J.M., Timmermans, M.L., Perovich, D.K., Krishfield, R.A., Proshutinsky, A. and Richter-Menge, J.A., 2010. Influences of the Ocean Surface Mixed Layer and Thermohaline Stratification on Arctic Sea Ice in the Central Canada Basin. *Journal of Geophysical Research: Oceans*, 115(C10), C10018. <https://doi.org/10.1029/2009JC005660>
19. Jackson, J.M., Williams, W.J. and Carmack, E.C., 2012. Winter Sea-Ice Melt in the Canada Basin, Arctic Ocean. *Geophysical Research Letters*, 39(3), L03603. <https://doi.org/10.1029/2011gl050219>
20. Lisitsyn, A.P., ed., 2021. *The Barents Sea System*. Moscow: GEOS, 672 p. [https://doi.org/10.29006/978-5-6045110-0-8/\(4\)](https://doi.org/10.29006/978-5-6045110-0-8/(4)) (in Russian).
21. Bukatov, A.A., Pavlenko, E.A. and Solovei, N.M., 2018. Features of Spatial-Time Variability of Väisälä-Brunt Frequency in Barents and Kara Seas. *Processes in GeoMedia*, 3(16), pp. 1004-1013 (in Russian).
22. Bukatov, A.A., Solovei, N.M. and Pavlenko, E.A., 2023. Regional Features of Water Density Stratification and Internal Wave Characteristics in the Arctic Seas. *Physical Oceanography*, 30(6), pp. 731-746.
23. Ivanov, V.V., Frolov, I.E. and Filchuk, K.V., 2020. Transformation of Atlantic Water in the North-Eastern Barents Sea in Winter. *Arctic and Antarctic Research*, 66(3), pp. 246-266. <https://doi.org/10.30758/0555-2648-2020-66-3-246-266>

24. Viazilova, A.E., Alekseev, G.V., Balakin, A.A. and Smirnov, A.V., 2015. Influence of the Arctic on Salinity Anomaly Formation in the North-West Atlantic and North European Basin. *Arctic and Antarctic Research*, (3), pp. 39-50 (in Russian).

Submitted 10.09.2024; approved after review 17.10.2024;
accepted for publication 29.01.2025.

About the authors:

Anton A. Bukatov, Leading Research Associate, Oceanography Department, Marine Hydrophysical Institute of RAS (2 Kapitanskaya Str., Sevastopol, 299011, Russian Federation), CSc (Phys.-Math.), **ORCID ID: 0000-0002-1165-8428**, **ResearcherID: P-6733-2017**, **Scopus Author ID: 7004175272**, **SPIN-code: 7790-4651**, newisland@list.ru

Ekaterina A. Pavlenko, Junior Research Associate, Oceanography Department, Marine Hydrophysical Institute of RAS (2 Kapitanskaya Str., Sevastopol, 299011, Russian Federation), **ORCID ID: 0000-0001-9146-5708**, **Scopus Author ID: 57222031207**, **SPIN-code: 3047-6419**, ekk.pavlenko@yandex.ru

Nelya M. Solovei, Junior Research Associate, Oceanography Department, Marine Hydrophysical Institute of RAS (2 Kapitanskaya Str., Sevastopol, 299011, Russian Federation), **ORCID ID: 0000-0003-3359-0345**, **Scopus Author ID: 14059043600**, **SPIN-code: 4078-4270**, nele7@mail.ru

Contribution of the co-authors:

Anton A. Bukatov – problem statement, research data analysis, analysis and revision of the text

Ekaterina A. Pavlenko – preparation of the text, analysis and validation of the results and numerical experiments, preparation of graphic materials.

Nelya M. Solovei – development of program algorithms, analysis of the results, paper correction, literature reviewing.

The authors have read and approved the final manuscript.

The authors declare that they have no conflict of interest.

Original article

Long-Term Dynamics of the Annual Average Wave Heights in the Baltic Sea

A. N. Sokolov^{1, 2} ✉, B. V. Chubarenko¹

¹ *Shirshov Institute of Oceanology, Russian Academy of Sciences, Moscow, Russian Federation*

² *Immanuel Kant Baltic Federal University, Kaliningrad, Russian Federation* ✉
tengritag@gmail.com

Abstract

Purpose. The paper is purposed at revealing the time periods since the mid-20th century when the annual average wave heights in the Baltic Sea tended to increase or decrease, assessing the statistical significance of potential time trends, as well as analyzing the statistical relationship between annual average wave heights in the Baltic Sea and the North Atlantic Oscillation.

Methods and Results. The analysis is based on several points located in different parts of the Baltic Sea, in which the data on annual average wave heights cover the time intervals of several decades and are obtained by instrumental methods (one point), from field observations (two points) and modeling results (six points). The time series of annual average wave heights at these points are divided into the time segments of conditional monotony with predominant tendencies towards increase or decrease. The rates of change in wave heights at each segment and statistical significance of potential time trends are assessed using the non-parametric techniques. In the majority of cases, the trends within the segments under consideration are found to be statistically significant at the 90% level or more and the rates of change in the trend can range from 5 to 20 mm per year. The statistical relationship between annual average wave heights and the North Atlantic Oscillation is evaluated using the Pearson and Spearman correlation analysis. The correlation coefficients between the North Atlantic Oscillation indices and the annual average wave heights are statistically significant at the 90% level or more. Their numerical values within the interannual variability range constitute 0.3–0.6 and those between the five-year moving averages – 0.4–0.8.

Conclusions. The increasing and decreasing phases in wave heights in the Baltic Sea alternate, at that each phase lasts ~ 20 years. The time trends for each phase are statistically significant at least at some points in the sea. The correlation between the North Atlantic Oscillation index and the annual average wave heights is statistically significant but not high. Such correlation can account for ~ 30–65% of the variations in wave characteristics.

Keywords: Baltic Sea, significant wave height, NAO index, time trend, statistical significance, correlation coefficient

Acknowledgments: The work was carried out within the framework of state assignment of IO RAS (theme FMWE-2024-0025).

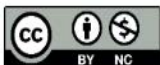
For citation: Sokolov, A.N. and Chubarenko, B.V., 2025. Long-Term Dynamics of the Annual Average Wave Heights in the Baltic Sea. *Physical Oceanography*, 32(2), pp. 197-210.

© 2025, A. N. Sokolov, B. V. Chubarenko

© 2025, Physical Oceanography

Introduction

It can be considered that visual wind and wave situation observations in the Baltic Sea with its written recording have been carried out onboard vessels and



in various parts of the coast since the early 19th century [1] when the well-known Beaufort scale for wind strength and wave height estimate appeared, later approved by the World Meteorological Organization¹. During visual observations, the attention is intuitively concentrated on relatively large waves with no regard for small ones, i.e. a certain general state of the sea is under estimation, not the height of individual waves [2, pp. 49–50]. Obviously, such estimates are quite subjective and far from being accurate. Instrumental measurements with precise recording of wave parameters began in the Baltic Sea only in the 1970s [3]. Modern wave recorders permit to determine both characteristics of individual waves passing through the point where the device is installed and statistical wave parameters, which can be correlated with the Beaufort scale.

One of the most important statistical characteristics of the waves is significant wave height (SWH), defined as the average height of one third of the highest waves recorded at a given point. This is the parameter that an experienced observer visually evaluates as the wave height. Later in the paper we will refer to significant wave heights and use the abbreviation SWH.

Many works have been devoted to the study of the Baltic Sea wave regime parameters [4]. However, most of them focus on the SWH spatial distribution. Temporal variability is analyzed in much fewer papers [1, 5–9].

The Baltic Sea wave regime parameters are related directly to global atmospheric circulation processes, in particular, to cyclonic activity. It is known [10, pp. 11–12] that the trajectories and intensity of atmospheric cyclones over the Atlantic and Europe are significantly affected by the North Atlantic Circulation (NAO). The typical state of the atmosphere over the North Atlantic is characterized by the Azores Maximum and the Iceland Minimum (in atmospheric pressure). If these extremes are clearly expressed (a large pressure difference is observed between them), a positive phase of the NAO takes place, otherwise – a negative one. For a quantitative estimate of the phenomenon, the NAO index is used. Its monthly average values from January 1950 to the present are published by the US Climate Prediction Center².

Works devoted to the analysis of the relationship between the North Atlantic Oscillation and wave heights in various water areas appeared in the 1990s. For example, in [11], the relationship between the SWH in the North Atlantic and the pressure gradient between the Azores Maximum and the Iceland Minimum in 1962–1988 is considered. The statistical relationship is noted both among

¹ WMO, 1970. *The Beaufort Scale of Wind Force (Technical and Operational Aspects): Report Submitted by the President of the Commission for Maritime Meteorology to the WMO Executive Committee at Its Twenty-Second Session*. Reports on Marine Science Affairs; No. 3. Geneva: WMO, 22 p.

² Near Real-Time Ocean. In: W. Shi, ed., 2025. *Atmosphere Monitoring, Assessments, and Prediction*. Climate Diagnostics Bulletin; February 2025. U.S. Department of Commerce, 87 p. [online] Available at: https://www.cpc.ncep.noaa.gov/products/CDB/CDB_Archive_pdf/CDB.monthly_color.pdf [Accessed: 25 March 2025].

the annual average and among the monthly average values of the quantities compared. Here, for the first time, an assumption that the North Atlantic Oscillation is primarily associated with the SWH interannual variability rather than long-term trends is made. This assumption for the North Atlantic and North Sea region is further developed in [12–14] and it is noted that the SWH annual average correlate better with the NAO indices averaged over the winter months (December – March) than the SWH monthly average and the monthly average NAO indices with each other.

Let us briefly touch on the works devoted to the study of the relationship between the North Atlantic Oscillation and wave heights in the Baltic Sea. In [7], based on the modeling data for 44 years (1958–2001), it is indicated that the relationship exists but no numerical values are given. In [5], a correlation (with a coefficient of 0.61) is noted between the annual average SWH off the Estonian coast for 1966–2006 and the NAO indices averaged over August–February period. At the same time, in [15], where the relationship between the annual average SWH off the coast of Poland for 1958–2002 and the annual average NAO indices as well as the monthly average SWH and the monthly average NAO indices is considered, the author concludes that although the relationship exists, it is quite weak.

In [16, 17], only storm events were considered. The relationship between annual average or monthly average SWH and NAO indices was not analyzed. The existence of a correlation at the 30–50% level between the number of storm events in the Baltic (with SWH > 2 m) and the NAO index was revealed.

Paper [18] analyzes the results of modeling the wave situation off the southern coast of Sweden for 62 years (1959–2021). It is noted that the interannual variability of the annual average energies and wave propagation directions is significantly correlated with the winter NAO indices (averaged for December – March). The statistical relationship is quantitatively measured by the Spearman correlation coefficient, which is 0.5–0.7 for different points in the coastal zone.

As can be seen from the brief review of published works, the existence of a correlation between the wave regime parameters in the Baltic and the NAO is beyond doubt but a number of questions remain open including the following: which of the NAO index averaging options shows the best correlation with the wave parameters and what is the degree of NAO influence on the wave parameters within the framework of interannual and multi-year variability.

In their previous works [8, 9], the authors considered the parameters of the Baltic Sea wave regime based on the results of numerical modeling for 1979–2018. Time trends in SWH changes in certain areas were identified and statistical significance of these trends was estimated. This paper is purposed at revealing the time periods since the mid-20th century when the annual average wave heights in the Baltic Sea tended to increase or decrease, assessing the statistical significance of potential time trends as well as analyzing the statistical relationship between annual average wave heights in the Baltic Sea and the North Atlantic Oscillation.

Materials and methods

Data used for the analysis. Let us consider the dynamics of wave heights in the Baltic Sea. Fig. 1 shows the location of the points and the time series of annual average SWH used for the analysis. The shades of gray reflect information about the spatial distribution of average SWH (for 1979–2018). The data on the time series of annual average SWH at points 1, 2 and 3 are taken from [1, 5, 6], at points 4–9 – results obtained by the authors. Below, the method for obtaining data for each of the points shown in Fig. 1 is considered in more detail.

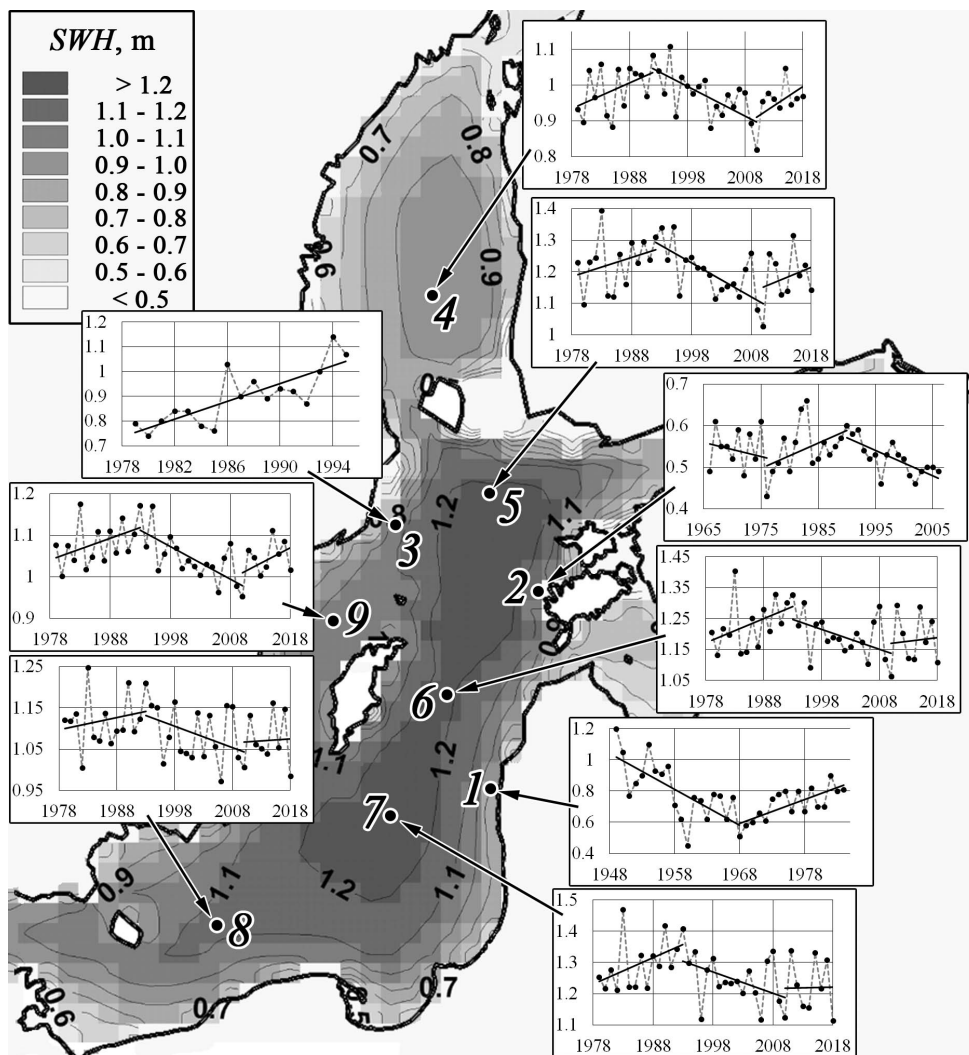


Fig. 1. Long-term dynamics of wave heights in the Baltic Sea. Color and isolines show the average SWH in the Baltic Sea based on numerical simulating data for 1979–2018 [8, 9]. White numerals highlight the points used in the study. Insets show the time series of annual average SWH for each point and the linear approximations for the areas that can be considered supposedly monotonic in visual analysis

Wave heights near the coast of Latvia in the Liepaja region (point 1 in Fig. 1) were estimated based on visual observations. Data on annual average SWH obtained using this method for 1949–1984 is presented in [6]. The time series in the inset for point 1 were constructed from these materials. The results given in [5] were used for the Estonian coast (point 2). The author of the study carried out calculations using a semi-empirical model based on the wave height dependence on the wave fetch. Data from the Vilsandi weather station located near the western end of Saaremaa Island were used to account for the wind effect. Annual average SWH calculations in this region (point 2) were carried out for the 1966–2006 period. Point 3 reflects the results of pioneering instrumental SWH measurements in the Baltic Sea at Almagrundet located several dozen kilometers from the Swedish coast. The results described in [1] cover the 1979–1995 period and form the basis for constructing a time series for point 3.

The time series for points 4–9 were obtained by the authors using the MIKE 21 SW spectral wave model³ for the 40-year period from 1979 to 2018. The unstructured computational grid covered the entire Baltic Sea. The side size of the triangular grid elements varied from 2–3 to 10–15 km. The model had no open boundaries. The time step during the calculations was adjusted by the model based on the stability condition but did not exceed 10 min. To take into account the wind effect, open ERA-Interim reanalysis data⁴ was used on a spatial grid of 1° in latitude and longitude with a time step of 6 hours. The model was calibrated and verified by comparing the calculation results with the data of wave buoys located in various parts of the Baltic Sea. Detailed information on the settings, calibration and verification of the model used for the calculations is given in [8, 9]. The choice of location of points 4–9 from the entire data set was due to the fact that they yielded the maximum significant wave heights for different Baltic Sea subregions according to model calculations for 1979–2018.

Analysis of temporal variability of annual average wave heights.

The analysis of the dynamics of annual average SWH was carried out by studying their time series at the aforementioned points of the Baltic Sea. Each of the considered time series was subjected to processing including three stages.

At the first stage, time intervals were visually identified when the dependence of annual average SWH on time could be conditionally considered linear. The linear functions approximating them are shown as straight line segments in the insets. Then, for each of the identified intervals, the slope of the linear approximating function (Sen's slope [19]) was determined using a non-parametric approach, and

³ *Spectral Wave Modelling. MIKE 21 Spectral Waves.* [online] Available at: <https://www.dhigroup.com/technologies/mikepoweredbydhi/mike-21-spectral-waves> [Accessed: 21 July 2024].

⁴ *ECMWF Reanalysis-Interim (ERA-Interim).* [online] Available at: <https://www.ecmwf.int/en/forecasts/datasets/reanalysis-datasets/era-interim> [Accessed: 12 July 2020].

the statistical significance of the potential time trend was estimated using the Mann-Kendall Test [20, 21]. Statistical analysis was performed in Excel using the Real Statistics add-in⁵ for statistical significance level $\alpha = 0.1$ (90% probability). At the last stage, statistical indicators for different spatial points were compared and conclusions about dynamics of annual average SWH in a particular time interval were made.

Estimate of relationship between annual average SWH and NAO index.

The correlation of the time series of annual average SWH with the time series of the NAO index was analyzed for all the points shown in Fig. 1. The NAO index values used in this paper represent normalized pressure difference between the Gibraltar and Reykjavik (Iceland) weather stations. They are calculated using the method from [22] and their monthly average values are available online in the open database of the US Climate Prediction Center⁶. These monthly average values were the initial data for the analysis of the relationship between NAO and wave height in the Baltic Sea.

In this study, both annual average NAO index values and its values averaged for various combinations of months from October to March were considered. Particular attention was paid to the cold months because winter processes of interaction between the ocean and the atmosphere have the greatest impact on the atmospheric circulation in the following months of the calendar year [23; 24; 10, p. 23]. For example, the most common averaging of the NAO index for winter months is abbreviated as JFM (January, February, March) which correlates well with various meteorological parameters [25, 26]. The works contain various options for averaging for October – March⁷ [27, 28].

The relationship was calculated using the Pearson and Spearman correlation coefficients (CC)⁸. In addition, the statistical significance of the calculated correlation coefficients was estimated for level $\alpha = 0.1$. Statistical analysis was carried out in Excel using the Real Statistics add-in⁵.

Results and discussion

Analysis of temporal variability of annual average SWH. Visual analysis (inserts in Fig. 1) shows that areas of decrease and increase in annual average SWH in the Baltic Sea alternate. From 1950 to the late 1960s – early 1970s, a decrease trend is

⁵ Zaiontz, C., 2023. *Real Statistics Resource Pack Software (Release 8.9.1)*. [online] Available at: <https://www.real-statistics.com> [Accessed: 20 July 2024].

⁶ National Weather Service. Climate Prediction Center. *North Atlantic Oscillation (NAO)*. [online] Available at: <https://www.cpc.ncep.noaa.gov/products/precip/CWlink/pna/nao.shtml> [Accessed: 20 March 2005].

⁷ North Atlantic Oscillation (NAO). *NAO data*. [online] Available at: <https://crudata.uea.ac.uk/cru/data/nao/values.htm> [Accessed: 28 July 2024].

⁸ Zarubin, V.S. and Krishchenko, A.P., eds., 2001. [*Mathematical Statistics*]. Moscow: Publishing House of Bauman Moscow State Technical University, 240 p. (in Russian).

observed. The rates of decrease range from 5 (point 2) to 23 (point 1) mm/year. This period is covered by very little data obtained mainly by visual observation. Therefore, the results are quite subjective and not very reliable.

Since the late 1960s – early 1970s, a tendency for annual average SWH to increase has been observed, which is confirmed by time series at all points. The rates of increase range from 6 (point 9) to 17 (point 3) mm/year. Significantly more data here were obtained by both visual and more objective methods – using instrumental measurements and mathematical modeling.

From the early 1990s until approximately 2010, a decrease trend in annual average SWH was observed again. This conclusion is based on both calculations of the authors (points 4–9) and the modeling results [5] for point 2. The rates of decrease vary from 4 mm/year for point 8 to 13 mm/year for point 5. Presumably, an increase phase began again in 2010 but since the period covered by the data is limited to 2018, it is incorrect to draw conclusions about the increase rates as the period is too short for the analysis.

Table 1

Rate of annual average SWH change for the periods when the time trends can be considered statistically significant at level $\alpha = 0.1$ (90% probability)

Point	Period	Trend is significant at $\alpha = 0.1$	Trend value, mm/year
1	1949–1968	yes	–23.0
	1968–1985	yes	15.0
2	1966–1976	no	–
	1976–1990	yes	7.5
	1990–2006	yes	–6.0
3	1979–1995	yes	17.0
	1979–1992	no	–
4	1992–2010	yes	–8.6
	2010–2018	no	–
	1979–1992	yes	6.9
5	1992–2010	yes	–13.0
	2010–2018	no	–
	1979–1993	yes	8.8
6	1993–2010	yes	–9.5
	2010–2018	no	–
	1979–1993	yes	9.0
7	1993–2010	yes	–8.3
	2010–2018	no	–
	1979–1993	no	–
8	1993–2010	yes	–4.2
	2010–2018	no	–
	1979–1993	yes	5.9
9	1993–2010	yes	–7.6
	2010–2018	no	–

To sum up, it can be assumed that the increase and decrease phases of annual average SWH in the Baltic have a duration of ~ 20 years: from 1950 to 1970 – decrease, from 1970 to 1990 – increase, from 1990 to 2010 – decrease. The rates of annual average SWH change vary spatially and can be ~ 5–20 mm/year.

In addition to calculating the rates of annual average SWH change, statistical significance of time trends was estimated for each of the time intervals under consideration. Calculations were carried out for level $\alpha = 0.1$. The statistical significance of a potential time trend was estimated using the non-parametric Mann–Kendall method [20, 21] and the trend value was estimated using Sen’s slope formula [19]. Table 1 shows the calculation results.

The period up to the mid-1970s is presented in Table 1 only by points 1 (the Baltic coast near Liepaja, visual observations) and 2 (the western end of Saaremaa Island; a model based on the wave fetch). It is evident that for the period of SWH decrease from 1950 to the early to mid-1970s, the trend at point 1 is statistically significant, while at point 2 it is not. The absence of statistical significance at point 2 is explained, first of all, by the very short time period covered by the data (10 years of potential decrease in 1966–1976). For the increase period from the 1970s to the 1990s, data at all the points under consideration are available. The trend is statistically significant almost everywhere. The exceptions are points 4 (the Bothnian Sea) and 8 (the Bornholm Basin). Since the early 1990s, a decrease trend in SWH is observed again. It is statistically significant at all data points (all points except 1 and 3). For the period after 2010, a weak increase trend in SWH is observed and the trends are not statistically significant due to the short time interval covered by the data (8 years until 2018).

Estimate of relationship between annual average SWH and NAO index.

To estimate the relationship, the correlation coefficients between the time series of annual average SWH and NAO indices averaged over different time intervals were calculated. The time series were not divided into segments of conditional monotonicity as in the trend analysis but the entire time series available at the point was taken as a whole. Table 2 presents the correlation analysis results. Statistical reliability of the given CCs is different: for minimal values of CCs, the p-value does not exceed 0.1 (i.e. probability of the statistical relationship existence is over 90%), for relatively high CCs (~ 0.5 and more), the p-value is 0.001 or less (99.9% probability).

For each of the time series, Table 2 shows at least one variant of averaging the NAO indices, in which the relationship with the annual average SWH is statistically significant at level $\alpha = 0.1$. The highest CC values (0.3–0.6) are highlighted in bold. Most often (in all cases except point 2), the highest CC values correspond to the NAO index averaging period from January to March (JFM). This

result coincides with the practice of using this averaging interval in scientific research. For example, on the US Climate Prediction Center website, this type of averaging, like no other, is the subject of a separate page ⁹.

Table 2

Pearson and Spearman correlation coefficients statistically significant at level $\alpha = 0.1$ (90% probability)

Point	Period	CC	Y	JFM	ONDJFM	DJFM	NDJFM
1	1949–1976	Pearson (P.)	–	0.31	–	–	–
		Spearman (S.)	–	0.29	–	–	–
2	1966–2006	P.	0.29	–	0.29	0.29	–
		S.	0.33	–	0.32	0.34	–
3	1979–1995	P.	–	0.56	–	–	–
		S.	–	0.58	0.48	–	0.47
4	1979–2018	P.	0.41	0.60	0.31	–	–
		S.	0.33	0.53	–	–	–
5	1979–2018	P.	0.40	0.60	0.41	0.32	0.34
		S.	0.40	0.51	0.37	0.31	0.30
6	1979–2018	P.	0.32	0.54	0.33	–	–
		S.	0.35	0.49	0.29	–	–
7	1979–2018	P.	0.29	0.51	0.29	–	–
		S.	0.34	0.47	–	–	–
8	1979–2018	P.	–	0.40	–	–	–
		S.	–	0.39	–	–	–
9	1979–2018	P.	0.34	0.53	0.37	0.28	0.28
		S.	0.35	0.47	0.37	0.30	0.27

Note. The Y column indicates the CCs between the annual average SWH and the annual average NAO indices. The remaining columns contain the CC values between the annual average SWH and the NAO indices averaged for different combinations of cold months of a year: O – October, N – November, D – December, J – January, F – February, M – March.

Thus, the calculations showed that the interannual variations of NAO and annual average SWH were in a statistically significant correlation. The second important thing was to find out which statistical relationship was more significant – for annual data or data with long time averaging. For this purpose, the CCs between the moving five-year averages of NAO indices and annual average SWH were additionally calculated. The calculations were carried out at all points for those cases of averaging for NAO indices that yielded the highest CC values when analyzing interannual variability. Table 3 demonstrates the results of the comparison of the correlation relationship.

⁹ National Weather Service. Climate Prediction Center. *Monitoring Weather & Climate*. [online] Available at: https://www.cpc.ncep.noaa.gov/products/precip/CWlink/pna/JFM_season_ao_index.shtml [Accessed: 20 March 2005].

Table 3

Pearson and Spearman correlation coefficients between the NAO index annual values and the SWH annual average values as well as between their five-year moving averages

Point	Period	CC	Annual values	Five-year averages
1	1949–1976	Pearson (P.)	0.31	0.22
	(JFM)	Spearman (S.)	0.29	0.38
2	1966–2006	P.	0.29	0.36
	(DJFM)	S.	0.34	0.41
3	1979–1995	P.	0.56	0.71
	(JFM)	S.	0.58	0.72
4	1979–2018	P.	0.60	0.83
	(JFM)	S.	0.53	0.82
5	1979–2018	P.	0.60	0.76
	(JFM)	S.	0.51	0.73
6	1979–2018	P.	0.54	0.65
	(JFM)	S.	0.49	0.58
7	1979–2018	P.	0.51	0.58
	(JFM)	S.	0.47	0.51
8	1979–2018	P.	0.40	0.54
	(JFM)	S.	0.39	0.50
9	1979–2018	P.	0.53	0.73
	(JFM)	S.	0.47	0.71

Note. The Period column specifies the option used for averaging the NAO index.

Table 3 shows that in all cases except for the Pearson CC for point 1, the CC for five-year averages is greater than for annual data, i.e. interannual SWH variations are statistically less significantly related to similar variations in NAO than longer-term ones. As for the spatial distribution, it is noteworthy that the CC for the offshore points is higher than the CC for the points near the coast. In addition, the SWH relationship with the North Atlantic Oscillation appears to increase from south to north: the highest CCs are calculated for points 3, 4, 5 and 9, with the strongest relationship for the northernmost point 4 in the Bothnian Sea.

Fig. 2 shows the SWH and NAO relationship by years as well as the effect of five-year averaging on the CC. Points 4 and 9 were chosen because the difference between the annual and five-year CCs is maximum for them – 0.2 or higher.

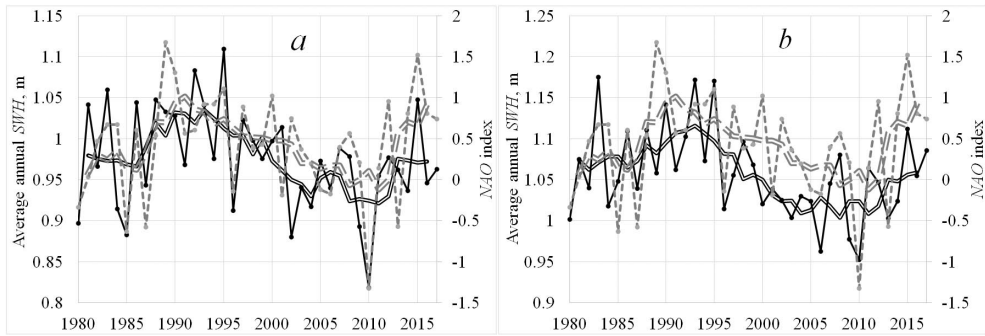


Fig. 2. Annual average SWH and NAO index averaged from January to March (JFM) for 1980–2017 at points 4 (*a*) and 9 (*b*). SWH: annual average values are indicated by a thin solid line, and five-year moving average – by a double solid line; NAO index (JFM): annual value is indicated by a dashed line, and five-year moving average – by a double dashed line

It can be seen from Fig. 2 that the fluctuations in the annual average SWH repeat the fluctuations in the annual NAO indices to a significant extent, which is confirmed by fairly high CCs for their interannual variations. Comparing the moving averages, it is easy to see that up to the early 1990s, an increase in both NAO indices and annual average SWH was observed. From the early 1990s until approximately 2010, a decrease in both annual average SWH and NAO indices took place. Finally, after 2010, both parameters have increase trends. Analyzing the results given in Fig. 2 and Table 3, it can be concluded that the NAO indices and the annual average SWH correlate both within the interannual variability and over longer time intervals.

Taking into account the determination coefficient (square of the correlation coefficient magnitude), showing in general terms what part of the analyzed variable (wave characteristic) variability can be explained using a regression model of its dependence on the NAO factor, it can be concluded that in the present case, the NAO influence can explain ~30–65% of the variability of wave characteristics both within the framework of interannual dynamics and over longer time periods.

The authors of this paper do not attempt to explain the mechanism of the NAO impact on wave height in the Baltic Sea physically. The paper estimates the relationship and, most importantly, evaluates its statistical significance, which allows, based on these evaluations, discussing possible mechanisms of the relationship (or declaring their insignificance).

Conclusion

1. The trends of increasing and decreasing annual average SWH in the Baltic Sea alternate. The duration of each of the conditional monotony phases is ~20 years. During the period from the mid-20th century to the 2020s, the trends changed three times.

2. The observed trends are statistically significant at level $\alpha = 0.1$ (90% probability) at least at some points in the sea. The rates of annual average SWH

change are small and can be 5–20 mm/year depending on the spatial position of the points.

3. The correlation between the NAO index and annual average wave heights is statistically significant at a level of at least 90% probability, but not high. This influence can explain ~ 30–65% of the change in wave characteristics both within the framework of interannual variability and over longer time periods.

4. The preferred averaging option for the NAO index, providing the highest correlation with annual average SWH, is in most cases the January to March (JFM) averaging.

REFERENCES

1. Broman, B., Hammarklint, T., Rannat, K., Soomere, T. and Valdmann, A., 2006. Trends and Extremes of Wave Fields in the North-Eastern Part of the Baltic Proper. *Oceanologia*, 48(S), pp. 165-184.
2. Nesterov, E.S., ed., 2013. *Regime, Diagnosis and Forecast of Wind Waves in the Oceans and Seas*. Moscow: Hydrometeorological Research Center of Russian Federation, 292 p. (in Russian).
3. Tuomi, L., Kahma, K.K. and Pettersson, H., 2011. Wave Hindcast Statistics in the Seasonally Ice-Covered Baltic Sea. *Boreal Environment Research*, 16(6), pp. 451-472.
4. Soomere, T., 2023. Numerical Simulations of Wave Climate in the Baltic Sea: A Review. *Oceanologia*, 65(1), pp. 117-140. <https://doi.org/10.1016/j.oceano.2022.01.004>
5. Suursaar, Ü. and Kullas, T., 2009. Decadal Variations in Wave Heights near The Cape Kelba, Saaremaa Island, and Their Relationships with Changes in Wind Climate. *Oceanologia*, 51(1), pp. 39-61. <https://doi.org/10.5697/oc.51-1.039>
6. Soomere, T., 2013. Extending the Observed Baltic Sea Wave Climate back to the 1940s. *Journal of Coastal Research*, 65(sp. 2), pp. 1969-1974. <https://doi.org/10.2112/SI65-333.1>
7. Cieřlikiewicz, W., Papińska-Swerpel, B. and Soares, C.G., 2005. Multi-Decadal Wind Wave Modelling over the Baltic Sea. In: National Civil Engineering Laboratory, 2005. *Coastal Engineering 2004: Proceedings of the 29th International Conference*. Lisbon, Portugal: World Scientific Publishing Company, pp. 778-790. https://doi.org/10.1142/9789812701916_0062
8. Sokolov, A.N. and Chubarenko, B.V., 2020. Temporal Variability of the Wind Wave Parameters in the Baltic Sea in 1979–2018 Based on the Numerical Modeling Results. *Physical Oceanography*, 27(4), pp. 352-363. <https://doi.org/10.22449/1573-160X-2020-4-352-363>
9. Sokolov, A. and Chubarenko, B., 2024. Baltic Sea Wave Climate in 1979–2018: Numerical Modelling Results. *Ocean Engineering*, 297, 117088. <https://doi.org/10.1016/j.oceaneng.2024.117088>
10. Nesterov, E.S., 2013. [*The North Atlantic Oscillation: Atmosphere and Ocean*]. Moscow: Triada Ltd, 127 p. (in Russian).
11. Bacon, S. and Carter, D.J.T., 1993. A Connection between Mean Wave Height and Atmospheric Pressure Gradient in the North Atlantic. *International Journal of Climatology*, 13(4), pp. 423-436. <https://doi.org/10.1002/joc.3370130406>
12. Bauer, E., 2001. Interannual Changes of the Ocean Wave Variability in the North Atlantic and in the North Sea. *Climate Research*, 18(1-2), pp. 63-69. <https://doi.org/10.3354/cr018063>
13. Woolf, D.K., Challenor, P.G. and Cotton, P.D., 2002. Variability and Predictability of the North Atlantic Wave Climate. *Journal of Geophysical Research: Oceans*, 107(C10), 3145. <https://doi.org/10.1029/2001JC001124>

14. Dodet, G., Bertin, X. and Taborda, R., 2010. Wave Climate Variability in the North-East Atlantic Ocean over the Last Six Decades. *Ocean Modelling*, 31(3-4), pp. 120-131. <https://doi.org/10.1016/j.ocemod.2009.10.010>
15. Różyński, G., 2010. Long-Term Evolution of Baltic Sea Wave Climate near a Coastal Segment in Poland; Its Drivers and Impacts. *Ocean Engineering*, 37(2-3), pp. 186-199. <https://doi.org/10.1016/j.oceaneng.2009.11.008>
16. Surkova, G.V., Arkhipkin, V.S. and Kislov, A.V., 2015. Atmospheric Circulation and Storm Events in the Baltic Sea. *Open Geosciences*, 7(1), 20150030. <https://doi.org/10.1515/geo-2015-0030>
17. Myslenkov, S., Medvedeva, A., Arkhipkin, V., Markina, M., Surkova, G., Krylov, A., Dobrolyubov, S., Zilitinkevich, S. and Koltermann, P., 2018. Long-Term Statistics of Storms in the Baltic, Barents and White Seas and Their Future Climate Projections. *Geography, Environment, Sustainability*, 11(1), pp. 93-112. <https://doi.org/10.24057/2071-9388-2018-11-1-93-112>
18. Adell, A., Almström, B., Kroon, A., Larson, M., Uvo, C.B. and Hallin, C., 2023. Spatial and Temporal Wave Climate Variability along the South Coast of Sweden during 1959–2021. *Regional Studies in Marine Science*, 63, 103011. <https://doi.org/10.1016/j.rsma.2023.103011>
19. Sen, P.K., 1968. Estimates of the Regression Coefficient Based on Kendall's Tau. *Journal of the American Statistical Association*, 63(324), pp. 1379-1389. <https://doi.org/10.1080/01621459.1968.10480934>
20. Mann, H.B., 1945. Nonparametric Tests against Trend. *Econometrica*, 13(3), pp. 245-259. <https://doi.org/10.2307/1907187>
21. Kendall, M.G., 1975. *Rank Correlation Methods*. London: Charles Griffin, 202 p.
22. Jones, P.D., Jonsson, T. and Wheeler, D., 1997. Extension to the North Atlantic Oscillation Using Early Instrumental Pressure Observations from Gibraltar and South-West Iceland. *International Journal of Climatology*, 17(13), pp. 1433-1450. [https://doi.org/10.1002/\(SICI\)1097-0088\(19971115\)17:13%3C1433::AID-JOC203%3E3.0.CO;2-P](https://doi.org/10.1002/(SICI)1097-0088(19971115)17:13%3C1433::AID-JOC203%3E3.0.CO;2-P)
23. Hurrell, J.W., 1995. Decadal Trends in the North Atlantic Oscillation: Regional Temperatures and Precipitation. *Science*, 269(5224), pp. 676-679. <https://doi.org/10.1126/science.269.5224.676>
24. Rodwell, M.J., Rowell, D.P. and Folland, C.K., 1999. Oceanic Forcing of the Wintertime North Atlantic Oscillation and European Climate. *Nature*, 398, pp. 320-323. <https://doi.org/10.1038/18648>
25. Post, E. and Stenseth, N.C., 1999. Climatic Variability, Plant Phenology, and Northern Ungulates. *Ecology*, 80(4), pp. 1322-1339. [https://doi.org/10.1890/0012-9658\(1999\)080\[1322:CVPPAN\]2.0.CO;2](https://doi.org/10.1890/0012-9658(1999)080[1322:CVPPAN]2.0.CO;2)
26. D'Odorico, P., Yoo, J.C. and Jaeger, S., 2002. Changing Seasons: An Effect of the North Atlantic Oscillation. *Journal of Climate*, 15(4), pp. 435-445. [https://doi.org/10.1175/1520-0442\(2002\)015<0435:CSAEOT>2.0.CO;2](https://doi.org/10.1175/1520-0442(2002)015<0435:CSAEOT>2.0.CO;2)
27. Kolstad, E.W. and O'Reilly, C.H., 2024. Causal Oceanic Feedbacks onto the Winter NAO. *Climate Dynamics*, 62(5), pp. 4223-4236. <https://doi.org/10.1007/s00382-024-07128-y>
28. Zhang, W. and Jiang, F., 2023. Subseasonal Variation in the Winter ENSO-NAO Relationship and the Modulation of Tropical North Atlantic SST Variability. *Climate*, 11(2), 47. <https://doi.org/10.3390/cli11020047>

About the authors:

Andrei N. Sokolov, Senior Researcher, Shirshov Institute of Oceanology of RAS, Atlantic Branch (1 Mira Ave., Kaliningrad, 236022, Russian Federation); Assistant Professor, Immanuel Kant Baltic Federal University (14 Nevskogo Str., Kaliningrad, 236016, Russian Federation), CSc (Techn.),

Assistant Professor, **ResearcherID: B-4523-2017**, **Scopus Author ID: 56998131000**, **ORCID ID: 0000-0002-7593-9739**, **SPIN-code: 2884-6132**, tengritag@gmail.com

Boris V. Chubarenko, Head of Laboratory, Leading Researcher, Shirshov Institute of Oceanology of RAS, Atlantic Branch (1 Mira Ave., Kaliningrad, 236022, Russian Federation), CSc (Phys.-Math.), **ResearcherID: I-6118-2016**, **Scopus Author ID: 6507102508**, **ORCID ID: 0000-0001-7988-1717**, **SPIN-code: 2691-5872**, chuboris@mail.ru

Contribution of the co-authors:

Andrei N. Sokolov – research idea, data preparation, calculations, analysis and visualization of results, preparation of the paper text

Boris V. Chubarenko – participation in the analysis and interpretation of results, revision of the paper text

The authors have read and approved the final manuscript.

The authors declare that they have no conflict of interest.

Original article

Modeling of the Major Baltic Inflow Using a Joint Model of the North and Baltic Seas

N. A. Tikhonova^{1, 2} ✉, E. A. Zakharchuk¹, M. V. Vinogradov^{1, 2},
V. S. Travkin^{1, 2}

¹ Saint Petersburg State University, Saint Petersburg, Russian Federation

² N.N. Zubov's State Oceanographic Institute, Roshydromet, Moscow, Russian Federation

✉ nata-tik@yandex.ru

Abstract

Purpose. The purpose of the work consists in studying the structure and flow routes of the transformed North Sea waters in the Baltic Sea during the formation and spread of the Major Baltic inflow in December 2014 using numerical modeling.

Methods and Results. To achieve the stated aim, a three-dimensional baroclinic hydrodynamic model of the North and Baltic seas with a spherical grid area detailed in the Danish straits has been developed based on the INMOM model. Within the framework of the performed numerical experiment, the oceanological characteristic fields were assessed in the system of two seas for the period from 1 January 2014 to 31 December 2015. Comparison of the model-derived salinity and sea current characteristic values with those measured at the Darss Sill and Arkona stations as well as with the BSPAF regional reanalysis data has shown that in general, the INMOM model reproduces changes both in salinity and characteristics of the average currents better than the reanalysis data. The features of vertical variability of salinity and sea currents in the Danish straits during the Major Baltic inflow formation are described based on the modeling results. The daily average and total volumes of water transported in the Sound, Great Belt and Little Belt straits during the main period of the Major inflow are estimated. The features of distribution of the near-bottom salinity fields during different periods of its formation are described. The Lagrangian modeling made it possible to describe the ways in which the waters of the Major Baltic inflow spread.

Conclusions. The estimates of water exchange obtained due to the INMOM model indicate that during the main period of the Major Baltic inflow (December 2014), a total of 241.4 km³ of the Kattegat waters passed through the Danish straits. The inflow largest part, 170.9 km³, spread through the Great Belt Strait, while only 68.9 km³ passed through the Sound Strait. The effect of the Small Belt Strait on water transport during the Major Baltic inflow was very insignificant – only 1.6 km³. The study of distribution routes of the transformed North Sea waters over the Baltic Sea after the end of the Major Baltic inflow shows that having passed the Danish straits, its waters spread in a wide flow to the Southwestern Baltic, then penetrate to the Gulf of Gdansk, move further along a cyclonic trajectory through the deep-sea areas of the eastern and northern parts of the Gotland Basin without entering the Gulf of Finland and reach the Landsort Deep in the western part of the Gotland basin by the end of December 2015.

Keywords: hydrodynamic modeling, INMOM, Baltic Sea, North Sea, Danish straits, Major Baltic inflow, salinity of the Baltic Sea, currents of the Baltic Sea, regional reanalysis of hydrophysical fields, water exchange, water salinity, sea level, stratification of waters, Lagrangian modeling

Acknowledgements: The study was carried out at financial support of the RSF grant No. 24-27-00412 “Clarifying the mechanisms of generation and non-stationarity of the Major Baltic inflows” <https://rscf.ru/project/24-27-00412/>.



For citation: Tikhonova, N.A., Zakharchuk, E.A., Vinogradov, M.V. and Travkin, V.S., 2025. Modeling of the Major Baltic Inflow Using a Joint Model of the North and Baltic Seas. *Physical Oceanography*, 32(2), pp. 211-237.

© 2025, N. A. Tikhonova, E. A. Zakharchuk, M. V. Vinogradov, V. S. Travkin

© 2025, Physical Oceanography

Introduction

Major Baltic inflows (MBIs) represent the irregular introduction of extremely large volumes of the North Sea waters, from 90 to 258 km³, into the Baltic Sea, lasting 6–29 days, which penetrate into the deep-water areas of the Baltic Proper (Fig. 1), exerting a beneficial effect on the ecological state of this sea [1–7]. Weak inflows of the North Sea waters of 10–20 km³ in volume appear constantly but the penetration of these waters into the Baltic is most often limited to the Arkona Basin (Fig. 1). MBIs are a relatively rare phenomenon observed until the early 1980s from 1–2 times a year to once every few years [4]. Spreading far into the open part of the Baltic Sea, highly saline and oxygen-rich waters of large inflows renew the bottom and deep-water Baltic masses exposed to hypoxic conditions¹ [2, 4, 8]. Observations show that after 1983, the number of MBIs decreased significantly and the interval (stagnation period [8]) between them increased greatly and amounted to 10–11 years [4, 6, 7–9]. Physical mechanisms for the increase in stagnation periods remain unexplored to date. The last major inflow occurred in December 2014 [5], after which no new MBIs have been described in the scientific literature.

MBIs can be considered as an extreme water exchange component between the North and Baltic seas. For example, according to K. Wyrтки [10] and H. Fischer and W. Matthäus [3], about 200–225 km³ of the Kattegat waters passed through the Danish straits during the MBI in November – December 1951, which amounted to approximately 40% of the annual norm.

The accumulated information on the variability of hydrometeorological processes during MBI allowed scientists to identify four periods in the process of its formation: outflow period, precursory period, main inflow period and post inflow period [4, 5, 8].

The outflow period starts when eastern winds blow over Northwestern Europe, which contributes to the water outflow from the Baltic into the North Sea and its level decrease. This period is very important for the future formation of MBIs since the longer and more intense the water outflow from the Baltic is, the more its level will decrease and the greater the level gradient between the Kattegat and the Southwestern Baltic will form before the beginning of MBIs. The intensity of MBIs depends largely on this gradient [4, 5, 8].

¹ Antonov, A.E., 1987. [*Large-Scale Variability of Hydrometeorological Regime of the Baltic Sea and Its Impact on Fishing*]. Leningrad: Gidrometeoizdat, 247 p. (in Russian).

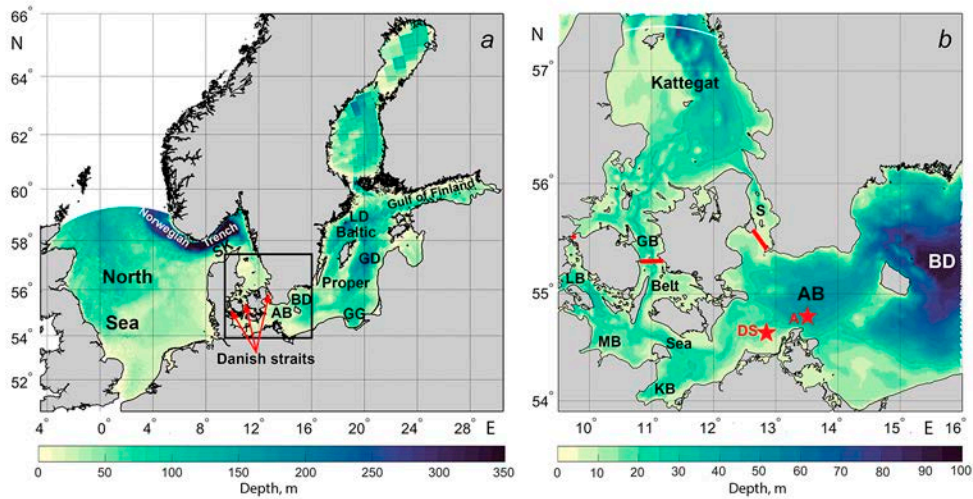


Fig. 1. Bathymetry of the North and Baltic seas (black square indicates the area of the Southwestern Baltic and the Kattegat) (a), enlarged image of the selected area (b). Designations: asterisks show location of the Darss Sill (DS) and Arkona (A) automatic stations; AB is the Arkona Basin, BD is the Bornholm Deep, GD is the Gotland Deep, LD is the Landsort Deep, LB is the Little Belt Strait, GB is the Great Belt Strait; S is the Sound Strait, SK is the Skagerrak, MB is Mecklenburg Bay, KB is Kiel Bay, GG is the Gulf of Gdansk

In the precursory period, the synoptic situation changes: the east wind weakens and begins to change its direction to the west one. This leads to the sea level elevation in the Kattegat, gradually approaching the level in the Southwestern Baltic [4, 5, 9].

The main inflow period occurs when the North Sea level elevation, which began in the previous period, reaches a critical value, at which the level gradient becomes directed from the Kattegat to the Southwestern Baltic and continues to grow under the influence of strong west winds, the duration of which reaches 2–3 weeks. At this time, the difference in level between the Kattegat Strait and the Southwestern Baltic (Fig. 1, b) can reach 1.0–1.7 m [11]. As a result, large masses of the highly saline and oxygen-rich Kattegat waters enter the Baltic Sea, which, in turn, leads to a further decrease in the North Sea level and an increase in the Baltic Sea [4, 5, 8].

The post inflow period begins when the west winds weaken and the North Sea waters cease to accumulate in the Danish straits. Since the Baltic Sea level is elevated relative to the North Sea level, the water outflow from the Baltic Sea begins and its level drops to a level close to its average value [4, 7, 8].

Mathematical modeling of water exchange and oceanographic conditions in the North and Baltic Seas is a complex task for two main reasons. Firstly, the oceanographic regimes of these seas are very different. The North Sea is a shallow (except for the Norwegian Trench) (Fig. 1, a), weakly stratified marine basin with intense tidal dynamics and vertical mixing, relatively freely

communicating with the ocean, so its salinity is close to oceanic. On the contrary, the Baltic Sea is an almost completely closed brackish marine basin with very weak tidal dynamics and sharp stratification, limiting vertical mixing between surface and deep-water masses. Secondly, due to the narrowness and shallowness of the Danish straits connecting the North and Baltic Seas (the Sound, the Great Belt and the Little Belt) (Fig. 1, *b*), which have a complex morphometry of the coastline and bottom topography. The minimum width of the Sound is less than 5 km and its smallest depth is 8 m; for the Great Belt Strait, these parameters are 3.7 km and more than 20 m; for the Little Belt Strait, they are 0.8 km and 12 m, respectively [8, 12, 13].

Such characteristics of the Danish straits require the use of a grid domain with cells of significantly smaller dimensions than the smallest width of the straits in numerical modeling for correct water flow simulation in these straits as well as the features of stratification and current structure. Processing power of modern computers does not make it possible to use uniform grids with such a high spatial resolution for modeling not only the combined water area of the North and Baltic seas, but also the Baltic Sea alone. To solve this problem, scientists expanded the Danish straits artificially when modeling the oceanographic conditions of the Baltic Sea, adjusting their width to the spatial resolution of the grid domain used in the model [14–16]. Such a procedure, with an unchanged depth, led to a change in the cross-sectional area of the straits. Therefore, the depth of the straits was reduced to maintain the cross-sectional area. Both changes in the morphometry of the straits lead to changes in stratification, current structure and salt transport volume in the Danish straits [12].

An important length scale that should be taken into account when modeling oceanographic fields for correct resolution of mesoscale eddies, upwellings [17] and structure of narrow jets caused by the dynamics of gravity currents in the Southwestern Baltic [18, 19] is the baroclinic Rossby radius of deformation. According to estimates by various researchers, its largest values (7–9 km) were observed in the Bornholm Basin and deep-water areas of the Baltic Proper, with the smallest (1–2 km) ones in the sea shallow areas with depths less than 50 m [20–23]. In this regard, models with nested grids have been used to improve the spatial resolution in numerical experiments. For example, in [12], the model domain with a nested uniform grid had a spatial resolution of 900 m and included the waters of the Kattegat, the Danish straits and the Arkona and Bornholm basins of the Baltic (Fig. 1, *b*). One of the liquid boundaries of the model was located in the north of the Kattegat and the other one – in the east of the Bornholm Basin [12]. However, such models do not allow studying the propagation routes of the MBI waters in other Baltic Sea areas.

In our opinion, models with unstructured grids with the highest condensation (detailing) in the area of the Danish straits are more promising for the MBI studying, which allows for a more accurate description of the structure of currents, stratification of water masses and salt transport through narrow and shallow straits. In [24], a joint model of the North and Baltic Seas with a mixed triangular-

quadrangular unstructured grid was used, which made it possible to achieve a nominal spatial resolution of 200 m in the Danish straits. Comparison of the modeling results with data from tide gauge measurements of sea level and measurements of temperature and salinity at the Fehmarn Belt and Arkona stationary stations showed good agreement overall, although in some areas of the compared series, the discrepancies between the measured and calculated values reached 30–50 cm for sea level, 3–5°C for temperature and 2–3‰ for salinity [24].

The main purpose of the paper is to estimate the capabilities of numerical hydrodynamic modeling of MBIs using a 3D baroclinic model of the North and Baltic Seas, which has a spherical grid area with detailing in the Danish straits, and, based on the modeling results, to study the structure and propagation routes of the transformed North Sea water flows in the Baltic Sea after the MBI in December 2014.

Data and methods

Model description

The Institute Numerical Mathematics Ocean Model (INMOM) of ocean and sea circulation developed at Marchuk Institute of Numerical Mathematics of RAS [25, 26] was chosen as the basic model to describe oceanological processes in the Baltic and North Sea systems during the 2014 MBI.

The INMOM is based on a complete system of nonlinear primitive equations of ocean hydrodynamics in spherical coordinates in the hydrostatic and Boussinesq approximations. Dimensionless quantity $\sigma = (z - \zeta)/(H - \zeta)$ is used as a vertical coordinate, where z is usual vertical coordinate; $\zeta = \zeta(\lambda, \varphi, t)$ is deviation of the sea level from the undisturbed surface as a function of longitude λ , latitude φ and time t ; $H = H(\lambda, \varphi)$ is sea depth. The number of vertical sigma layers in the model is 20.

The predictive variables of the model are horizontal components of the velocity vector, potential temperature, salinity and ocean level deviation from the undisturbed surface. To calculate the density, a specially designed for numerical models [27] equation of state that takes into account the compressibility of seawater is used.

The coefficients of vertical turbulent diffusion and viscosity were selected according to the Pacanowski – Philander parameterization [28]. The coefficient of turbulent diffusion varied from 1 to 50 cm²/s and the coefficient of turbulent viscosity varied from 1 to 250 cm²/s. Horizontal turbulent diffusion and viscosity were described by the usual Laplacian with coefficients $\nu = (3-8) \cdot 10^4$ cm²/s. Bottom friction was specified by a quadratic equation with coefficient $C_D = 2.5 \cdot 10^{-4}$.

The model includes a sea ice thermodynamics block [29] consisting of three modules. The thermodynamics module describes freezing, ice melting and snowfall. The ice dynamics module calculates its drift ² velocities. The ice transport module is used to calculate the ice and snow cover evolution due to the drift [30].

² Briegleb, B.P., Bitz, C., Hunke, E., Lipscomb, W., Holland, M.M., Schramm, J. and Moritz, R., 2004. *Scientific Description of the Sea Ice Component in the Community Climate System Model, Version 3*. NCAR/TN-463+STR. Boulder, Colorado: National Center for Atmospheric Research, 70 p. <https://doi.org/10.5065/D6HH6H1P>

The model uses a spherical grid with two poles, one of which is located on the Jutland Peninsula (Denmark) and the other – in the very south of Sweden (Fig. 2). The spatial resolution of the grid area nodes in the area of the Danish straits is about 300–700 m and increases proportionally to 6–12 km with distance from the straits towards the outskirts of two seas.

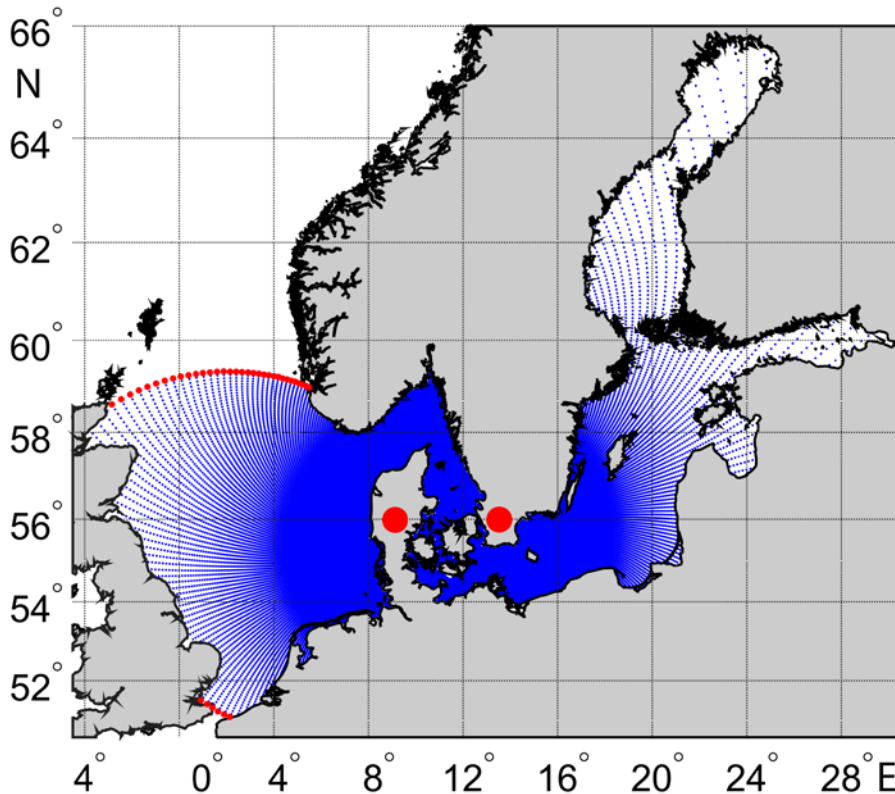


Fig. 2. Grid area of the model. Red dots indicate model liquid boundaries, black circles – grid area poles

For this model version, bathymetry from GEBCO 2015³ was combined. When preparing the model bathymetry, depth values were interpolated into grid nodes and smoothed with a Gaussian filter to eliminate their sharp differences, which increases significantly the stability of calculations during modeling.

Initial and boundary conditions

The initial conditions were monthly average water temperature and salinity data for January 2014 with a vertical resolution of 5 m and a spatial resolution

³ GEBCO. *General Bathymetric Chart of the Oceans*. [online] Available at: <https://gebco.net/> [Accessed: 24 March 2025].

of 4.5×9 km from the GLORYS12V1 ocean reanalysis⁴ (available at: <http://marine.copernicus.eu>).

For the boundary conditions on the sea surface in the INMOM atmospheric module, such meteorological characteristics as air temperature and humidity at a height of 2 m, pressure at sea level, wind speed at a level of 10 m, incident shortwave and longwave radiation, atmospheric precipitation were specified with a discreteness of 3 hours, a spatial step of 0.25° and duration from January 2014 to December 2015 obtained from the ERA5 reanalysis⁵.

At the liquid boundaries of the North Sea (Fig. 2), the average monthly values of water temperature and salinity observed from January 2014 to December 2015 as well as the amplitudes and phases of the oscillations of the level and currents of eight main tidal harmonics (M2, S2, N2, K2, K1, O1, P1, M4) taken from TPXO9 global tidal model (available at: <https://www.tpxo.net/global>) were specified.

On the solid sections of the lateral boundary, the heat and salt fluxes were set equal to zero and the no flow and free sliding conditions were used for the current velocity.

Model calculations were carried out from 1 January 2014 to 31 December 2015, with the average results being derived for each hour.

Verification of the model and comparison of the modeling results with the data of regional reanalysis of hydrophysical fields

To verify the model, we used the data from contact measurements of salinity and currents at different horizons of stationary automatic stations Darss Sill and Arkona located in the Southwestern Baltic at 21 and 45 m depths, respectively (Fig. 1, *b*). Observations of salinity at the Darss Sill station are made at 2, 5, 7, 12, 17 and 19 m horizons and at the Arkona station – 2, 5, 7, 16, 25, 33, 40 and 43 m. Current velocity and direction are measured with Doppler acoustic profilers at these stations.

The INMOM modeling results were compared with instrumental measurements as well as with salinity and current change data obtained using the regional reanalysis of the Baltic Sea Physics Analysis and Forecast (BSPAF)^{6,7} hydrophysical fields based on the numerical implementation of the Nucleus for European Modeling of

⁴ European Union-Copernicus Marine Service, 2018. *GLOBAL_MULTIYEAR_PHY_001_030*. Copernicus Marine Service Information (CMEMS). Marine Data Store (MDS). <https://doi.org/10.48670/moi-00021> [Accessed: 24 March 2025].

⁵ C3S, 2023. *ERA5 Hourly Data on Single Levels from 1940 to Present*. Copernicus Climate Change Service (C3S) Climate Data Store (CDS). <https://doi.org/10.24381/cds.adbb2d47> [Accessed: 24 March 2025].

⁶ European Union-Copernicus Marine Service, 2018. *BALTICSEA_MULTIYEAR_PHY_003_011*. Copernicus Marine Service Information (CMEMS). Marine Data Store (MDS). <https://doi.org/10.48670/moi-00013> [Accessed: 24 March 2025].

⁷ BALTICSEA_REANALYSIS_PHY_003_011. In: Y. Liu, 2019. *Issue 2.5: Quality Information Document*. Baltic Sea Production Centre. Copernicus Marine Environment Monitoring Service, 15 p. <https://doi.org/10.5281/zenodo.7935113>

the Ocean (NEMO) 3.6 hydrodynamic model [31, 32] for the Baltic Sea conditions. This model uses a procedure for contact and satellite information assimilation based on the algorithm of one of the varieties of the Kalman filter (local singular evolutive interpolated Kalman (LSEIK) filter) [33]. Satellite data on surface water temperature provided by the Swedish Meteorological and Hydrological Institute (SMHI) ice service as well as *in situ* T and S measurements from the ICES database (available at: <http://www.ices.dk>) were used as assimilated variables in the NEMO 3.6 model. The NEMO 3.6 model used meteorological data computed with the ECMWF ERA5 atmospheric model to set the sea surface boundary conditions. The BSPAF regional marine reanalysis data are daily averaged, they have a horizontal resolution of 3.9 km and 56 vertical horizons (layer thickness varies with depth from 3 to 22 m) and cover the 1993–2022 period.

To compare the salinity changes measured and calculated with the INMOM model and the BSPAF reanalysis data at different depths, mathematical expectations of salinity series m_s , their standard deviations (SD) σ_s , minimum S_{\min} and maximum S_{\max} values and correlation coefficient R_{ss} between the measured and model salinity values were estimated. The accuracy of the salinity values calculated using the INMOM and NEMO 3.6 models (BSPAF reanalysis) was estimated using accuracy criterion P_a , which shows the number of salinity values calculated using the models that fall within range $< 0,674\sigma$, where σ is SD of the salinity values measured at the Darss Sill and Arkona stations.

To compare the measured and model values of currents, the following statistical characteristics of the variability of the velocity and direction of currents were estimated using the vector-algebraic method of analysis of random processes^{8, 9}:

1) mathematical expectation of vector process \mathbf{m}_v (module direction $|\mathbf{m}_v|$ and direction α_m);

2) linear invariant of the SD tensor $[I_1(0)]^{0,5}$, where $I_1(0) = \lambda_1(0) + \lambda_2(0)$ is linear invariant of the vector process dispersion tensor determined through the half-lengths of principal axes $\lambda_1(0)$ и $\lambda_2(0)$ of the dispersion ellipse and orientation α° of its major axis relative to the geographic coordinate system:

$$\lambda_{1,2}(0) = \sqrt{\frac{1}{2} \left(D_{vv} + D_{uu} \pm \sqrt{(D_{vv} - D_{uu})^2 + (D_{vu} + D_{uv})^2} \right)},$$

where D_{vv}, D_{uu} are dispersions of the vector process components;

3) stability of currents $r = \sqrt{I_1(0)} / |\mathbf{m}_v|$, where $|\mathbf{m}_v|$ is module of the mathematical expectation of a vector process. When $r > 1$, the intensity of

⁸ Belyshev, A.P., Klevantsov, Iu.P. and Rozhkov, V.A., 1983. [*Probability Analysis of Sea Currents*]. Leningrad: Gidrometeoizdat, 264 p. (in Russian).

⁹ Ivanova, T.A., ed., 1984. [*A Methodological Circular on Probability Analysis for Vector Time Series for Current and Wind Speeds*]. Leningrad: Gidrometeoizdat, 61 p. (in Russian).

oscillatory motions in the flow prevails over the intensity of the average transfer, i.e. the current is unstable; when $r < 1$, currents become more stable;

4) two invariants of the normalized cross-correlation tensor function between the currents measured at the Darss Sill station and calculated using the INMOM model and BSPAF data: linear invariant $I_1^{\text{VU}}(\tau)$ and rotation indicator $D^{\text{VU}}(\tau)$. Linear invariant $I_1^{\text{VU}}(\tau)$ is equal to the trace of the matrix of correlation tensor function $K_{\text{VU}}(\tau)$, two vector processes $\mathbf{V}(t)$ and $\mathbf{U}(t)$ and characterizes the integral of the intensities of collinear changes in vector processes $\mathbf{V}(t)$ and $\mathbf{U}(t)$:

$$K_{\text{VU}}(\tau) = \begin{pmatrix} K_{v_1 u_1}(\tau), K_{v_1 u_2}(\tau) \\ K_{v_2 u_1}(\tau), K_{v_2 u_2}(\tau) \end{pmatrix},$$

where τ is time shift; v_1 is component of vector process $\mathbf{V}(t)$ on the parallel; v_2 is component of vector process $\mathbf{V}(t)$ on the meridian; u_1 is component of vector process $\mathbf{U}(t)$ on the parallel; u_2 is the component of vector process $\mathbf{U}(t)$ on the meridian.

Rotation indicator $D^{\text{VU}}(\tau)$ is equal to the difference of the non-diagonal components of the matrix of correlation tensor function $K_{\text{VU}}(\tau)$ and characterizes the integral of orthogonal changes in processes $\mathbf{V}(t)$ and $\mathbf{U}(t)$; when $D^{\text{VU}}(\tau) > 0$, process $\mathbf{U}(t)$ is rotated on average relative to process $\mathbf{V}(t)$ over a given time period clockwise and counterclockwise when $D^{\text{VU}}(\tau) < 0$.

Then the total correlation coefficient was calculated:

$$R_{\text{VU}}(\tau) = \sqrt{[I_1^{\text{VU}}(\tau)]^2 + [D^{\text{VU}}(\tau)]^2}.$$

In addition, the maximum modules of current velocity $|V|_{\text{max}}$ were estimated.

Flow rates of currents Q through the Danish straits during the 2014 MBI formation were estimated based on the current velocity vectors (V) calculated by the INMOM model at different horizons along three sections crossing the straits (see Fig. 1, *b*), using the following formula:

$$Q = \sum_{i=1}^n \sum_{z=1}^m VS, \quad (1)$$

where n is number of i -cells on the section; m is number of z -horizons in the given cell; V is meridional component of the current velocity in a grid cell at horizon z ; S is cross-sectional area of the cell determined as product of layer thickness (Δz) and distance between adjacent nodes of the grid region of model (Δi), i.e. $S = \Delta z \cdot \Delta i$.

To study the propagation routes of transformed North Sea waters after the MBI, two methods were used. The first method made it possible to construct two oceanographic sections along a system of interconnected deep-water basins of the marine relief. Their location was determined based on published information on the migration routes of the salty North Sea waters during the MBI in the Baltic Sea [4, 5]. Using the modeling data, diagrams of the temporal variability of salinity in

the bottom layer were constructed on these sections. In the second case, the Lagrangian method was used. Its detailed description is given in [34]. Within the framework of this method, 5000 passive markers were placed daily from 1 November to 31 December 2014 on a segment along the boundary passing north of the Danish straits along a line with coordinates 56.6°N, 10.85°E – 56.6°N, 11°E (Fig. 1, *b*). Based on the current velocity vector fields calculated using the INMOM model, each marker trajectory was calculated for a period of one year (until 31 December 2015).

Lagrangian trajectories were calculated using advection equation

$$\frac{d\lambda}{dt} = u(\lambda, \varphi, t),$$

$$\frac{d\varphi}{dt} = v(\lambda, \varphi, t),$$

where u and v are angular components of the current velocity calculated using the INMOM model in the penultimate σ -layer in depth; φ and λ denote latitude and longitude, respectively. Angular velocities are used to simplify the equation of motion on a sphere. Velocity values inside the grid cells were calculated using bicubic interpolation in space and third-degree Lagrange polynomial interpolation in time. When modeling the Lagrangian trajectories, the coordinates of the passive markers were recorded with the 1 h time resolution.

Results and discussion

Comparison of salinity and current values measured and calculated with the INMOM model and BSPAF reanalysis

Figs. 3 and 4 show changes in salinity values obtained during measurements at different horizons of the Darss Sill and Arkona automatic stations (see Fig. 1, *b* for the location of stations) based on the INMOM modeling results and the BSPAF regional reanalysis data for 1 November – 31 December 2014. Table 1 shows the statistical estimates of the measured and model salinity values. It is evident that the December 2014 MBI is modeled both by the BSPAF regional reanalysis data and by the INMOM modeling results as an anomalously large increase in salinity from the bottom horizons to the sea surface (Figs. 3 and 4). At the same time, the BSPAF reanalysis data, unlike the INMOM model, did not reproduce two weak inflows of the Kattegat waters that occurred on 22 and 26 November 2014 (Fig. 3). The correlation coefficients (R_{ss}) between the measured and model (INMOM and BSPAF) salinity series at different horizons are high and vary from 0.70 to 0.98 near the Darss Sill station and from 0.67 to 0.98 near the Arkona station (Table 1). This result indicates that the reanalysis data and the INMOM model describe adequately the main features of salinity changes during the MBI in the Southwestern Baltic, although the values of correlation coefficient R_{ss} between the measurement results and the INMOM data for three upper horizons near the Darss Sill station are noticeably higher than those of BSPAF, while they are close for three lower horizons. On the contrary, for the Arkona station area, the R_{ss} values at three upper horizons are lower for INMOM compared to BSPAF and the R_{ss} values at three lower horizons for INMOM are higher than those of BSPAF (Table 1).

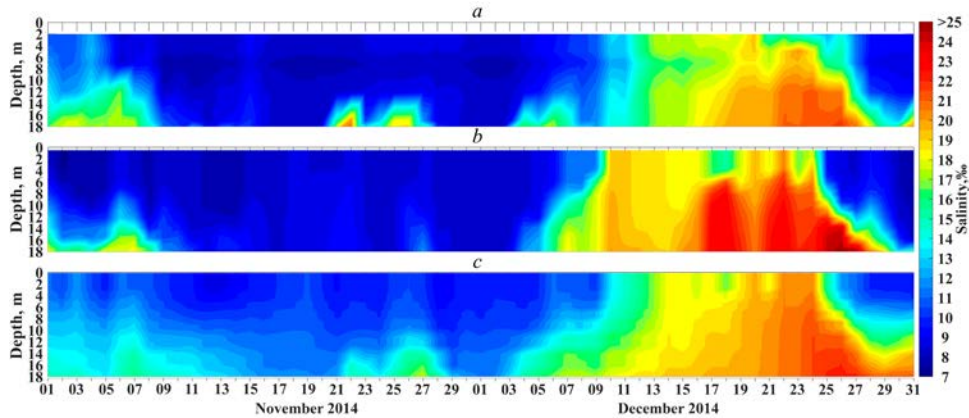


Fig. 3. Water salinity at the Darss Sill station based on the measurement (*a*), BSPAF reanalysis (*b*) and INMOM modeling (*c*) data from 1 November to 31 December 2014

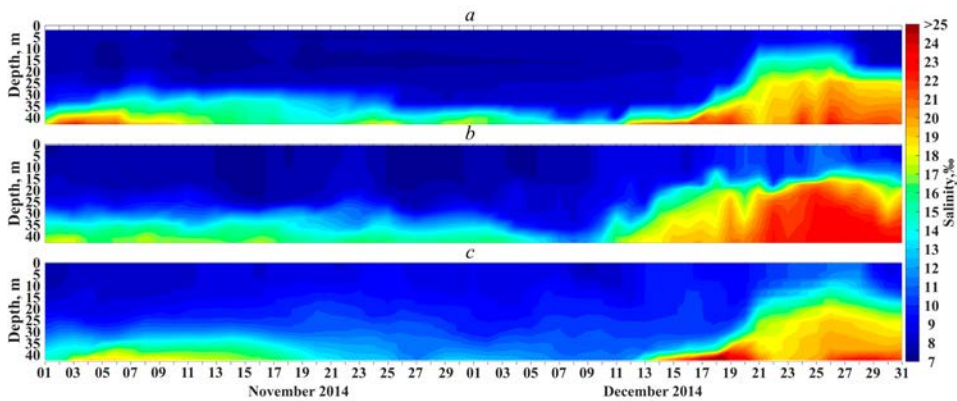


Fig. 4. Water salinity at the Arkona station based on measurement (*a*), BSPAF reanalysis (*b*) and INMOM modeling (*c*) data from 1 November to 31 December 2014

The values of the mathematical expectation of salinity changes during the BSPAF formation and propagation period estimated by INMOM in the Darss Sill station area are overestimated by 9–21% relative to the measured values at almost all horizons and by 4–22% in the area of the Arkona station. The exception is the 40 m horizon where the INMOM results in the Arkona area showed an underestimation of the mathematical expectation of salinity changes by 7% (Table 1). In contrast to the INMOM results, discrepancies between measured and calculated values of the mathematical expectation of salinity changes based on the BSPAF reanalysis data are generally significantly smaller and vary from 0.3 to 7% in the Darss Sill station area and from 2 to 17% near the Arkona station (Table 1). Only at the 25 and 33 m horizons in the Arkona area, the excess of the mathematical expectation values according to the BSPAF data relative to the measurements is noticeably greater than according to the INMOM data (Table 1).

Table 1

Statistical estimates of daily average seawater salinity at different horizons based on the measurements at the Darss Sill (DS) and Arkona (A) stations as well as the INMOM modeling and BSPAF reanalysis data for the period from 1 November to 31 December 2014

Data source	Horizon, m	m_s , ‰	σ_s , ‰	S_{\min} , ‰	S_{\max} , ‰	R_{ss}	P_a , %
<i>Darss Sill station</i>							
DS	2	10.93	3.37	8.07	19.21	–	–
INMOM		12.10	3.57	8.68	20.51	0.90	51
BSPAF		10.90	4.32	7.32	20.55	0.87	16
DS	5	11.22	3.81	8.07	20.15	–	–
INMOM		12.54	3.60	9.33	20.93	0.97	56
BSPAF		11.13	4.55	7.52	21.80	0.89	25
DS	7	10.86	3.85	7.47	19.45	–	–
INMOM		13.10	3.59	9.61	21.27	0.98	43
BSPAF		11.61	5.00	7.67	22.43	0.88	16
DS	12	12.28	4.42	8.05	21.26	–	–
INMOM		14.52	3.55	10.12	21.54	0.89	44
BSPAF		12.91	5.32	7.90	23.00	0.89	18
DS	17	14.44	4.47	8.13	21.57	–	–
INMOM		15.80	3.44	11.07	21.95	0.78	44
BSPAF		14.62	5.49	8.11	24.50	0.77	18
DS	19	15.80	4.32	8.21	21.93	–	–
INMOM		17.39	3.51	11.89	23.90	0.71	57
BSPAF		15.49	5.74	8.11	25.33	0.70	20
<i>Arkona station</i>							
A	2	8.16	0.52	7.58	9.71	–	–
INMOM		8.98	0.85	7.63	11.41	0.78	38
BSPAF		8.28	1.04	7.24	11.08	0.86	7
A	5	7.75	0.51	7.14	9.33	–	–
INMOM		9.03	0.90	7.63	11.86	0.67	38
BSPAF		8.29	1.05	7.32	11.11	0.81	7
A	7	7.93	0.54	7.36	9.69	–	–
INMOM		9.09	0.96	7.65	12.14	0.78	38
BSPAF		8.33	1.10	7.32	11.15	0.83	7
A	16	8.39	2.34	7.14	15.59	–	–
INMOM		10.2	2.10	8.35	16.86	0.83	72
BSPAF		9.59	3.24	7.32	19.26	0.70	26
A	25	10.15	4.08	7.65	19.87	–	–
INMOM		11.49	3.17	9.10	19.16	0.98	82
BSPAF		11.84	5.01	7.48	22.51	0.89	20
A	33	12.57	4.27	7.99	20.64	–	–
INMOM		13.12	3.09	10.04	19.93	0.93	77
BSPAF		14.51	4.35	8.36	23.19	0.80	49
A	40	16.56	3.15	9.09	21.98	–	–
INMOM		15.42	3.46	10.84	23.06	0.86	33
BSPAF		16.98	3.31	10.60	23.28	0.83	49

Note: m_s is average value; σ_s is SD; S_{\min} , S_{\max} are minimum and maximum salinity values; R_{ss} is correlation coefficient between the measured and modeled salinity values; P_a is accuracy criterion for the salinity values calculated by the models

Discrepancies between the SD values of salinity according to the INMOM model and results of measurements in the Darss Sill station area in the upper 2–7 m layer are small and do not exceed $\pm 5\text{--}7\%$ (Table 1). However, deeper down, the INMOM results show SD values that are underestimated by 19–23%. On the contrary, SD estimates according to the BSPAF reanalysis data show values that are overestimated by 19–33% at all horizons (Table 1).

The estimates of salinity SD measured at the Arkona station at the 2–7 m upper horizons are very small (0.51–0.54‰), which is 6.5–7.5 times less than the estimates of salinity SD based on the measurements at the Darss Sill station (Table 1). At these horizons, SD of salinity obtained from the modeling and reanalysis results shows overestimated values: 0.85–0.96‰ for INMOM and 1.04–1.10‰ for BSPAF. At a depth over 7 m, the estimates of salinity SD based on the measurements at the Arkona station increase significantly (by 4–8 times). Here, in the 16–33 m layer, the estimates of salinity SD obtained from the INMOM modeling results are underestimated by 10–28% relative to the measurement data and only at the bottom horizon of 44 m, they are overestimated by 10% (Table 1). The estimates of salinity SD obtained from the BSPAF reanalysis results are overestimated everywhere at depths from 16 to 40 m. They are overestimated most of all at the 16 m (38%) and 25 m (23%) horizons and not significantly at the 33 m (2%) and 40 m (5%) horizons (Table 1).

Comparison of the measured and model-calculated salinity minimum values shows that according to the INMOM results, they are always greater than their measured values at the Darss Sill and Arkona stations in all cases. Moreover, these discrepancies with the measured values increase from the surface where they do not exceed 1–8% to the bottom horizons where they reach 19–45%.

The discrepancies between the measured and BSPAF reanalysis-calculated salinity minimum values in the areas of the Darss Sill and Arkona stations are noticeably smaller and do not exceed $\pm 9\text{--}17\%$ (Table 1).

Comparison of the model-calculated estimates of salinity maxima (S_{max}) with their measured values at the Darss Sill and Arkona stations during the MBI formation and spread period shows that they exceed the measured values almost in all cases (Table 1). In the Darss Sill station area, the S_{max} model values based on the INMOM results are 1–9% higher than the measured values while they are significantly higher according to the BSPAF reanalysis data, amounting to 7–16% (Table 1).

For the Arkona station area, the S_{max} model estimates for INMOM exceed the measured values by 18–27% while those obtained from BSPAF reanalysis data are greater than the measured values by 14–19% (Table 1). At greater depths (16–40 m), discrepancies between the S_{max} estimates calculated from INMOM and its measured values are noticeably smaller and vary from –4 to +8%. The S_{max} estimates obtained from BSPAF reanalysis data exceed its measured values by 6–24% (Table 1).

Estimates of the P_a accuracy criterion show that the INMOM model simulates salinity changes in the Southwestern Baltic in general better than the BSPAF reanalysis (Table 1). In the Darss Sill area, 43 to 57% of the INMOM salinity estimates fall within the range of measured values less than 0.674σ while only 16 to 25% of the values from the BSPAF reanalysis fall within this range (Table 1). For the Arkona area, the estimates of the P_a accuracy criterion from the INMOM modeling results vary from 33 to 82% while from the BSPAF reanalysis they do not exceed 7–49% (Table 1).

Table 2

Statistical estimates of current velocity variability at different horizons (H) at the Darss Sill station (DS) based on the measurement, BSPAF reanalysis and INMOM modeling data for the period from 1 November to 31 December 2014

Data source	H , m	$ \mathbf{m}_w $, cm/s	$/\alpha_m$, degree	$[I_1(0)]^{0.5}$, cm/s	$\sqrt{\lambda_1(0)}$, cm/s	$\sqrt{\lambda_2(0)}$, cm/s	α° , degree	$R_{vu}(\tau)$	r	$ V _{\max}$, cm/s
DS	2.0	3.09	337	30.04	23.26	19.00	3.18	–	9.7	102.7
BSPAF	1.5	5.73	273	26.82	25.54	8.19	–0.25	0.71	4.7	59.9
INMOM	2.0	2.75	38	20.54	19.69	5.85	8.29	0.59	7.5	37.7
DS	5.0	3.22	346	26.93	22.51	14.79	–9.36	–	8.4	79.5
BSPAF	4.5	5.63	270	26.18	24.99	7.81	–0.79	0.67	4.6	59.1
INMOM	5.3	2.25	42	18.14	17.58	4.50	7.44	0.55	8.1	33.6
DS	11.0	1.31	94	20.54	19.52	6.39	–19.87	–	15.7	55.0
BSPAF	10.6	3.54	245	21.79	21.28	4.66	–8.92	0.51	6.2	52.6
INMOM	11.2	2.72	67	14.75	14.18	4.09	–2.41	0.60	5.4	27.8
DS	14.0	2.39	83	18.67	17.59	6.27	–21.55	–	7.8	46.1
BSPAF	13.6	2.22	190	19.94	19.27	5.15	–13.50	0.61	9.0	46.6
INMOM	14.2	3.38	76	13.77	13.02	4.47	–16.63	0.60	4.1	26.5
DS	16.0	2.62	70	17.42	16.59	5.32	–24.98	–	6.6	39.8
BSPAF	16.8	2.73	159	19.07	17.95	6.45	–18.50	0.66	7.0	38.1
INMOM	16.2	3.67	68	13.26	12.41	4.68	–24.57	0.66	3.6	22.5

Note: $|\mathbf{m}_w|$ is module of the average value; α_m is direction of the average value; $[I_1(0)]^{0.5}$ is linear invariant of the SD tensor; $\sqrt{\lambda_1(0)}$ and $\sqrt{\lambda_2(0)}$ are half-lengths of major and minor axes of the SD ellipse; α° is direction of the major axis of SD ellipse; $R_{vu}(\tau)$ is total correlation coefficient; r is current stability indicator; $|V|_{\max}$ is module of the maximum sea current vector.

Comparison of statistical estimates of current velocities measured at the Darss Sill station and calculated using BSPAF reanalysis data and the INMOM model shows that in the upper 11-meter layer, the $|\mathbf{m}_w|$ estimates of the mathematical expectation of current velocities obtained using BSPAF reanalysis data are overestimated by 1.8–2.7 times relative to the measured ones while the estimates are close to each other deeper than this layer (Table 2). According to the estimates of α_m mathematical expectation vector direction, discrepancies between the measured and BSPAF reanalysis values are very large: 64–76° in the upper 5-meter layer, almost opposite at a horizon of about 11 m and reaching 89–107° in deeper layers. In contrast to BSPAF, the INMOM model shows a slight underestimation of by 0.3–1.0 cm/cm in the upper 5-meter layer and their overestimation by 0.99–1.41 cm/s

in deeper layers (Table 2). In the α_m direction, the discrepancies between the measured and calculated estimates using the INMOM model reach 56–61° in the upper 5-meter layer and comparison shows the closeness of the measured and calculated α_m values deeper than this layer (Table 2).

Estimates of various invariants of the SD tensor of the velocity vectors of the measured and model currents show that in the upper 5-meter layer, the BSPAF results slightly underestimate (by 3–11%) the values of invariant $[I_1(0)]^{0.5}$, which describes the total intensity of current oscillations, and deeper than 5 m, on the contrary, they slightly overestimate it by 6–9%. Comparison of the measured and $[I_1(0)]^{0.5}$ INMOM-modeled estimates shows their significant underestimation (by 24–33%) at all horizons (Table 2). According to instrumental measurements, compression of the SD ellipses of current oscillations in the 2–5 m layer is small while, according to the BSPAF and INMOM model estimates, the minor axes of the SD ellipses in this layer are 3–4 times smaller than the major ones (Table 2). Deeper than this layer, both instrumental measurements and model estimates show a greater degree of compression of the SD ellipses (Table 2).

The directions of the large axes of the SD ellipses of the measured and modeled current oscillations are approximately the same (Table 2).

From the BSPAF reanalysis data and measurement results, correlation coefficients $R_{vU}(\tau)$ among current oscillations vary from 0,51 to 0,71 and for INMOM, they are 0.55–0.66 (Table 2).

Current stability index r for both measured and model currents at all horizons is significantly greater than 1, which indicates significant instability of the currents during the MBI formation (Table 2).

Comparison of the estimates of the $|V|_{\max}$ measured and model currents maxima shows that the INMOM model underestimates their values significantly at all horizons (Table 2). For the BSPAF reanalysis, the same trend is observed only for the 2–5 m layer, and deeper than this layer, the measured and model values of current maxima are comparable (Table 2).

Summarizing the results of the measured and model currents comparison, it can be concluded that the INMOM model reproduces the characteristics of average flows at different horizons during the 2014 MBI formation better and the BSPAF reanalysis data describe the characteristics of oscillatory movements in the deep and bottom layers often more realistically.

Peculiarities of current variability in the Danish straits during the MBI formation based on modeling results

Fig. 5 shows the time course of the daily average and maximum current velocity vectors in November–December 2014 calculated using the INMOM model in the Sound, Great Belt and Little Belt straits. The long period of the Baltic waters outflow through the Danish straits which always precedes MBIs [4, 5] started in early November and continued (with short breaks) until the end of November 2014.

The main MBI period in the Danish straits started on 2–3 December when the outflow from the Baltic to the Kattegat ceased and the directions of currents in the Sound, Great Belt and Little Belt straits changed to the opposite ones at all horizons. This unidirectional flow of the Kattegat waters into the Baltic continued in the Danish straits until 24 December (Fig. 5) after which it was replaced by the opposite Baltic waters flow towards the Kattegat. The average daily values of currents during the MBI in the Sound reached 0.8 m/s and the maximum values per day were 1.2 m/s. In the Great Belt, these estimates of average and maximum currents were 1.0 and 1.2 m/s, respectively. The noted differences between the average daily and maximum currents per day indicate that they are caused by intra-day variability associated with barotropic and baroclinic tides, non-tidal internal waves, inertial and seiche oscillations [2].

In the Sound and the Great Belt, a significant current velocity decrease with depth (by 1.5–2.0 times) is observed during the MBI without a significant change in their direction (Fig. 5, *a–d*). In the Little Belt, the sea depth is about 5 m and the current velocity decreases insignificantly with depth (Fig. 5, *e, f*).

It is noteworthy that the unidirectional movement of the North Sea water flow in the Danish straits during the main MBI period was not monotonous, but oscillatory (Fig. 5). The periods between velocity maxima varied from 2 to 4 days and the current velocities varied by 20–60 cm/s. It can be assumed that these features are possibly associated with wind variability. Wind measurements at the Darss Sill station indicate that with the same cyclicities in December 2014, the wind changed its direction (from south to west) and speed quasiperiodically [5].

In November, another feature is observed in the structure of currents in the Sound: when the currents are directed from the Baltic to the Kattegat, their cores are pressed to the surface and when they change direction to the opposite the cores of the currents are traced at the 10–14 m depths (Fig. 5, *a, b*). The same feature was observed on 2–3 December at the MBI beginning when the core of the Kattegat water flow was localized at the 10–14 m depths (Fig. 5, *a*). However, the core of the flow started rising to the surface later and the maximum of currents was observed in the surface layer from 7 to 23 December (Fig. 5, *a*). This feature of the currents in the Great Belt was expressed much weaker (Fig. 5, *c, d*).

Estimates of water transport through the Danish straits during the MBI

The estimates of the current flow rates shown in Fig. 6 indicate that the largest water transport during the MBI was carried out through the Great Belt (Fig. 6, *b*) where the maximum daily average volume of transported water reached $17 \cdot 10^4 \text{ m}^3/\text{s}$. In the Sound, the largest average daily transport ($6 \cdot 10^4 \text{ m}^3/\text{s}$) was almost three times less than in the Great Belt (Fig. 6a). In the Little Belt, the maximum daily average water transport was only $0.18 \cdot 10^4 \text{ m}^3/\text{s}$ which is almost two orders of magnitude less than in the Great Belt.

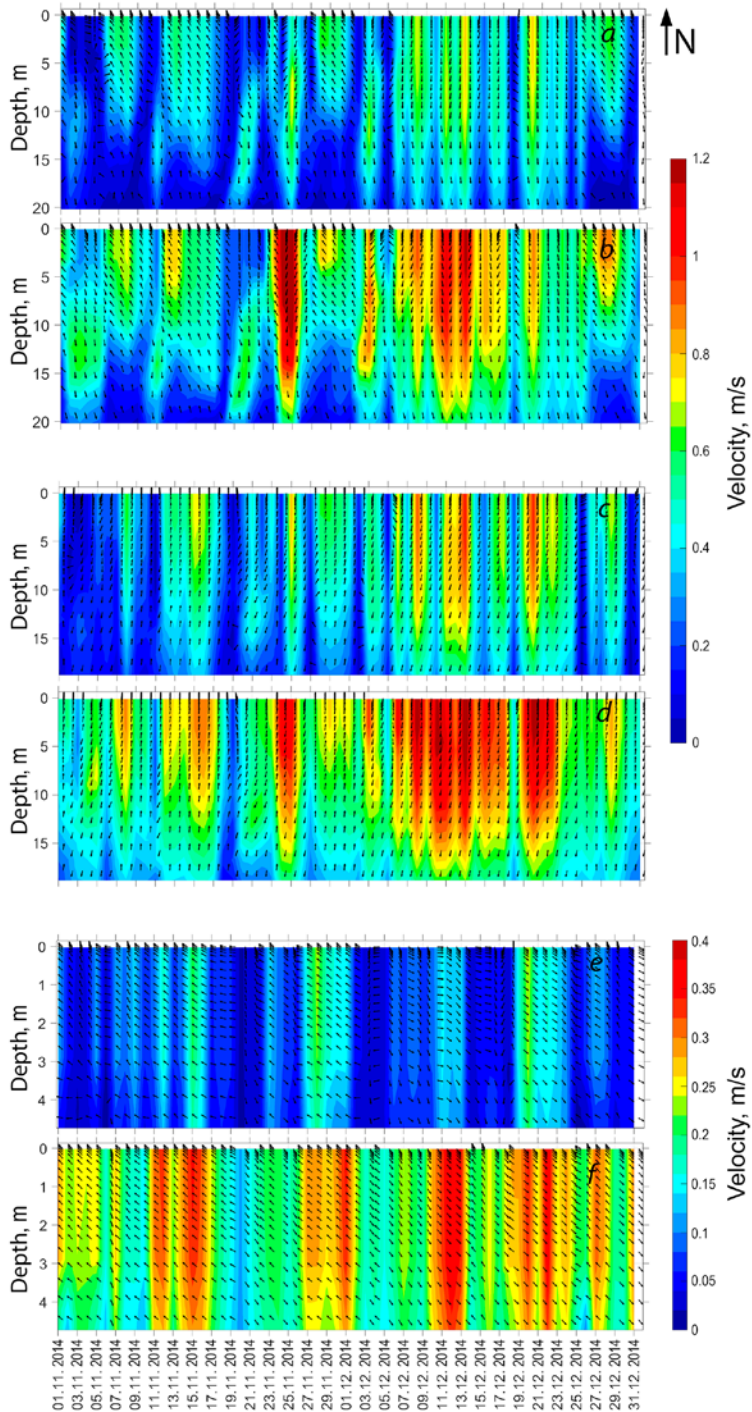


Fig. 5. Time variation of the daily average (*a, c, e*) and maximum (*b, d, f*) current velocity vectors at different horizons in the Sound (*a, b*), Great Belt (*c, d*) and Little Belt (*e, f*) straits calculated by the INMOM model for the period from 1 November to 31 December 2014 (see Fig. 1, *b*)

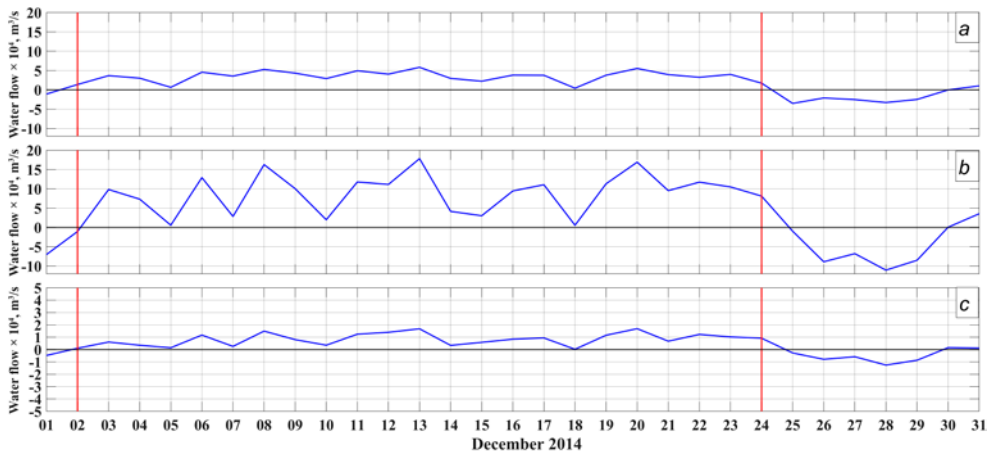


Fig. 6. Daily average flow rates of currents during the 2014 MBI in the Sound (a), Great Belt (b) and Little Belt (c) straits calculated based on the INMOM modeling results

Table 3

Estimates of total volume of the salty North Sea waters (km³) flowing to the Southwestern Baltic through the Danish straits during the 2014 MBI main period according to the INMOM modeling results and [5]

Straits	INMOM	[5]
Sound	68.9	64÷76
Great Belt	170.9	205÷248*
Little Belt	1.6	No data
Total	241.4	281÷323

* The estimates included values of water exchange through the Little Belt Strait.

Table 3 shows the total volumes of the salty North Sea waters calculated based on the INMOM model simulation results that entered the Southwestern Baltic during the main MBI period (2–24 December 2014) through the Danish straits. For comparison, Table 3 shows the same estimates obtained by V. Mohrholz using other methods [5]. In contrast to our calculations of transport through the Danish straits carried out with formula (1), V. Mohrholz applied two indirect methods to estimate water exchange between the Kattegat and the Baltic Sea during the MBI of the year: based on changes in the Baltic water volume calculated using the water balance equation and based on sea level slopes between the Kattegat and the Southwestern Baltic [5]. He used both sea level measurements at tide gauge stations and the results of numerical hydrodynamic modeling as initial data for such estimates [5]. The transport estimates obtained using the INMOM model indicate that in December 2014, only 241.4 km³ of the Kattegat water passed through the Danish straits during

the MBI. Its largest part passed through the Great Belt (170.9 km³) while only 68.9 km³ passed through the Sound. The Little Belt influence on the MBI water distribution turned out to be very insignificant (only 1.6 km³) (Table 3). These estimates are in good agreement with the conclusions in [35], according to which the volumes of water transport are distributed in the 7:3 ratio during large inflows between the Great Belt and the Sound. The results presented in Table 3 also show that our estimates of transport in the Sound are close to those obtained using other methods in [5] while for the Great Belt, our estimates of transport turned out to be somewhat smaller compared to the results in [5] (see Table 3).

Bottom salinity fields in the main MBI periods

Fig. 7 shows bottom salinity fields calculated using the INMOM model for four main periods of the 2014 MBI formation. During the outflow of the Baltic waters, the Sound is completely filled with the freshened Baltic waters with the 9–11‰ salinity (Fig. 7, *a*). Water masses with increased salinity of 17–20‰, which were there during previous weak inflows, are observed in the bottom layers of the Arkona and Bornholm basins (Fig. 7, *a*).

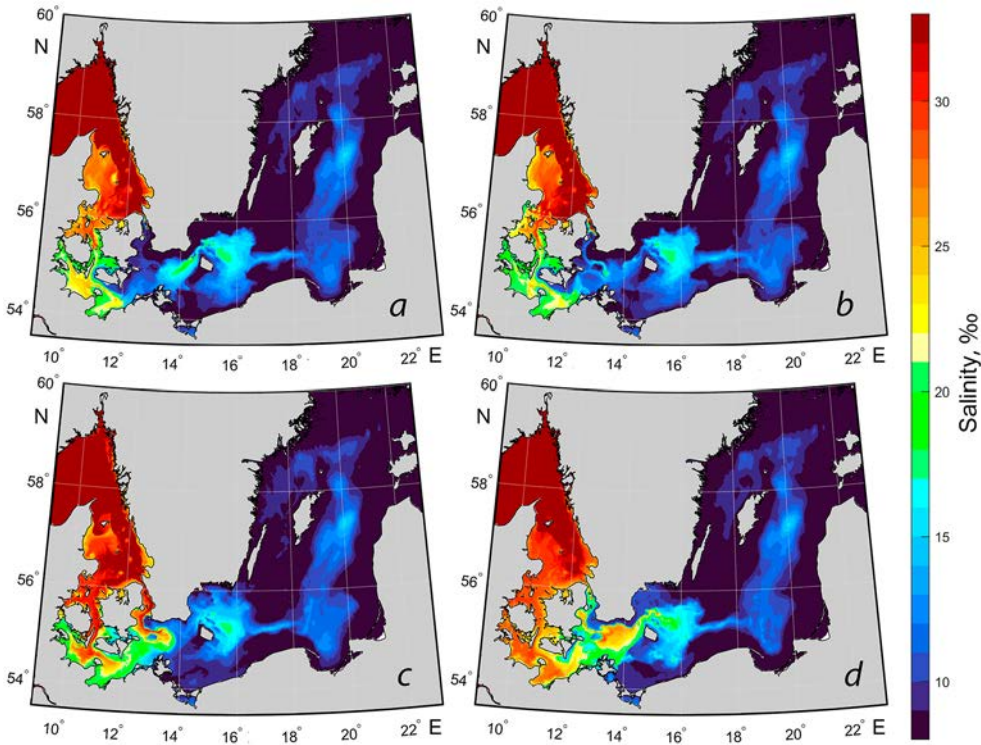


Fig. 7. Bottom salinity in four periods of the 2014 MBI formation: *a* – outflow period on 16.11.2014; *b* – precursor period on 01.12.2014; *c* – main inflow period on 12.12.2014; *d* – post inflow period on 29.12.2014

In the MBI preceding period, the outflow of the freshened Baltic waters through the Danish straits continues, resulting in a salinity decrease in Mecklenburg and Kiel bays and in the Little and Great Belts (Fig. 7, *b*). It is also evident that during this period, more saline bottom Arkona Basin waters move into the Sound, increasing the Arkona Basin water salinity (Fig. 7, *b*).

During the main inflow period, large volumes of the North Sea waters with the 30‰ salinity fill the Sound and Great Belt and spread further into the Southwestern Baltic (Fig. 7, *c*). From the Sound, they penetrate into the Arkona Basin and the northern part of the Bornholm, from the Great Belt – into Kiel and Mecklenburg bays as well as into the western part of the Belt Sea (Fig. 7, *c*). A very small amount of the salty North Sea waters enters through the Little Belt (Fig. 7, *c*).

In the period after the great inflow at the end of December 2014, almost the entire Arkona Basin, part of the Bornholm Basin, Kiel and Mecklenburg bays and the Belt Sea are filled with the transformed North Sea waters (Fig. 7, *d*). The salinity of the Sound and Great Belt waters decreases significantly.

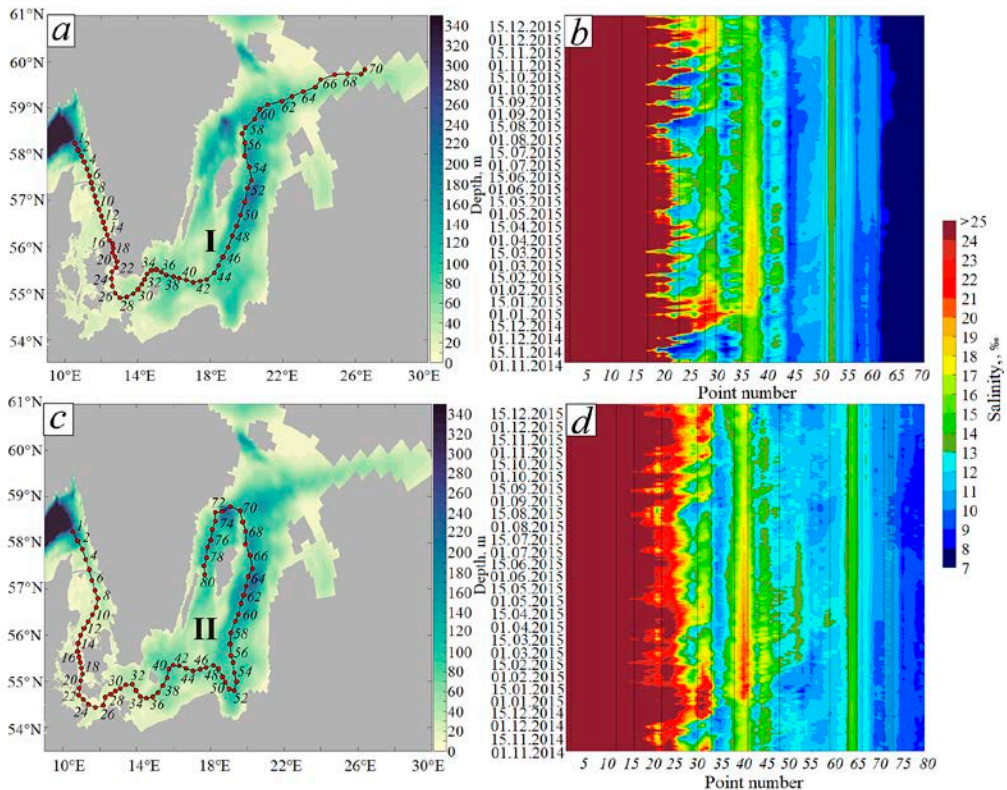


Fig. 8. Temporal variability of water salinity in the layer above the bottom on two sections: I (*a, b*) and II (*c, d*) based on the *INMOM* modeling data for the period from 1 November 2014 to 31 December 2015

Temporal changes in bottom salinity on sections across the open Baltic in 2014–2015

Fig. 8 demonstrates temporal variability in bottom salinity on two sections (Fig. 8, *a, c*) from 01.11.2014 to 31.12.2015. Spatio-temporal diagrams show that by mid-December 2014, after passing the Sound and the Great Belt, the salty MBI waters enter the Arkona Basin (Fig. 8, *b, d*), increasing the bottom salinity in it from 12 to 22–25‰ over the course of one and a half months until the end of January 2015. Then, the MBI waters spread into the Bornholm Basin where they enter in the first half of January 2015 with a salinity of 17–19‰ (Fig. 8, *b, d*). Comparison of Figs. 8, *b* and 8, *d* shows that the main route of the MBI water propagation passes north of Bornholm Island where a greater salinity increase to the south of it is observed.

The results given in Fig. 8, *d* show that in mid-February 2015, the transformed MBI waters enter the Gulf of Gdansk with the 12–13‰ salinity at the bottom. They spread then northward and enter the Gotland Deep in early April 2015 (Fig. 8, *b, d*). A further salinity increase in the bottom layer on section I is noted up to point 64, indicating that in 2015, the transformed MBI waters did not enter the Gulf of Finland. On section II, a salinity increase is observed up to point 71. These results demonstrate that the transformed MBI waters enter the western part of the Gotland Basin.

Trajectories of markers during the spread of MBI waters based on the Lagrangian modeling results

Fig. 9 shows the trajectories of markers placed in the southern Kattegat in November–December 2014 obtained with Lagrangian modeling. It can be seen that by the end of December 2014, most of the markers pass the Danish straits, the Arkona Basin and further enter the Bornholm Basin (Fig. 9, *a*) which is in good agreement with the results obtained by another method and presented in Fig. 8. A significant portion of the markers move from their placement site to the north of the Kattegat and penetrate the Skagerrak (Fig. 9, *a*). By the end of March 2015, the markers fill the Arkona and Bornholm basins almost completely and move in a wide flow to the east, to the Gulf of Gdansk. There, they split into two flows, the wider of which fills the Gulf of Gdansk actively, and the other, narrower, spreads north of the Gulf of Gdansk and moves to the Gotland Basin eastern part (Fig. 9, *b*). Another narrow flow spreads from the Bornholm Basin to the north-northeast (Fig. 9, *b*). By the end of July 2015, the markers moving in a wide flow penetrate in large numbers into the eastern part of the Gotland Basin and the Gotland Deep (Fig. 9, *c*). At the end of December 2015, they spread to the north of the open Baltic and, moving along a cyclonic trajectory, enter the Landsort Deep (Fig. 9, *d*).

Thus, two different methods of studying the December 2014 spread of transformed MBI waters indicate that its waters did not penetrate into the Gulf of Finland by the end of 2015 (see Figs. 8 and 9). These results are in good agreement with the estimates of the spread of the transformed Baltic Basin waters obtained in

[36] using hydrochemical analysis of water samples on the oceanographic section between the Gotland Deep and the central part of the Gulf of Finland. Based on an analysis of the results of temperature, salinity and oxygen measurements at oceanographic stations, the authors of [36] note that nine months after the December 2014 MBI, deep stagnant waters from the northern part of the open Baltic, which were there before the MBI, were forced into the Gulf of Finland; the directly transformed waters of the 2014 MBI entered the Gulf of Finland only in 2016, 14–15 months after the MBI [36], but with very low oxygen content.

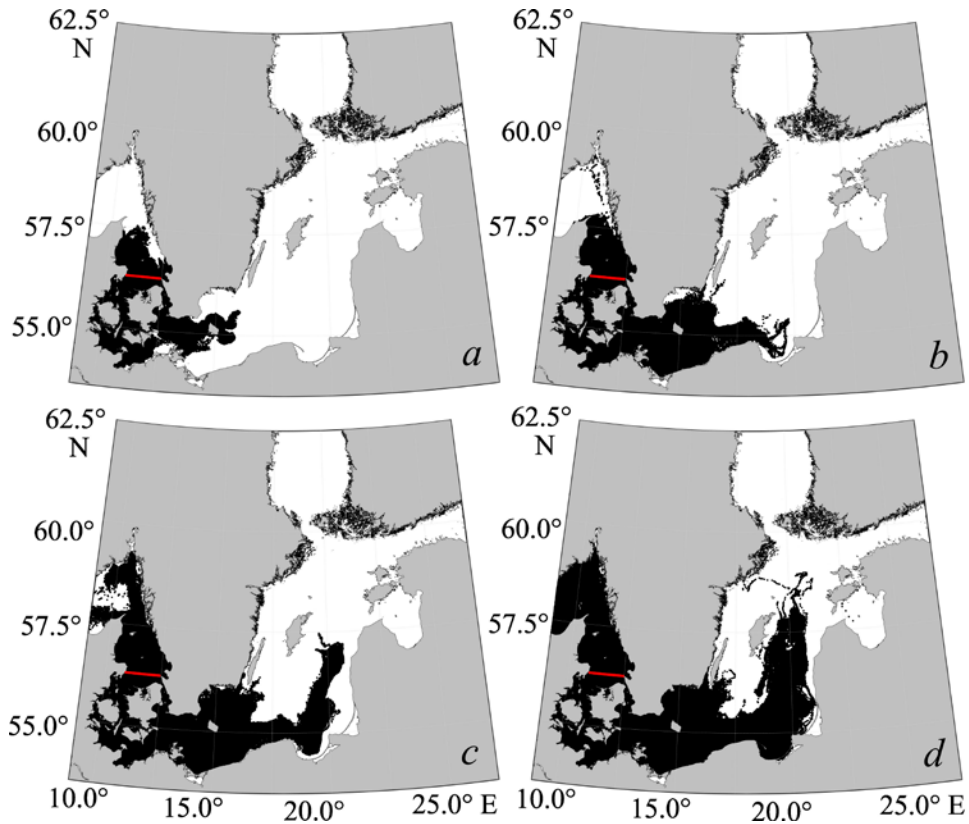


Fig. 9. Trajectories of the Lagrangian particles from the moment of launch up to 31 December 2014 (a); 31 March 2015 (b); 31 July 2015 (c); 31 December 2015 (d). Red line shows the place where the markers were launched

Conclusion

The performed study makes it possible to draw the following principal conclusions:

1. According to the INMOM base model, a joint numerical baroclinic hydrodynamic model of the North and Baltic seas, having a spherical grid domain with detailing in the Danish straits, to study the MBI formation and propagation, was developed. Modeling of the variability of oceanographic conditions in the North and

Baltic Sea system during the December 2014 MBI formation and propagation was carried out.

2. To test the developed model performance, the model estimates were compared with the results of salinity and current measurements at different horizons of the Darss Sill and Arkona automatic stations as well as with the regional BSPAF reanalysis data implementing the NEMO 3.6 model. The comparison showed that the INMOM model reproduces salinity changes generally in the Southwestern Baltic better: in the Darss Sill station area, the values of the P_a accuracy criterion show that 43–57% of the salinity estimates calculated by INMOM fall within the range of measured values not exceeding 0.674σ while, according to the BSPAF reanalysis, only 16–25% of the values fall within this range. For the Arkona station area, the estimates of accuracy criterion P_a based on the INMOM modeling results vary from 33 to 82% while according to the BSPAF reanalysis data, they do not exceed 7–49%. Comparison of statistical estimates of the calculated and measured characteristics of currents showed that the INMOM model reproduced the characteristics of average flows at different horizons during the 2014 MBI formation better while the BSPAF reanalysis data often described the characteristics of oscillatory movements in the deep and bottom layers more realistically.

3. Modeling of oceanographic conditions during the 2014 MBI using the INMOM model shows that its main period started on 2–3 December 2014 and lasted until 24 December 2014. During it, unidirectional flows of the Kattegat waters into the Baltic Sea are observed in the Danish straits, decreasing with depth by 1.5–2 times in terms of velocity module, with maximum velocities reaching 1.2 m/s in the Sound and the Great Belt and only 0.4 m/s in the Little Belt. The movement nature of unidirectional flows of the Kattegat waters in the straits is not monotonous but fluctuating. Periods between current fluctuations vary from 2 to 4 days and current velocities change by 20–60 cm/s.

4. The bottom salinity fields calculated using the INMOM model during the main periods of formation and spread of the major inflow of 2014 show that during the outflow of the Baltic waters, the Sound is completely filled with the freshened Baltic waters of the 9–11‰ salinity and in the bottom layers of the Arkona and Bornholm basins, water masses of increased salinity of 17–20‰, which spread here during previous weak inflows, are observed. In the precursory period, the outflow of the freshened Baltic waters through the Danish straits goes on, resulting in a salinity decrease in Mecklenburg and Kiel bays and in the Little Belt. The bottom waters from the Arkona Basin move to the Sound, resulting in the salinity decrease in the Arkona Basin. During the influx main period, large volumes of the North Sea waters with the 30‰ salinity fill the Sound and the Great Belt, penetrating into the Arkona Basin and the northern part of the Bornholm Basin as well as into Kiel and Mecklenburg bays and into the Belt Sea. A very small amount of the salty North Sea waters enters through the Little Belt.

5. Water exchange estimates obtained using the INMOM model indicate that in December 2014, during the main MBI period, a total of 241.4 km³ of the Kattegat water passed through the Danish straits. The largest part of this was distributed through the Great Belt (170.9 km³), while only 68.9 km³ passed through the Sound. The Little Belt influence on water transport during the MBI was very insignificant – only 1.6 km³.

6. A study of the propagation routes of the transformed North Sea waters across the Baltic after the MBI end on two sections with Lagrangian modeling shows that after passing the Danish straits, the MBI waters spread in a wide flow into the Southwestern Baltic, then penetrate into the Gulf of Gdansk and move further along a cyclonic trajectory through the deep-water areas of the eastern and northern parts of the Gotland Basin, without penetrating into the Gulf of Finland, and they reach the Landsort Deep in the western part of the Gotland Basin by the end of December 2015.

REFERENCES

1. Dickson, R.R., 1973. *The Prediction of Major Baltic Inflows*. *Deutsche Hydrographische Zeitschrift*, 26, pp. 97-105. <https://doi.org/10.1007/BF02232597>
2. Terziev, F.S., Rozhkov, V.A. and Smirnova, A.I., eds., 1992. *Hydrometeorology and Hydrochemistry of the Seas of the USSR. Volume 3. Baltic Sea. Issue 1. Hydrometeorological Conditions*. Saint Petersburg: Gidrometeoizdat, 450 p. (in Russian).
3. Fischer, H. and Matthäus, W., 1996. The Importance of the Drogden Sill in the Sound for Major Baltic Inflows. *Journal of Marine Systems*, 9(3-4), pp. 137-157. [https://doi.org/10.1016/S0924-7963\(96\)00046-2](https://doi.org/10.1016/S0924-7963(96)00046-2)
4. Matthäus, W., 2006. The History of Investigation of Salt Water Inflows into the Baltic Sea – from the Early Beginning to Recent Results. In: Institut für Ostseeforschung, 2006. *Meereswissenschaftliche Berichte = Marine Science Reports*. Warnemünde: Institut für Ostseeforschung. No. 65, 73 p. URL: <https://doi.io-warnemuende.de/10.12754/msr-2006-0065> [Accessed: 20.02.2025].
5. Mohrholz, V., Naumann, M., Nausch, G., Krüger, S. and Gräwe, U., 2015. Fresh Oxygen for the Baltic Sea – An Exceptional Saline Inflow after a Decade of Stagnation. *Journal of Marine Systems*, 148, pp. 152-166. <https://doi.org/10.1016/j.jmarsys.2015.03.005>
6. Tikhonova, N.A. and Sukhachev, V.N., 2017. Wave Interpretation of Major Baltic Inflows. *Russian Meteorology and Hydrology*, 42(4), pp. 258-266. <https://doi.org/10.3103/S1068373917040069>
7. Zakharchuk, E.A., Litina, E.N., Klevantsov, Yu.P., Sukhachev, V.N. and Tikhonova, N.A., 2017. Nonstationarity of the Hydrometeorological Processes in the Baltic Sea under Changing Climate. *Proceedings of State Oceanographic Institute*, (218), pp. 6-62 (in Russian).
8. Leppäranta, M. and Myrberg, K., 2009. Topography and Hydrography of the Baltic Sea. In: M. Leppäranta and K. Myrberg, 2009. *Physical Oceanography of the Baltic Sea*. Berlin; Heidelberg: Springer, pp. 41-88. <https://doi.org/10.1007/978-3-540-79703-6>
9. Zakharchuk, E.A., Kudryavtsev, A.S. and Sukhachev, V.N., 2014. On the Resonance-Wave Mechanism of Major Baltic Inflows. *Russian Meteorology and Hydrology*, 39(2), pp. 100-108. <https://doi.org/10.3103/S1068373914020058>

10. Wyrtki, K., 1953. Die Dynamik der Wasserbewegungen im Fehmarnbelt. *Kieler Meeresforschungen*, 9(2), pp. 155-170 (in German).
11. Madsen, K.S. and Højerslev, N.K., 2009. Long-Term Temperature and Salinity Records from the Baltic Sea Transition Zone. *Boreal Environment Research*, 14, pp. 125-131.
12. Gräwe, U., Friedland, R. and Burchard, H., 2013. The Future of the Western Baltic Sea: Two Possible Scenarios. *Ocean Dynamics*, 63(8), pp. 901-921. <https://doi.org/10.1007/s10236-013-0634-0>
13. Stigebrandt, A., 1983. A Model for the Exchange of Water and Salt between the Baltic and the Skagerrak. *Journal of Physical Oceanography*, 13(3), pp. 411-427. [https://doi.org/10.1175/1520-0485\(1983\)013<0411:AMFTEO>2.0.CO;2](https://doi.org/10.1175/1520-0485(1983)013<0411:AMFTEO>2.0.CO;2)
14. Meier, H.E.M., Kjellström, E. and Graham, L.P., 2006. Estimating Uncertainties of Projected Baltic Sea Salinity in the Late 21st Century. *Geophysical Research Letters*, 33(15), L15705. <https://doi.org/10.1029/2006GL026488>
15. Neumann, T., 2010. Climate-Change Effects on the Baltic Sea Ecosystem: A Model Study. *Journal of Marine Systems*, 81(3), pp. 213-224. <https://doi.org/10.1016/j.jmarsys.2009.12.001>
16. Hordoir, R., Dieterich, C., Basu, C., Dietze, H. and Meier, H.E.M., 2013. Freshwater Outflow of the Baltic Sea and Transport in the Norwegian Current: A Statistical Correlation Analysis Based on a Numerical Experiment. *Continental Shelf Research*, 64, pp. 1-9. <https://doi.org/10.1016/j.csr.2013.05.006>
17. Burchard, H., Lass, H.U., Mohrholz, V., Umlauf, L., Sellschopp, J., Fiekas, V., Bolding, K. and Arneborg, L., 2005. Dynamics of Medium-Intensity Dense Water Plumes in the Arkona Basin, Western Baltic Sea. *Ocean Dynamics*, 55(5), pp. 391-402. <https://doi.org/10.1007/s10236-005-0025-2>
18. Umlauf, L., Arneborg, L., Burchard, H., Fiekas, V., Lass, H.U., Mohrholz, V. and Prandke, H., 2007. Transverse Structure of Turbulence in a Rotating Gravity Current. *Geophysical Research Letters*, 34(8), L08601. <https://doi.org/10.1029/2007GL029521>
19. Lehmann, A. and Myrberg, K., 2008. Upwelling in the Baltic Sea – A Review. *Journal of Marine Systems*, 74(1), pp. S3-S12. <https://doi.org/10.1016/j.jmarsys.2008.02.010>
20. Fennel, W., Seifert, T. and Kayser, B., 1991. Rossby Radii and Phase Speeds in the Baltic Sea. *Continental Shelf Research*, 11(1), pp. 23-36. [https://doi.org/10.1016/0278-4343\(91\)90032-2](https://doi.org/10.1016/0278-4343(91)90032-2)
21. Reißmann, J.H., 2006. On the Representation of Regional Characteristics by Hydrographic Measurements at Central Stations in Four Deep Basins of the Baltic Sea. *Ocean Science*, 2(1), pp. 71-86. <https://doi.org/10.5194/os-2-71-2006>
22. Osiński, R., Rak, D., Walczowski, W. and Piechura, J., 2010. Baroclinic Rossby Radius of Deformation in the Southern Baltic Sea. *Oceanologia*, 52(3), pp. 417-429. <http://dx.doi.org/10.5697/oc.52-3.417>
23. Kurkin, A., Kurkina, O., Rybin, A. and Talipova, T., 2020. Comparative Analysis of the First Baroclinic Rossby Radius in the Baltic, Black, Okhotsk, and Mediterranean Seas. *Russian Journal of Earth Sciences*, 20(4), ES4008. <https://doi.org/10.2205/2020ES000737>
24. Zhang, Y.J., Stanev, E.V. and Grashorn, S., 2016. Unstructured-Grid Model for the North Sea and Baltic Sea: Validation against Observations. *Ocean Modelling*, 97, pp. 91-108. <https://doi.org/10.1016/j.ocemod.2015.11.009>
25. Zalesny, V.B., Marchuk, G.I., Agoshkov, V.I., Bagno, A.V., Gusev, A.V., Diansky, N.A. Moshonkin, S.N., Tamsalu, R. and Volodin, E.M., 2010. Numerical Simulation of Large-Scale Ocean Circulation Based on the Multicomponent Splitting Method. *Russian Journal of Numerical Analysis and Mathematical Modelling*, 25(6), pp. 581-609. <https://doi.org/10.1515/rjnamm.2010.036>

26. Diansky, N.A., 2013. [*Modeling the Ocean Circulation and Study of Its Response to Short- and Long-Period Atmospheric Influences*]. Moscow: Fizmatlit, 272 p. (in Russian).
27. Brydon, D., Sun, S. and Bleck, R., 1999. A New Approximation of the Equation of State for Seawater, Suitable for Numerical Ocean Models. *Journal of Geophysical Research: Oceans*, 104(C1), pp. 1537-1540. <https://doi.org/10.1029/1998JC900059>
28. Pacanovsky, R.C. and Philander, G.H., 1981. Parametrization of Vertical Mixing in Numerical Models of Tropical Oceans. *Journal of Physical Oceanography*, 11(11), pp. 1443-1451. [https://doi.org/10.1175/1520-0485\(1981\)011<1443:POVMIN>2.0.CO;2](https://doi.org/10.1175/1520-0485(1981)011<1443:POVMIN>2.0.CO;2)
29. Yakovlev, N.G., 2009. Reproduction of the Large-Scale State of Water and Sea Ice in the Arctic Ocean from 1948 to 2002: Part II. The State of Ice and Snow Cover. *Izvestiya, Atmospheric and Oceanic Physics*, 45(4), pp. 478-494. <https://doi.org/10.1134/S0001433809040082>
30. Hunke, E.C. and Dukowicz, J.K., 1997. An Elastic-Viscous-Plastic Model for Sea Ice Dynamics. *Journal of Physical Oceanography*, 27(9), pp. 1849-1867. [https://doi.org/10.1175/1520-0485\(1997\)027<1849:AEVPMF>2.0.CO;2](https://doi.org/10.1175/1520-0485(1997)027<1849:AEVPMF>2.0.CO;2)
31. Hordoir, R., Axell, L., Löptien, U., Dietze, H. and Kuznetsov, I., 2015. Influence of Sea Level Rise on the Dynamics of Salt Inflows in the Baltic Sea. *Journal of Geophysical Research: Oceans*, 120(10), pp. 6653-6668. <https://doi.org/10.1002/2014JC010642>
32. Pemberton, P., Löptien, U., Hordoir, R., Höglund, A., Schimanke, S., Axell, L. and Haapala, J., 2017. Sea-Ice Evaluation of NEMO-Nordic 1.0: A NEMO-LIM3.6-Based Ocean-Sea-Ice Model Setup for the North Sea and Baltic Sea. *Geoscientific Model Development*, 10(8), pp. 3105-3123. <https://doi.org/10.5194/gmd-10-3105-2017>
33. Nerger, L., Hiller, W. and Schröter, J., 2005. A Comparison of Error Subspace Kalman Filters. *Tellus A: Dynamic Meteorology and Oceanography*, 57(5), pp. 715-735. <https://doi.org/10.3402/tellusa.v57i5.14732>
34. Prants, S.V., Uleysky, M.Yu. and Budyansky, M.V., 2017. *Lagrangian Oceanography: Large-Scale Transport and Mixing in the Ocean*. Physics of Earth and Space Environments. Cham: Springer, 273 p. <https://doi.org/10.1007/978-3-319-53022-2>
35. Mattsson, J., 1996. Some Comments on the Barotropic Flow through the Danish Straits and the Division of the Flow between the Belt Sea and the Öresund. *Tellus A: Dynamic Meteorology and Oceanography*, 48(3), pp. 456-464. <https://doi.org/10.3402/tellusa.v48i3.12071>
36. Liblik, T., Naumann, M., Alenius, P., Hansson, M., Lips, U., Nausch, G., Tuomi, L., Wesslander, K., Laanemets J. [et al.], 2018. Propagation of Impact of the Recent Major Baltic Inflows from the Eastern Gotland Basin to the Gulf of Finland. *Frontiers in Marine Science*, 5, 222. <https://doi.org/10.3389/fmars.2018.00222>

Submitted 07.10.2024; approved after review 18.11.2024;
accepted for publication 29.01.2025.

About the authors:

Natalya A. Tikhonova, Associate Professor, Department of Oceanology, Institute of Earth Sciences, Saint Petersburg State University (33–35, 10th Line of Vasilyevsky Island, Saint Petersburg, 199178, Russian Federation); Acting Head of Laboratory, Saint Petersburg Branch of N.N. Zubov State Oceanographic Institute (38 Beringa Str., Saint Petersburg, 199397, Russian Federation), CSc (Geogr.), **ORCID ID: 0000-0002-4546-4920**, **ResearcherID: I-4647-2015**, **Scopus Author ID: 11239410500**, i@ntikhonova.ru

Evgeny A. Zakharchuk, Head of Department of Oceanology, Institute of Earth Sciences, Saint Petersburg State University (33–35, 10th Line of Vasilyevsky Island, Saint Petersburg, 199178, Russian Federation), DSc (Geogr.), **ORCID ID: 0000-0001-6079-5739**, **ResearcherID: N-1644-2013**, **Scopus Author ID: 6603158329**, ezakharchuk@yandex.ru

Mikhail V. Vinogradov, Postgraduate Student, Department of Oceanology, Institute of Earth Sciences, Saint Petersburg State University (33–35, 10th Line of Vasilyevsky Island, Saint Petersburg, 199178, Russian Federation); Researcher, Saint Petersburg Branch of N.N. Zubov State Oceanographic Institute (38 Beringa Str., Saint Petersburg, 199397, Russian Federation), Master of Science in Hydrometeorology, **ORCID ID: 0009-0003-3744-8204**, **ResearcherID: LIH-6593-2024**, Vinogradovm2000@gmail.com

Vladimir S. Travkin, Postgraduate Student, Department of Oceanology, Institute of Earth Sciences, Saint Petersburg State University (33–35, 10th Line of Vasilyevsky Island, Saint Petersburg, 199178, Russian Federation); Researcher, Saint Petersburg Branch of N.N. Zubov State Oceanographic Institute (38 Beringa Str., Saint Petersburg, 199397, Russian Federation), Master of Science in Hydrometeorology, **ORCID ID: 0000-0002-7254-9313**, **ResearcherID: HCH-2630-2022**, **Scopus Author ID: 57509420800**, vtravkin99@gmail.com

Contribution of the co-authors:

Natalya A. Tikhonova – problem statement, preparation of modeling data, performance of calculations, preparation of the article text and graphic materials, discussion of modeling results

Evgeny A. Zakharchuk – formulation of the goals and objectives of the study, scientific supervision, preparation of the article text, analysis of research results

Mikhail V. Vinogradov – data verification, performance of calculations, preparation of graphic materials

Vladimir S. Travkin – preparation of modeling data, preparation of the article text and graphic materials

The authors have read and approved the final manuscript.

The authors declare that they have no conflict of interest.

Original article

Granulometric Characteristics of Bottom Sediments in the Sublittoral Region of the Southern Coast of Crimea in the Area of Limenskaya Bay

A. V. Bagaev , K. I. Gurov, S. A. Nuriev

Marine Hydrophysical Institute of RAS, Sevastopol, Russian Federation

 *a.bagaev1984@gmail.com*

Abstract

Purpose. The purpose of the study consists in obtaining modern accurate data on the bottom relief features and the granulometric composition of bottom sediments in Limenskaya Bay region of the Southern Coast of Crimea.

Methods and Results. The samples of the surface layer (0–5 cm) of bottom sediments were taken using the Peterson grab sampler in September 2022. The granulometric composition of bottom sediments was studied using the decantation and scattering method. The hydroacoustic research of the seabed was performed from the small vessels of Marine Hydrophysical Institute and the Black Sea Hydrophysical Subsatellite Polygon in 2022 and 2023. The *Lowrance Elite FS7* instrument which includes a built-in single-beam echo sounder (200 kHz) for determining the sea depth, the side-scan sonar (455/800 kHz) and the global satellite navigation system receiver for defining the coordinates was applied. It is noted that at present, the sea bottom in the coastal part and in Limenskaya Bay sublittoral is covered with the unevenly distributed sedimentary material of heterogeneous composition. In the shallowest part (0–10 m), the boulder-pebble forms of sediments are widespread, their active movement is a result of storm impact and anthropogenic activity.

Conclusions. The predominance of gravel fraction in the western and eastern study areas results from the landslide-prone coastal morphology. In the deeper parts (10–15 m) of Limenskaya Bay, the bottom is covered mainly with the well-sorted sand sediments. At the depths exceeding 20 m, the proportion of silt fraction increases, which is consistent with the previously studied features of general dynamics of sediment fractions in this region. Having been deciphered, the results of bottom relief hydroacoustic scanning in the coastal zone made it possible to outline the boundaries of boulder-pebble area, as well as to estimate the predominant sizes at various parts of the bottom.

Keywords: Black Sea, sublittoral, Limenskaya Bay, bottom sediments, granulometric composition, bottom relief

Acknowledgements: The study was carried out within the framework of state assignment of FSBSI FRC MHI on theme FNNN-2024-0016 “Coastal research”. The authors are grateful to E. M. Lemesenko, V. V. Nikishin, S. V. Shcherbachenko, L. V. Verzhetskaya, V. A. Kalpa and E. A. Kotelyanets for their assistance in organizing and conducting expeditionary research.

For citation: Bagaev, A.V., Gurov, K.I. and Nuriev, S.A., 2025. Granulometric Characteristics of Bottom Sediments in the Sublittoral Region of the Southern Coast of Crimea in the Area of Limenskaya Bay. *Physical Oceanography*, 32(2), pp. 238-252.

© 2025, A. V. Bagaev, K. I. Gurov, S. A. Nuriev

© 2025, Physical Oceanography



Introduction

Bottom sediments are one of the most informative elements of the natural environment of the coastal zone of the sea. They accumulate pollutants entering the sea and enable characterization of the presence and development of negative biogeochemical processes, both in the sediments and in the water column [1]. The surface layer of bottom sediments is the most dynamically active, its state being determined both by rapid synoptic processes at the atmosphere-sea boundary and slower processes of sedimentogenesis at the sea-bottom boundary.

It is the surface layer of sediments on the beach and in the near-shore zone of the sea that determines the recreational attractiveness of the coast, and in deeper water areas it is important for monitoring the ecological state of the coastal zone and for estimating the geomorphological characteristics of a coastal section when planning construction [2, 3].

The Southern Coast of Crimea (SCC) is a unique region due to its diverse landscapes and biocenoses [4]. A large number of recreational infrastructure facilities are concentrated along its coastline – health resorts and complexes [2, 3, 5]. The SCC characterized by a high density of development.

The study of meteorological, hydrological, hydrochemical and optical characteristics of the SCC waters in general and Limenskaya Bay in particular has been carried out over a long period of time [6–10] at the Black Sea Hydrophysical Subsatellite Polygon (BSHSP), partly due to the location of the stationary oceanographic platform of Marine Hydrophysical Institute (MHI) of the Russian Academy of Sciences in the waters of the bay [11].

Despite great interest in the research of the coastal areas of the SCC, detailed studies of the characteristics of the modern structure of the bottom relief in the coastal and near-shore zones, as well as the grain size distribution of bottom sediments in the waters of Limenskaya Bay have not been carried out. The main information on the grain size distribution of the bottom sediments in Limenskaya Bay dates back to the middle and second half of the 19th century and is presented in the works ^{1, 2, 3}, and the main factors controlling the flow of terrigenous material into the bay waters are described in the works [12, 13]. Among the most recent studies devoted to the grain size distribution of bottom sediments and their dynamics in the waters of Limenskaya Bay and adjacent areas of the SCC, the works [14–16] can be noted. However, based on the data on the sedimentation rates in the coastal areas of Crimea [17, 18], it can be assumed that the previously obtained information on the structure of sediments is very outdated, does not reflect the real picture and requires updating. The acquisition of new data will make it possible to study in more detail the characteristics of the formation of bottom sediments under anthropogenic load.

¹ Zenkovich, V.P., 1958. [*Morphology and Dynamics of the Soviet Black Sea Coast. Vol.1*]. Moscow: Publishing House of the USSR Academy of Sciences, 188 p. (in Russian).

² Zenkovich, V.P., 1962. [*Fundamentals of the Theory of Sea Shore Development*]. Moscow: Publishing House of the USSR Academy of Sciences, 710 p. (in Russian).

³ Melnyk, V.I. and Mitin L.I, eds., 1982. [*The Geology of the USSR Shelf. Environment. History and Methods of Study*]. Kiev: Naukova Dumka, 180 p. (in Russian).

The purpose of the study is to obtain modern, accurate data on the bottom relief characteristics and granulometric composition of the bottom sediments in the Limenskaya Bay region of the SCC.

Characteristics of the research area

The study area spans 0.8×4 km water body covering the coastal (1–10 m depth) and sublittoral (10–40 m depth) sections of the SCC shelf in the vicinity of Limenskaya Bay between Katsiveli and Simeiz. Limenskaya Bay, or (as it is also known) Goluboy Zaliv, is a relatively shallow bay bounded to the west by Cape Kikineiz and to the east by the foot of Mount Koshka.

The Limenskaya Bay area belongs to the tectonic structure of the anticlinorium of the western part of the SCC⁴. In general, the entire SCC from the Morskoye settlement in the east to the Batiliman tract in the west has a similar structure. The narrow coastal strip consists of clayey and sandy deposits of the Tauride series and the Middle Jurassic. It is cut through by numerous ravines and gullies, which carry surface runoff water only during flood periods. It is bounded to the north by very steep and often precipitous slopes of the Main Ridge, composed of Upper Jurassic carbonate rocks [19]. The geological structure of the bay is characterized by a complex combination of folded and faulted sedimentary rocks, including Jurassic and Cretaceous limestones, sandstones and shales⁵. The study area contains the most significant outcrops of effusive rocks in the western part of the SCC. Due to the relatively easy destruction of the rocks that make up the coast and the steep slope, erosion processes achieve a considerable efficiency, which is expressed in the high degree of development of the gully system. The Limenka River gully is an almost permanent watercourse, fed not only by surface runoff but also by springs located along the edges of the gully [20]. The bay waters also receive purified municipal wastewater from the settlements of Katsiveli and Goluboy Zaliv and the Goluboy Zaliv Water Park [21].

The coastal area of the SCC is characterized by a shallow bay structure due to the different erosion resistance of the rocks and the presence of block piles. The SCC is characterized by steep underwater slopes and significant depth³. The underwater slope of the Black Sea in the area of Limenskaya Bay is a gentle plain with a southeasterly slope, in places with boulders and underwater rocks. On the SCC, in areas where the bottom consists of large transported material, the slopes in the first ten meters of depth are 0.04–0.06. In areas complicated by the presence of block piles, the bottom slopes reach 0.08–0.1. In places where rocks of the Tauride series develop and an abrasion terrace is present, the slopes decrease to 0.03–0.04¹.

The past and present oceanographic characteristics of Limenskaya Bay are closely related to its geological structure. The bottom of the bay is covered by a thick

⁴ Sidorenko, A.V., ed., 1969. *Geology of the USSR. Vol. 8. Crimea. I. Geological Description*. Moscow: Nedra, 576 p. (in Russian).

⁵ Shnyukov, E.F., Ogorodnikov, V.I., Kovalyukh, N.N. and Maslakov, N.A., 1984. [Modern Sediments and Sedimentation Rates in the Holocene on the Black Sea Shelf of the Ukrainian SSR]. In: *Proceedings of the International Symposium: Study of the Geologic History and Processes of Modern Sedimentation of the Black and Baltic Seas. Part I*. Kiev: Naukova Dumka, p. 122-130 (in Russian).

layer of quaternary sediments. The sedimentary deposits of the bay provide valuable information about past changes in sea level, climate and ocean circulation. The modern composition of the bottom sediments in Limenskaya Bay is characterized by a mixture of sand, silt and gravel-shell material. In the coastal zone they were represented by medium-grained sands with the inclusion of shell material and limestone gravel, in the marine part of the polygon – by silt-pelitic silts [15]. The reason for such heterogeneity in the distribution of fractions of granulometric composition is the change in the sedimentation conditions of suspended matter, and the main source of sediment material is coastal abrasion and alongshore sediment transport during intense storms [15].

In [16] it is shown for the Limenskaya Bay water area that during the storm impact, coarse-grained material accumulates in the coastal zone in the area of capes, medium-grained fractions accumulate in the central shallow part of the bay, and fine-grained material is transported to the seaward part of the water area and accumulates due to the weakening of hydrodynamic activity. In general, the main redistribution of fractions takes place during the first 6 hours of the storm and is limited by the 20 m isobath. The main factors regulating the movement of material are depth and bottom slope.

In [22] the level of anthropogenic load on the SCC is generally considered to be extreme. In particular, on the shores of Limenskaya Bay, the beaches have been developed and filled in, a water park has been built, an underwater outlet for the Katsiveli sewage treatment plant is under construction, and a pipe has already been laid in the area of the Goluboy Zaliv settlement.

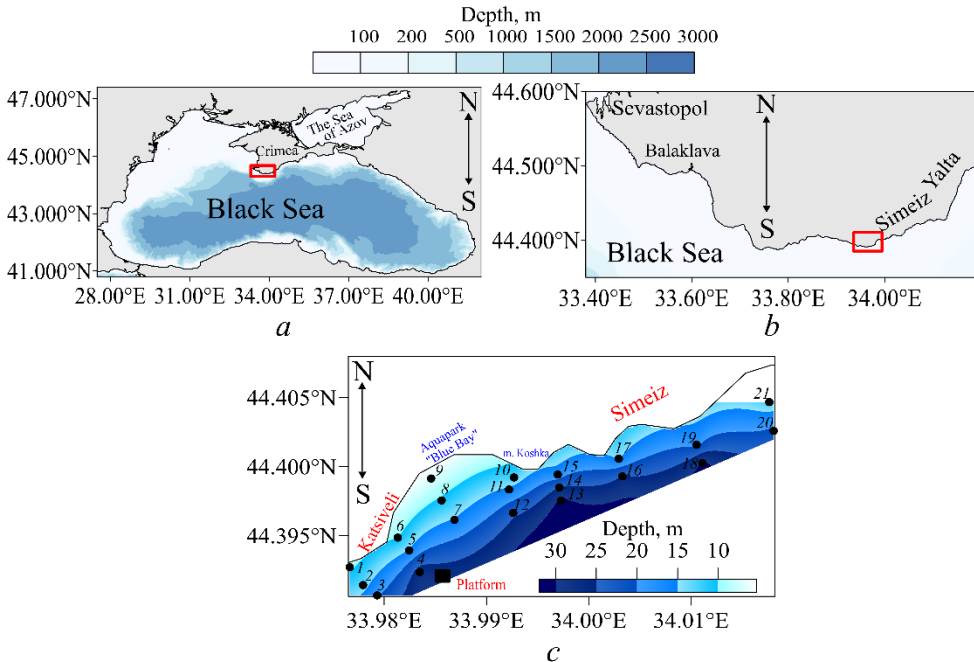


Fig. 1. Location of study area (shown in red rectangles) on the maps of the Black Sea (a) and the Southern Coast of Crimea (b), and scheme of bottom sediments sampling stations in Limenskaya Bay and the adjacent area of the SCC (c)

Materials and methods

The surface layer of bottom sediments (0–5 cm) used for analysis in this study was sampled in September 2022 using a Peterson grab sampler with an area of 0.025 m². The location of the sampling station is shown in Fig. 1. The particle size distribution of the bottom sediments was investigated by a combined sieve analysis (decantation and dispersion method) using a set of sieves with openings of 10; 7; 5; 2.5; 2; 1; 0.5; 0.25; 0.1; 0.05 mm. The sampling data of the bottom sediments and a general description of their composition are given in Table 1.

Table 1

General description of the surface layer (0–5 cm) of bottom sediments in Limenskaya Bay and the adjacent area of the SCC (sampling on September 8, 2022)

Station number	Depth, m	Characteristics of bottom sediments
1	9	Coarse- and fine-grained gravel
2	13	Coarse- and fine-grained gravel with shells
3	20	Coarse-grained shells with coarse sand (15%)
4	28	Coarse-grained shell with fine-grained sand (33%)
5	15	Fine- (42%) and medium-grained (31%) sand
6	10	Fine-grained sand
7	15	Coarse-grained sand and small shells (26%)
8	11	Coarse- (67%) and medium-grained (21%) sand
9	7	Fine-grained gravel (48%) and coarse sand (15%)
10	12	Fine-grained sand (59%) with medium-grained sand (18%) and aleurite (13%)
11	16	Fine-grained sand (54%) with aleurite (25%)
12	24	Aleurite (66%) with fine-grained sand (23%)
13	31	Large shells (35%) and coarse-grained sand (15%)
14	25	Fine-grained sand
15	17	Coarse- and medium-grained gravel
16	26	Coarse- and medium-grained gravel
17	15	Coarse-grained sand (62%) and small shells (26%)
18	31	Fine-grained sand (55%) with aleurite (40%)
19	19	Coarse- and medium-grained sand with fine gravel (15%)
20	21	Fine- and medium-grained gravel with coarse sand (19%)
21	12	Coarse shells (24%) and fine-grained sand (18%) with aleurite (23%) and pelite (20%)

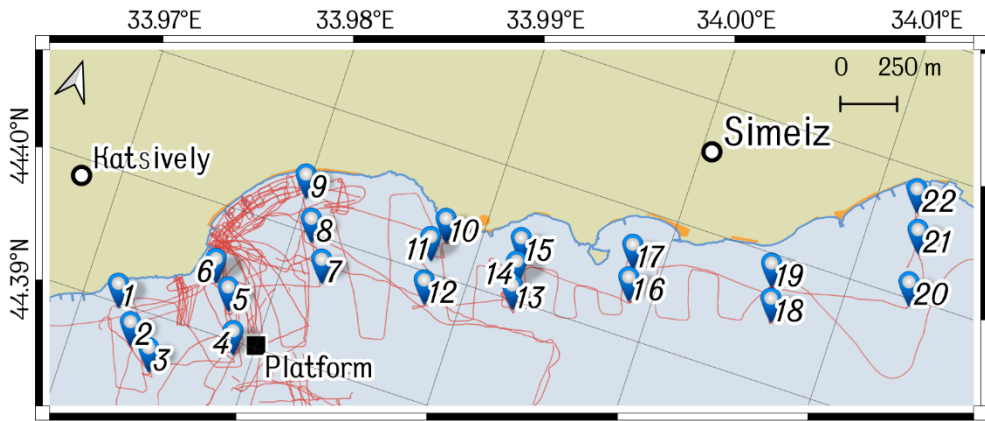


Fig. 2. Scheme of the study area. Blue markers show the sites of bottom sediments sampling, red line – the tracks of relief hydroacoustic scanning, orange polygons along the coast are the municipal beaches, and black triangle is location of the BSHSP oceanographic platform

Table 2

Characteristics of expeditionary hydroacoustic studies

Date	Number of points	Length, m	Date	Number of points	Length, m
18.08.2022	3397	2548	14.06.2023	8001	6001
19.08.2022	8088	6066	15.06.2023	6648	4986
07.09.2022	16638	12479	18.07.2023	3670	2753
08.09.2022	32995	24746	20.07.2023	8699	6524

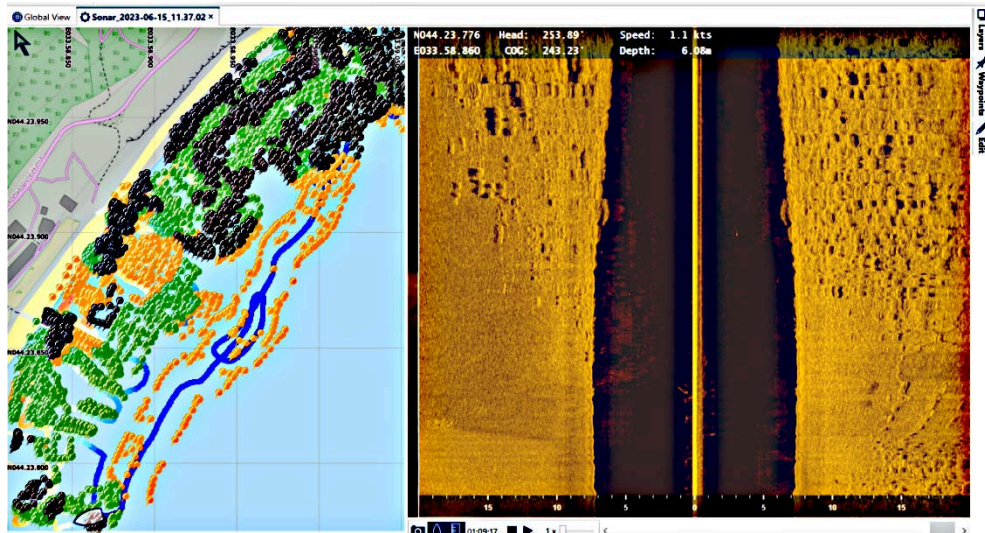


Fig. 3. Example of SSS data analysis using the ReefMaster software: left – types of deposits, right – visualization of the SSS data scanning in time; boundary between the coarse and sandy deposits is clearly seen

The hydroacoustic survey of the underwater relief was carried out from small MHI and BSHSP vessels in 2022 and 2023. A *Lowrance Elite FS7* device with an integrated single-beam echo sounder (200 kHz) was used to determine the depth of the surveyed area, a side-scan sonar (SSS) (455/800 kHz) and a Global Navigation Satellite System receiver to determine the coordinates. The working area and vessel tracks are shown in Fig. 2, and information on the survey dates and track lengths is given in Table 2. Depth data were recorded with a horizontal resolution of 0.75 m with an error of up to 3 m. The accuracy of depth determination is ~ 5 cm. The SSS scanning bandwidth is up to 60 m, and the SSS beam power allowed the detection of bottom irregularities down to 40 m depth.

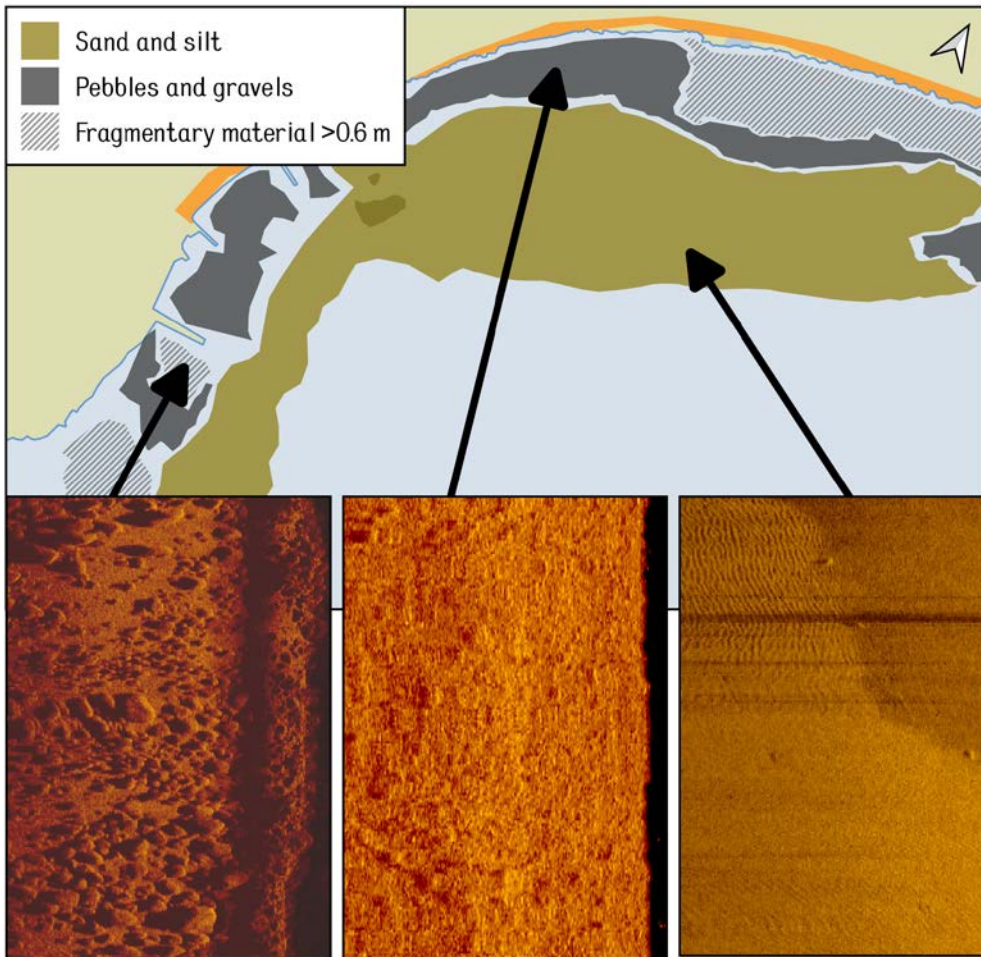


Fig. 4. Example of constructing the polygons with different types of sediments using QGIS. The data are from the expedition in 14–15.06.2023. Insets show the fragments of SSS echograms corresponding to the identified types of bottom sections

Post-processing and data analysis were carried out using QGIS GIS, Python programming language and the ReefMaster application. The initial data from the echo sounder in sqlite database format (.sl3) were loaded into the ReefMaster

program (Fig. 3). Then, based on the analysis of the images obtained during the hydroacoustic survey, a point cloud was manually generated with the coordinates of the bottom sediment boundaries (boulders, pebbles, sand/silt). After defining the boundaries in ReefMaster, their coordinates were exported to a vector file (.shp). These coordinates and sediment type were then transferred to QGIS and polygons were created in semi-automatic mode to delineate areas of relatively homogeneous sediment. Three sediment types were distinguished by size: coarse-grained material and boulders (> 0.6 m), large pebbles and gravel (< 0.6 m) and sandy-silty material (< 0.1 m) (Fig. 4).

Results and discussion

Despite the uneven coverage of the study area by hydroacoustic scanning lines, as a result of the SSS data analysis it was possible to construct a set of polygons that define the position of the bottom sediment fields in Limenskaya Bay and its environs in sufficient detail.

According to Fig. 5, the bottom sediments in the coastal area (80–100 m along the normal from the water's edge to depths of 10–15 m) are fields of large clastic material (> 0.6 m in diameter) of varying concentration, partly interspersed with a smaller fraction of pebbles and gravel, partly covered by sand sediments. In shallow water the coarse clastic deposits provide a substrate for macrophytes.

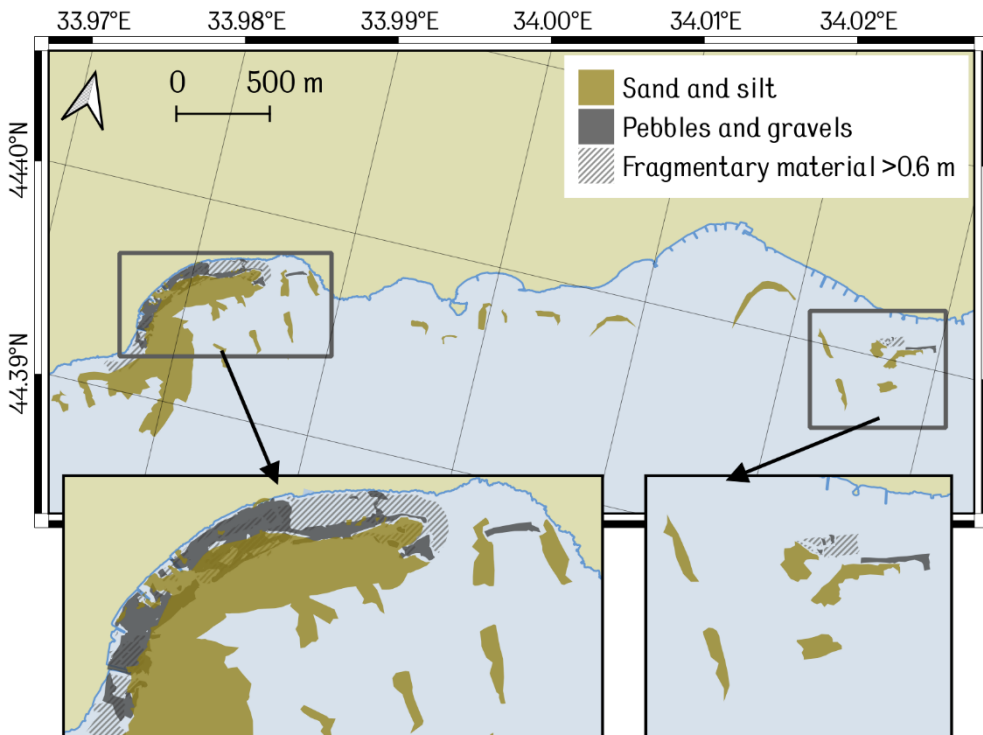


Fig. 5. Lithological scheme of the bottom surface in Limenskaya Bay and the adjacent sublittoral. The inset left part shows Limenskaya Bay, its right part – the Cape Opasny region

Near Cape Kikineiz, opposite the mouth of the Limenka River, and near Cape Opasny, large fragments predominate, while at the same depths in Limenskaya Bay, a smaller pebble fraction is more common. At 90–120 m from the shore (15–20 m depths), opposite Cape Kikineiz, large fields of fragmental material change abruptly to sand, and in the concave part of the coast they sometimes alternate with gravel and pebbles (Fig. 5). Away from the shore, at depths of more than 25 m, sands of varying sizes predominate. Moreover (as will be shown below), with increasing depth, the granularity of the sand decreases and the proportion of silt increases.

Fig. 5 shows that the polygons limiting the areas of sediments of different sizes overlap in some areas of the bottom. This is most often explained by the insignificant movement of sediments between expeditions (for example, in the western and eastern parts of Limenskaya Bay). Small overlaps are also due to errors in the determination of coordinates (± 3 m).

The most significant changes were observed on the eastern side of Cape Kikineiz, in the space between the groins in the Katsiveli beach area and to the east of it, where a relatively gentle artificial beach gives way to a narrow strip of boulders at the base of a rocky cliff. This is explained by the influx of debris under the influence of erosion processes during the flood-mudflow runoff of the Limenka River in Limenskaya Bay [23].

Also of interest is the overlap of various fields of sedimentary material in the inter-bubble space between the middle and eastern groins. This can be explained by anthropogenic influence in the form of beach replenishment with imported material, as well as the influence of storm waves.

Granulometric composition of bottom sediments

Granulometric analysis confirmed heterogeneous sediment distribution in Limenskaya Bay presented in [15]. In the shallow part of Limenskaya Bay up to 15 m depth, sandy material predominates (average content 76%), with inclusions of gravel and shell material near the shore at depths of up to 6 m (Fig. 6). Near the western (stations 5, 6) and eastern (stations 10, 11) shores of the bay, the fine-grained sand fraction (0.25–0.1 mm) with inclusions of medium-grained sand (0.5–0.25 mm) predominates, whereas in the center of the bay (stations 7, 8, 9) coarse-grained sand (1–0.5 mm) with inclusions of fine gravel and shell detritus (2–1 mm) predominates (Fig. 6). The sand fraction decreases west of Cape Kikineiz (< 40%) and increases east towards Simeiz (up to 80%). A good degree of sorting (1.3–1.4) is observed for sand material in the waters of Limenskaya Bay.

An increased gravel fraction is also observed near the coast west of Cape Kikineiz (59–97%) and east in the seaward section between Mount Koshka and Diva Rock (30–80%) (Fig. 7). The increased proportion of gravel in this section is explained by the landslide nature of the shoreline, which is composed of large boulders and blocks, and the contribution of the autochthonous component, represented by inclusions of large shells and shell detritus at stations above 20 m depth. This is confirmed by the results of the bottom measurements in this section (Fig. 5), as well as by the increased values of the median particle diameter (2–4 mm in the western part and

1.5–4 mm in the eastern part) and the poor sorting of the material ($S_0 = 2.1–5.9$ in the western part and 2.2–3.6 in the eastern part) (Fig. 7).

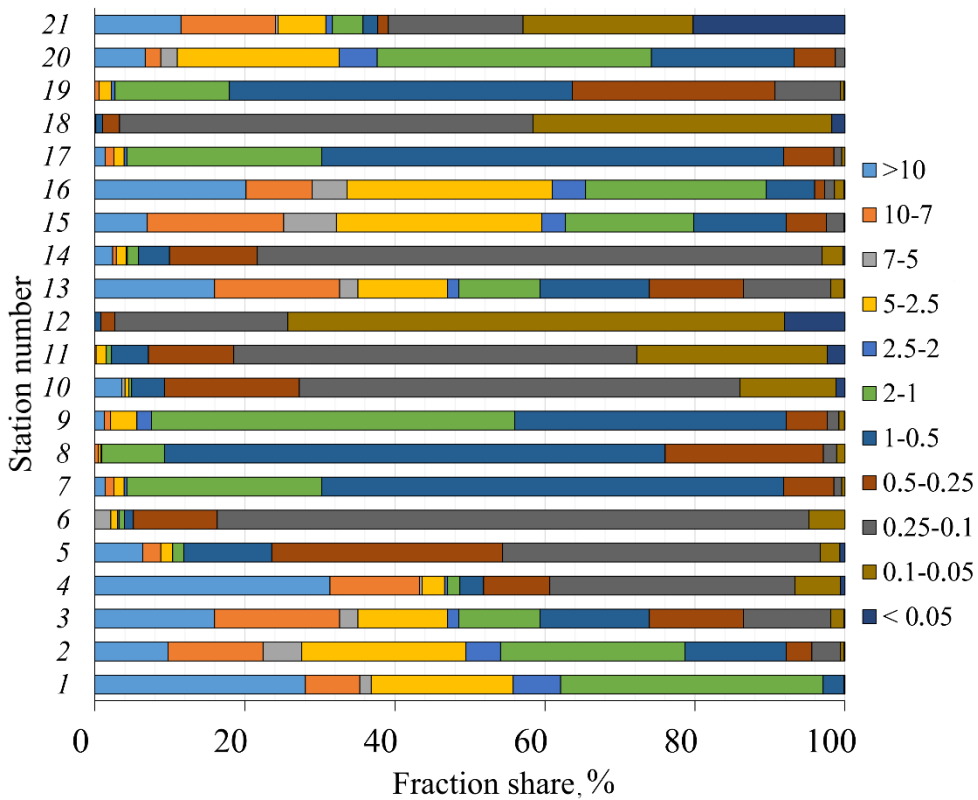


Fig. 6. Bar charts of distribution of the percentage content of size fractions in the sediments samples taken between the Katsiveli and Simeiz settlements at the SCC

The silt fraction in the samples collected is insignificant. On average, the fine-grained fraction was only 11%, of which 9% was coarse silt and 2% were fine silt and pelitic. Geographically, the minimum proportion of silt material share was recorded in the area of Cape Kikineiz (0.1–0.5%), at shallow water stations in Limenskaya Bay (0.5–0.7%) and in the area to the east of Mount Koshka (0.1–0.5%) (Fig. 7). The maximum silt fraction (41–74%) is observed in the seaward part of the study area, deeper than the 21 m isobath. This is in agreement with the results of [14, 16], which found that the dynamics of fine-grained material is limited by the 10 m isobath, with maximum values being reached from the 20 m isobath onwards. Such a low proportion of silt in the surface sediment layer, even compared to the data described in [14], is mainly explained by the sampling depth. On average, the sampling depth in 2022 was 18 m, in 2012–25 m. The increased proportion of fine-grained silt material near the eastern shore of Limenskaya Bay, as well as the increased values of the fine-grained sand fraction in this area, are associated with the abrasive nature of the coast in the central part of the bay and the peculiarities of the sediment fraction dynamics in this area.

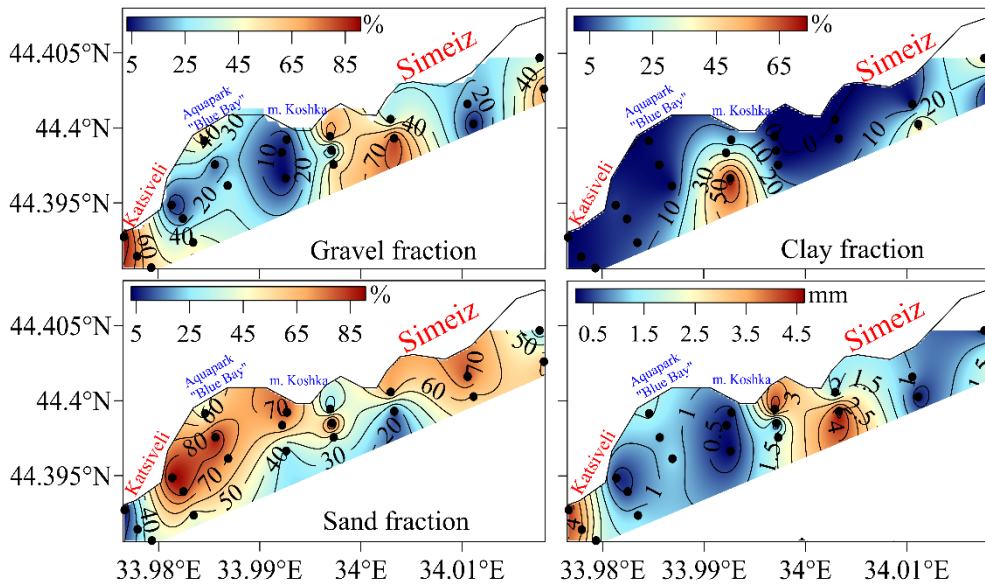


Fig. 7. Spatial distribution of particle size fractions (%) and median particle diameter (mm) in the surface layer of bottom sediments between the Katsiveli and Simeiz settlements at the SCC

For some stations (stations 2, 8, 10) in Limenskaya Bay, a comparison of the grain size distribution of the sediments with the results of previous studies in this area was additionally carried out. It was found that the results of the grain size distribution analysis at the selected stations were in good agreement, and no significant changes in the structure of the spatial distribution of sediments were observed (Fig. 8). For station 2, located in the western part of the study area in the Cape Kikineiz area, the predominance of the gravel fraction of various sizes with inclusions of coarse sand remains, and the correlation coefficient of the two-year data was 0.71. Discrepancies in the ratio of fractions in this area are explained by active hydrodynamic processes in the 10-15 m depth drop area, as well as the intensive influx of coarse gravel and pebbles from the coastal zone. This is confirmed by the results of [16], which studied the dynamics of the bottom sediments in Limenskaya Bay using numerical modeling methods. For station 8, located in the central part of the bay, the data ratio is even higher (correlation coefficient 0.90). The dominant fractions of coarse and medium sand are preserved and the proportion of fine gravel has decreased. This indicates an insignificant redistribution of material in this area. The features of accumulation of sand fractions in the center of the bay are confirmed by the results of model calculations of sediment dynamics under the influence of storm impact [16]. For station 10, located at the foot of Mount Koshka in the eastern part of the bay, changes in particle size distribution are minimal (correlation coefficient is 0.94). The change in the dominant fraction of fine sand is tenths of a percent (58.7% in 2011 and 59.1% in 2022). The decrease of the silt fraction from 28 to 13% and the increase of the coarse sand fraction from 8 to 18% are explained by the location of the station closer to the coast

in 2022, as well as an insignificant redistribution of the fractions due to lithodynamic processes. In [16] it is noted that fine-grained sand and silt fractions in the eastern part of Limenskaya Bay can be shifted beyond the 14 m isobath during storm impacts.

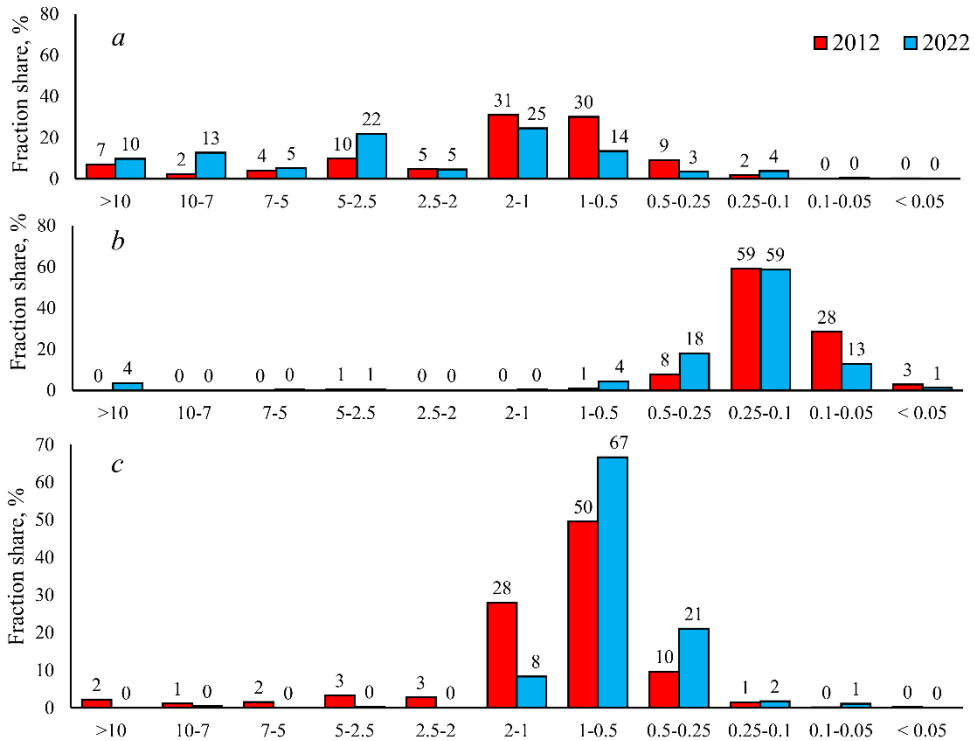


Fig. 8. Comparison of the fractions of granulometric composition of bottom sediments in Limenskaya Bay at stations 2 (a), 8 (b) and 10 (c) with the data obtained in 2012 [14]

Conclusion

This study presents an updated granulometric map of surface sediments in the sublittoral part of the shelf of the Southern Coast of Crimea in the vicinity of Limenskaya Bay. The granulometric composition of the bottom sediments is of crucial importance for the diagnosis of the ecological state of the coastal zone and the estimation of the geomorphological characteristics of a coastal area for the planning of recreational construction and coastal protection.

The obtained data show that the sea bottom in the coastal and sublittoral areas of Limenskaya Bay is currently covered with sedimentary material of heterogeneous composition and uneven spatial distribution. The shallowest part (0–10 m) is dominated by boulder-pebble sediments, which are actively moving under the influence of storm impacts and anthropogenic activity. At the same time, additional high-precision surveys are required to provide a quantitative estimate of changes in bottom relief caused by active wind and wave action. In deeper areas (5–15 m) of the Limenskaya Bay water area, the bottom is mainly covered with well-

sorted sand sediments. In the western and eastern parts of the surveyed polygon, the gravel fraction predominates, which is explained by the collapse type of the shores. There is also an increase in the contribution of large shells and shell debris. At depths greater than 20 m, the silt fraction increases – consistent with known dynamics of sediment fractions in the study area. Comparison of the results with data from previous studies showed that in the central part of the bay and in the cape areas the fractional content of the fractions remains similar and that changes in the ratio of sand and gravel material can be attributed to lithodynamic processes in the coastal zone and material redistribution. Our findings align with prior studies in this region.

Methodologically, the presented paper showed that echolocation data can be used to study sedimentary material in areas of the sea bottom where sampling with a bottom grab is impossible due to the abundance of boulders and rock debris.

REFERENCES

1. Egorov, V., 2021. *Theory of Radioisotopic and Chemical Homeostasis of Marine Ecosystems*. Cham, Switzerland: Springer, 320 p. (Springer Oceanography Series). <https://doi.org/10.1007/978-3-030-80579-1>
2. Goryachkin, Yu.N., ed., 2015. [*Current State of the Crimean Coastal Area*]. Sevastopol: ECOSI-Gidrofizika, 252 p. (in Russian).
3. Goryachkin, Yu.N. and Dolotov, V.V., 2019. *Sea Coasts of Crimea*. Sevastopol: Colorit, 256 p. (in Russian).
4. Belyaev, V.I., Doroguntsov, S.I., Sovga, E.E. and Nikolaenko, T.S., 2001. Estimation of Degree of Anthropogenic Loads on Coastal Zones and Ecotons of the Black Sea Coast of Ukraine. *Morskoy Gidrofizicheskiy Zhurnal*, (1), pp. 55-63 (in Russian).
5. Gurova, Y.S., Gurov, K.I. and Orekhova, N.A., 2022. Characteristics of Bottom Sediments in the Coastal Areas of the Crimean Peninsula. *Land*, 11(11), 1884. <https://doi.org/10.3390/land11111884>
6. Blatov, A.S. and Ivanov, V.A., 1992. *Hydrology and Hydrodynamics of the Black Sea Shelf Zone*. Kiev: Naukova Dumka, 244 p. (in Russian).
7. Goryachkin, Yu.N. and Repetin, L.N., 2009. Storm Wind and Wave Regime near the Black Sea Coast of Crimea. In: *Ecological Safety of Coastal and Shelf Zones and Comprehensive Use of Shelf Resources*. Sevastopol: ECOSI-Gidrofizika. Iss. 19, pp. 56-69 (in Russian).
8. Kondratev, S.I., Varenik, A.V., Vnukov, Yu.L., Gurov, K.I., Kozlovskaya, O.N., Kotelianets, E.A., Medvedev, E.V., Orekhova, N.A., Svishchev, S.V., [et al.], 2016. Blue Bay as a Sub-Satellite Ground for Evaluating Hydrochemical Characteristics in the Shelf Areas of the Crimea. *Physical Oceanography*, (1), pp. 48-59. <https://doi.org/10.22449/1573-160X-2016-1-48-59>
9. Ivanov, V.A., Kuznetsov, A.S. and Morozov, A.N., 2019. Monitoring Coastal Water Circulation along the South Coast of Crimea. *Doklady Earth Sciences*, 485(2), pp. 405-408. <https://doi.org/10.1134/S1028334X19040044>
10. Artamonov, Yu.V., Skripaleva, E.A., Fedirko, A.V., Shutov, S.A., Derjushkin, D.V., Shapovalov, R.O., Shapovalov, Yu.I. and Shcherbachenko, S.V., 2020. Waters Circulation in the Northern Part of the Black Sea in Summer – Winter of 2018. *Ecological Safety of Coastal and Shelf Zones of Sea*, (1), pp. 69-90. <https://doi.org/10.22449/2413-5577-2020-1-69-90> (in Russian).
11. Dulov, V.A. and Ivanov, V.A., eds., 2014. *Monitoring of the Coastal Zone in the Black Sea Experimental Sub-Satellite Testing Area*. Sevastopol: ECOSI-Gidrofizika, 526 p. (in Russian).

12. Nasedkin, E.I., Kuznetsov, A.S., Tzikhotskaya, N.N. and Klyushina, A.K., 2005. Monitoring of Seasonal Changes in the Mineral Composition of Suspended Matter. In: *Ecological Safety of Coastal and Shelf Zones and Comprehensive Use of Shelf Resources*. Sevastopol: ECOSI-Gidrofizika. Iss. 12, pp. 236-241 (in Russian).
13. Nasedkin, E.I., Ivanova, A.N., Kuznetsov, A.S., Klyushina, A.K., Dovbysh, S.N. and Timofeeva, Zh.B., 2009. Some Results of Studies of the Influence of Meteorological Factors on the Processes of Modern Sedimentation. In: *Ecological Safety of Coastal and Shelf Zones and Comprehensive Use of Shelf Resources*. Sevastopol: ECOSI-Gidrofizika. Iss. 19, pp. 44-55 (in Russian).
14. Alekseev, D.V., 2013. [Modeling of Bottom Sediment Transport in Blue Bay Region of the Black Sea]. *Reports of the National Academy of Sciences of Ukraine*, (12), pp. 94-100 (in Russian).
15. Ovsyany, E.I. and Gurov, K.I., 2016. Research of Organic Carbon and Carbonate Content in the Bottom Sediments of the Crimean Southern Coast Shelf. *Physical Oceanography*, (1), pp. 60-70. <https://doi.org/10.22449/1573-160X-2016-1-60-70>
16. Gurov, K.I. and Fomin, V.V. 2017. The Dynamics of Sediments Grain-Size in Limensky Gulf. In: *Proceedings of the Thirteenth International MEDCOAST Congress on Coastal and Marine Sciences, Engineering, Management and Conservation, MEDCOAST 2017*. Dalyan, Mugla, Turkey: MEDCOAST Foundation. Vol. 2, pp. 925-934.
17. Denisov, V.I. 2018. Suspended Matter Fluxes in the Coastal Part of the Shelf in the Russian Sector of the Black Sea. In: *The Black Sea System*. Moscow: Scientific World, pp. 397-425. <https://doi.org/10.29006/978-5-91522-473-4.2018.397> (in Russian).
18. Mirzoeva, N.Y., Gulin, S.B., Sidorov, I.G and Gulina, L.V., 2018. Estimation of Sedimentation and Sedimentation Rates in the Coastal and Deep-Water Areas of the Black Sea Using Natural and Anthropogenic (Chernobyl) Radionuclides. In: *The Black Sea System*. Moscow: Scientific World, pp. 659-670. <https://doi.org/10.29006/978-5-91522-473-4.2018.659> (in Russian).
19. Shestopalov, V.M., Boguslavskiy, S.G., Boguslavskiy, A.S., Ivanov, V.A. and Kuznetsov, A.S., 2005. Engineering-Geological Hazards of the Coastal Zone of the Mountainous Crimea. In: *Ecological Safety of Coastal and Shelf Zones and Comprehensive Use of Shelf Resources*. Sevastopol: ECOSI-Gidrofizika, (13), pp. 43-61 (in Russian).
20. Melnik, V.I., 2001. Influence of the Terrestrial River Network on Topography and Sedimentation in the Black Sea. In: *Ecological Safety of Coastal and Shelf Zones and Comprehensive Use of Shelf Resources*. Sevastopol: ECOSI-Gidrofizika, (4), pp. 112-124 (in Russian).
21. Kondratev, S.I., Varenik, A.V., Vnukov, Yu.L., Gurov, K.I., Kozlovskaya, O.N., Kotelianets, E.A., Medvedev, E.V., Orekhova, N.A., Svishchev, S.V., [et al.], 2016. Blue Bay as a Sub-Satellite Ground for Evaluating Hydrochemical Characteristics in the Shelf Areas of the Crimea. *Physical Oceanography*, (1), pp. 48-59. <https://doi.org/10.22449/1573-160X-2016-1-48-59>
22. Goryachkin, Yu.N. and Efremova, T.V., 2022. Anthropogenic Impact on the Lithodynamics of the Black Sea Coastal Zone of the Crimean Peninsula. *Ecological Safety of Coastal and Shelf Zones of Sea*, (1), pp. 6-30. <https://doi.org/10.22449/2413-5577-2022-1-6-30>
23. Boguslavsky, A.S. and Kazakov, S.I., 2021. Features of Lithodynamics of Pebble Beaches at South Coast of Crimea. In: *InterCarto. InterGIS. GI Support of Sustainable Development of Territories: Proceedings of the International Conference*. Moscow: Faculty of Geography MSU. Vol. 27, part 3, pp. 85-97. <https://doi.org/10.35595/2414-9179-2021-3-27-85-97> (in Russian).

Submitted 18.07.2024; approved after review 12.09.2024;
accepted for publication 29.01.2025.

About the authors:

Andrei V. Bagaev, Leading Researcher, Shelf Hydrophysics Department, Marine Hydrophysical Institute of RAS (2 Kapitanskaya Str., Sevastopol, 299011, Russian Federation), CSc (Phys.-Math.), **ORCID ID: 0000-0003-4018-7642**, **ResearcherID: K-5373-2016**, **Scopus Author ID: 57189266640**, **SPIN-code: 5426-7176**, a.bagaev1984@mhi-ras.ru

Konstantin I. Gurov, Researcher, Biogeochemistry Department, Marine Hydrophysical Institute of RAS (2 Kapitanskaya Str., Sevastopol, 299011, Russian Federation), CSc (Geogr.), **ORCID ID: 0000-0003-3460-9650**, **ResearcherID: L-7895-2017**, **SPIN-code: 5962-7697**, gurovki@gmail.com

Suri A. Nuriev, Leading Research Engineer, Hydrophysical Subsatellite Research Laboratory, Black Sea Hydrophysical Subsatellite Polygon of Marine Hydrophysical Institute of RAS (9 Academician V. Shuleikin Str., Katsiveli, 298688, Russian Federation), **ORCID ID: 0009-0008-1760-8844**, **SPIN-code: 2240-3635**, surinuriev@gmail.com

Contribution of the co-authors:

Andrei V. Bagaev – general scientific supervision of the research, data preparation, analysis and synthesis of research result, interpretation of the results, processing and description of the study results, analysis and preparation of initial conclusions

Konstantin I. Gurov – formulation of goals and objectives of the study, sampling, presentation of data in the text and their analysis, paper correction, discussion of the study results, preparation of graphic and text materials, formulation of the conclusions

Suri A. Nuriev – data processing, analysis and interpretation of data, participation in the discussion of the paper materials

The authors have read and approved the final manuscript.

The authors declare that they have no conflict of interest

Features of Hydrological Regime nearby the Pacific Coast of the Northern Kuril Islands Based on Ship Oceanographic Surveys

G. V. Shevchenko^{1, 2, ✉}, V. N. Chastikov¹, V. A. Ulchenko³

¹ Sakhalin Branch of Russian Federal Research Institute of Fisheries and Oceanography,
Yuzhno-Sakhalinsk, Russian Federation

² Institute of Marine Geology and Geophysics, Far Eastern Branch of Russian Academy of Sciences,
Yuzhno-Sakhalinsk, Russian Federation

³ Russian Federal Research Institute of Fisheries and Oceanography, Moscow, Russian Federation
✉ Shevchenko_zhora@mail.ru

Abstract

Purpose. This study aims to examine the vertical distributions of temperature, salinity, and geostrophic currents along repeated sections during different seasons, based on oceanographic survey data.

Methods and Results. The analysis is based on data from seven surveys conducted in spring (May), summer (July–September), and autumn (November) along four selected transects crossing the shelf and continental slope off the southeastern coast of Kamchatka, the Fourth Kuril Strait, and the Severgin Strait. Variations in the surface heated layer, as well as in the cold and warm intermediate layers, are assessed. It is shown that in spring and autumn, the cold intermediate layer extends throughout the water column, whereas in the deep-sea area, it is underlain by a warm intermediate layer. In autumn, the upper boundary of the cold intermediate layer deepens, likely due to wind-wave mixing. Freshened water (with salinity as low as 31.5 PSU), resulting from ice melt in the Bering Sea, is observed off the southeastern coast of Kamchatka in July. However, salinity in the study area remains generally high. Calculated geostrophic current velocities indicate that a consolidated southwestward flow, extending through the entire water column and most pronounced above the slope, is observed only in spring—likely a remnant of winter circulation patterns. In summer and autumn, currents are more variable, with different directions in different layers and along various parts of the transects.

Conclusions. The analysis of oceanographic survey data demonstrates that the underwater Vityaz Ridge significantly influences the hydrological conditions in the Northern Kuril Islands region. Specifically, warm intermediate layer waters weakly penetrate into the northern part of the trough between the ridge and the Kuril Islands, while the cold intermediate layer develops down to depths of 500 m. In this area, current directions often differ from those over the continental slope. Although rare, negative seawater temperatures are occasionally recorded in the cores of the cold intermediate layer. The Kamchatka and Kuril currents are clearly defined in spring and become weaker during summer and autumn.

Keywords: northern Kuril Islands, seawater temperature, salinity, oceanographic section, Kamchatka Current, Kuril Current, cold intermediate layer, warm intermediate layer

Acknowledgements: This work was carried out within the framework of the state assignment of FSBSI VNIRO under the theme: “Regular observations of the distribution, quantity, quality, and reproduction of aquatic bioresources that are the objects of fisheries, as well as their habitat.”

For citation: Shevchenko, G.V., Chastikov, V.N. and Ulchenko, V.A., 2025. Features of Hydrological Regime nearby the Pacific Coast of the Northern Kuril Islands Based on Ship Oceanographic Surveys. *Physical Oceanography*, 32(2), pp. 253-269.

© 2025, G. V. Shevchenko, V. N. Chastikov, V. A. Ulchenko

© 2025, Physical Oceanography



Introduction

The waters of the northwestern Pacific Ocean adjacent to the Northern Kuril Islands constitute one of Russia's most active fishing zones. Significant amounts of cod, halibut, flounder, saury, and Pacific salmon are harvested in this region. This economic relevance underscores the importance of studying the oceanographic – primarily thermal – conditions, which play a key role in shaping the habitat of marine biota.

In addition to practical relevance, this area is of considerable scientific interest due to the transformation of the Kamchatka Current. Near the Fourth Kuril Strait, the current bifurcates into the West Kamchatka Current, which turns toward the Sea of Okhotsk, and the Kuril Current, which continues southwestward. Investigating the seasonal variability of these currents is particularly important, as they remain insufficiently studied. Moreover, current formation is influenced by the complex bottom topography, especially south of the Fourth Kuril Strait, where the underwater Vityaz Ridge runs parallel to the island chain. Water exchange with the Sea of Okhotsk through the Kuril Straits must also be considered [1].

Due to the remoteness of the region, the Sakhalin branch of VNIRO conducted oceanographic surveys only occasionally – three times in total: in April 2013 and in May 2015 and 2016, as part of ichthyoplankton studies. In contrast, the Pacific branch of VNIRO regularly performs hydrological profiling in this area. However, its analyses have mainly focused on long-term changes in the hydrological regime of the northwestern Pacific Ocean (NWPO) in the context of global warming [2–4].

The most comprehensive surveys of the continental slope off the northern Kuril Islands and southeastern Kamchatka were carried out from 1992 to 2000 during scientific support for industrial fishing by Japanese vessels. Notably, these operations took place outside Russia's 12-mile territorial zone, covering only a limited portion of the shelf area. Most of these data were summarized by G.A. Kantakov [5], who introduced a useful methodological innovation by selecting a standard section perpendicular to the coast of Paramushir Island. Oceanographic profiling was relatively frequent along this line, allowing it to be treated as a repeatable reference section. This approach enabled analysis of the variability in depth-averaged seawater temperature, salinity, and geostrophic currents. Among 14 analyzed surveys, the strongest Kamchatka Current velocities were recorded in October 1992 (16 cm/s) and in May 1992 and 1995 (10 cm/s), while the weakest were observed during summer (1–5 cm/s).

More detailed studies of hydrological conditions on the shelf and continental slope are presented in [1, 6, 7]. For the present work, we selected data from a substantial number of oceanographic profiles collected during cruises by POI FEB RAS, FERHRI of Roshydromet, and the TINRO-Center, focusing on several cross-sections [6]. Of these, three were particularly relevant, with endpoints located near southeastern Kamchatka, the Fourth Kuril Strait, and the Kruzenshtern Strait. This extensive dataset enabled the construction of generalized vertical distributions of temperature and salinity across seasons, down to depths of 5000 m.

These studies revealed that hydrological conditions along the sections were similar. The vertical structure consisted of a surface-heated layer about 30 m thick, a cold intermediate layer (CIL) down to 250 m, a warm intermediate layer (WIL), and deeper waters. In the cold season, cooling of the surface layer causes the CIL to lose its intermediate character, especially on the shelf, where water temperature becomes uniform from surface to bottom by December. In deeper areas, however, the CIL is underlain by the WIL, which persists year-round.

The CIL is a key feature of the hydrological regime not only in the study area but across the NWPO as a whole [8, 9]. As shown in [10], CIL waters originating from both the Bering Sea and the Sea of Okhotsk are transported southwestward along the Kuril Island chain.

This study follows a similar approach to that in [5, 6], selecting four sections in different parts of the study area, closely aligned with the positions in [6] (discussed in detail below). Vertical profiles of temperature, salinity, and geostrophic currents were analyzed along these sections.

We also reference [11], which examined monthly average anomalies of sea surface height (mean dynamic topography) in the Sea of Okhotsk and adjacent waters, including the northern Kuril region. These surfaces were derived from TOPEX/Poseidon satellite altimetry data collected over a 10-year period (September 1992 to October 2002), and used to calculate gradient currents for different seasons.

The most intense water circulation in the study area occurs during winter. In this season, sea level is higher near the coast and lower in the open ocean, corresponding to a well-defined Kamchatka Current, which partially flows into the Sea of Okhotsk (mainly through the Fourth Kuril Strait, and to a lesser extent through the Severgin Strait), forming the West Kamchatka Current. Another branch continues southwest along the Kuril chain as the Kuril Current. The main flow of the latter bypasses the Vityaz Ridge from the east, diverted offshore from the island chain.

In spring, sea surface height gradients weaken across the region, and the Kamchatka and Kuril currents become less distinct, with the West Kamchatka Current nearly disappearing. Multiple eddy structures emerge, generating multidirectional flows and scattered, chaotic circulation. In summer, sea level in the shelf zone off southeastern Kamchatka and the northern Kuril Islands is lower than in the open ocean and the deep trench area, though the gradients remain weaker than in winter. A northeastward flow develops over the continental slope, some distance offshore.

This summer pattern of low coastal sea level persists into autumn, likely driven by prevailing northwesterly winds associated with the winter monsoon. A northeastward current continues to be observed above the continental slope, while the Kamchatka and Kuril currents remain weak.

It is important to note that [11] analyzed sea level anomalies relative to an average surface representing long-term, slowly varying currents. Nevertheless, comparing this broader view with in situ oceanographic data on specific cross-sections remains valuable. Despite significant intra-annual [12, 13] and interannual

[14, 15] variability in hydrological conditions, circulation, and sea level, such comparisons offer key insights.

This study places particular emphasis on the influence of the Vityaz Ridge in shaping hydrological conditions south of the Fourth Kuril Strait – especially within the poorly studied trough between the ridge and the Kuril Islands.

Thus, the objective of this work is to investigate the vertical distributions of temperature, salinity, and geostrophic currents along repeated sections across different seasons, using oceanographic survey data.

Observation materials and research methods

Between 1992 and 2000, 25 oceanographic surveys were conducted over the shelf and continental slope of the northern Kuril Islands: one in winter (December) and eight in each of the other seasons. Observations were performed to depths of 1000 meters or to the seabed in shallower regions using an Alec Electronics oceanographic probe.

To analyze current variability, seven of the most detailed surveys were selected from the total of 25. These included several repeated cross-shelf sections, which were consistently surveyed in each of the selected studies (see Table).

Fig. 1 illustrates the locations of the selected sections in relation to the oceanographic stations occupied during the cruise from April 30 to May 3, 1996. Two of these sections were situated off the southeastern coast of Kamchatka – one near the southeastern tip of the peninsula, close to the First Kuril Strait. The third was positioned near the Fourth Kuril Strait, which separates the islands of Paramushir and Onkotan. The fourth was located in the area of the Severgin Strait, between the islands of Kharimkotan and Shiashkotan. These sections can be considered standard; while station coordinates were not fixed precisely, they remained closely aligned across surveys.

Oceanographic surveys in the region of the northern Kuril Islands

No. of cruise	Year	Period	Number of CTD-stations	Depth range, m
1	1994	14–19 July	91	189–784
2	1994	10–15 September	48	196–794
3	1995	27–30 August	74	178–833
4	1996	30 April – 3 May	80	197–810
5	1996	10–15 July	77	200–750
6	1996	4–7 September	83	192–705
7	1998	15–26 November	100	80–683

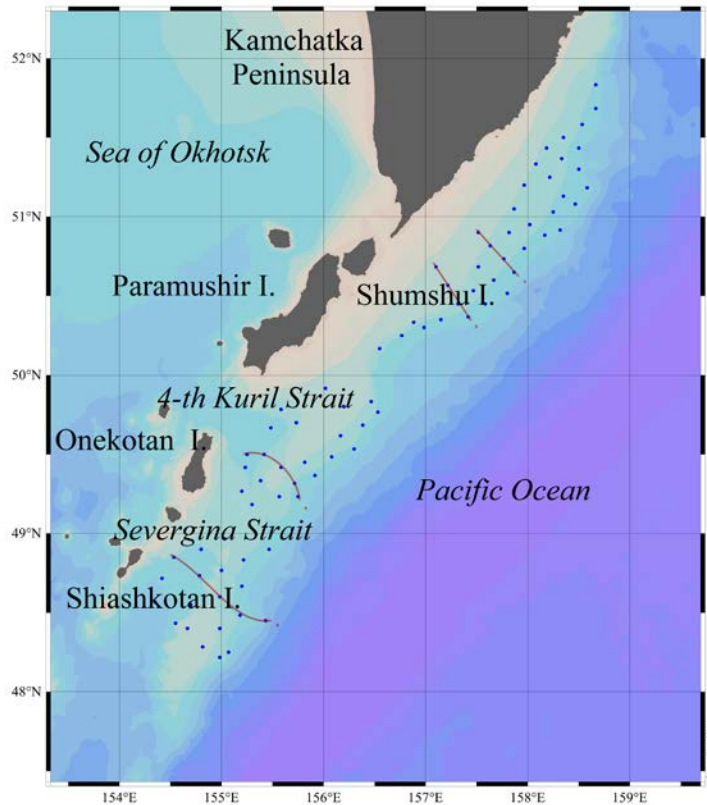


Fig. 1. Location of oceanographic stations occupied on April 30 – May 3, 1996. Red lines indicate the positions of the selected sections

This made it possible to examine the features of oceanographic conditions and, most importantly, the velocity and direction of geostrophic currents near the northern Kuril Islands in different seasons (excluding winter). Most of the selected surveys were conducted during the warm season: two (in July and September) in 1994 and 1996, one in August 1995, one in spring (April – May 1996), and one in autumn (November 1998). It should be noted that in the Far Eastern seas, September is generally considered part of the summer season due to its warm thermal conditions, second only to August. Therefore, the autumn oceanographic conditions could only be assessed using data from the November 1998 cruise.

It is important to note that estimates of geostrophic currents can be influenced by strong diurnal tidal currents, which, as shown in [16], occur in this region due to the presence of trapped shelf waves.

Given the number of surveys and their uneven monthly distribution, it was difficult to draw definitive conclusions about the seasonal and interannual variability of alongshore currents in the study area. Furthermore, as noted earlier, the surveys were carried out beyond the 12-mile zone and almost entirely excluded the shelf area. Nevertheless, despite these limitations, the findings remain of significant interest. Vertical distributions of temperature, salinity, and geostrophic current

velocity along the selected sections, based on the oceanographic survey results, are discussed below. These distributions were produced using OceanDataView, a specialized software tool for processing oceanographic data (available at: odv.awi.de). In this software, current characteristics are derived from the differences in dynamic height between adjacent oceanographic stations. Dynamic heights were calculated at each depth level (after interpolation to a standard 5-meter depth step). The resulting geostrophic velocities are representative of the midpoints between the paired stations.

A brief note on the bottom topography of the study area: it differs markedly between the northern and southern parts. In the north – off the southeastern coast of Kamchatka and near Shumshu and Paramushir Islands – there is an extended, relatively shallow shelf followed by a steep continental slope descending into a deep-sea trench. In contrast, in the southern region, near Onekotan, Kharimkotan, and Shiashkotan Islands, the shelf is shorter and deeper. Approximately 100 km offshore lies the Vityaz Ridge, which terminates near the southern tip of Paramushir Island. Between the islands and the ridge lies a unique trough, with depths ranging from 1500 m in the south to 300 m in the north. These bottom topography features have a significant influence on the formation of hydrological conditions and the pattern of water circulation in the study area.

Results and discussion

Survey on 30 April – 3 May 1996. The oceanographic studies conducted in late April and early May are of particular interest, as they represent the only data from early spring, a period when circulation patterns characteristic of the winter season may still be present. As mentioned earlier, during the cold season, all elements of the anticyclonic circulation system in the Sea of Okhotsk become more pronounced [11]. In particular, a steady southwesterly flow is observed in the study area.

In the vertical temperature distribution along the northernmost section *I* (Fig. 2), initial signs of surface layer warming are visible, but only in the central and eastern parts of the section (up to 2.5 °C). The cold intermediate layer (CIL) is well pronounced, although its temperature exceeded 0.5 °C throughout the section. As noted in [6], the CIL loses its intermediate-layer characteristics over the shelf during the cold season, and the water column becomes vertically homogeneous. However, in the eastern part of the section, it is underlain by the warm intermediate layer (WIL), and a surface-heated layer is already beginning to form.

The boundary between the CIL and WIL – conventionally marked by the 3 °C isotherm – is clearly seen in the eastern deep-water part of the section. It deepens to around 280 m at the edge of the section and reaches the continental slope at a depth of approximately 400 m. The highest seawater temperature (3.5 °C) was recorded at the station furthest offshore, at a depth of about 350 m.

No very low salinity values typically associated with freshwater inflow from the Bering Sea were observed in this section, suggesting that such waters had not reached the area during the observation period. The 33 PSU isohaline was found at

a depth of about 100 m, dipping to 200 m in the western part of the section. Maximum salinity values exceeding 34.5 PSU were recorded at depths of about 600 m.

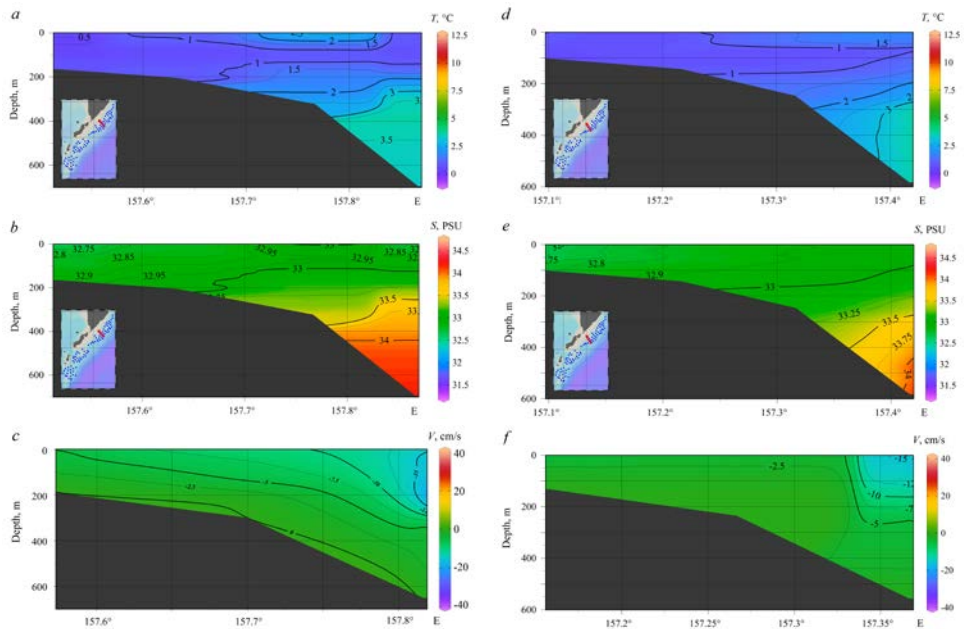


Fig. 2. Vertical distributions of seawater temperature (*a, d*), salinity (*b, e*), and geostrophic currents (*c, f*) along sections 1 (*left*) and 2 (*right*) in May 1996

Water stratification was well developed, with density anomaly values ranging from 26 to 30 kg/m³. In the lower layers, upward-sloping isopycnals were observed in the eastern part of the section. A southward flow was present along the entire section, with maximum velocities near the eastern boundary. The velocity decreased westward and with depth, reaching zero near the bottom.

Oceanographic conditions in section 2 were similar to those in section 1 (Fig. 2). In the upper layer, signs of warming were observed only in the eastern part, and these were weaker, with maximum temperatures around 1.5 °C.

Signs of surface layer warming along section 3 were as weak as those observed along section 2. A small area with temperatures reaching up to 3 °C in the eastern part of the section may be considered such a sign (Fig. 3). The minimum temperatures within the cold intermediate layer (CIL) were about 0.7 °C. Warmer water appeared below 300 m, and maximum temperatures exceeding 3.5 °C were found near the eastern edge of the section.

The salinity distribution was similar to that observed in the previously discussed sections. Very low salinity values were not detected, but the 33 PSU isohaline was found slightly deeper – at about 200 m. At depths below 350 m, salinity exceeded 33.5 PSU, reaching 34 PSU at the eastern boundary.

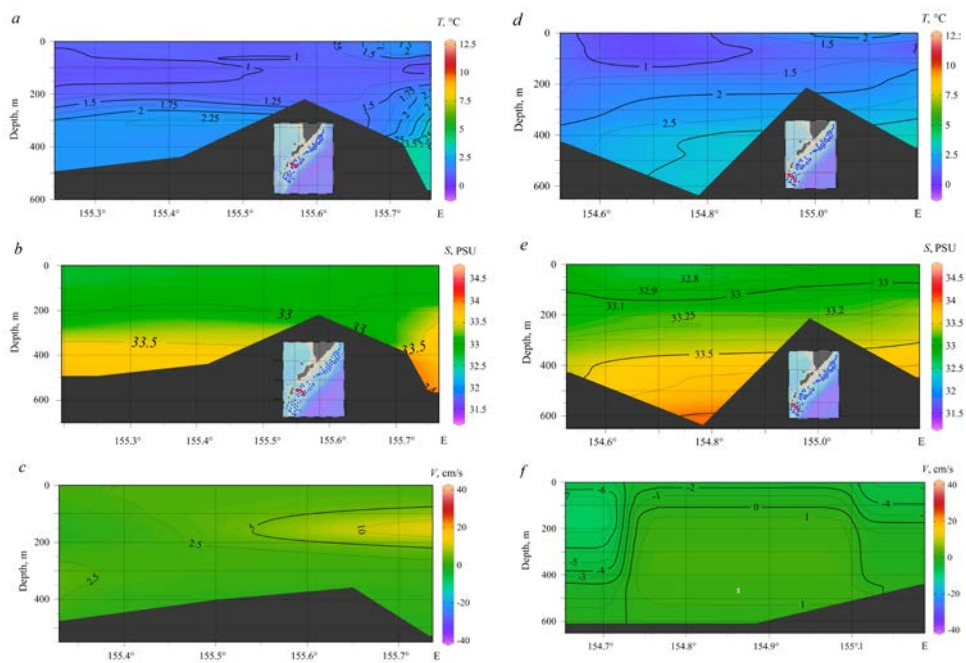


Fig. 3. Vertical distributions of seawater temperature (*a*, *d*), salinity (*b*, *e*), and geostrophic currents (*c*, *f*) along sections 3 (*left*) and 4 (*right*) in May 1996

Variations in isotherms and isohalines occurred in the area of the underwater ridge, though they were not as pronounced as in some other surveys discussed later. The most likely cause of changes in oceanographic parameters near this bottom feature is tidal mixing, as diurnal shelf waves generating strong tidal currents have been identified in this area [16].

The slopes of isopycnals in the upper 200-m layer were insignificant, becoming more noticeable at greater depths, particularly east of the underwater ridge. Here, a well-defined southward flow with a maximum speed of 25 cm/s was observed near the section boundary. On the western side of the ridge, the currents were weak and mainly northward-oriented, turning southward near the boundary.

Along section 4, only the earliest signs of surface layer warming were also observed. Two small areas with temperatures up to 1.5 °C were identified. One of them, located at the eastern edge of the section (Fig. 3), extended down to depths of 50–80 m. In the eastern part, cold water with a temperature slightly below 1 °C reached the surface. The warmest water (above 3 °C) was concentrated in the bottom layer. Current velocities throughout most of the section were negative (indicating southward flow along the coast) and relatively weak (up to 5 cm/s).

Thus, in late April to early May 1996, the Kamchatka Current remained strong and was primarily observed over the continental slope. The Kuril Current, which was also evident over the western slope of the deep-sea trench, showed varying intensity

along sections 3 and 4 – it was weaker in the latter. A weak northward flow was noted on the western side of the Vityaz Ridge, consistent with the findings of [11].

Survey of 14–19 July 1994. In the northern Kuril Islands region, July marks the beginning of the summer season when a thin, warmed surface layer starts to form, although temperatures are still far from seasonal maxima. Here, we examine the results of an oceanographic survey conducted in mid-July 1994 in greater detail.

By mid-July, the thin surface layer had warmed to 5–6 °C. According to the survey data, a distinct cold intermediate layer (CIL) was observed between 50 and 200 m, with temperatures below 2 °C, increasing to 3.5–4 °C at depths exceeding 250 m. The surface layer was characterized not only by higher temperatures but also by low salinity. In the western part of the section, salinity values in the thin surface layer were particularly low for the region – 31.5 PSU or less.

The most probable cause of this low-salinity water near the southeastern Kamchatka shelf is the influence of melting ice from the southwestern Bering Sea and meltwater runoff through the Kamchatka Strait. Runoff from the rivers of the Kamchatka Peninsula may have also contributed, though the estuary of the main river lies far from the section under consideration, making this influence less likely.

The 33 PSU isohaline was found at a depth of 60–65 m in the western (coastal) part of the section, rising to 50 m in the eastern part. Water with salinity over 33.5 PSU was found at depths below 200 m.

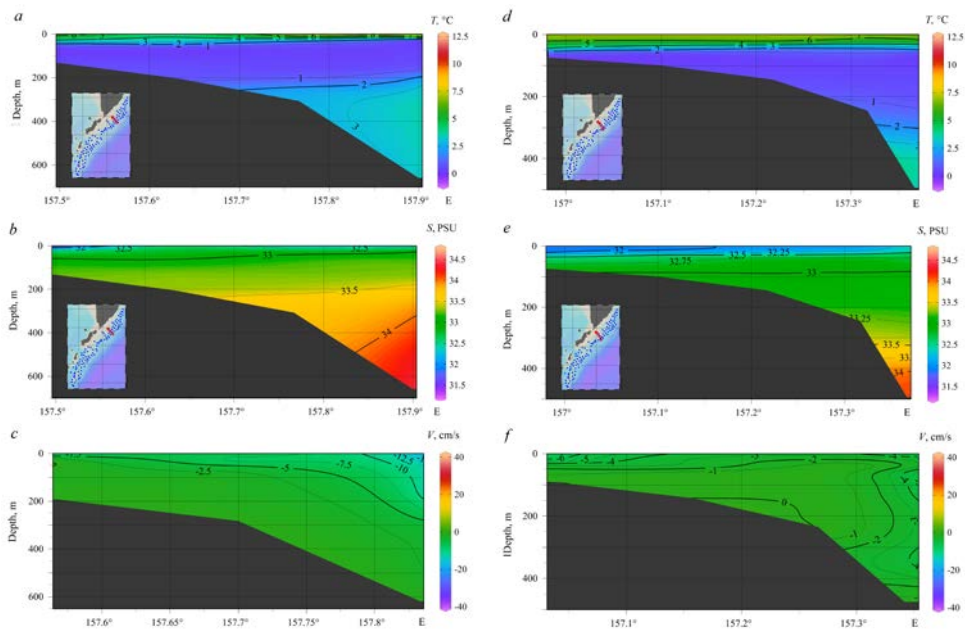


Fig. 4. Vertical distributions of seawater temperature (*a, d*), salinity (*b, e*), and geostrophic currents (*c, f*) along sections 1 (left) and 2 (right) in July 1994

The calculation of currents showed that a southward flow was observed throughout the section, with its maximum velocities (up to 10 cm/s) recorded at depths of 100–250 m near the eastern edge of the section, above the continental slope; its values decreased rapidly with depth as well as from east to west. The nature of temperature and salinity vertical distributions on section 2 is similar to that discussed above on section 1 (upper heated layer, well-defined CIL, freshened water in the surface layer), primarily in the western part of the section (Fig. 4). At the edges of the section and at depths over 200 m (over 150 m in the shallow part), the flows were directed southward, while in the central part of the section in the upper 150-m layer – northward. Maximum velocities of about 5 cm/s were recorded here; the southern component reached its maximum at the western edge of the section (up to 8 cm/s). In general, current velocities were small and did not exceed 2 cm/s. On section 3, the nature of temperature and salinity distributions differed from those considered above on the sections related to the southeastern coast of Kamchatka (Fig. 5). Here, warmer and less saline water was observed in the eastern part of the section; in general, the ridge effect on the distribution of oceanographic parameters was very pronounced. At the same time, WIL was practically absent between Onekotan Island and the Vityaz Ridge, with the CIL reaching a depth of about 500 m (its core with negative seawater temperature values was located above the ridge). The 33 PSU isohaline passed almost parallel to the 4 °C isotherm but at a slightly greater depth. High salinity values west of the underwater ridge do not allow the significant thickness of the CIL to be associated with the effect of Sea of Okhotsk water, the salinity of which does not reach such values.

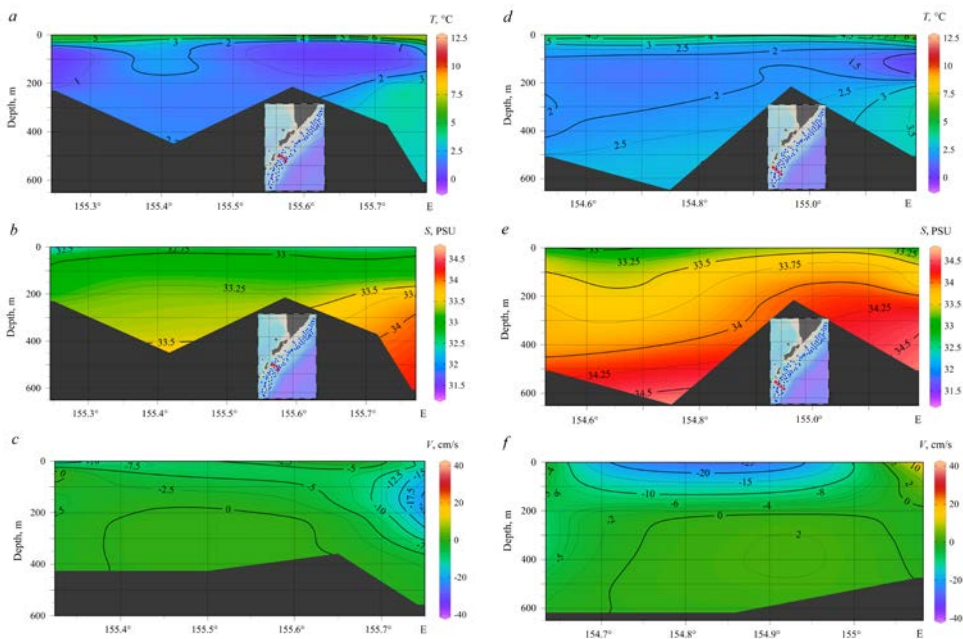


Fig. 5. Vertical distributions of seawater temperature (*a, d*) and salinity (*b, e*) as well as geostrophic currents (*c, f*) on sections 3 (*left*) and 4 (*right*) in July 1994

In the eastern part of the section, a uniform southward flow was observed; the highest velocities (up to 15 cm/s) occurred in the depth range from the surface to 250 m. In the western and central parts, the coastal flow was directed northward, with maximum velocities reaching 10 cm/s.

The lowest temperature and highest salinity values of seawater were recorded at the southernmost section 4. In the thin heated surface layer, the temperature fluctuated between 3 and 4 °C and reached 6 °C only at the easternmost station. The CIL had significant thickness, especially in the western part of the section (depth range from 50 to 500 m). In the eastern part, its lower boundary varied from 300 to 200 m in the easterly direction, with the coldest water (temperature less than 1 °C) recorded at the easternmost station. At the same station, the least saline water (down to 32.5 PSU) was also observed in the surface layer, although, in general, water with a salinity of more than 33.5 PSU predominated on the section, and at depths over 300 m – more than 34 PSU.

At the edges of the section, northward flows were observed, and the flow was very intense in the western part, with velocity reaching 20 cm/s (up to 5 cm/s in the eastern part). In the central part of the section, a southward flow was indicated. At depths over 200 m, the currents were insignificant, except at the western edge of the section.

Survey on 10–15 July 1996. Another survey was carried out at approximately the same time in 1996. In the vertical distribution of seawater temperature on sections 1 and 2, a thin heated layer with temperatures up to 6–7 °C stood out, also characterized by low salinity values of less than 32.5 PSU. A southward flow with low velocities, increasing to 10 cm/s at the eastern boundary, was observed throughout the section.

Temperature and salinity vertical distributions on section 3 were noticeably affected by the underwater ridge. The thin heated layer above it was almost absent, and the CIL had a greater thickness in the western part of the section, where the 2 °C isotherm passed near the bottom. In the eastern part, the 3 °C isotherm, taken as the CIL lower boundary, rose from a depth of about 300 m to 200 m towards the edge of the section. Geostrophic currents were multidirectional: northward in the western part of the section and southward in its eastern part.

On section 4, thermal conditions were colder than in other parts of the study area. The heated layer had maximum thickness and temperature (up to 4 °C) in the western part of the section. Northward currents, more pronounced in the western part, were observed along the edges of the section, with maximum velocity reaching 20 cm/s. Current velocity decreased to zero at a depth of about 200 m.

Survey on 27–30 August 1995. Three surveys can be attributed to the period of maximum water warming in the study area: they were carried out at the end of August 1995, in the first ten days of September 1996, and the second ten days of

September 1994. In summer 1995, high surface temperature values of 11–12 °C were noted throughout most of the study area, except for the zone near the Severgin Strait, where section 4 passes. However, the heated layer was very thin, about 10 m, and a well-defined CIL was located beneath it; in the northern section, its boundaries were at depths of about 15 to 250 m. A band of negative temperatures was found along the entire length of the section, which is quite rare and unexpected during the period of maximum warming. According to a more fragmentary survey in May 1995, water with negative temperatures in the 20–100 m layer was also observed at most stations, suggesting that the winter of that year may have been abnormally cold in the northwestern Pacific Ocean. Geostrophic currents with low velocities were differently directed in the central and eastern parts of the section.

In the southern part of the study area, on sections 3 and 4, CIL cores with negative temperatures were also identified at the edges of the sections. In deeper layers, relatively warm water was concentrated at the eastern and western boundaries of the sections and at the western slope of the Vityaz Ridge. No CIL was observed in the trough; the 2 °C isotherm reached the bottom.

A weak southward flow was found at the western edge, and a northward flow was observed in the central and eastern parts (on different sides of the ridge). Current velocity was close to zero in the rise area.

Survey on 4–7 September 1996. In the first ten days of September 1996, thermal conditions in the study area were unusually cold for this time of year – this was the main feature revealed by the oceanographic survey. The heated layer was very thin, almost absent in the western part of sections 1 and 2, and weakly expressed in the eastern part of sections 3 and 4 (the maximum temperature in the entire area was about 8 °C). The CIL thickness decreased towards the open ocean; in the southern sections west of the rise, it reached the bottom (no WIL was observed). In the western part of sections 3 and 4, a pronounced southwestward flow was observed in the trough between the Vityaz Ridge and the Kuril Islands; elsewhere, current velocities were low.

Survey on 10–15 September 1994. In the second ten days of September, surface seawater temperature had a complex spatial distribution: on section 1, warmer water was found near the shore, while on the other sections, it was located in the deep-water part. Spatial differences decreased with depth, and the CIL occupied its usual position at depths of 50 to 250 m in the northern part of the area. On section 3, west of the Vityaz Ridge, it extended down to the bottom; on section 4 – to a depth of 500 m and was underlain by WIL. Negative temperatures occurred in the CIL core at the eastern boundary of the southern sections. Salinity distributions were normal; currents were multidirectional and of low magnitude.

Survey of 15–26 November 1998. The results of soundings carried out in the second half of November were the most representative of the cold season among

all expeditions under consideration, which made them particularly valuable. The vertical distribution of seawater temperature on sections 1 and 2 (Fig. 6) shows that the surface layer had cooled to 2.5–4 °C (with increasing values from east to west). The CIL was well developed and occupied the water column at typical depths from 50 to 200 m. Temperature in the cores was slightly higher than usual – over 1 °C.

The salinity distribution was characterized by relatively low values. The 33 PSU isohaline was located quite deep (70–80 m), and salinity values above this level were observed in the western part of the section. The 34 PSU isohaline was found at depths greater than 400 m, and values above this threshold were observed only in small areas. The currents were directed southwestward throughout the sections but had relatively low velocities. This indicates that the Kamchatka Current had not yet been activated by the time of the survey.

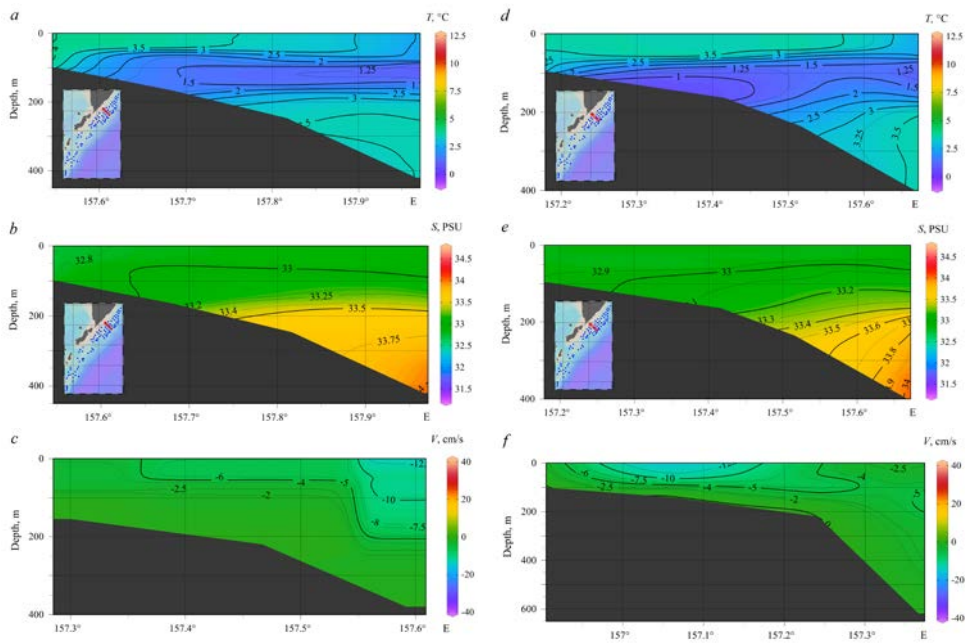


Fig. 6. Vertical distributions of seawater temperature (*a, d*), salinity (*b, e*), and geostrophic currents (*c, f*) along sections 1 (*left*) and 2 (*right*) in November 1998

In the southern part of the study area, the surface layer was further cooled to 2–3 °C. The CIL reached the surface across most of section 4 and extended to the bottom along section 3, while no WIL was observed (Fig. 7). Salinity values were relatively low; values around 33.4 PSU were recorded only in the deepest areas at the edges of the section. Across most of the section, salinity varied within a narrow range of 32.8–33.2 PSU. The velocities of the multidirectional currents were relatively low. The autumn–winter intensification of both the Kuril and Kamchatka Currents had not yet occurred.

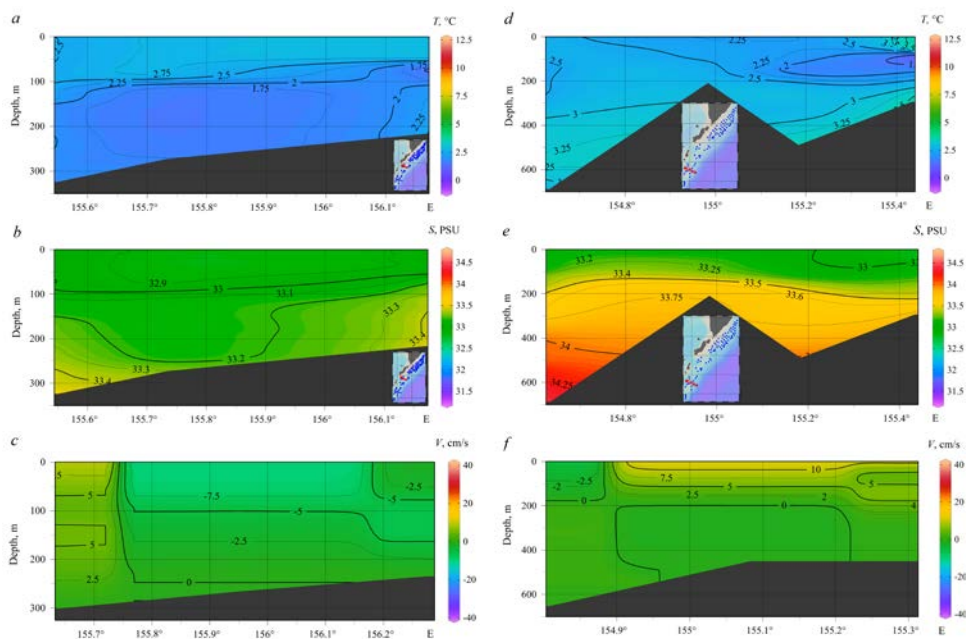


Fig. 7. Vertical distributions of seawater temperature (*a, d*), salinity (*b, e*), and geostrophic currents (*c, f*) along sections 3 (*left*) and 4 (*right*) in November 1998

Let us summarize the results of the study aimed at assessing the intensity of the Kamchatka Current near the southeastern coast of Kamchatka and in the zone where it transforms into the Kuril Current. In sections 1 and 2, which represent the Kamchatka Current prior to its bifurcation zone, the most distinct flow was observed in late April–early May; the expected intensification in the second half of November 1998 was not detected. In July, the southward flow persisted, while during the period of maximum surface heating in August–September, geostrophic currents were weak or even northward-directed in some areas of the sections. Typically, the core of the current was observed above the continental slope in the eastern part of the sections.

In the southern part of the study area, the bottom topography – particularly the Vityaz Ridge – significantly affected the characteristics of the Kuril Current, with contrasting oceanographic conditions on either side. Notably, WIL was weakly developed in the trough between the ridge and the islands. In the northern part of this trough (section 3), the CIL reached the bottom in most cases – i.e., to depths of around 500 m – which is considerably deeper than in the Kamchatka region. In the southern part of the trough (section 4), WIL was present, but also less developed than over the continental slope.

The currents on either side of the ridge were predominantly multidirectional. The most pronounced southward flow was observed in May 1996 in the eastern part of the section. A similarly complex distribution of oceanographic parameters and current velocities was typical for the southernmost section 4. This is consistent with

satellite altimetry data [11], which revealed the complex structure of the Kuril Current: it divides into several multidirectional jets and does not form a consolidated flow, except during the winter season.

Conclusion

Based on data from seven oceanographic cruises, the hydrological regime of a poorly studied region off the Pacific coast of the northern Kuril Islands was characterized along four repeated sections. This allowed for refinement of existing concepts and the acquisition of new results.

During the warm season, the entire water column over the shelf was occupied by the CIL, primarily of Bering Sea origin, with core temperatures that can reach negative values. Below the CIL, in the deep continental slope area, the WIL was present, with an average upper boundary at 250 m depth (3 °C). In autumn, due to intensive cooling and wind-wave mixing, the upper boundary of the CIL began to deepen until an upper mixed layer formed in winter.

Against a background of typical surface salinity values of 32–33 PSU for the northern Pacific Ocean, fresher waters (down to 31.5 PSU) were observed off the southeastern Kamchatka coast in July, resulting from the melting of Bering Sea ice cover.

Although three of the four selected sections were located near straits in the Kuril Chain, the influence of Sea of Okhotsk waters – characterized by lower salinity – was not evident, even in summer, when reduced Pacific inflow through the straits might have allowed for such influence.

The Kamchatka and Kuril Currents were well developed in spring but weakened in summer and autumn. A general southwestern flow, extending throughout the water column and most pronounced above the continental slope, was observed only in spring. During summer and autumn, the current patterns were unstable and characterized by weak, multidirectional flows both in depth and horizontally.

The Vityaz Ridge significantly influenced the thermohaline structure and circulation in the study area. In particular, WIL waters penetrated only weakly into the northern part of the trough between the ridge and the Kuril Islands, whereas the CIL was well developed there down to depths of 500 m. The direction of geostrophic currents over the underwater trough was often opposite to the flow over the continental slope.

REFERENCES

1. Bogdanov, K.T. and Moroz, V.V., 2000. *Structure, Dynamic and Hydrology-Acoustical Water Characteristics Peculiarities of the Kuril Straits Area*. Vladivostok: Dalnauka, 152 p. (in Russian).
2. Byshev, V.I., Figurkin, A.L. and Anisimov, I.M., 2016. Recent Climate Changes of Thermohaline Structure in the North-West Pacific. *Izvestiya TINRO*, 185(2), pp. 215-227. <https://doi.org/10.26428/1606-9919-2016-185-215-227> (in Russian).
3. Khen, G.V., Ustinova, E.I., Figurkin, A.L., Zuenko, Yu.I., Novikov, Yu.V., Sorokin, Yu.D. and Gamanyuk, M.V., 2004. Hydrological Conditions of the Northwestern Pacific and the Far Eastern

- Seas at the Beginning of the 21st Century and Expected Trends. *Voprosy Promyslovoi Okeanologii*, (1), pp. 40-58 (in Russian).
4. Khen, G.V., Ustinova, E.I. and Sorokin, Yu.D., 2022. Long-Term Changes in Thermal Conditions on the Surface of the Far-Eastern Seas and North-West Pacific and Their Relationship with Large-Scale Climate Processes. *Izvestiya TINRO*, 202(1), pp. 187-207. <https://doi.org/10.26428/1606-9919-2022-202-187-207> (in Russian).
 5. Kantakov, G.A., 2000. Oceanographic Regime of the Pacific Shelf and Continental Slope of the Northern Kuril Islands and Its Influence on Distribution of Commercial Fishery Targets. In: B. N. Kotenev, ed., 2000. *Commercial and Biological Studies of Fishes in the Pacific Waters of the Kuril Islands and Adjacent Areas of the Okhotsk and Bering Seas in 1992-1998*. Moscow: VNIRO Publishing, pp. 54-64 (in Russian).
 6. Bogdanov, K.T. and Moroz, V.V., 2004. The *Kuril-Kamchatka Current and Oyashio Current Water*. Vladivostok: Dalnauka, 141 p. (in Russian).
 7. Moroz, V.V., 2011. The Water Thermohaline Structure Peculiarities and Temperature Anomalies Dynamics in the Kuril Island Zone and the Adjacent Areas. *Vestnik of the Far East Branch of the Russian Academy of Sciences*, 3(157), pp. 96-103 (in Russian).
 8. Uda, M., 1963. Oceanography of the Subarctic Pacific Ocean. *Journal of the Fisheries Board of Canada*, 20(1), pp. 119-179. <https://doi.org/10.1139/f63-011>
 9. Talley, L.D., 1993. Distribution and Formation of North Pacific Intermediate Water. *Journal of Physical Oceanography*, 23(3), pp. 517-537. [https://doi.org/10.1175/1520-0485\(1993\)023<0517:DAFONP>2.0.CO;2](https://doi.org/10.1175/1520-0485(1993)023<0517:DAFONP>2.0.CO;2)
 10. Zhukov, L.A., 1954. [Fundamentals of the Hydrological Regime of the Kuril Region of the Pacific Ocean]. In: AS SSSR, 1954. *The Works of the Kuril-Sakhalin Marine Complex Expedition of the ZIN-TINRO, 1947-1949*. Publishing House of the USSR Academy of Sciences. Vol. 1, pp. 304-390 (in Russian).
 11. Shevchenko, G.V. and Romanov, A.A., 2006. [Seasonal Variability in the Upper Layer of the Sea of Okhotsk from Altimetry Data]. *Meteorologiya i Gidrologiya*, (8), pp. 59-71 (in Russian).
 12. Glukhovskiy, B.Kh., ed., 1998. *Hydrometeorology and Hydrochemistry of the Seas. Vol. IX: The Sea of Okhotsk. Issue 1: Hydrometeorological Conditions*. Saint Petersburg: Hydrometeoizdat, 343 p. (in Russian).
 13. Moroz, V.V., 1999. [Variability of Hydrological Conditions of the Kuril Islands Region in the Warm Half-Year Due to the Peculiarities of Atmospheric Circulation]. *Meteorologiya i Gidrologiya*, (12), pp. 88-93 (in Russian).
 14. Rogachev, K.A. and Shlyk, N.V., 2005. Multiyear Variability of the Wind Stress Curl and Sea Level in the Kamchatka Current. *Oceanology*, 45(3), pp. 317-326.
 15. Sedaeva, O.S. and Shevchenko, G.V., 2001. Investigation of Seasonal Fluctuations of Sea Level and Atmospheric Pressure in the Area of Kuril Ridge. In: G. V. Shevchenko, ed., 2001. *Dynamic Processes on the Shelf of Sakhalin and the Kuril Islands*. Yuzhno-Sakhalinsk: IMGIG FEB RAS, pp. 81-93 (in Russian).
 16. Shevchenko, G.V. and Romanov, A.A., 2008. Determination of Parameters of Tidal Diurnal Shelf Waves in the Area of the North Kuril Islands from the Satellite Altimetry Data. *Issledovanie Zemli iz Kosmosa*, (3), pp. 76-87 (in Russian).

Submitted 30.05.2024; approved after review 04.06.2024;
accepted for publication 29.01.2025.

About the authors:

Georgy V. Shevchenko, Head of Oceanography Laboratory, Sakhalin Branch of Russian Federal Research Institute of Fisheries and Oceanography (VNIRO) (196 Komsomolskaya Str., Yuzhno-Sakhalinsk, 693023, Russian Federation), Leading Research Associate of Tsunami Laboratory, Institute of Marine Geology and Geophysics, Far Eastern Branch of Russian Academy of Sciences (1B,

Nauki Str., Yuzhno-Sakhalinsk, 693023, Russian Federation), DSc (Phys.-Math.), **ORCID ID: 0000-0003-0785-4618**, shevchenko_zhora@mail.ru

Valeriy N. Chastikov, Leading Researcher of Oceanography Laboratory, Sakhalin Branch of Russian Federal Research Institute of Fisheries and Oceanography (VNIRO) (196 Komsomolskaya Str., Yuzhno-Sakhalinsk, 693023, Russian Federation), **Scopus Author ID: 8510411400**

Vasily A. Ulchenko, Deputy Head of Marine Fish Department, Russian Federal Research Institute of Fisheries and Oceanography (VNIRO) (19 Okruzhnoy Proezd, Moscow, 105187, Russian Federation),

Contribution of the co-authors:

Georgy V. Shevchenko – analyzing and summarizing research results, paper preparation

Valeriy N. Chastikov – processing and complex data analysis, construction of graphs and distributions, discussion of the results of work

Vasily A. Ulchenko – participation in field expeditions, data preparation and processing, discussion of the results of work

The authors have read and approved the final manuscript.

The authors declare that they have no conflict of interest.

Relationship between the Energy of Gravity and Infragravity Sea Waves

G. I. Dolgikh¹, S. G. Dolgikh^{1,✉}, M. A. Bolsunovskii^{1,2}

¹ V.I. Il'ichev Pacific Oceanological Institute, Far Eastern Branch of RAS, Vladivostok, Russian Federation
² Institute of Automation and Control Processes, Far Eastern Branch of RAS, Vladivostok, Russian Federation
✉ sdolgikh@poi.dvo.ru

Abstract

Purpose. A comprehensive analysis of data regarding sea waves of gravity and infragravity ranges, obtained with the help of a supersensitive detector of hydrosphere pressure variations, was conducted. This detector was installed at a depth of 25 m on the shelf of the Sea of Japan.

Methods and Results. The synchronous data of the instrument on infragravity (25 s – 8 min) and gravity (2–25 s) ranges were analyzed, and it was established that the change in the total energy of harmonics in the infragravity range almost always correlates with the change in the total energy of harmonics in the gravity range. However, the total energy of harmonics in the gravity range is always greater than the total energy of harmonics in the infragravity range. A detailed analysis of 629 fragments of the supersensitive detector of hydrosphere pressure variation records reveals a variation in the ratio of the total energy of harmonics of the gravity range to the total energy of harmonics of the infragravity range, varying from 1.16 to 19.70.

Conclusions. In the context of the 629 sections of recordings considered, 16 cases demonstrated an anticorrelation between the total energy of the harmonics of the gravitational range and the total energy of the harmonics of the infragravity range. For the remaining 613 cases, the correlation coefficient ranged from 0.81 to 0.96.

Keywords: sea excitement, gravity range, infragravity range, abnormal behavior, harmonics, supersensitive detector, hydrosphere pressure variations

Acknowledgments: This research was conducted with partial financial support from grant No. 075-15-2024-642, entitled “Study of the processes and patterns of occurrence, development, and transformation of catastrophic phenomena in the oceans and on continents using seismoacoustic monitoring methods”. The authors would like to express their profound gratitude to all employees of the Physics of Geospheres Laboratory.

For citation: Dolgikh, G.I., Dolgikh, S.G. and Bolsunovskii, M.A., 2025. Relationship between the Energy of Gravity and Infragravity Sea Waves. *Physical Oceanography*, 32(2), pp. 270-285.

© 2025, G. I. Dolgikh, S. G. Dolgikh, M. A. Bolsunovskii

© 2025, Physical Oceanography

Introduction

As demonstrated in [1], the change in the total energy of infragravity sea waves (20 s – 8 min) is associated with the change in the total energy of gravity sea waves (2–20 s). The same work also suggested that this testifies in favor of the theory of generation of infragravity sea waves by gravity sea waves. This assertion, however, does not contradict the findings of previously published works, which associate the nature of infragravity sea wave occurrence with gravity sea waves, and those that originate far from or near the shelf inshore [2–4]. Papers [5–7] posit that infragravity



sea waves are the cause of the “infragravity noise of the Earth”. However, other authors reasonably attribute the origin of the “infragravity noise of the Earth” to atmospheric processes [8–10]. These seemingly contradictory results suggest that atmospheric and oceanic processes may be the primary sources of oscillations/waves of the corresponding periods. Furthermore, these phenomena have been detected within the range of eigen oscillations of the Earth. However, the present study will focus on variations in the energy balance between gravity and infragravity sea waves, which, as stated in paper [1], are interrelated. This is of particular interest when considering the nonlinear interaction of infragravity and gravity sea waves during the occurrence of “two sisters” and “three sisters” rogue waves, the mechanism of which is described in [11–13].

In the absence of a comprehensive description of the origin of infragravity sea waves, the mechanism of the origin and dynamics of surface gravity sea waves of the wind range is, at first glance, fully spelled out, as for example in [14]. However, when studying the dynamic features of gravity sea waves moving along a sea of finite depth, nonlinear effects emerge. Of particular interest is the behavior of nonlinear gravity sea waves moving along the shelf of decreasing depth [15, 16]. It is evident that a considerable number of unknowns remain in the range of surface gravity sea waves, especially with regard to the emergence of waves of extreme amplitudes. It is also important to note the role of gravity sea waves of extreme amplitudes in generating of infragravity signals, also known as “voice of the sea”, in the near-water atmosphere, previously discovered by Shuleikin in 1935 [17]. These waves are the cause of unique microseisms, or “voice of the sea”, which propagate along the Earth’s crust over long distances from their point of generation.

In this study, the aim is to explore the relationship between the total energy of harmonics in gravity and infragravity ranges, while taking into account the unique characteristics of gravity and infragravity sea wave interaction, and their role in the process of anomalous hydrophysical phenomena emergence.

Materials and methods

In the present paper, we use *in-situ* data obtained during monitoring works on the registration of changes in hydrosphere pressure on the shelf of the Sea of Japan, using the supersensitive detector (see Fig. 1) described in [18]. Fig. 2 shows the installation diagram of the instrument, which was located on the bottom at a depth of 25 m.

The laser interference device is based on the Michelson equal-arm interferometer, which uses a frequency-blocked gas laser as a light source. The interferometer, together with the compensation chamber and the registration system, is placed in a sealed, corrosion-resistant housing, which is protected by a lattice against difficult operating conditions (rocky or muddy bottom). The housing is constructed in the form of a cylinder, with sealed lids closing the ends. A hermetic connector is incorporated into one cover, enabling the connection of a power cable and data transmission. The second cover contains a sensitive element in the form of an ultra-sensitive sensor, namely a membrane. The membrane is in contact with water on one side, and its second side is part of the interferometer. A rigidly fixed mirror is located at the center of the membrane. The use of the membrane allows the hydrosphere pressure variations to be transmitted directly to the measuring arm

of the interferometer, changing its length. In addition to the device itself, there is an air chamber in the protective cage, which is hermetically connected to the compensation chamber of the device through a shut-off valve. When the device is submerged to the working depth, the valve is opened and the pressure inside the compensation chamber is equalized with the external pressure. Upon reaching the desired depth, the valve closes, and an ultra-sensitive sensor begins to register variations in the pressure of the hydrosphere. The registration system then records the change in the interference pattern, and, following preliminary processing, transmits it via a cable line to the coastal observation post in the form of variations in the pressure of the hydrosphere. This design of the device enables measurements ranging from 0 (conditionally) to 1 kHz with an accuracy of 0.24 mPa at depths of up to 50 m. The reduction of noise in photoelectronic equipment, temperature expansion, and the more accurate equalization of the interferometer arms will improve the technical characteristics of the ultra-sensitive sensor. As a result, the operational range can be expanded to 10 kHz, thereby enhancing the precision of measuring variations in the pressure of the hydrosphere to 1.8 μ Pa.



Fig. 1. Supersensitive detector of hydrosphere pressure variations, inside



Fig. 2. Installation diagram of the supersensitive detector of hydrosphere pressure variations (SSDHPV)

The in-kind data received in real time following pre-processing (filtering, decimation) are located on the recording computer. Thereafter, they are placed in the experimental database. Synchronization of all installations is achieved through the use of a precision clock of the Trimble 5700 GPS receiver with an accuracy of 1 microsecond. Depending on the set tasks, the data were then subjected to further processing (filtering, decimation, spectral processing by the periodogram method or the maximum likelihood method). In this study, the focus was on the data in the range of gravity (2–25 s) and infragravity (25 s – 8 min) sea waves. The boundary between gravity and infragravity ranges was determined at 25 s, as per experimental findings reported in [19], which were obtained for the western part of the Sea of Japan/the East Sea.

Obtained *in-situ* data and their discussion

The data obtained from the supersensitive detector of hydrosphere pressure variations were preprocessed using a low-pass Hamming filter with a cutoff frequency of 1 Hz, and downsampled to a sampling rate of 2 Hz. Subsequently, the data underwent sequential processing in two stages. At the initial stage, the recording was subjected to high-frequency filtering by a Hamming filter with a duration of 10.000 and a cutoff frequency of 0.0004 Hz. At the second stage, the filtered series was filtered by a high-frequency filter with duration of 5000 and cutoff frequency of 0.002 Hz (8 min 20 s). The duration of the entire series was 18373329 points at a sampling frequency of 2 Hz. The final record of the supersensitive detector of hydrosphere pressure variations, which was subjected to further processing, is shown in Fig. 3.

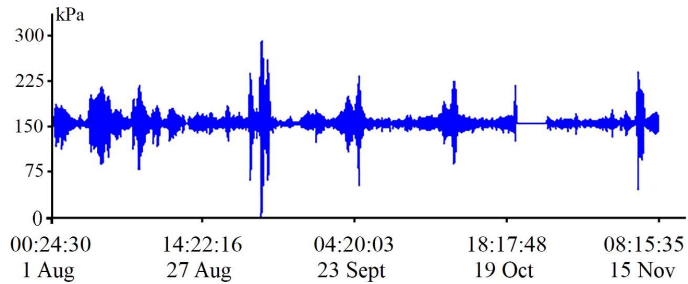


Fig. 3. Filtered record of the supersensitive detector of hydrosphere pressure variations from August 01, 2022 00:24:30 to November 15, 2022 08:15:35 (UTC)

As is evident from this Figure, there were gaps in the instrument's record associated with power failures. These gaps, naturally, were eliminated during the material analysis. In the course of work, 629 fragments of the record containing reliable data were processed. The processing was carried out as follows. The initial processed dataset began at 04:02:57:00 on 01 August 2022, as there was no power supply during the initial phase of the experiment, i.e. from 00 h 24 min 30.0 s to 04 h 02 min 57.0 s on 01 August 2022. The duration of a single processed fragment was 131072 points, which at a sampling rate of 2 Hz amounted to 18 h 12 min 16 s. The spectral processing was performed by the periodogram method with averaging over 3 points. The subsequent step involved the estimation of total energy across the entire range of gravity and infragravity sea waves. This was followed by the estimation of total energy within two ranges: infragravity and gravity. The gravity range was set from 1 to 25 s, and the infragravity range was set from 25 s to 8 min. In each range, the total energy was determined by integrating the spectra. The duration of the series made it possible to obtain a good frequency resolution, which was equal to 0.000015 Hz. In the subsequent stage, 26214 points were selected (3 h 38 min 27 s) and a similar processing was carried out. All subsequent steps were performed strictly in this sequence. In instances where *in-situ* data were absent, the corresponding area was bypassed, and the missing data was documented in the information bulletin.

In the domain of gravity range, when processing various fragments from the supersensitive detector of hydrosphere pressure variations, significant peaks were identified across multiple periods. The maximum with the longest period in the gravity range was identified as that with a period of 14.1 s (see Fig. 4), and the maximum with the shortest period in the gravity range was identified as that with a period of 5.7 s (see Fig. 5).

Furthermore, spectral maxima in gravity range were identified in different time intervals at periods ranging from 22.8 to 1.6 s. Consequently, several ranges of the selected periods of gravity sea waves can be identified. The range of periods from 1.6 to 3.6 s is attributed to wind waves of regional significance, which are excited by the wind at the location of the measurement instrument. Finally, waves with periods of 5–6.5 s are identified as background wind waves (background swell waves) of the Sea of Japan. Gravity sea waves with periods ranging from 14 to 15 s belong to the waves excited by the passage of powerful typhoons. Over time, swell waves arrive at the measuring point, successively with decreasing periods (due to

dispersion) until they reach background swell waves of the Sea of Japan. These unique gravity sea waves have periods in the range of 22–23 s and could be generated by passing tropical cyclones (typhoons) with unique meteorological characteristics. However, given that waves with such periods, as a rule, do not have great amplitudes (their amplitudes are 10–15 times lower than the amplitudes of the main gravity sea waves), we believe that these gravity sea waves are swell waves of oceanic origin.

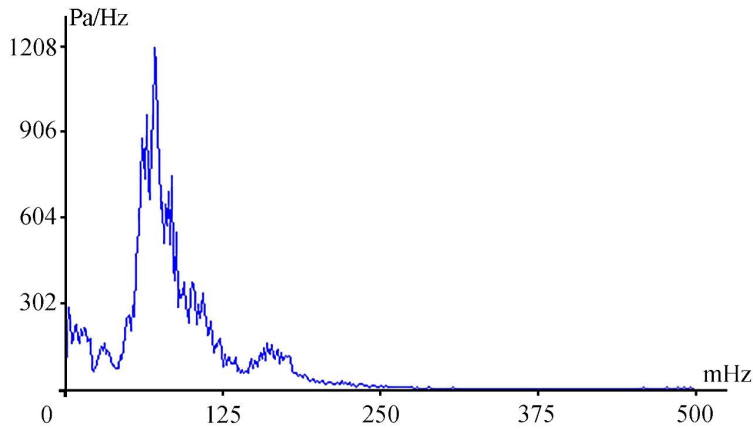


Fig. 4. Maximum with the longest period in the gravity range with a period of 14.1 s

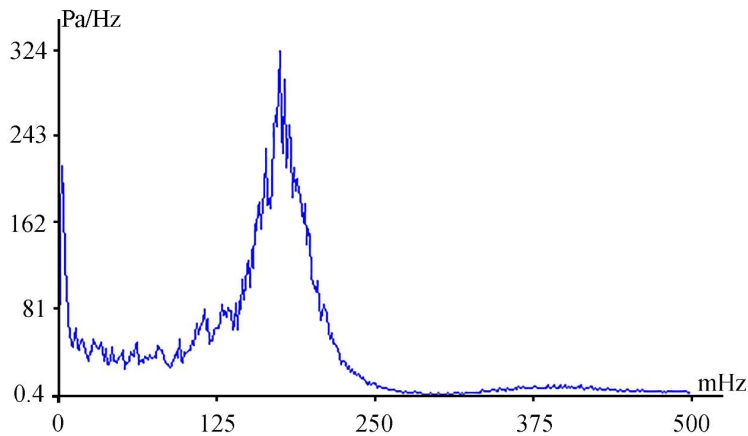


Fig. 5. Maximum with the shortest period in the gravity range with a period of 5.7 s

As illustrated in Fig. 6, the dynamic spectrogram of a fragment of the supersensitive detector of hydrosphere pressure variations record depicts several wave ranges simultaneously. Two powerful segments are visible in the infragravity range, and perturbations in the gravity range at periods of 13–14 and 6 s. In the central part of the figure, the periods of gravity sea waves (swell waves) are shown, starting from the period of about 15.5 s and ending with the period of about 7.5 s. These swell waves originated in the Sea of Japan during the passage of a powerful typhoon in this zone. A study of 629 fragments of the record of

hydrosphere pressure variations obtained during observations from August 01, 00:24:30 to November 15, 08:15:35 revealed that sea gravity waves with periods ranging from 14.1 to 5.7 s exhibited maximum amplitudes at different times.

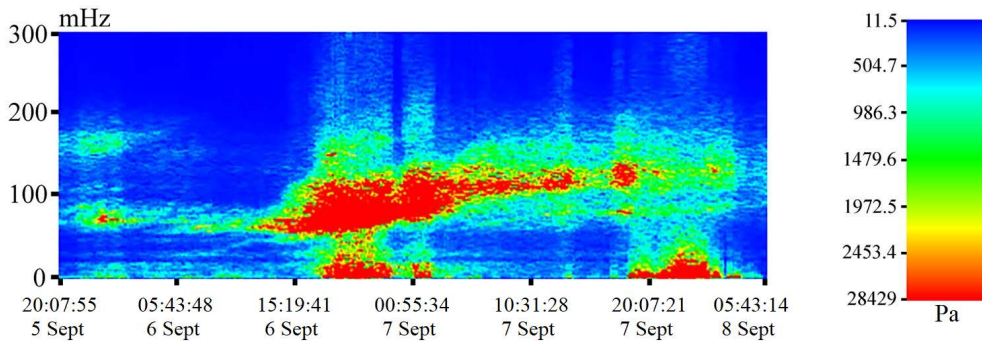


Fig. 6. Dynamic spectrogram of a fragment of hydrosphere pressure variations record from September 05, 2022 20:07:550 to September 08, 2022 05:43:14 (UTC)

When processing all segments, the maximum peak in the gravity range was identified at a period of 12.4 s, with an amplitude of 3757.5 Pa/Hz (see Fig. 7). In accordance with the findings of [14], the amplitude of a surface sea wave can be estimated from the formula

$$a = \frac{P \cosh(2\pi h/\lambda)}{\rho g}$$

Where a is the wave amplitude; P is registered pressure; h is the depth in the instrument installation point; λ is the length of the gravity wave; g is gravity acceleration, and ρ is the density of the sea wave. The resultant wave amplitude is approximately 0.4 m, with a corresponding wave height of about 0.8 m. It should be noted that these figures represent an average wave amplitude in the fragment of 65536 s (18 h 12 min 16 s).

When processing the same record, but of a shorter duration (e.g. 2048 s), the amplitude of the same wave is 3.3 m (i.e. the height is 6.6 m), which at this time is very close to the maximum height of the wave created by a passing powerful typhoon in the Sea of Japan. Concurrently with the maximum amplitude of the gravity sea wave at a period of 12.4 s, a high amplitude of the infragravity sea wave is also observed, which is equal to 2921.5 Pa/Hz at a period of 5 min 18.1 s (see Fig. 8). At the same time, the total energy of the harmonics of the gravity range (25–1 s) is much higher than the total energy of the harmonics of the infragravity range (8 min – 25 s). In this case, the former is 5.5 times higher. To enhance the visual clarity of the infragravity range, particularly the higher frequencies, Fig. 8 (and subsequent figures) has been modified by the exclusion of a segment of the graph ranging from 15.6 to 40 mHz, containing mostly non-informative spectral components with considerably smaller amplitudes.

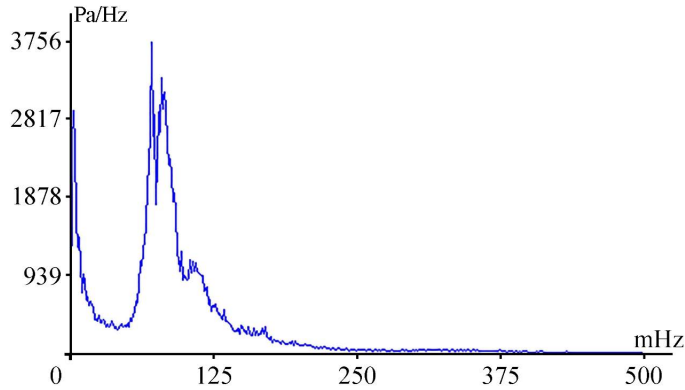


Fig. 7. Amplitude spectrum of the signal of gravity range of the supersensitive detector of hydrosphere pressure variations record fragment

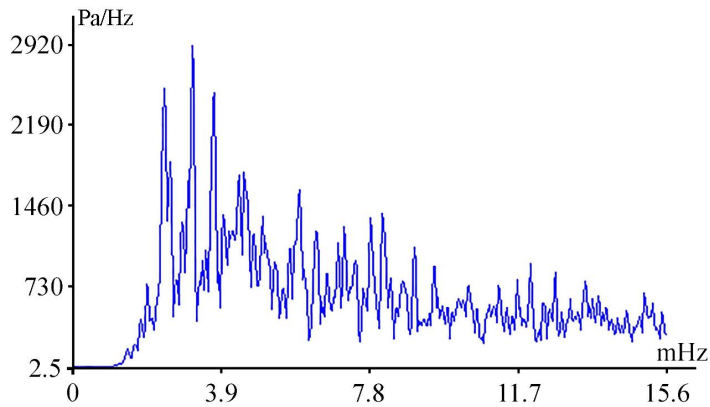


Fig. 8. Amplitude spectrum of the signal of infragravity range of the supersensitive detector of hydrosphere pressure variations record fragment

It is evident that an increase in this ratio generally results in the highest amplitude of one of the harmonics of the gravity range exceeding the highest amplitude of one of the harmonics of the infragravity range. As this ratio decreases, the highest amplitude of one of the harmonics in the infragravity range is usually greater than the highest amplitude of one of the harmonics in the gravity range. Typical examples can be found in Figs. 9 and 10, which illustrate the amplitude spectrum of the signal from the gravity and infragravity ranges of a single fragment of the record of the supersensitive detector of hydrosphere pressure variations.

In the latter case, the total energy of harmonics in the gravity range (25–2 s) is only 1.3 times greater than the total energy of harmonics in the infragravity range (8 min – 25 s), and the largest amplitude of harmonic in the infragravity range is greater than the largest amplitude of harmonic in the gravity range.

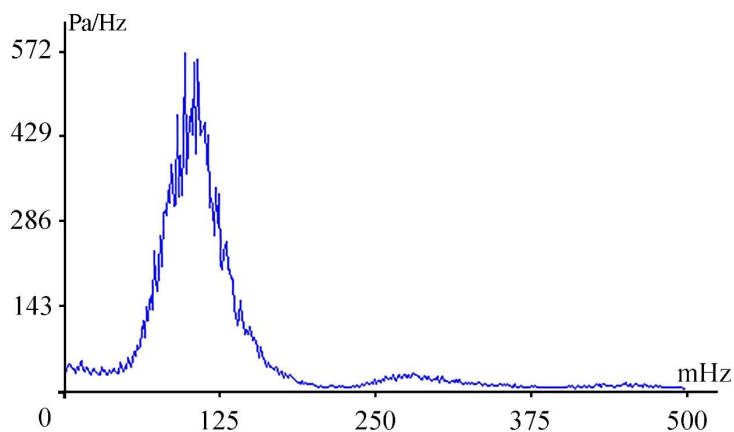


Fig. 9. Amplitude spectrum of the signal of gravity range of the supersensitive detector of hydrosphere pressure variations record fragment (maximum at a period of 6.8 s)

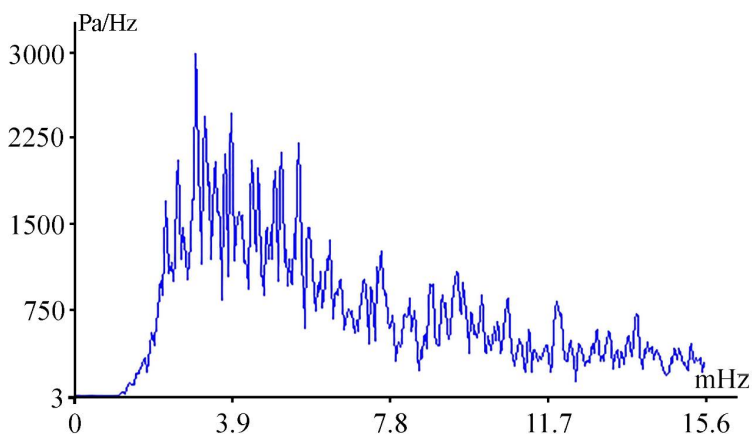


Fig. 10. Amplitude spectrum of the signal of infragravity range of the supersensitive detector of hydrosphere pressure variations record fragment (maximum at a period of 5 min 34.4 s)

When analyzing the situations in Figs. 7–10, the question remains: are the total energies of the infragravity and gravity ranges related, and how are they related? After processing the entire data array, we found that the relationship does exist, and that it is mainly directly proportional, i.e. a decrease in the total energy of the gravity range is accompanied by a decrease in the total energy of the infragravity range, and vice versa – an increase in the total energy of the gravity range is accompanied by an increase in the total energy of the infragravity range. This assertion is supported by the graphs shown in Figs. 11–13.

In rare cases, anomalous behavior of the total energy of the gravity and infragravity ranges is observed. By anomalous behavior we mean the discrepancy (uncorrelated behavior) in the behavior of the total energy of the harmonics of the gravity and infragravity ranges. Pronounced anomalous behavior is observed in the graphs shown in Fig. 14.

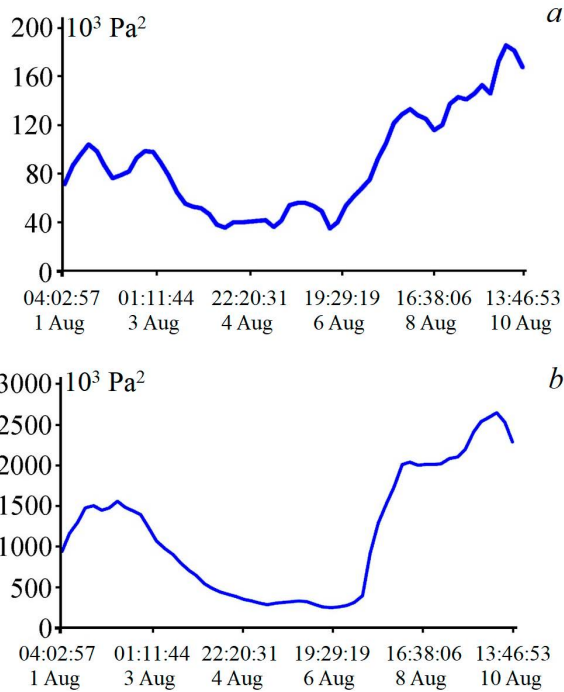


Fig. 11. Graph of change in the total energy of the infragravity (a) and gravity (b) ranges (correlation coefficient 0.96) from August 01, 2022 04:02:57 to August 10, 2022 13:46:53 (UTC)

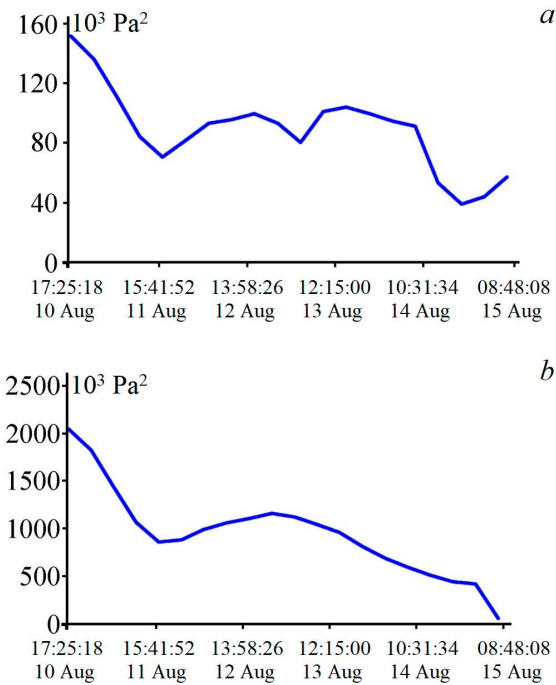


Fig. 12. Graph of change in the total energy of the infragravity (a) and gravity (b) ranges (correlation coefficient 0.88) from August 10, 2022 17:25:18 to August 15, 2022 08:48:08 (UTC)

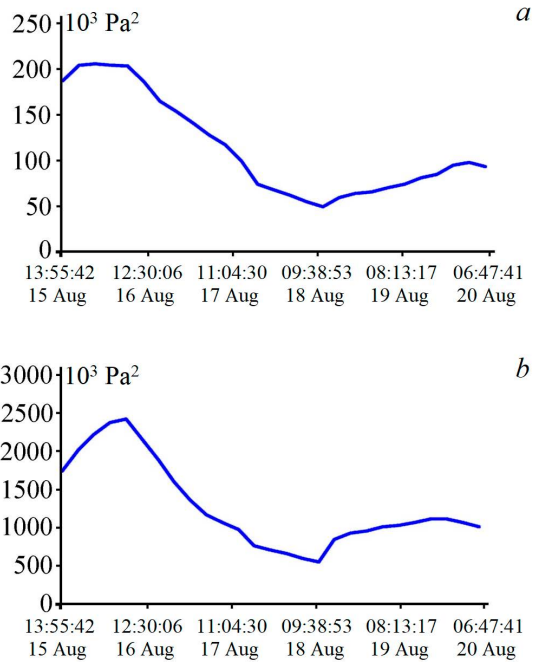


Fig. 13. Graph of change in the total energy of the infragravity (a) and gravity (b) ranges (correlation coefficient 0.96) from August 15, 2022 13:55:42 to August 20, 2022 06:47:41 (UTC)

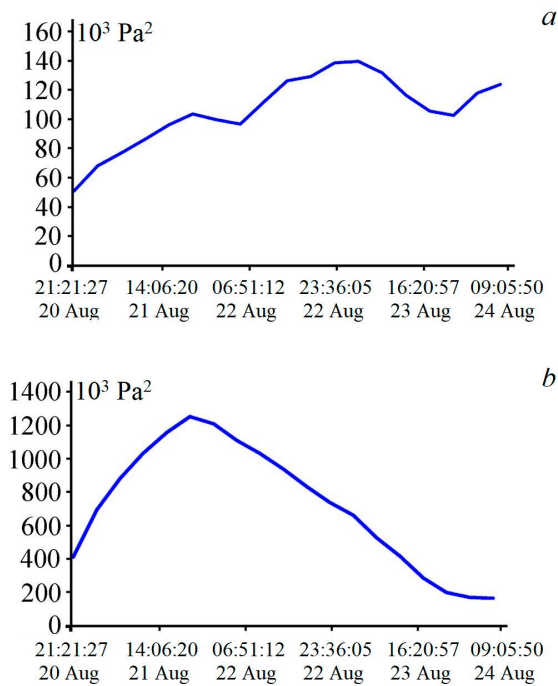


Fig. 14. Graph of change in the total energy of the infragravity (a) and gravity (b) ranges (correlation coefficient 0.19) from August 20, 2022 21:21:27 to August 24, 2022 09:05:50 (UTC)

As demonstrated by the comparison of the graphs shown in Fig. 14, the behavior of the total energy of the harmonics of gravity and infragravity ranges is observed to be normal on 1/3 of the segment. However, in the remaining 2/3 of the segment, an anomalous behavior of the total energy of the harmonics of gravity and infragravity ranges is observed. How does the anomalous behavior of the total energy of harmonics of gravity and infragravity ranges manifest itself? Firstly, at elevated values, the ratio of the total energy of the harmonics of gravity range to the total energy of the harmonics of infragravity range is substantial, and the maximum peak is not at the harmonic of gravity range, but at the harmonic of infragravity range. As illustrated in the second segment of the graph presented in Fig. 14, this ratio reaches a value of 7.5, and the maximum signal amplitude occurs at the harmonic of infragravity range (4 min 51.3 s (3.43 mHz – amplitude 443 Pa/Hz)). A similar outcome is observed at the ratio of 6.5, where the maximum amplitude is also at the harmonic of infragravity range (4 min 51.3 s (3.43 mHz – 440 Pa/Hz)).

From the series of observations, it is evident that there are other cases of anomalous behavior of this ratio at maximum harmonics of gravity or infragravity ranges. Anomalous behavior of this nature is observed when the ratio of the total energy of the harmonics of gravity range to the total energy of the harmonics of infragravity range is 7.0 (6 min 16.6 s (2.65 mHz – 494 Pa/Hz)), 7.8 (6 min 16.6 s (2.65 mHz – 690 Pa/Hz)), 7.9 (5 min 34.4 s (2.99 mHz – 182 Pa/Hz)), 8.3 (5 min 36.1 s (2.98 mHz – 172 Pa/Hz)), 7.9 (4 min 53.9 s (3.4 mHz – 145 Pa/Hz)), 8.0 (5 min 44.9 s (2.9 mHz – 104 Pa/Hz)), 8.4 (5 min 00.6 s (3.33 mHz – 122 Pa/Hz)). Anomalous behavior has been observed at other ratios. For instance, at the ratio of 3.6, the maximum signal amplitude is observed not at the harmonic of the infragravity range, but at the harmonic of the gravity range, in this case, at the harmonic with a period of 5.8 s (0.172 Hz – 127 Pa/Hz). A similar anomaly is also observed for other ratios, for example, 3.4 (5.8 s (0.172 Hz – 128 Pa/Hz)), 4.8 (12.0 s (0.083 Hz – 267 Pa/Hz)), 4.6 (12.1 s (0.0826 Hz – 260 Pa/Hz)), 4.0 (12.3 s (0.081 Hz – 245 Pa/Hz)), 2.9 (9.3 s (0.107 Hz – 130 Pa/Hz)), 3.0 (12.8 s (0.078 Hz – 272 Pa/Hz)).

We assume that the nature of the observed anomalies is associated with the focusing or defocusing of harmonics of infragravity or gravity ranges, i.e. with a concentration of energy on individual harmonics or diffusion of energy between the harmonics of infragravity or gravity ranges.

Fig. 15 shows the amplitude spectrum of the signal obtained from processing a fragment of the supersensitive detector of hydrosphere pressure variations record, which shows focusing of the infragravity harmonics (see the bottom graph) and defocusing of the gravity harmonics (see the top graph). In this case, the ratio of the total energy of the harmonics of the gravity range to the total energy of the harmonics of the infragravity range is 8.4.

On the contrary, we would say that more anomalous cases are observed when the harmonics of the infragravity range are defocused and the harmonics of the gravity range are focused. As demonstrated in Fig. 16, the amplitude spectrum of the signal from a fragment of the supersensitive detector of hydrosphere pressure variations record exhibits a ratio of the total energy of the harmonics of gravity range to the total energy of the harmonics of infragravity range of 3.1.

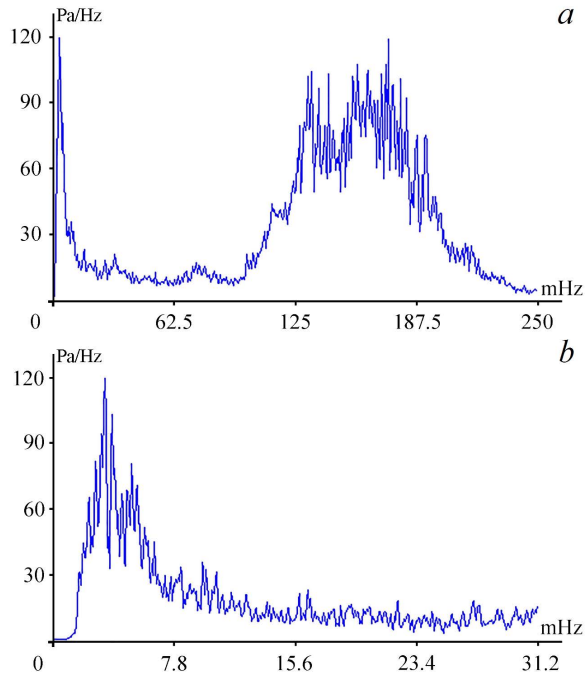


Fig. 15. Amplitude spectrum of the signal of gravity range (a) and infragravity range (b) of the supersensitive detector of hydrosphere pressure variations record fragment

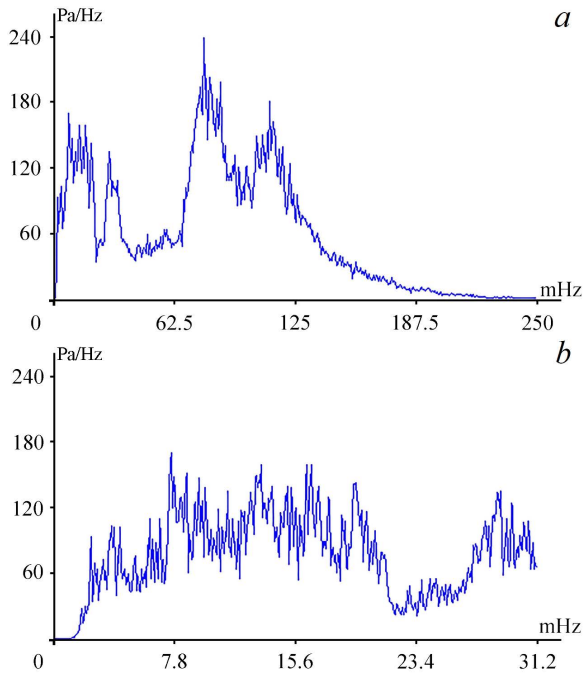


Fig. 16. Amplitude spectrum of the signal of gravity range (a) and infragravity range (b) of the supersensitive detector of hydrosphere pressure variations record fragment

Of particular interest are the cases of anomalous situations, where defocusing of the harmonics of infragravity range is observed, subsequently accompanied by focusing of the harmonics of infragravity range. This is followed by interaction of the harmonics of infragravity range with the harmonics of gravity range, resulting in the emergence of anomalous waves of high amplitudes, such as “one sister”, “two sisters”, “three sisters” [20]. An illustration of such a recording section of the supersensitive detector of hydrosphere pressure variations is presented in Fig. 17.

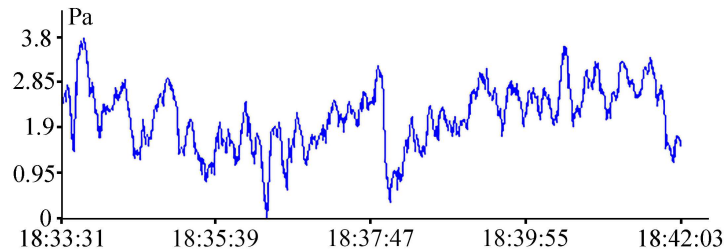


Fig. 17. A recording section of the supersensitive detector of hydrosphere pressure variations for September 2, 2022

Conclusions

It has been established that the total energy of the harmonics of gravity range is invariably greater than the total energy of the harmonics of infragravity range. When the ratio of the total energy of the harmonics of gravity range to the total energy of the harmonics of infragravity range exceeds 5.5 in the spectra (2 s – 8 min), the maximum peak is almost always at the harmonic of gravity range. When this ratio is lower than 5.5, the maximum peak in the spectra (2 s – 8 min) is almost always at the harmonic of infragravity range.

Anomalous cases are observed when the statement given in the previous paragraph is not adhered to. A particularly pronounced anomaly is characterized by a substantial discrepancy. For instance, at values of this ratio of 2.9, 3.0 and 3.4, the maximum peak is observed to occur not on the harmonic of infragravity range, but rather on the harmonic of gravity range. Conversely, at values of this ratio of 8.4, 8.3 and 8.0, and other substantial numbers, the maximum peak is not on the harmonic of gravity range, but on the harmonic of infragravity range.

The occurrence of anomalous cases is observed in instances where the harmonics of infragravity or gravity ranges are defocused. In some cases, the defocusing of harmonics within the infragravity range is accompanied by the focusing of harmonics within the infragravity range. This is followed by the interaction of the harmonics within the infragravity range with those within the gravity range, resulting in the emergence of anomalous waves of large amplitudes, such as “two sisters” and “three sisters”.

REFERENCES

1. Dolgikh, G., Budrin, S. and Dolgikh, S., 2020. Fluctuations of the Sea Level, Caused by Gravitational and Infra-Gravitational Sea Waves. *Journal of Marine Science and Engineering*, 8(10), 796. <https://doi.org/10.3390/jmse8100796>

2. Rabinovich, A.B., 1993. *Long Gravitational Waves in the Ocean: Capture, Resonance, and Radiation*. Saint Petersburg: Gidrometeoizdat, 325 p. (in Russian).
3. Longuet-Higgins, M.S., 1984. Statistical Properties of Wave Groups in a Random Sea State. *Philosophical Transactions of the Royal Society A: Mathematical, Physical and Engineering Sciences*, 312(1521), pp. 219-250. <https://doi.org/10.1098/rsta.1984.0061>
4. Thompson, W.C., Nelson, A.R. and Sedivy, D.G., 1985. Wave Group Anatomy of Ocean Wave Spectra. In: B. L. Edge, ed., 1985. *Coastal Engineering 1984 Proceedings*. Houston, Texas, United States: ASCE Press, pp. 661-677. <https://doi.org/10.1061/9780872624382.046>
5. Ekstrom, G. and Ekstrom, S., 2005. Correlation of Earth's Long-Period Background Seismic Radiation with the Height of Ocean Waves. In: AGU, 2005. *American Geophysical Union (AGU) 2005 Fall Meeting*. San Francisco, CA, USA: AGU. Vol. 86(52), abstract S34B-02.
6. Romanowicz, B., Rhie, J. and Colas, B., 2005. Insights into the Origin of the Earth's Hum and Microseisms. In: AGU, 2005. *American Geophysical Union (AGU) 2005 Fall Meeting*. San Francisco, CA, USA: AGU. Vol. 86(52), abstract S31A-0271.
7. Webb, S.C., 2007. The Earth's "Hum" Is Driven by Ocean Waves over the Continental Shelves. *Nature*, 445, pp. 754-756. <https://doi.org/10.1038/nature05536>
8. Nishida, K., Kobayashi, N. and Fukao, Y., 2000. Resonant Oscillations between the Solid Earth and Atmosphere. *Science*, 287(5461), pp. 2244-2246. <https://doi.org/10.1126/science.287.5461.2244>
9. Kobayashi, N. and Nishida, K., 1998. Continuous Excitation of Planetary Free Oscillations by Atmospheric Disturbances. *Nature*, 395, pp. 357-360. <https://doi.org/10.1038/26427>
10. Nishida, K., Kobayashi, N. and Fukao, Y., 2002. Origin of Earth's Ground Noise from 2 to mHz. *Geophysical Research Letters*, 29(10), pp. 52-1-52-4. <https://doi.org/10.1029/2001GL013862>
11. Dolgikh, G., Dolgikh, S., Chupin, V., Ovcharenko, V., Shvets, V. and Yakovenko, S., 2022. Registration of Nonlinear Hydrophysical Disturbances – Rogue Waves in Full-Scale Conditions. *Journal of Marine Science and Engineering*, 10(12), 1997. <https://doi.org/10.3390/jmse10121997>
12. Pelinovsky, E., Polukhina, O. and Kurkin, A., 2010. Rogue Edge Waves in the Ocean. *The European Physical Journal Special Topics*, 185, pp. 35-44. <https://doi.org/10.1140/epjst/e2010-01236-9>
13. Shurgalina, E.G. and Pelinovsky, E.N., 2012. Development of Freak Swell Wave in a Weak Wave Field. *Fundamental and Applied Hydrophysics*, 5(1), pp. 77-88 (in Russian).
14. Bowden, K.F., 1983. *Physical Oceanography of Coastal Waters*. Ellis Horwood Series in Marine Science. Chichester, New York: Halsted Press, Ellis Horwood Limited, 302 p.
15. Bjørnstad, M., Buckley, M., Kalisch, H., Streßer, M., Horstmann, J., Frøysa, H.G., Ige, O.E., Cysewski, M. and Carrasco-Alvarez, R., 2021. Lagrangian Measurements of Orbital Velocities in the Surf Zone. *Geophysical Research Letters*, 48(21), e2021GL095722. <https://doi.org/10.1029/2021GL095722>
16. Flores, R.P., Williams, M.E. and Horner-Devine, A.R., 2022. River Plume Modulation by Infragravity Wave Forcing. *Geophysical Research Letters*, 49(15), e2021GL097467. <https://doi.org/10.1029/2021GL097467>
17. Shuleikin, V.V., 1935. On Sea Voice. *Doklady Akademii Nauk SSSR*, 3(6), p. 259 (in Russian).
18. Dolgikh, G.I., Budrin, S.S., Dolgikh, S.G. and Plotnikov, A.A., 2020. Supersensitive Detector of Hydrosphere Pressure Variations. *Sensors*, 20(23), 6998. <https://doi.org/10.3390/s20236998>
19. Oh, J.-E., Jeong, W.-M., Chang, Y.S. and Oh, S.-H., 2020. On the Separation Period Discriminating Gravity and Infragravity Waves off Gyeongpo Beach, Korea. *Journal of Marine Science and Engineering*, 8(3), 167. <https://doi.org/10.3390/jmse8030167>
20. Dolgikh, G. and Dolgikh, S., 2023. Nonlinear Interaction of Infragravity and Wind Sea Waves. *Journal of Marine Science and Engineering*, 11(7), 1442. <https://doi.org/10.3390/jmse11071442>

Submitted 23.12.2024; approved after review 16.01.2025;
accepted for publication 29.01.2025.

About the authors:

Grigory I. Dolgikh, Chief Researcher, V.I. Il'ichev Pacific Oceanological Institute, Far Eastern Branch of RAS (43 Baltiyskaya Str., Vladivostok, 690041, Russian Federation), DSc (Phys.-Math.), Academician of RAS, **SPIN-code: 5241-3375**, **ORCID ID: 0000-0002-2806-3834**, **Scopus Author ID: 7003888822**, **Web of Science ResearcherID: A-7685-2014**, dolgikh@poi.dvo.ru

Stanislav G. Dolgikh, Head of the Laboratory of Nonlinear Hydrophysics and Natural Disasters, V.I. Il'ichev Pacific Oceanological Institute, Far Eastern Branch of RAS (43 Baltiyskaya Str., Vladivostok, 690041, Russian Federation), DSc (Tech.), **SPIN-code: 1836-2541**, **ORCID ID: 0000-0001-9828-5929**, **Scopus Author ID: 6604069353**, **Web of Science ResearcherID**, sdolgikh@poi.dvo.ru

Mikhail A. Bolsunovskii, Graduate Student, V.I. Il'ichev Pacific Oceanological Institute, Far Eastern Branch of RAS (43 Baltiyskaya Str., Vladivostok, 690041, Russian Federation), **SPIN-code: 8711-4746**, **ORCID ID: 0000-0002-9197-7452**, **Scopus Author ID: 58405940300**, **Web of Science ResearcherID: HMO-8458-2023**, bolsunovsky.ma@poi.dvo.ru

Contribution of the co-authors:

Grigory I. Dolgikh – scientific supervision of the research, analysis of results and their interpretation, participation in the discussion of article materials and editing the article text

Stanislav G. Dolgikh – data visualization and presentation, participation in the discussion of article materials, writing an article text and participation in the discussion of article materials

Mikhail A. Bolsunovskii – data visualization and presentation, participation in the discussion of article materials

The authors have read and approved the final manuscript.

The authors declare that they have no conflict of interest.